

# **Computational Investigation into the Influence of Yaw & Rotation on the Bluff-Body Aerodynamics of an Isolated Wheel**

---

A thesis submitted for the degree of  
Doctor of Philosophy (PhD)

By

Tharaka D Kothalawala (BEng)

Brunel University, UK

School of Engineering & Design

October 2014

## Declaration

I, Tharaka D Kothalawala, hereby declare that the work presented in this thesis is my own research, and has not been published for a degree at any other university or institution. Any material that could be interpreted as the work of others is cited and referenced.

Signed:



Name: Tharaka .D. Kothalawala

Date: 13<sup>th</sup> February 2015

# Abstract

A computational study was conducted, to understand the aerodynamic flow-field around isolated wheel configurations in free-air. Landing gear is known to be one of the most prominent noise sources on approach generating significant aircraft noise, due to the complex configurations consisting of many small components interacting with the oncoming airstream within close proximity to one another. This noise produces disruption and discomfort affecting millions of people in the vicinity of airports on a daily basis. In order to fully understand the aerodynamics around this complex configuration, focusing on specific components of a landing gear would fundamentally provide insight to the complex flow interactions related to these components. As a first step, the aerodynamic flow-field around a single stationary isolated wheel was analysed, as a baseline case, with subsequent application of wheel rotation, wheel yaw, and both yaw and rotation combined to model the take-off phase, and landing and take-off phase with the presence of a crosswind respectively. The ‘A2’ wheel geometry, primarily introduced by Fackrell, was computationally modelled for this study, due to the literature available for comparisons, although previous investigations using this geometry were conducted with ground effect. Wheel rotation was applied with a peripheral velocity of 192.31rad/s, equivalent to the free-stream velocity of 40m/s, providing a Reynolds number of  $1.1 \times 10^6$  based on wheel diameter. Time-averaged Unsteady Reynolds-Averaged Navier-Stokes (URANS) were simulated on a structured hexahedral grid consisting of 5 million cells. Results obtained from the CFD simulations provided data such as surface pressure distribution, velocity, central vortex core vorticity magnitude and position with downstream propagation into the wake, and aerodynamic force coefficients. The data was compared to the available literature where possible, although investigations regarding ‘free-air’ wheel configurations are limited. Overall, results showed good agreement to the available literature. Additionally, comparisons were made between the cases to identify the key effects of the baseline case, influence of rotation, influence of applied wheel yaw and the influence of both yaw and rotation combined.

# Acknowledgements

First & foremost, I would like to thank my supervisor Dr Alvin Gatto for all his valuable insight, guidance and support, as well as the time he has invested in me throughout this PhD.

I would also like to thank my second supervisor, Prof. Luiz Wrobel for his advice and support. I am also grateful for his general concerns about my welfare and research during my time at Brunel University.

Additionally, I would like to acknowledge Mr John Stone from CFD Technologies for assisting me whilst learning the grid generation software Pointwise™.

I would also like to show my appreciation to my dear family and friends, for their encouragement and support during the course of this degree.

Most importantly, I would like to dedicate this thesis to my father, Mr N. Kothalawala, who has dedicated his life to providing me with love, patience and support throughout my educational career. The strength and encouragement he has given me has helped me overcome setbacks, and to remain focussed on the ultimate goal in completing this PhD; for that I am forever indebted to my father for all he has sacrificed in ensuring me a better future.



# Contents

Declaration.....	ii
Abstract.....	iii
Acknowledgements.....	iv
List of Figures.....	vii
List of Tables.....	xiv
List of Publications.....	xv
Nomenclature.....	xvi
Abbreviations.....	xviii
1. Introduction.....	1
1.1 The Aircraft Noise Problem.....	1
1.2 Aims & Objectives.....	4
1.3 Thesis Structure.....	5
2. Literature Review.....	6
2.1 The 2D Cylinder.....	8
2.1.1 Influence of Reynolds Number ( $Re_n$ ).....	9
2.1.2 Influence of Aspect Ratio (AR).....	11
2.1.3 Influence of Rotation on Cylinder Flows.....	13
2.1.4 Influence of applied Yaw angle.....	16
2.1.5 Influence of Ground Proximity.....	18
2.2 3D Wheel Aerodynamics.....	22
2.2.1 Wheels in Free – Air.....	22
2.2.2 Wheels in contact with the ground.....	25
2.3 Aerodynamics & Aeroacoustics of Aircraft Landing Gear.....	66
3. Computational Methodology & Set-Up.....	81
3.1 Introduction to CFD.....	81
3.2 Description & Justification of selected Wheel Geometry.....	81
3.3 Computational Method & Grids.....	82
3.3.1 Numerical Methods & Turbulence Models.....	88
3.3.2 Solver Settings.....	91
3.3.3 Convergence.....	92
3.3.4 Boundary Refinement Study.....	93
3.3.5 Mesh Refinement Study.....	94
3.3.6 Time Step Study.....	96

3.3.7	Final Computational Grid .....	97
4.	Validation of Computational Methodology .....	101
5.	Results & Discussion .....	112
5.1	Characterisation of the baseline flow case (zero yaw, zero rotation).....	112
5.1.1	Surface Pressure Characteristics .....	112
5.1.2	Wake Physics .....	114
5.1.3	Aerodynamic Forces .....	118
5.2	The Influence of Wheel Yaw .....	119
5.2.1	Surface Pressure Characteristics .....	120
5.2.2	Wake Physics .....	124
5.2.3	Aerodynamic Forces .....	132
5.2.4	The effect of Yaw .....	134
5.3	The Influence of Wheel Rotation.....	140
5.3.1	Surface Pressure Characteristics .....	140
5.3.2	Wake Physics .....	144
5.3.3	Aerodynamic Forces .....	146
5.3.4	The effect of Rotation .....	148
5.4	The Influence of Wheel Rotation and applied Wheel Yaw .....	151
5.4.1	Surface Pressure Characteristics .....	151
5.4.2	Wake Physics .....	156
5.4.3	Aerodynamic Forces .....	163
5.4.4	The combined effect of both Yaw & Rotation.....	164
6	Conclusion .....	171
6.1	Effect of stationary wheel in free air.....	171
6.2	Effect of Yaw .....	172
6.3	Effect of Rotation.....	173
6.4	Effect of Yaw & Rotation .....	173
7	Recommendations for future work .....	176
	Bibliography .....	178

# List of Figures

Figure 1 – Aircraft noise sources [1] .....	1
Figure 2 - Flow field characteristics past a 2D cylinder at critical Reynolds Number regimes [12, 13].....	9
Figure 3 - Variation of drag coefficient of a circular cylinder as a function of Reynolds number [19].....	10
Figure 4 – Drag coefficient based on (a) L/D, (b) using projected side area [20] .....	11
Figure 5 – General flow structure around a cylinder [20] .....	12
Figure 6 – General flow structure around coin-like cylinders [20] .....	13
Figure 7 – Magnus Effect .....	13
Figure 8 – Flow visualisation around a rotating cylinder in water, (a) $V_r/V=0$ , (b) $V_r/V=1$ , (c) $V_r/V=2$ , (d) $V_r/V=4$ , (e) $V_r/V=6$ , $V_r/V=\infty$ . [20] .....	14
Figure 9 - Flow patterns for various Strouhal numbers ( $St$ ) and velocity ratios ( $\alpha$ ); flow direction left to right and clockwise cylinder rotation [23, 24] .....	15
Figure 10 – Effect of Yaw on pressure coefficient [20, 26] .....	17
Figure 11 – Distribution of $C_p$ around the cylinder and ground plane plate at different $G/d$ ratios (continued on next two pages) [28]...(continued on to next page).....	20
Figure 12 – Streaklines on rear surface of wheel [32] .....	22
Figure 13 – Surface pressure distribution along three circumferential cuts through wheel [32] .....	23
Figure 14 – Normalised velocity components for simple hub at $x=0\text{mm}$ plane, (a) streamwise $z$ -velocity, (b) vertical $y$ -velocity [32] .....	24
Figure 15 – Drag coefficient of fully exposed wheel against test speeds at different yaw angles [33].....	25
Figure 16 – Drag coefficient against yaw angle at various fairing heights tested [33] .....	26
Figure 17 – Lift coefficient against yaw angle at various fairing heights tested [33] .....	26
Figure 18 – Distribution of surface pressure at different ground clearances around (a) stationary wheel, (b) rotating wheel [34] .....	27
Figure 19 – Flow pattern around stationary and rotating wheels in free air and in contact with the ground [34].....	29
Figure 20 – Force coefficients on different wheel geometries tested in [22] .....	30
Figure 21 – Centreline pressure distribution around rotating wheels A1 & A2 [22] .....	30

Figure 22 – Pressure distribution around wheels A1, B1 & C1 (Different wheel width, same edge profile) [22] .....	31
Figure 23 – Centreline Pressure distribution around stationary and rotating wheel B2 [22] ..	32
Figure 24 – Total head contour at Plane 1; 1.7 inches from the centre of the wheel, stationary & rotating [22] .....	33
Figure 25 – Smoke Visualisation of flow past wheel, (a) side view on rotating wheel, (b) side view on stationary wheel [22]. Flow direction: Right to Left.....	34
Figure 26 – Details of the separation point and ‘jetting’ flow [22] .....	35
Figure 27 – Pressure distributions under a rotating wheel at different ground clearances [36] .....	36
Figure 28 – Rear near wake pattern, (a) stationary wheel, (b) rotating wheel, (c) rotating wheel in contact with the ground [36] .....	37
Figure 29 - Comparisons of velocity field in the rear wake of the stationary wheel at $x = 150\text{mm}$ , illustrating velocity vectors and contours of the velocity component in streamwise $x$ -direction [37].....	39
Figure 30 - Comparisons of velocity field in the rear wake of the rotating wheel at $x = 150\text{mm}$ , illustrating velocity vectors and contours of the velocity component in streamwise $x$ -direction [37].....	40
Figure 31 - Streamlines and iso-surfaces of vorticity magnitude in the rear wake of the stationary wheel [29].....	41
Figure 32 – Iso-surface of vorticity magnitude on the upper rear wake of the rotating wheel [29].....	42
Figure 33 – Comparisons of surface pressure distribution on the centreline of (a) stationary & (b) rotating wheel to Fackrell’s [22] experiment. [29] .....	43
Figure 34 – Flow characteristics on general isolated wheel, (a) stationary (b) rotating [29] ..	44
Figure 35 - Time-averaged force coefficients from [29] with a comparison to Fackrell's [22] experimental results .....	45
Figure 36 – 90% total head contour behind stationary wheel at a plane $x = 0.699$ [38] .....	45
Figure 37 - Centreline Pressure distribution, (a) stationary (b) rotating wheel [39].....	47
Figure 38 - Pressure contours at $z = 2.5D$ , (a) stationary (b) rotating wheel [39] .....	48
Figure 39 - Velocity vector plot on the centreline of the lower rear (a) stationary (b) rotating wheel [40] .....	49

Figure 40 - Velocity vector plot on the centreline of the upper rear (a) stationary (b) rotating wheel [40] .....	50
Figure 41 – Centreline Pressure dsitribution, experimentally [40] & CFD, [41] .....	51
Figure 42 – Vorticity plots for (a) RANS (b) URANS (c) LES (d) DES; upper row: $z/d = 0.22$ , lower row: $z/d = -0.04$ [42]. Flow travelling towards $-z/d$ .....	52
Figure 43 – Vorticity plots at $z/d = -0.52$ , for (a) RANS (b) URANS (c) LES (d) DES from [42]. Flow travelling towards $-z/d$ .....	53
Figure 44 - Time-averaged URANS velocity vectors at $x/d = 1.14$ in the wake of CI wheel configuration [30] .....	54
Figure 45 - Velocity vectors in $x/d=0.57$ plane in the wake of CII wheel configuration, (a) PIV (b) CFD [30].....	55
Figure 46 - Time-averaged URANS velocity vectors in $x/d=1.14$ plane in the wake of CII wheel configuration [30].....	56
Figure 47 – CII streamwise velocity profiles for centre plane from experimental and CFD URANS simulations [30].....	56
Figure 48 – Contours of mean streamwise velocity at $x/d = 0.6$ [10].....	57
Figure 49 – Velocity Vectors (left) & line integral convolution image (right) from [10] .....	58
Figure 50 – Line integral convolution image from [10] .....	58
Figure 51 – Contours of mean streamwise velocity at $x/d = 0.75$ and $x/d = 1$ [43] .....	59
Figure 52 – CFD Line integral convolution images at different planes downstream F1 wheel with & without sting from [31].....	60
Figure 53 – Contours of velocity magnitude with velocity vectors at different yaw angles from [12].....	64
Figure 54 - Drag coefficients for a rotating wheel using different hub sealing arrangements [12].....	65
Figure 55 – Velocity magnitude contours inplane bisecting inline wheels from [7].....	66
Figure 56 – Mean centreline pressure on front (fore) wheel, from [7] .....	67
Figure 57 - Mean vorticity in mid-plane of wheels [7].....	68
Figure 58 – Change of positions of vortex between wheels from [7].....	69
Figure 59 – $C_p$ around the wheel when placed in the top view, (a) Front wheel, (b) rear wheel [9].....	70
Figure 60 – Instantaneous vorticity magnitude, (a) DES, (b) URANS [9].....	71

Figure 61 – Instantaneous pressure contours [47]; red = high pressure, green = low pressure .....	72
Figure 62 – Spanwise velocity contours (blue: -0.12 and red: 0.12), left: $z=0$ plane, right: $z=1.3$ plane [47] .....	73
Figure 63 – Streamwise velocity contours, $y = 0.463$ plane (blue: -0.1 and red: 0.25) [47] ...	74
Figure 64 – Half landing gear model showing oil flow visualisation data – (a) top view, (b) isometric view from front [48].....	75
Figure 65 – Surface flow visualisation on rear surface of front wheel [48] .....	76
Figure 66 – Schematic representation of an unstable node (UN), stable focus (SF) & saddle point (SP) [49].....	77
Figure 67 – Iso-surface of Vorticity [51] .....	79
Figure 68 – Acoustic Signals, (a) Directly above the wheel, (b) Directly below the wheel, (c) Upstream of the wheel, (d) Downstream of the wheel [51].....	79
Figure 69 - Cross-sectional view of wheel showing dimensions (mm).....	82
Figure 70 - Representation of (a) block topology - 'C' grid and (b) circular topology - 'O' grid .....	84
Figure 71 – Surface mesh on wheel .....	87
Figure 72 - Force coefficient against real time, for different far-field boundary distances .....	94
Figure 73 - Force coefficient against real time, for different sized grids .....	95
Figure 74 - Force coefficient against real time, for different time-steps .....	96
Figure 75 - Near-field computational grid .....	97
Figure 76 – Geometry of computational domain .....	97
Figure 77 – Side view (+x) of computational grid.....	98
Figure 78 – Top view of Computational grid including wheel showing applied yaw angle, (a) no yaw (b) $15^\circ$ yaw .....	98
Figure 79 - Representation of rotational axis on a wheel with applied yaw angle .....	100
Figure 80 – Comparison of centreline mean pressure coefficient with experimental literature, (a) centreline (b) $x/d = \pm 0.17$ .....	101
Figure 81 - Centreline pressure data on front wheel [48] .....	104
Figure 82 - Surface pressure distribution along the centreline of the front left wheel; (a) single front left wheel, (b) with comparisons to Lazos [7], from [47] .....	105
Figure 83 - Wheel geometry used in [32], indicating 'hub side' & 'boss side' .....	107

Figure 84 – Contour plots of streamwise velocity on wheel centreline plane $x/d=0$ ; (a) present study, (b) from [32].....	107
Figure 85 – Contours plots of streamwise velocity on wheel centreline plane $y/d=0.5$ ; (a) present study, (b) from [32], .....	108
Figure 86 – Contour plot of y-velocity on wheel centreline, at $x/d=0$ ; (a) present study, (b) from [32] .....	109
Figure 87 – Streamlines on the upper rear surface – (a) present URANS study, (b) front wheel [48].....	109
Figure 88 - Streamwise velocity contours with streamlines behind the wheel at plane $z/d=0.5$ .....	110
Figure 89 – Contours of mean $C_p$ for $0^\circ$ yaw + no rotation, (a) wheel surface looking downstream from left, (b) wheel surface looking downstream from right (c) cross-sectional plane at $y/d=0.5$ .....	113
Figure 90 – Non-dimensional vorticity plots for $0^\circ$ yaw; (a) $z/d=0.75$ , (b) $z/d=1$ , (c) $z/d=1.5$ , (d) $z/d=2.5$ .....	114
Figure 91 - Streamlines showing hub flow on the, (a) left side (b) right side, when looking in the streamwise direction .....	117
Figure 92 – Stationary wheel centreline mean surface pressure coefficient with added yaw angle.....	120
Figure 93 – Contours of mean $C_p$ on stationary wheel surface when looking downstream: (a) $5^\circ$ left, (b) $5^\circ$ right, (c) $10^\circ$ left, (d) $10^\circ$ right, (e) $15^\circ$ left, (f) $15^\circ$ right .....	122
Figure 94 – Contours of mean $C_p$ on stationary wheel at cross-sectional plane at $y/d=0.5$ : (a) $5^\circ$ , (b) $10^\circ$ , (c) $15^\circ$ .....	123
Figure 95 – Non-dimensional vorticity plots for $5^\circ$ yaw; (a) $z/d=0.75$ , (b) $z/d=1$ , (c) $z/d=1.5$ , (d) $z/d=2.5$ .....	125
Figure 96 - Streamlines (coloured by mean streamwise velocity) showing hub flow on the $5^\circ$ yaw wheel, (a) windward side (b) leeward side, when looking in the streamwise direction.....	126
Figure 97 – Non-dimensional vorticity plots for $10^\circ$ yaw; (a) $z/d=0.75$ , (b) $z/d=1$ , (c) $z/d=1.5$ , (d) $z/d=2.5$ .....	128
Figure 98 - Streamlines (coloured by mean streamwise velocity) showing hub flow on the the $10^\circ$ yaw wheel, (a) windward side (b) leeward side, when looking in the streamwise direction ...	129
Figure 99 – Non-dimensional vorticity plots for $15^\circ$ yaw; (a) $z/d=0.75$ , (b) $z/d=1$ , (c) $z/d=1.5$ , (d) $z/d=2.5$ .....	131

Figure 100 - Streamlines (coloured by mean streamwise velocity) showing hub flow on the 15° yaw wheel, (a) windward side (b) leeside, when looking in the streamwise direction ...	132
Figure 101 - Change in transverse displacement of stagnation region from stationary wheel centreline with increasing yaw angle .....	134
Figure 102 - Vortex core vorticity magnitude (on yawed stationary wheel) with downstream propagation into the rear wake; Upper vortex - $V_2$ (dashed), Lower vortex - $V_4$ (solid) .....	136
Figure 103 – Vortex core displacements (on yawed stationary wheel) relative to $z/d = 0.75$ with downstream propagation; $V_2$ (dashed), $V_4$ (solid). (a) Transverse (b) Longitudinal.....	136
Figure 104 – Contour plots of velocity magnitude on stationary wheel centreline cross-sectional plane; (a) 0° yaw, (b) 5° yaw, (c) 10° yaw & (d) 15° yaw, with velocity streamlines .....	138
Figure 105 - Force coefficients for stationary wheel with applied yaw angle .....	139
Figure 106 – Centreline mean surface pressure coefficient on rotating wheel with no yaw .	141
Figure 107 - Mean $z$ velocity contours and streamlines on $x/d=0$ plane, with ‘D’ showing a detailed illustration of the separation region.....	142
Figure 108 - Contours of mean $y$ velocity with velocity vectors in $x/d=0$ centreline plane..	142
Figure 109 – Contours of mean $C_P$ for 0° yaw + rotation, (a) wheel surface looking downstream from left, (b) wheel surface looking downstream from right (c) cross-sectional plane at $y/d=0.5$ .....	143
Figure 110 – Non-dimensional vorticity plots for 0° yaw + rotation; (a) $z/d=0.75$ , (b) $z/d=1$ , (c) $z/d=1.5$ , (d) $z/d=2.5$ .....	144
Figure 111 - Streamlines coloured by $y$ -velocity.....	146
Figure 112 - Vortex core vorticity magnitude on rotating with downstream propagation into the rear wake; $V_{1R}$ (dashed), $V_{2R}$ (solid).....	148
Figure 113 - Vortex core displacements (on yawed rotating wheel) relative to $z/d = 0.75$ with downstream propagation; $V_{1R}$ (dashed), $V_{2R}$ (solid). (a) Transverse (b) Longitudinal .....	149
Figure 114 – Rotating wheel centreline mean surface pressure coefficient with added yaw angle.....	151
Figure 115 – Contours of mean $C_P$ on rotating wheel surface when looking downstream: (a) 5° left, (b) 5° right, (c) 10° left, (d) 10° right, (e) 15° left, (f) 15° right .....	153
Figure 116 – Contours of mean $C_P$ on rotating wheel at cross-sectional plane at $y/d=0.5$ : (a) 5°, (b) 10°, (c) 15° .....	155



Figure 117 – Non-dimensional vorticity plots for 5° yaw + rotation; (a) $z/d=0.75$ , (b) $z/d=1$ , (c) $z/d=1.5$ , (d) $z/d=2.5$ .....	156
Figure 118 - Streamlines (coloured by mean streamwise velocity) showing hub flow on the 5° yaw rotating wheel, (a) windward side (b) leeside, when looking in the streamwise direction .....	157
Figure 119 – Non-dimensional vorticity plots for 10° yaw + rotation; (a) $z/d=0.75$ , (b) $z/d=1$ , (c) $z/d=1.5$ , (d) $z/d=2.5$ .....	158
Figure 120 - Streamlines (coloured by mean streamwise velocity) showing hub flow on the 10° yaw rotating wheel, (a) windward side (b) leeside, when looking in the streamwise direction & (c) rear view .....	159
Figure 121 – Non-dimensional vorticity plots for 15° yaw + rotation; (a) $z/d=0.75$ , (b) $z/d=1$ , (c) $z/d=1.5$ , (d) $z/d=2.5$ .....	161
Figure 122 - Streamlines (coloured by mean streamwise velocity) showing hub flow on the 15° yaw rotating wheel, (a) left side (b) right side, when looking in the streamwise direction & (c) rear view .....	162
Figure 123 - Change in transverse displacement of stagnation region from rotating wheel centreline with increasing yaw angle .....	164
Figure 124 - Velocity magnitude around sides of the wheel at $y/d = 0.5$ , Solid line: Windward side & Dashed line: Leeside .....	165
Figure 125 - Vortex core vorticity magnitude (on yawed rotating wheel) with downstream propagation into the rear wake; Upper vortex - $V_{1R}$ (dashed), Lower vortex – $V_{2R}$ (solid) ..	166
Figure 126 – Vortex core displacements (on yawed rotating wheel) relative to $z/d = 0.75$ with downstream propagation; $V_{1R}$ (dashed), $V_{2R}$ (solid).....	167
Figure 127 – Contour plots of velocity magnitude on rotating wheel centreline cross-sectional plane; (a) 0° yaw, (b) 5° yaw, (c) 10° yaw & (d) 15° yaw, with velocity streamlines .....	169
Figure 128 - Force coefficients on the rotating wheel with increasing yaw angle .....	170

## List of Tables

Table 1 - Drag force coefficient with comparisons to [32].....	106
Table 2 – Stationary wheel force coefficients with applied yaw .....	133
Table 3 - Force coefficients of stationary and rotating wheel .....	147
Table 4 – Rotating wheel force coefficients .....	163
Table 5 - Variation in aerodynamic force coefficients with applied variables relative to the stationary un-yawed case ('-' representing a negligible force) .....	174

# List of Publications

## Journal Papers

**Title:** Computational Investigation into the Influence of Yaw on the Aerodynamics of an Isolated Wheel in Free Air  
**Authors:** T. D. Kothalawala, A. Gatto  
**Journal:** International Journal of Computational Science and Engineering  
**Year:** 2014  
**Status:** In-Press

**Title:** Computational Investigation into the Influence of Yaw on the Aerodynamics of a Rotating Wheel in Free Air  
**Authors:** A. Gatto, T. D. Kothalawala  
**Journal:** International Journal of Computational Science and Engineering  
**Year:** 2014  
**Status:** Submitted for publication

## Conference Papers

**Conference:** CEAS 2015 Air & Space Conference  
**Date:** 7<sup>th</sup> – 11<sup>th</sup> September 2015  
**Location:** Delft University of Technology (The Netherlands)  
**Title:** Computational Investigation on the Influence of Rotation on the Aerodynamics of an Isolated Wheel  
**Authors:** T. D. Kothalawala  
**Status:** Abstract Submitted

**Conference:** CEAS 2013 Air & Space Conference  
**Date:** 16<sup>th</sup> – 19<sup>th</sup> September 2013  
**Location:** Linköping, Sweden  
**Title:** Computational Investigation of the Influence of Ground Proximity on the Aerodynamics of a Wheel  
**Authors:** T. D. Kothalawala, A. Gatto, L. Wrobel  
**URL:** <http://liu.diva-portal.org/smash/get/diva2:657370/FULLTEXT01.pdf>  
**Paper No:** 261  
**Page:** 170 - 179

**Conference:** WASET – World Academy of Science, Engineering & Technology  
**Date:** 5<sup>th</sup> – 6<sup>th</sup> September 2013  
**Location:** Wembley, London  
**Title:** Computational Investigation of the Combined Effects of Yaw, Rotation & Ground Proximity on the Aerodynamics of an Isolated Wheel  
**Authors:** T. D. Kothalawala, A. Gatto, L. Wrobel  
**URL:** <http://www.waset.org/journals/waset/v81/v81-42.pdf>

## Nomenclature

$C_D$  – Drag Coefficient;  $C_D = \frac{D}{\frac{1}{2}\rho V^2 S}$

$C_L$  – Lift Coefficient;  $C_L = \frac{L}{\frac{1}{2}\rho V^2 S}$

$C_P$  – Pressure Coefficient;  $C_P = \frac{P - P_\infty}{\frac{1}{2}\rho_\infty U_\infty^2}$

$U_\infty$  – Free-stream velocity (m/s)

$U_N$  – Normal Velocity (m/s)

$U_T$  – Tangential/Spanwise Velocity (m/s)

$V_r$  – Rotational velocity of a cylinder

$d$  – Wheel Diameter (m)

$L$  – Length (m)

$Re_n$  – Reynolds Number based on wheel diameter

$AR$  – Aspect Ratio

$St$  – Strouhal Number;  $St = \frac{fd}{U_\infty}$

$F$  – Frequency (Hz)

$t$  – Time (s)

$\Psi$  – Yaw Angle

$\omega$  – Angular Velocity (rad/s)

$\theta$  – Angular position on wheel, (degrees, °), measured from the horizontal

$\Omega$  – Vorticity magnitude ( $s^{-1}$ )

$\Omega d/U_\infty$  – Non-dimensional vorticity

$\mu$  – Dynamic viscosity (kg/ms)

$\varepsilon$  – Turbulent Dissipation Rate

$k$  – Turbulent Kinetic Energy

$r$  – Radius (m)

$U, V, W$  – Streamwise, spanwise and chord-wise velocity components, m/s

$x, y, z$  – Cartesian coordinate system; lateral, vertical and streamwise axis

# Abbreviations

CFD – Computational Fluid Dynamics

RANS – Reynolds-Averaged Navier-Stokes equation

URANS – Unsteady Reynolds-Averaged Navier-Stokes equation

LES – Large Eddy Simulation

DES – Detached Eddy Simulation

RKE – Realizable  $k$ - $\epsilon$  turbulence model

S-A – Spalart-Allmaras turbulence model

LES – Large Eddy Simulation

LDA – Laser Doppler Anemometry

PIV – Particle Image Velocimetry

DPIV – Digital Particle Image Velocimetry

# 1. Introduction

## 1.1 The Aircraft Noise Problem

Aircraft noise, which comprises principally of a combination of engine noise and airframe noise, remains a significant problem within the aviation industry. Every day across the world, thousands of commercial aircraft take-off, travel to a destination, then land. Within the landing phase in particular, the aircraft is configured in a high lift state with slats and flaps extended as well as the landing gear deployed (Figure 1). Being exposed to the oncoming airstream, the interaction of these devices with the flowing airstream generates significant areas of unsteady flow and subsequent aerodynamic noise. On approach, the flow interaction with the devices can generate noise levels up to 105dB, with significant spectral levels of intensity within the frequency range of 0.5-3kHz corresponding to the most sensitive range of the human auditory system [1]. Exposure to these levels of discomfort can therefore result in serious psychological and physiological effects to many of the millions of people living in close proximity to airports. Disturbed sleep, low level repetitious and periodic discomfort, as well as short term excessive noise exposure can all effect social relationships, physical/mental health and well-being, as well as effectiveness and efficiency at work. Therefore, there is an urgency to both better understand and develop solutions to minimise the aircraft noise problem and reduce the effects on the population. It is also important this

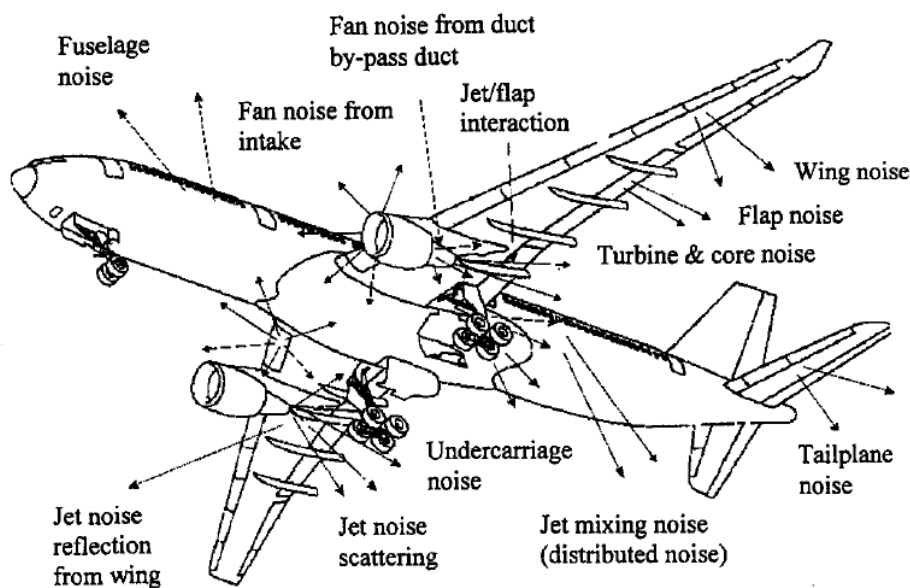


Figure 1 – Aircraft noise sources [1]

goal be achieved whilst ensuring that this multi-billion pound worldwide economic industry is not widely hindered.

Currently, aircraft operators have to adhere to operational restrictions in many airports across the world through the imposition of curfews, noise abatement procedures, total noise quotas, limits and surcharges [2]. These restrictions represent a loss of billions of dollars to the aviation industry but are nevertheless essential to providing and ensuring a peaceful quality of life for the affected nearby residents. Overall, aircraft noise has been reduced by more than 20dB over the last 50 years [3], with progress over the last few decades in particular focused primarily on engine and high-lift aerodynamic aeroacoustic emissions [1]. However, as aircraft engine systems are being improved, aircraft landing gear has received much less attention, and is now one of the most prominent sources of the total aircraft/airframe noise on approach [1]. Within the European Union, Directive 2002/30/EC limits large commercial aircraft noise on approach to 95-105dB, depending on the type of aircraft, with commitments to reduce this noise by up to 10db between years 2000-2020. However with a three-fold expansion in air traffic expected by 2025, a considerable amount of effort needs to be dedicated to the problem, as a reduction of 5dB will be required just to maintain the expected growth of airport operations [4].

Large scale commercial aircraft landing gear configurations can comprise from two to six individual wheels, depending on the aircraft type with the wheels being connected together by axles, and with the axles fixed to the main gear via a support strut or through an articulated bogie.

The overall aerodynamic noise from landing gear is considered broadband in nature, although due to the different spatial relationships of gear components; landing gear is considered as a cluster of aerodynamic noise sources. One approach of understanding the noise profile from landing gear has been to categorise the overall signature in to three spatial domains [5];

- Low frequency – Contributions from vortex shedding over the wheels, with a significant level of noise radiated over large distances
- Mid-frequency – Contribution from main support struts propagated over shorter distances than the low frequency, with increased atmospheric dissipation
- And; High frequency – Contributions resulting from smaller feature detail such as hydraulic lines, wires and linkages.



Unfortunately, the complexity of a modern commercial landing gear is substantial with the overall configuration containing several dissimilar bluff body components, operating and interacting within close proximity to one another. As a result of this complexity, accurate and realistic analysis of this configuration is hindered and is a principal reason why the detailed flow physics on an aircraft landing gear continues to remain poorly understood and interpreted [6]. Moreover, if goals regarding noise emission targets are to be met, it is of utmost urgency to gain more detailed understanding of the principal and underlying flow mechanisms of the aerodynamics and subsequent aero-acoustics of landing gear components. As a first step to enhancing this fundamental understanding, work centred on the individual components such as the wheels themselves, can provide a solid foundation for subsequent landing gear analysis. Unfortunately, for aircraft landing gear, previous studies considering the aerodynamics of an isolated wheel in free air are particularly scarce. The similar case of an isolated wheel in contact with the ground, which is also particularly relevant to landing gear is more prevalent, but applied within the motorsport area. Nevertheless, in an attempt to provide insight into the aerodynamics of aircraft landing gear, this study considers the fundamental investigations of a free air configuration of a single isolated wheel with both applied rotation speed and yaw. The work conducted is primarily computational, with the influence of added yaw angle and rotation, representing everyday operational conditions common to aircraft operations.

## **1.2 Aims & Objectives**

The aims & objectives of the work are as follows;

1. Computationally investigate the key characteristics of the flow field around an isolated wheel in free air. With zero yaw and no applied rotation, compare and validate computational results obtained to previous work.
2. Determine and understand the principal influences of applied yaw angle and wheel rotation, as well as both applied wheel yaw and wheel rotation combined on the resulting flow physics.
3. Characterise these influences in terms of vortex core position and through characterisation of aerodynamic force generation.

### **1.3 Thesis Structure**

This thesis was completed with results obtained using a computational approach, over the previous three years taken to complete this PhD. The thesis consists of seven chapters.

Initially a brief introduction is presented in Chapter One regarding the current problem, detailing how aircraft noise has affected the population in everyday life, subsequently outlining the aims and objectives for the investigation.

Chapter Two consists of an extensive literature review on the work carried out within this field of study. Literature regarding a wheel in free-air is limited as the bulk of the work is concentrated on ‘in-contact with the ground’ configurations. However, the latter was still extensively reviewed to provide insight into the flow-field and wake characteristics.

The computational methodology is described in Chapter Three, providing details on the solver settings and refinement studies, which subsequently indicated the type and size of the grid to use providing the constraints present.

Chapter Four focuses on validating the computational methodology using the baseline case in this study, to make comparisons to the available literature, where possible. Providing the comparisons are in agreement, it can be concluded that the methodology used is acceptable.

Chapter Five consists of the results for each test case, followed by a discussion providing insight into the results, identifying key flow characteristics. The results are focused on surface pressure distribution, wake velocity, central vortex core vorticity magnitude, central vortex core displacement and aerodynamic force coefficients, with all results obtained using time-averaged data.

To end with, a conclusion is presented in Chapter Six identifying the key influences of yaw, rotation and both combined; subsequently, followed by recommendations for future work in Chapter Seven.

## 2. Literature Review

This chapter contains a detailed literature review to provide a fundamental understanding about the aerodynamic flow-field around simplified landing gear configurations and wheels by reviewing the influence of Reynolds number, aspect ratio, applied rotation, applied wheel yaw and ground proximity. The flow-field around a cylinder will also be reviewed as the shape of a cylinder, particularly low aspect ratio cylinders, is comparable to a wheel. Although nearly all the literature regarding wheel studies comprise of a configuration ‘in contact with the ground’, these were still reviewed as they provide an understanding of the flow physics.

From an aerodynamics perspective, very little is still known about the complex flow interactions taking place over large scale landing gear configurations. However, particularly in the last two decades, there has been progress with mean flow and selected wake flow field characteristics presented [7, 8]. Unfortunately, time-dependant analysis has received little attention. As a result of flow separation, re-attachment and wake/body interaction, the time dependent aerodynamics dictates many of the noise producing mechanisms established. The extent, structure and behaviour of surface and wake fluctuations can, to some extent, contribute to the overall noise signature and are therefore the reason why this information remains eagerly sought by landing gear designers and manufacturers. An important aspect to be considered in reference to this topic is the use of simplified, overly idealised, single or dual wheel arrangements, which lack realistic details. Although these studies are of significant value as a first exploratory step, it has also been recognised that the addition of the small scale crucial elements would substantially reconfigure the flow-field dynamics and overall noise footprint. Predominantly, much of this work has been completed using mean surface pressure and flow visualisation techniques in the experimental domain [7, 8], and Unsteady Reynolds-Averaged Navier-Stokes (URANS) and Detached Eddy Simulation (DES) in the computational domain [9]. All of these studies indicated the nature of the flow-field to be highly complex and unsteady, with asymmetry between the upper and lower sides of the landing gear as a result of the presence of the main support strut. Large areas of flow stagnation were found on the front faces of the front wheels, with flow separation and near immediate re-attachment when subjected to severe adverse pressure gradients at the wheel edges. Comparison of previous computational [10] and experimental [7, 8] works, showed good agreement in areas of flow attachment and stagnation regions whilst degrading in

agreement in areas of flow separation and within the complex wake region. Therefore there is a critical need for more detailed understanding within these areas. DES has been shown to be the most suitable for this case; however, using this technique is complex to set up, requiring more computational time with no assurance of obtaining a stable solution. URANS was therefore found to be more user-friendly; although being less accurate when resolving fine detail, it remains to be a valuable tool in assisting existing analysis methods.

### *The Bluff-Body*

In the engineering industry, a common term used to describe an object which generates significant base pressure drag as opposed to skin friction drag, when exposed to an external flow, is referred to a ‘bluff body’. Examples of bluff bodies of significant engineering interest include buildings, automobiles, aircraft landing gear and have enormous interest in modern engineering. Fundamentally, characteristics of bluff body flows can be classified into two groups: inviscid flow and viscous flow.

For the case of inviscid flows, viscosity is negligible resulting in no friction to create boundary layer separation, vortices or a subsequent wake. Inviscid flow over a typical cylinder shows two stagnation regions, one at the front central region of the cylinder and the other behind the cylinder, indicating a classical stagnation surface pressure coefficient of one. Due to the symmetry of the cylinder body, the pressure distribution around the cylinder is also symmetric. Additionally, due to the symmetric body, aerodynamic forces acting on the cylinder will be equal to those present in the opposing direction, indicating no resultant aerodynamic forces. However, it is a widely known characteristic that bluff bodies experience aerodynamic forces, therefore invalidating this simplified inviscid flow theory for bluff bodies.

Analysing a flow field as ‘viscous’ indicates that friction exists on the boundary of bluff bodies. This causes a reduction in flow velocity, forming an adverse pressure gradient (shown by Equation 1; where  $S$  is the distance travelled over a body), resulting in boundary layer flow separation which subsequently forms vortices.

$$\frac{dP}{dS} > 0 \quad \text{Equation 1}$$

Considering a typical viscous flow around a cylinder, after boundary layer separation, vortices are shed from the top and bottom surfaces creating two rows of vortices that propagate into the rear wake. The wake is suggested to be unsteady, and is affected by the influences of Aspect ratio, Reynolds numbers and vortex shedding frequencies (Strouhal numbers), resulting in unsteady aerodynamic forces, such as lift and drag, acting on the cylinder.

## 2.1 The 2D Cylinder

The flow field around a wheel is typically much more complex compared to an infinitely long 2D cylinder, due to the significant changes and characteristics of length to diameter in tyre profiles, hub detail, tyre tread, rim configuration, etc.; but as the general shape of a cylinder in the streamwise direction is of a similar nature to a wheel, albeit over a larger length, initial consideration of the flow around a 2D cylinder (particularly those with very low aspect ratios) can be used as a first step to understanding the basics of how air flows around short circular objects such as wheels.

A considerable amount of work over the last century has been for the topic of flow around 2D cylinders. Cylinder Aspect Ratio (AR); defined in Equation 2 where  $L$  is referred to the characteristic length of a cylinder, does have a significant impact on the resulting flow physics, however, initially the case of an infinitely long 2D cylinder is considered as a basis for comparison.

$$AR = \frac{L}{d} \quad \text{Equation 2}$$

Fundamentally, the flow around a 2D cylinder contains several regions of stagnation, separation and recirculating shear layers. At the front of the cylinder, a stagnation region occurs where the dynamic motion of the fluid is brought to rest. Either side of this region, the flow accelerates around the top and bottom surfaces with the formation of thin boundary layers. Large adverse pressure gradients near the top and bottom of the cylinder cause the flow on the boundary to decelerate rapidly, creating a separated shear layer, reversed flow, and a large base pressure drag. Two free shear layers are formed as a consequence of the flow separating, increasing the surface pressure on the surface and forming a recirculation region resulting in the formation of vortices, which propagate in the rear wake of the cylinder [11]. The size of the wake and vortices are dependent on many factors, including the location of separation, cylinder profile, Reynolds number, surface roughness and free-stream turbulence

intensity, but typically as the separation point moves further downstream, a smaller wake is created and will result in a lower drag force. Within the wake region, once the separated shear layers meet, the flow is forced back to the base region (rear surface of the cylinder within the wake region), where the surface pressure is usually constant, typical of wake physics. However, the location of the separation positions, as previously mentioned, is a result of boundary layer physics including where transition occurs from laminar to turbulent. This is explained by, and is reliant on the Reynolds number.

$$Re = \frac{\rho U_{\infty} d}{\mu} \quad \text{Equation 3}$$

### 2.1.1 Influence of Reynolds Number ( $Re_n$ )

The Reynolds number, as defined by Equation 3, is often used as an indication of determining the fundamental characteristics of cylinder flows and characterises whether the boundary layer flow is laminar or turbulent [14]. As shown in Figure 2, the characteristic of cylinder flows has delineated different regimes for flow around cylinders, each consisting with a different flow topology. At very low Reynolds numbers ( $Re_n < 5$ ) the flow does not separate on the walls of a cylinder, resulting in no vortex shedding, therefore providing a symmetrical

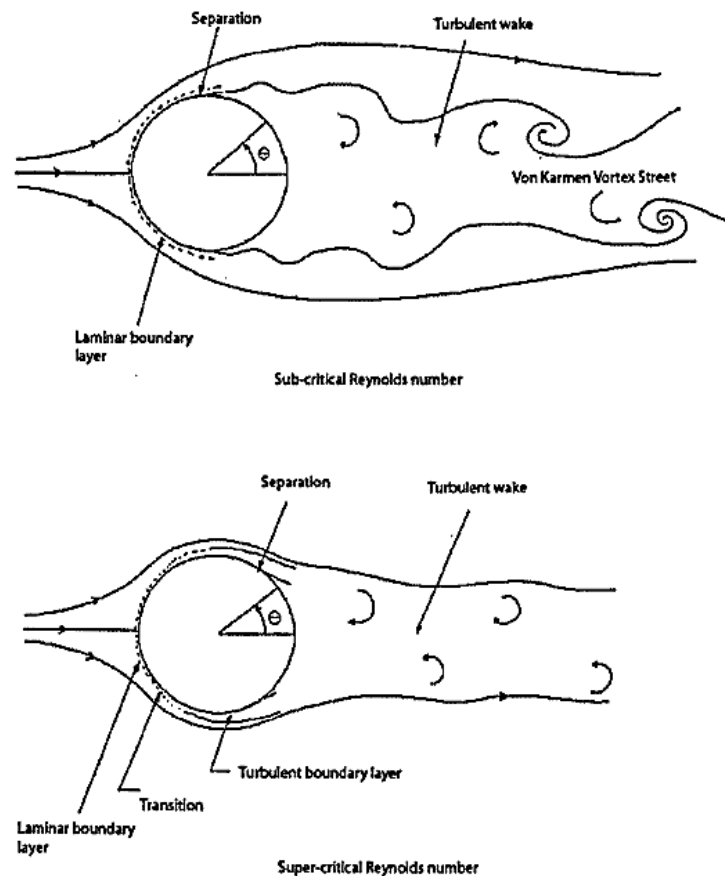


Figure 2 - Flow field characteristics past a 2D cylinder at critical Reynolds Number regimes [12, 13]

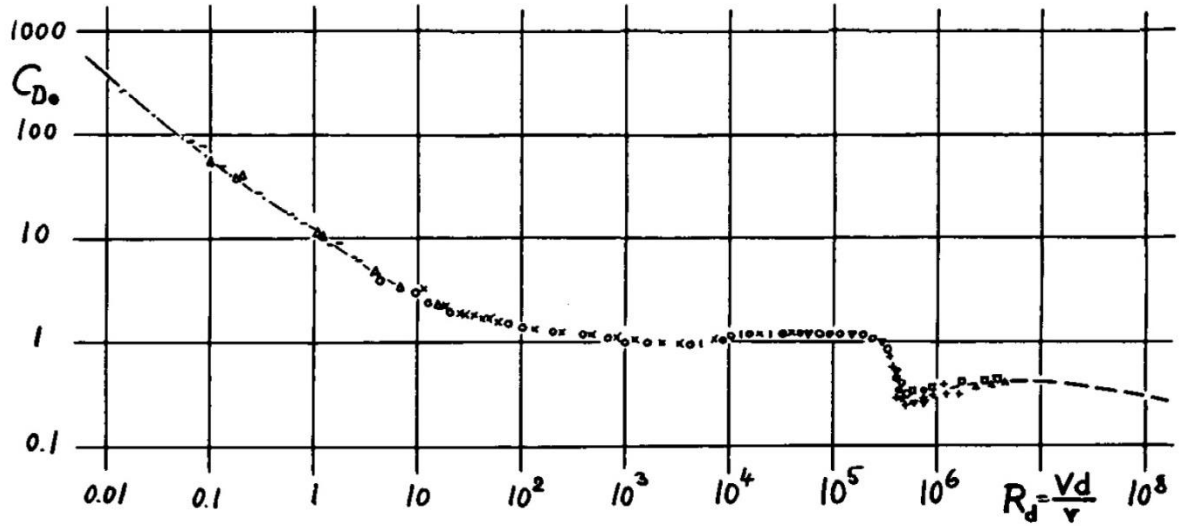


Figure 3 - Variation of drag coefficient of a circular cylinder as a function of Reynolds number [19]

wake. As the Reynolds number increases to  $1 \times 10^2$ , laminar vortex shedding is experienced as the flow separates on the upper and lower surfaces forming shear layers that oscillate, eventually rolling up, enacting alternate vortex shedding into the rear wake. Subcritical flow regimes (between  $1 \times 10^2 < Re_n < 2 \times 10^5$ ) [13], are characterised by a laminar flow upstream of the cylinder, subsequently separating slightly before the upper and lower surfaces of the cylinder, predicted at  $80^\circ$  on either side relative to the stagnation region [14]. The shear layers formed from these regions, entrain the rear wake containing the separated wake flow, creating a Von Kármán vortex street (shown in Figure 2) propagating downstream. This large alternating separated region, results in the pressure drag contributing more than half of the overall drag force of  $C_D \approx 1.2$  [15]. Strouhal number (defined by Equation 4) is a dimensionless parameter used to describe the vortex shedding frequency within this region and is near constant at approximately  $St = 0.2$ . Beyond  $Re > 10^4$ , the effect of the friction drag is negligible [16]. The critical regime is a region where transition occurs from laminar to turbulent within the boundary layer. This critical regime is characterised to occur at  $Re_n > 2 \times 10^5$  [12], as values of  $C_D$  undergo a sudden decrease as  $Re_n$  is increased (shown in Figure 3). Past this critical regime, the super-critical region (shown in Figure 2) is characterised by a boundary layer which is fully turbulent and remains attached until separation occurs further downstream on the cylinder surface. The turbulent boundary layers formed, are inherently able to withstand the adverse pressure gradients much more effectively than the laminar shear layers, resulting in a smaller wake and a decrease in the total drag force,  $C_D \approx 0.3$ .

$$St = \frac{fd}{U_\infty}$$

Equation 4



### 2.1.2 Influence of Aspect Ratio (AR)

Zdravkovich [20] has reviewed and analysed the flow field around cylinders with regard to changing aspect ratio and has found fundamentally, that as the aspect ratio decreased, there was a decrease in  $C_D$ . This reduction in drag was found to be caused by the higher pressure in the rear wake, as the end effects at low aspect ratios become more prominent. However, additional work also indicated that with further reductions in aspect ratio below one, a substantial increase in  $C_D$  occurs, as shown in Figure 4. This is a result of the increasing amount of skin friction being contributed to the total drag force. At this level of aspect ratio magnitude, it was suggested that this result using the side area of the cylinder as the reference in calculating the drag force coefficient would be more beneficial [20]. However, this has not been widely accepted. Figure 5 shows the typical flow field around a low aspect ratio

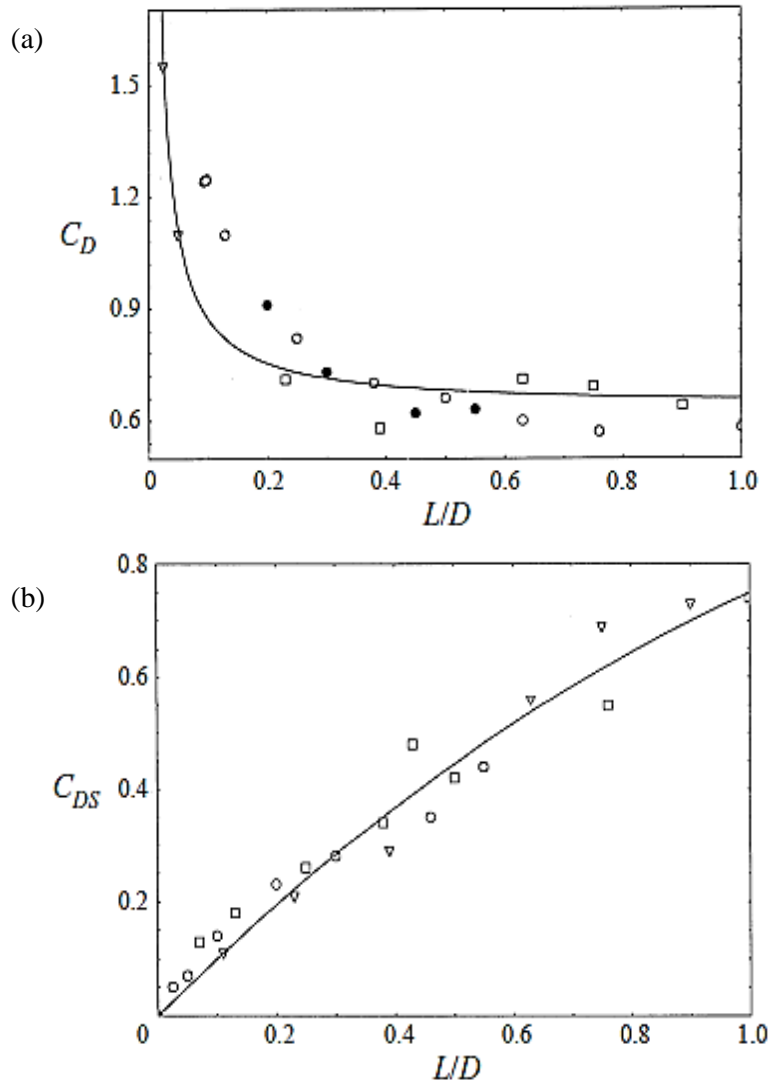


Figure 4 – Drag coefficient based on (a)  $L/D$ , (b) using projected side area [20]

cylinder, with the development of substantial longitudinal vortices formed as a result of separation around the edges. For the special case of cylinders with an aspect ratio less than one, separation occurs from the sharp ends, solely with shear layers formed by this separation, reattaching on the flat sides of the cylinder. The more extreme case of the flow field around cylinders with small aspect ratios (coin-like cylinders), is shown in Figure 6 [20], and shows the areas of separation at the edges and on the bottom surface where secondary separation would occur if the flow was to reattach, depending on the aspect ratio. This demonstrates the effect that the edges of a cylinder have on drag, as the presence of leading-edge separation would result in a greater drag; therefore with respect to aircraft wheels, the most appropriate curvature on the wheels should be used to minimise this drag force. Zdravkovich et al [21] later conducted additional studies on coin like cylinders. In an attempt to better characterise the flow, a revised equation for calculating  $C_D$  was used by replacing the projected area with the side area,  $D^2\pi/4$ . A decrease in drag coefficient was observed for  $AR < 1$ , in agreement with [20], as the friction drag dominates as the aspect ratio decreases to this level. Separation from the sharp edges of the cylinders formed separation bubbles on the flat sides, as this separated flow reattaches on to the flat sides. Reversed flow underneath the separation bubble eventually detaches and separates as secondary separation. Zdravkovich found that rounding the edges of the cylinder reduces the value of  $C_D$ , as the separation bubbles would be eliminated. This was also confirmed by Fackrell [22], as the effect of the more rounded edge profile resulted in a lower drag force.

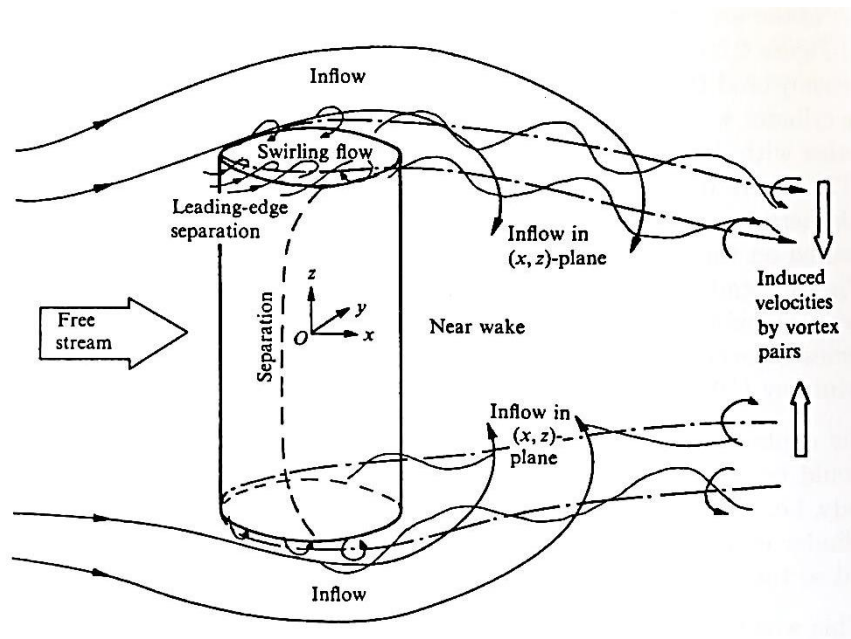


Figure 5 – General flow structure around a cylinder [20]

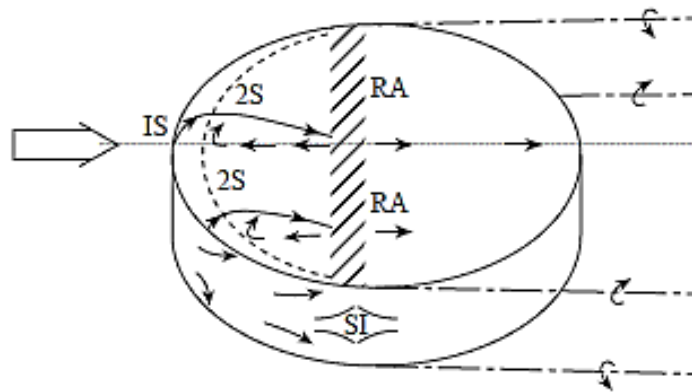


Figure 6 – General flow structure around coin-like cylinders [20]

### 2.1.3 Influence of Rotation on Cylinder Flows

When a cylinder is rotating in a fluid, if the rotational speed of the cylinder is equivalent to the free stream velocity, the attached flow on the side of the cylinder travelling in the same direction as the free stream flow is accelerated, resulting in a negative pressure on that respective side. However on the opposite side, the flow opposes the direction of rotation reducing the free stream velocity, resulting in a higher pressure. As a result, an asymmetry in the pressure distribution on the cylinder is observed, as the flow travelling in the same direction as the rotational velocity will induce a lower pressure, Figure 7 (A), with the flow travelling opposite to the direction of the rotational velocity, Figure 7 (B), producing a higher pressure. Therefore, a pressure differential is set up on the two sides of the cylinder, with the overall result being the production of a resultant lift force, acting towards the lower pressure surface side. This is known as the Magnus Effect.

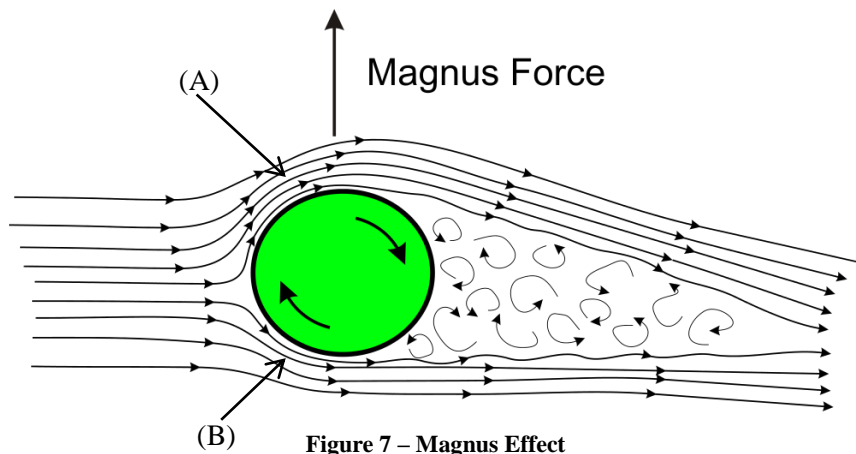
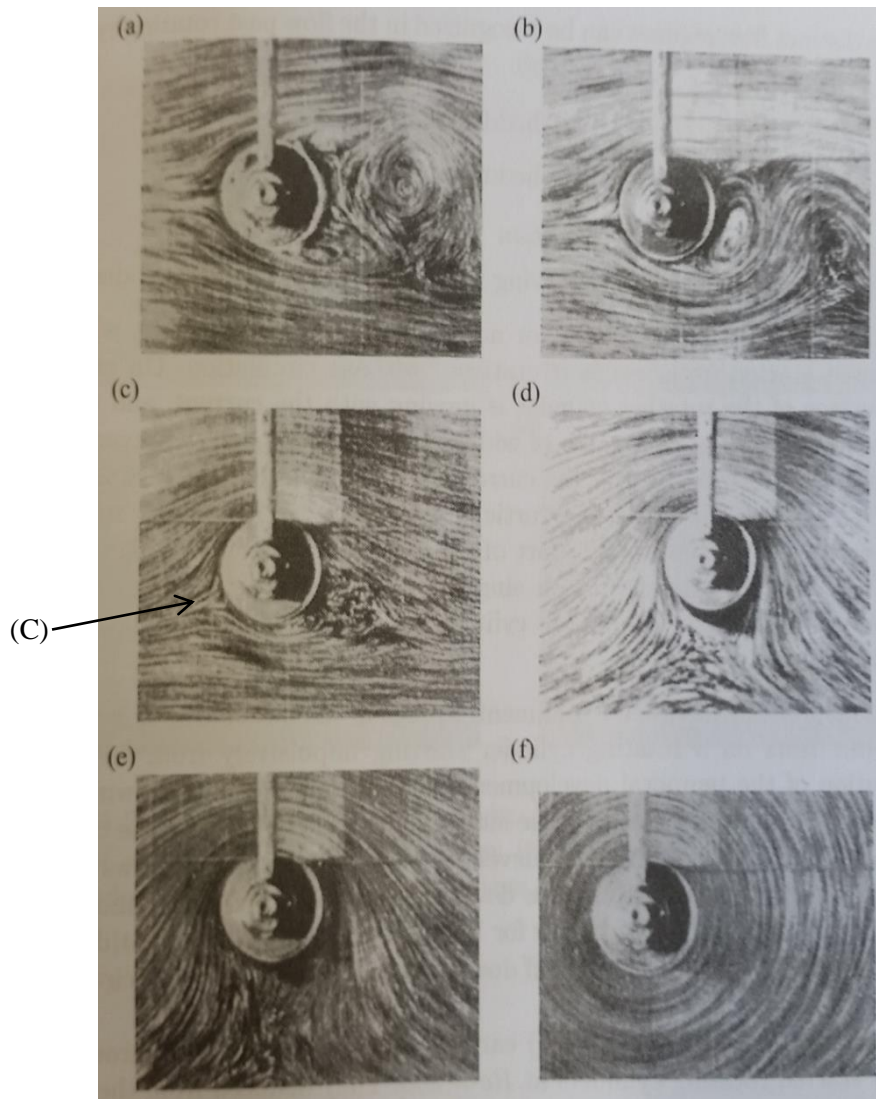









Figure 7 – Magnus Effect

Prandtl investigated the flow around a rotating cylinder at  $Re \approx 4 \times 10^3$  at six different ratios of  $V_r/V$  (where  $V_r$  = rotational velocity of the cylinder and  $V$  = the free stream velocity), observing the fluid flow patterns on the six different ratios analysed ( $V_r/V=0$ ,  $V_r/V=1$ ,  $V_r/V=2$ ,  $V_r/V=4$ ,  $V_r/V=6$ , and  $V_r/V=\infty$ ), as shown in Figure 8 (a-f respectively). Water surface flow visualization, shows maximum separation downstream of the cylinder diameter to the right of the vertical centreline axis for the stationary cylinder, as well as upper and lower eddies being formed and shed alternately in the near wake. Once the rotational speed of the cylinder is equivalent to the free stream (b),  $V_r/V=1$ , the size of the eddy street is reduced and separation is observed to occur on the side of the cylinder where the rotational flow opposes the free stream. As the ratio of  $V_r/V$  increases from zero, the stagnation point initially seen in (a) at the front of the cylinder, is moved further down towards the side where  $V_r$  &  $V$  are travelling in opposite directions (C). Similarly, the wake is shifted



**Figure 8 – Flow visualisation around a rotating cylinder in water, (a)  $V_r/V=0$ , (b)  $V_r/V=1$ , (c)  $V_r/V=2$ , (d)  $V_r/V=4$ , (e)  $V_r/V=6$ ,  $V_r/V=\infty$ . [20]**

further down. The formation and shedding of eddies are not visible in (c) at  $V_r/V=2$  and beyond, as a result of reduced near-wake size. At the maximum ratio of  $V_r/V=\infty$  when the cylinder is rotating in stationary fluid, only a single large eddy is formed, Figure 8 (f). Overall, with rotation speed, eddy shedding was found to exist only at  $V_r/V \leq 2$  and with rotational speed increasing beyond  $V_r/V > 2$ , eddy shedding ceases. With these findings, Prandtl concluded [20], that when one side of a rotating cylinder moves in the same direction as the free stream flow, separation does not occur and eddies are not formed on that corresponding side. However, on the other side, with the free stream opposing the direction of the rotational velocity, separation occurs and produces vorticity as the flow propagates in the near wake. Seifert [23] reviewed a study which also investigated the influence of velocity ratio around a rotating cylinder, at  $Re = 7.2 \times 10^4$ , using numerical flow visualisation [24], with their results illustrated in Figure 9. The velocity ratio ( $\alpha$ ) from their investigation is defined  $\alpha = V_r/U_\infty$ , indicating the first ratio,  $\alpha = 0$ , to represent a stationary cylinder in free stream, demonstrating an increase in  $\alpha$  with increasing cylinder rotational velocity. For low velocity ratios in the region  $\alpha = 0 - 2$ , alternate eddy shedding from either side of the cylinder

$\alpha = 0.0$ $St = 0.20$		First shedding mode. Alternate vortex shedding of Von Kármán type
$\alpha = 1.0$ $St = 0.26$		
$\alpha = 2.0$ $St = 0.46$		
$\alpha = 3.0$		Quasi-steady flow. Closed streamlines around cylinder. Two stationary vortices located on the cylinder lower side.
$\alpha = 3.5$ $St = 0.02$		Second shedding mode. Only one vortex is shed
$\alpha = 4.0$		Quasi steady flow. Flow topology is comparable to the potential theory solution
$\alpha = 6.0$		

**Figure 9 - Flow patterns for various Strouhal numbers ( $St$ ) and velocity ratios ( $\alpha$ ); flow direction left to right and clockwise cylinder rotation [23, 24]**

is observed, representative of a Von Kármán vortex street propagating in to the wake, with the length of the eddy shedding significantly shortened as the higher ratios are approached; similar to that observed by Prandtl [20] (Figure (a) – (c)). At velocity ratios  $\alpha > 2$ , eddy shedding can no longer be seen, with the visible displacement of the rear wake towards the side where the rotational velocity of the cylinder opposes the free stream direction. Two vortices are observed only on the lower side of the cylinder ( $\alpha = 3$ ), due to flow separation caused by the opposing flow directions; however, reducing to a single large eddy at  $\alpha = 6$ , with results showing general agreement to Prandtl's investigation [20].

#### **2.1.4 Influence of applied Yaw angle**

For the special case of a cylinder which is yawed to the free stream direction, the configuration can be decomposed in to streamwise and velocity components, normal to and parallel to the cylinder axis given by  $V_n = V\cos\Psi$  and  $V_t = V\sin\Psi$  respectively. This independence principle, also known as the cosine law, effectively segregates the flow past yawed cylinders, with the flow projected on the plane normal to the cylinder given by  $V\cos\Psi$  shown to be nearly identical when analysing zero-yaw cylinders. However, several limitations and caveats should be adhered to when applying the independence rule [25];

- Due to laminar boundary layer theory becoming invalid after areas of separation, the independence rule is only valid up to this.
- The mathematical idealization of two dimensional flow past cylinders of infinite aspect ratio cannot be realized in practise, as the flow past cylinders of finite aspect ratio are subjected to end effects.
- The transition around separation for cylinders with no yaw occurs at a specific Reynolds number due to the instability of the laminar boundary layers. It is expected that the instability would occur at the same Reynolds number on yawed cylinders, assuming that the yawed cylinder experiences the same flow disturbances. However, as the flow past yawed cylinders has a spanwise component, this is likely to affect the disturbances and the Reynolds number at which separation occurs.

Smith et al [26] carried out some of the early experiments around a yawed circular cylinder to investigate the effect of yaw angle on the near wake and drag coefficient. At lower Reynolds numbers ( $40 < Re < 250$ ), the flow is expected to be laminar and stable. As the Reynolds number increases, transition from laminar to turbulent flow occurs in the near wake

significantly decreasing the base pressure on the cylinder, resulting in an increase in  $C_D$ . Tests were carried out on polished brass cylinders, with diameter and aspect ratio of 0.375 inches & 30 respectively, at yaw angles of  $0^\circ$ ,  $15^\circ$ ,  $30^\circ$ ,  $45^\circ$  &  $60^\circ$  in the Reynolds region of  $2000 < Re < 20,000$  (free stream speed of 6-30m/s). One characteristic evident in the results was the decrease in base pressure coefficient (when based on the normal velocity component ( $V_n$ )) with increasing the yaw angle (Figure 10). This was somewhat expected, as the transition from laminar to turbulent flow in the near wake of a body results in a decrease in base pressure coefficient and wake size reduction, which is also evident when analysing the base pressure coefficient on a cylinder with zero yaw within this range of Reynolds numbers.

Smith et al [26] also investigated cylinder vortex shedding frequency. Frequency peaks for cylinders with zero yaw are known to be very defined, sharp and narrow, around a Strouhal number of 0.21. Smith et al [26] proposed that as the turbulence levels rise with increasing yaw angle, the energy related to the shedding frequency is less dominant compared to a cylinder with no yaw. As Smith et al [26] only measured these shedding frequencies at a single point behind the mid-span of the yawed cylinder, Hayashi et al [27] attempted to confirm this hypothesis by measuring the eddy shedding frequency along the span of yawed cylinders. Measurements were acquired with  $10^\circ$  &  $20^\circ$  yaw, at a Reynolds number of 20,000 on a test cylinder with and without endplates ( $AR = 15$ ). Power spectra along the span of these four different cases [20, 27], indicated that eddy shedding is not uniform along the entire span of the cylinder. However, results did support the fluctuations in eddy shedding

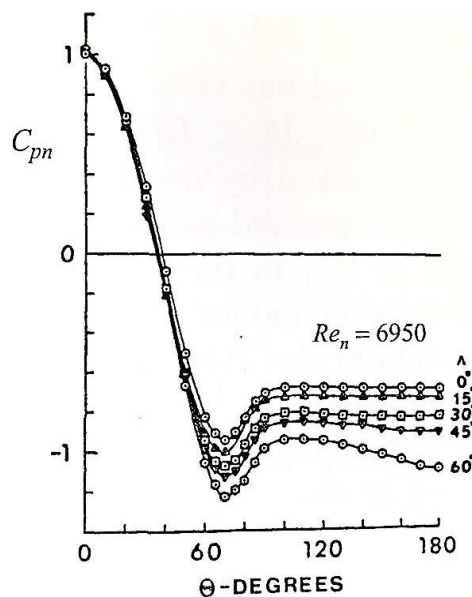


Figure 10 – Effect of Yaw on pressure coefficient  
[20, 26]

and was found to become more uniform with the addition of end plates. For the test case of a cylinder with  $20^\circ$  yaw, the intensity and strength of eddy shedding was found to decrease through observed action of the spectral peaks being less pronounced as they appear weaker, and wider in frequency bandwidth than previously seen in the  $10^\circ$  yaw case. This was thought to be due to the spanwise velocity component influencing the eddy shedding frequency.

### **2.1.5 Influence of Ground Proximity**

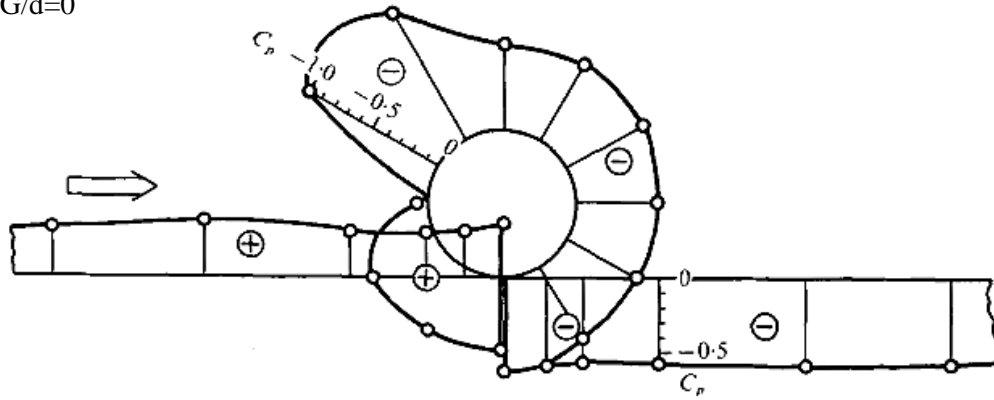
Bearman & Zdravkovich [28] have experimentally investigated the flow field around a cylinder with length and diameter of 0.61m and 0.019m respectively ( $AR = 32$ ). The tests were performed in a wind tunnel with a maximum top speed of 38m/s, with different ground diameter ratios ( $G/d$ ; where  $G$  is defined as the distance from the bottom of the cylinder to the ground plane and  $d$  is defined as the cylinder diameter) to investigate the influence of ground effect. Pressure distributions measured on the cylinder surface and along the ground plane plate for the various  $G/d$  ratios, are shown Figure 11. The cylinder in contact with the ground (a) indicates an asymmetric pressure distribution around the cylinder with a discontinuity in pressure at the contact patch. This is also a characteristic of wheel in contact with the ground investigations. In general, a positive pressure peak was observed at the stagnation position ( $C_p = 1$ ) and negative peaks observed where the flow is accelerated. At  $G/d = 0.1$  (b), a maximum negative  $C_p = -0.7$  is observed at the bottom of the cylinder, as the fluid is squeezed through the gap between the cylinder and the ground plane. As  $G/d > 0.4$ , the pressure distribution becomes symmetrical about the horizontal axis from the front stagnation point, indicating a relative insensitivity with the ground plane. The base pressure in the near wake of the wheel decreases as the  $G/d$  ratio increases; however after  $G/d > 1$ , very little change is observed in the base pressure. Upstream and downstream of the cylinder, larger separation bubbles were found to be attached when  $G/d = 0$ , but these bubbles were eliminated as the gap increased, due to the accelerated flow through this region. As the  $G/d$  ratio  $> 0.4$ , the bubbles started to fade away until they were no longer visible at  $G/d = 0.6$ . The wake behind the wheel was also analysed using smoke filaments, and showed that at  $G/d=0.4$ , the curvature of the smoke was seen to increase, indicating a lower base pressure in the near wake with a short recirculation region. As the  $G/d$  ratio increased, the smoke filaments in the wake of the cylinder were rarely affected by the existence of the ground plane. Visualisations also indicated a displacement of the front stagnation point downstream towards the gap with decreasing ground proximity. Separation locations were also found to



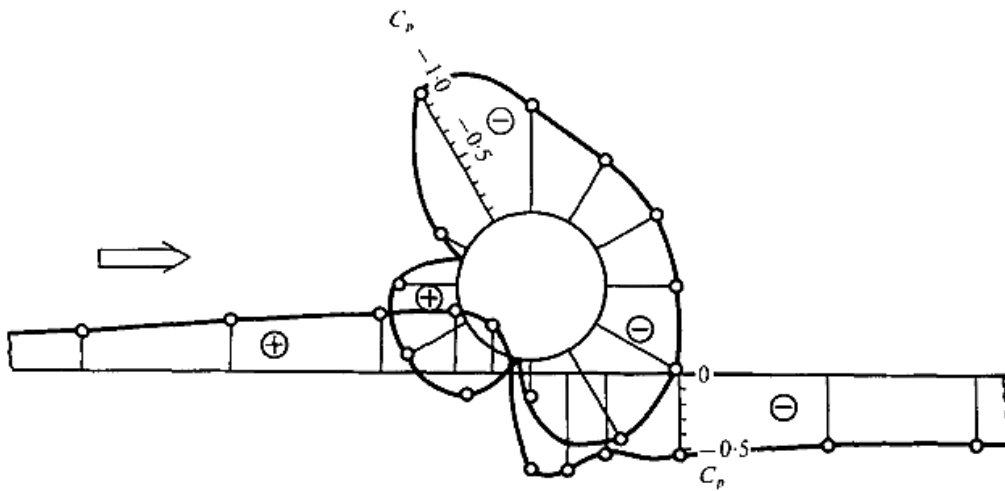
be affected by the  $G/d$  ratio, due to the favourable pressure gradient produced by the gap. Therefore as the  $G/d$  ratio was reduced, the separation location nearest to the ground plane was displaced further downstream of the narrowest point of the gap, as the upper separation position was displaced upstream of the cylinder shoulder.

At small  $G/d$  ratios, pressure distributions around the cylinder indicate the presence of a mean force acting on the cylinder, away from the ground plane. Negative pressure peaks observed on the lower surface of the cylinder at low  $G/d$  ratios represent an increase in flow velocity, as air is pushed through the gap. However, as the cylinder moves away from the ground, the low pressure region is reduced in size as the flow has more space when travelling through the gap. Subsequently, as the  $G/d$  ratio increases and the pressure distribution on the top and bottom surface becomes symmetrical, the mean force, initially observed at low  $G/d$  ratios, decreases rapidly to values close to zero.

(a)  $G/d=0$



(b)  $G/d=0.1$



(c)  $G/d=0.4$

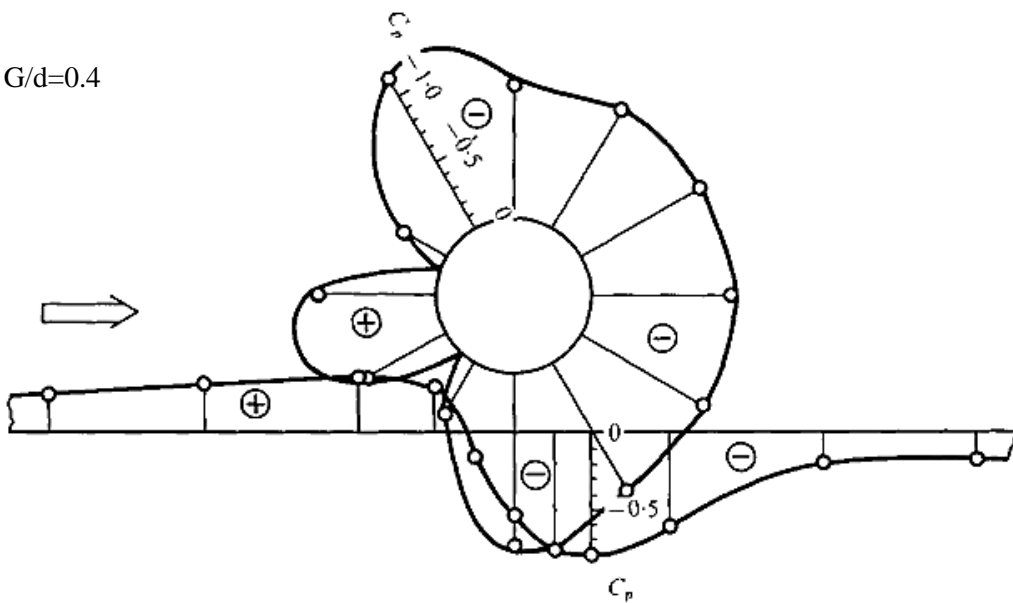
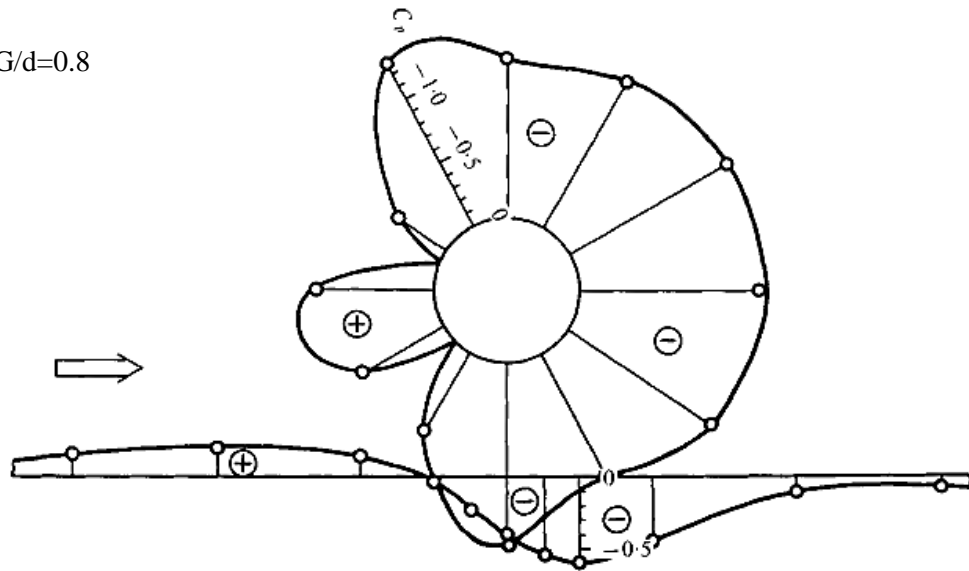
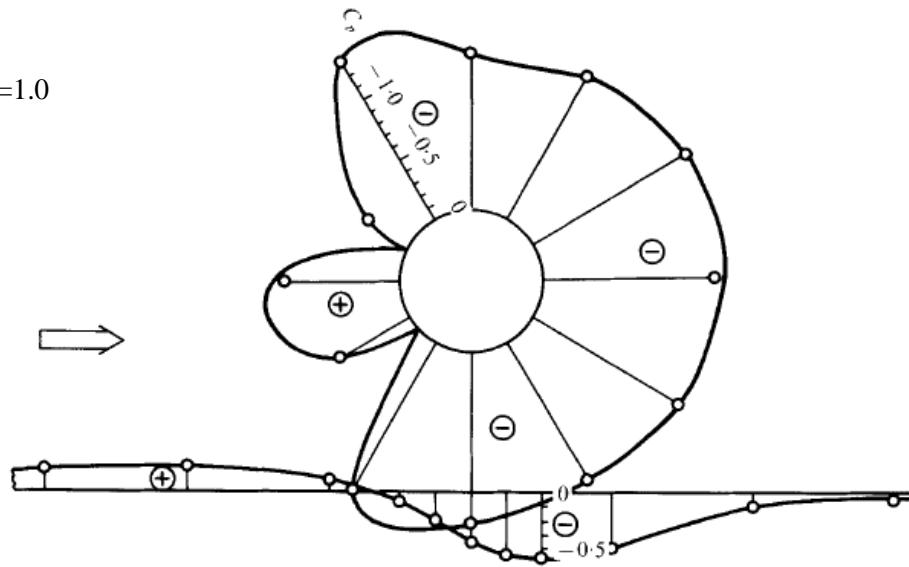


Figure 11 – Distribution of  $C_p$  around the cylinder and ground plane plate at different  $G/d$  ratios (continued on next two pages) [28]...(continued on to next page)

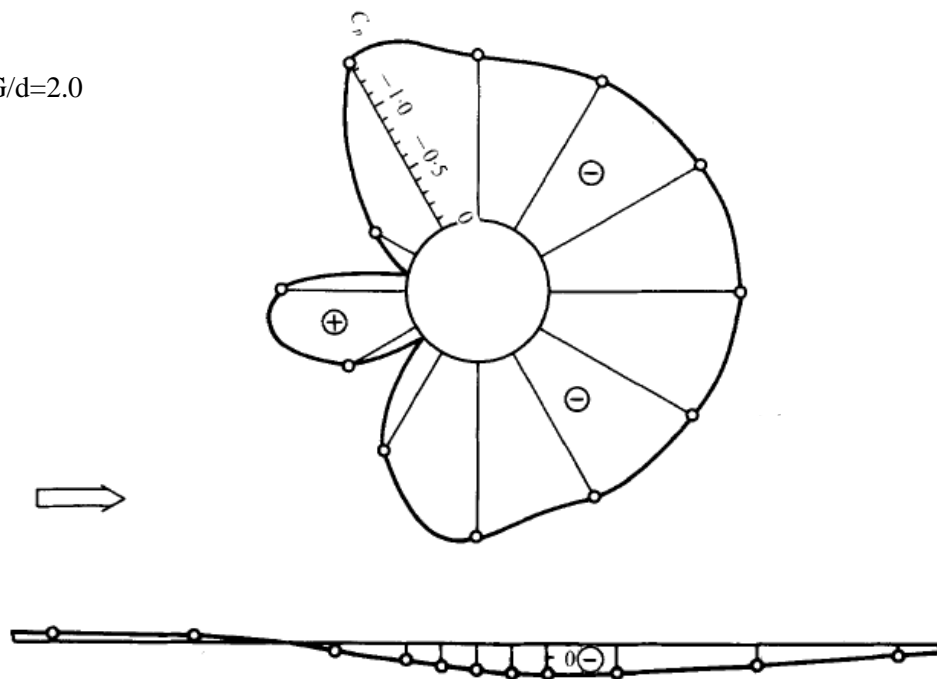
(c)  $G/d=0.8$



(c)  $G/d=1.0$



(c)  $G/d=2.0$



## 2.2 3D Wheel Aerodynamics

This section of the literature review discusses the key characteristics of the flow field around single wheels, whether in free-air, in contact with the ground or as part of a larger combination of components. The aerodynamic flow field around a wheel is of upmost importance when trying to gain an understanding of the flow field around aircraft landing gear, as they comprise a significant proportion of the overall combination of components.

### 2.2.1 Wheels in Free – Air

A large gap in the understanding currently exists for the specific case of a single wheel in free air. The aerodynamics of single wheels in-contact with the ground are much more prevalent, with a significant number of investigations being carried out in the last 10 years due to their importance in the automotive and motorsport industry [29, 30, 31]. Only recently has more focus been placed on wheels in free-air, with the most recent investigation being an experimental investigation on a scaled landing gear wheel in free air conducted by Zhang et al [32]. For this study, two individual wheel configurations were used for the experiments, each having a diameter and width of 0.478m and 0.186m respectively. Investigations were also performed on both simple and complex hub profiles. These configurations were tested in a wind tunnel supported by a single symmetrical airfoil strut at a free stream velocity of 40m/s corresponding to a Reynolds number, based on wheel diameter, of  $1.31 \times 10^6$ . Fundamentally, areas of separation were observed upstream of the central hub cavities with a characteristic four streamwise trailing vortex system convecting downstream within the wake of the wheel, Figure 12. Results from pressure distributions along the circumference of the

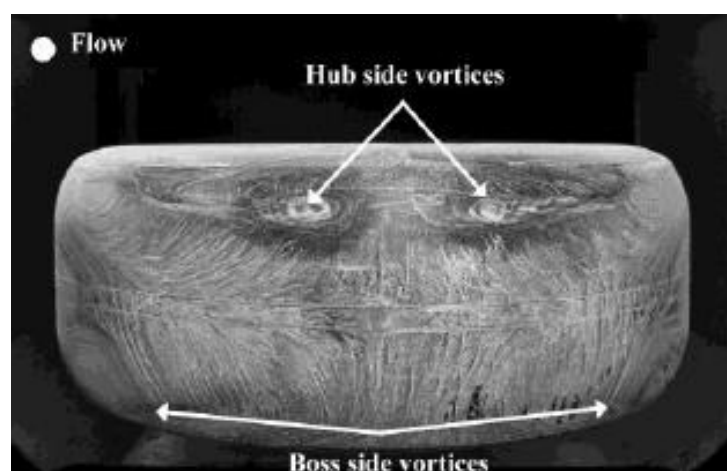


Figure 12 – Streaklines on rear surface of wheel [32]

wheel at  $x = 0\text{mm}$  (centreline), and  $x = \pm 70\text{mm}$  are shown in Figure 13. Fundamentally, the flow around the front of the wheel was found to be reasonably simple, with the trademark front stagnation pressure value of  $C_P = 1$  observed on the front face of the wheel. As the flow travels over the top and bottom of the wheel however, negative pressure peaks of  $C_P = -1$ , were found as the flow accelerates on the face of the wheel. Figure 13 indicates these low pressure flow regions present on the top and bottom surfaces of the wheel, interacting with the side-flow rolling up to form a wake vortex. Analysing the pressure distribution at circumferential cuts obtained at  $x = \pm 70\text{mm}$  showed pressure peaks at  $\theta = \pm 135^\circ$ , which from flow visualisation correspond to the locations of the vortices observed at the back of the wheel. Two stronger vortices were formed on the hub side (Figure 12) of both the complex and simple hub, due to the higher pressures on the boss side of the wheel caused by the flow recirculation behind the support strut. Velocity contour plots behind the wheel were also measured, showing areas of recirculation and strong spanwise velocity distributions in the wake region (Figure 14). Drag coefficients (un-tripped) were also measured with the wheel and supporting strut combination at  $C_D = 0.29 - 0.30$  for Reynolds numbers  $> 1.1 \times 10^6$ , with inferred isolated-wheel results (corrected for measurements from the support strut itself) yielding  $C_D \approx 0.19$ .

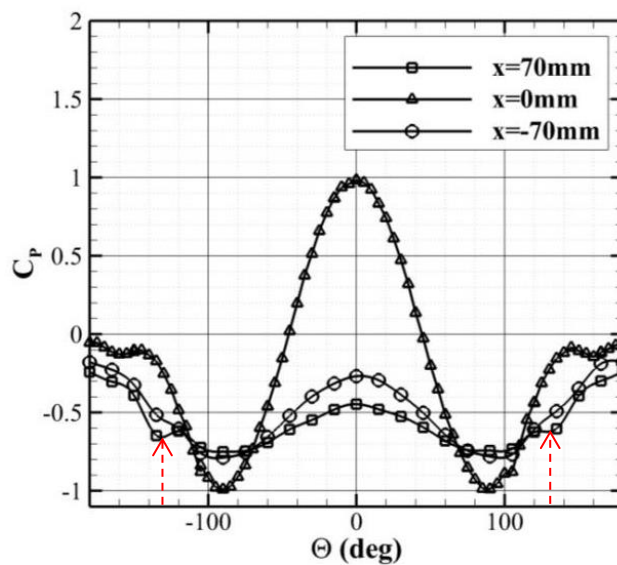
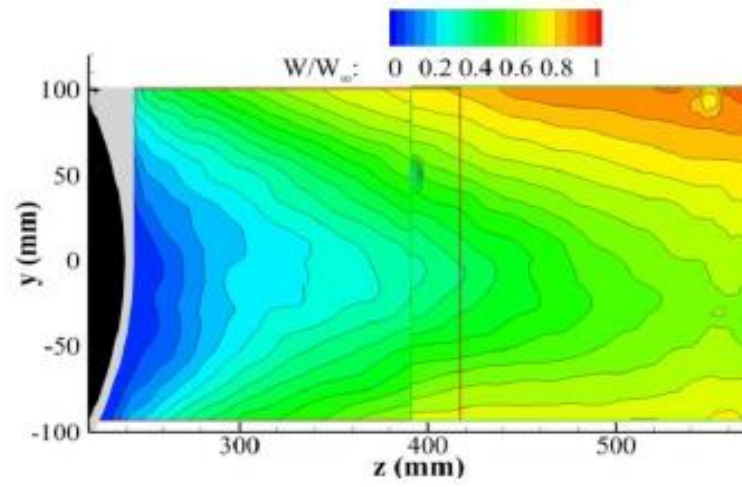
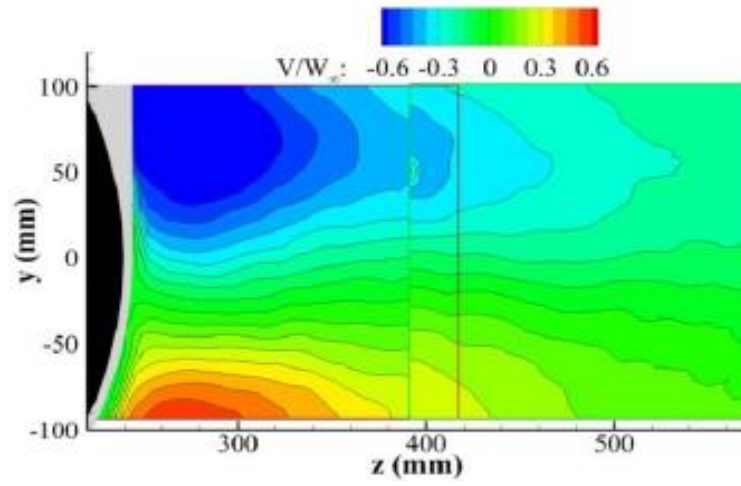


Figure 13 – Surface pressure distribution along three circumferential cuts through wheel [32]



(a)



(b)

Figure 14 – Normalised velocity components for simple hub at  $x=0$ mm plane, (a) streamwise z-velocity, (b) vertical y-velocity [32]

### 2.2.2 Wheels in contact with the ground

In view of the lack of data currently available for an isolated wheel in free air, the work performed on isolated wheels in contact with the ground is reviewed. This work, while not directly applicable to the case of free-air, can still provide valuable insight into the flow field dynamics.

Morelli [33] performed one of the first studies on isolated wheel aerodynamics, experimentally measuring the aerodynamic forces on both a stationary and rotating racing car wheel in contact with the ground. The tests were conducted at several flow speeds including different yaw angles from 0 - 20°. The effect of fairing the rims was also investigated by completely enclosing the wheel with a fairing covering the upper half of the wheel. Experimentally, the wheel was placed on top of a ground plane supported by two stands with a DC motor connected to one end of a support shaft, which rotated the wheel at a speed equivalent to the free stream flow. To model the wheel ‘in contact with the ground’, the wheel was positioned about 15mm into a ‘cut out’ in the ground plane, which represented and questioned the methodology as the wheel had no physical contact with the ground plane. Experiments carried out with the wheel fully exposed to the oncoming flow, showed that a larger yaw angle corresponded to a larger measured value in  $C_D$ , as shown in Figure 15 ( $C_D$  denoted by  $C_x$ ). The effect of the addition of fairings on the rim, was found to result in a reduction of drag by  $\approx 22\%$ ; from  $C_D = 0.45$  (without fairing) to  $C_D = 0.35$  (with fairing) respectively. Through the inclusion of the housing on top of the wheel, the drag coefficient

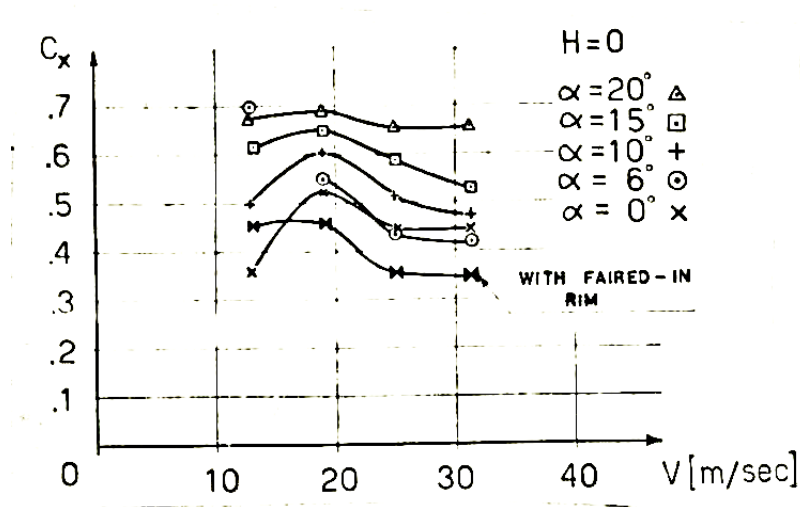


Figure 15 – Drag coefficient of fully exposed wheel against test speeds at different yaw angles [33]

was found to increase with increasing yaw angle. However, as the wheel was covered by the housing to an increasing degree,  $C_D$  remained fairly constant with a slight reduction in the value ( $C_D$ ) by approximately  $\Delta C_D = 0.05$ , being observed as the yaw angle increased to a maximum (Figure 16).

Only a test speed of 31m/s was used when analysing the lift. Lift was also measured (denoted  $C_Z$  in [33], Figure 17), but was found to be relatively insensitive by the increase in yaw angle or housing cover, however, slight variations were observed with maximum coverage of the wheel. When rotation was applied to the wheel in this configuration, a negative lift force was typical of the results measured. This was later confirmed in other studies [22] as a major problem, due to the contact patch/moving ground plane not being modelled correctly. Once the wheel to ground contact was configured more accurately, a positive lift force is experienced.

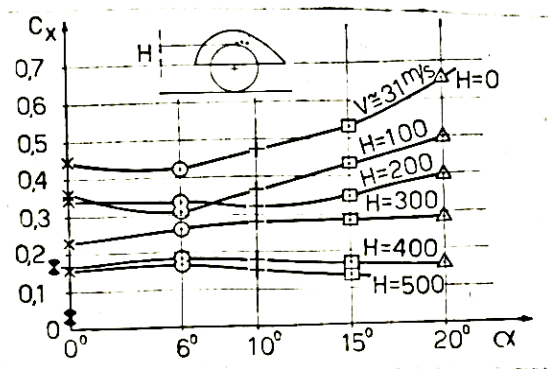


Figure 16 – Drag coefficient against yaw angle at various fairing heights tested [33]

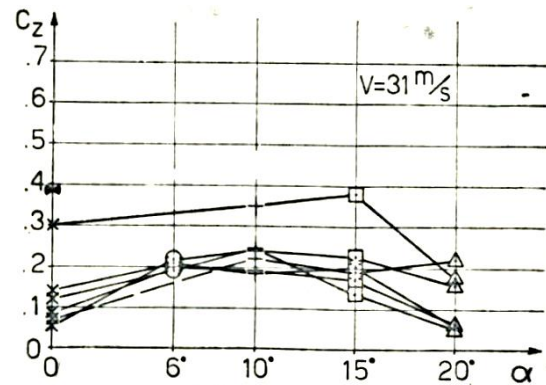


Figure 17 – Lift coefficient against yaw angle at various fairing heights tested [33]

Stapleford and Carr [34] also investigated the aerodynamic forces on the wheels of a race car, with both stationary and rotating wheels at different ground clearances. For their case with a minimum ground clearance, tests were conducted to obtain lift and drag coefficients for the stationary and rotating wheels on both a stationary and moving ground. Analysing the drag and lift coefficients for both the stationary and moving ground cases, Stapleford and Carr [34] proposed that the effect of a moving ground does not make a substantial difference to these measured force coefficients; albeit erroneously deciding thereafter to conduct the remainder of their experiments on a stationary ground surface. With the wheels maintained at a ground clearance of 0.25inches, they concluded that sealing the gaps between the ground plane and the bottom of the wheel made no significant difference to the resulting flow field; as the boundary layer was thought to restrict the flow under the wheels when the gaps were



open. However, changes in the flow field are indeed seen in their results, as the air flowing beneath the wheel is pushed through the gap once rotation was applied on the wheel. For the case of the stationary wheel, Figure 18(a), at maximum ground clearance of 2.0inches, an expected stagnation pressure peak of  $C_p = 1$  was observed on the front face of the wheel, together with the flow passing over the top and bottom of the wheel producing a decrease in surface pressure to  $C_p \approx -2$  (A). Pressure recovery to a level just below zero in the rear near wake was subsequently observed within the region of  $\theta = 150^\circ - 210^\circ$ . As the ground clearance was decreased to 0.5inches, the pressure below the wheel was found to decrease to  $C_p \approx -2.5$  (B), whilst the pressure over the top of the wheels increased to  $C_p \approx -1.5$  (B'), indicating larger suction peaks representative of increased flow acceleration beneath the wheel. Reducing the ground clearance further beyond this level, reversed this trend and at zero ground clearance, the pressure was found to be only below zero in the region from  $\theta \approx 150^\circ - 270^\circ$ . A similar pattern in the pressure distribution was observed on the rear wheels, however, as a result of the interference from the front wheels and reduced effective velocity on the rear wheels, lower pressures ( $C_p \approx 0.5$ ) were observed at the stagnation region on the rear wheels.

Stapleford and Carr [34] found asymmetry in the wake and pressure flow physics as a result of applying rotation to the wheels, Figure 18(b). For the test case at 2.0inches ground clearance, an increase in surface pressure to  $C_p \approx -1$  was found on the upper surface (C') of the rotating wheel, with a reduction in surface pressure to  $C_p \approx -2.5$  over the bottom surface (C) when comparing to the stationary case. Reducing the ground clearance to 0.5inches,

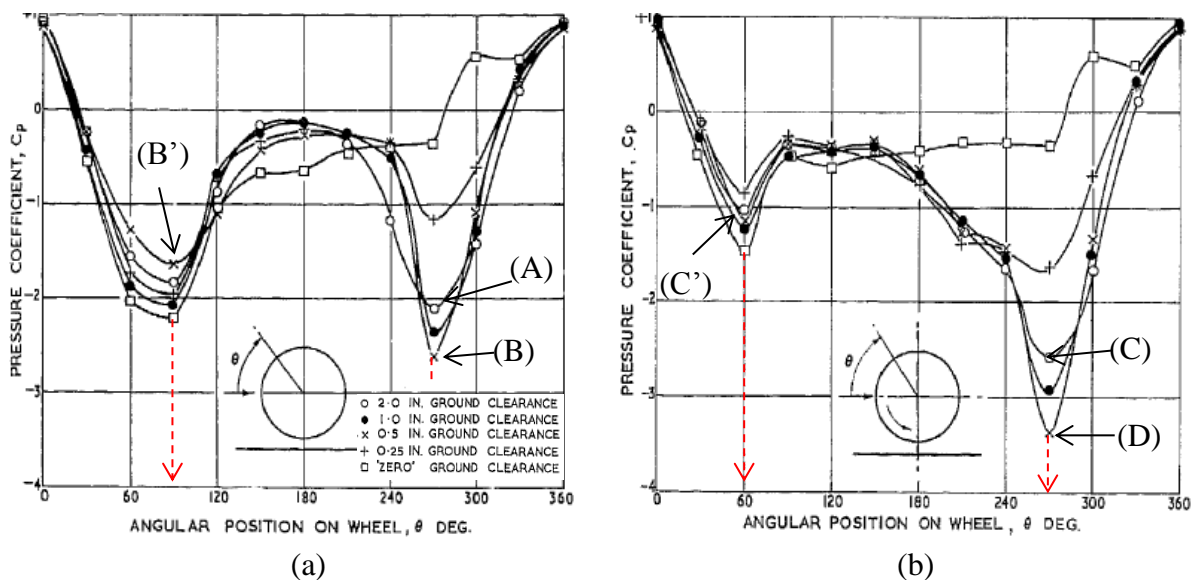


**Figure 18 – Distribution of surface pressure at different ground clearances around (a) stationary wheel, (b) rotating wheel [34]**

shows a significant reduction in surface pressure up to  $C_p \approx -3.4$  on the bottom of the wheel (D), representative of increased flow acceleration beneath the wheels, as the both the wheel and the free-stream airflow is moving in the same direction. However with zero ground clearance, although a reduction in surface pressure ( $C_p \approx -1.5$ ) is observed on the upper surface, a recovery in pressure to  $C_p \approx -0.5$  was obtained and maintained on the rear surface of the wheel. It is important to note that when comparing the locations of the pressure peaks for both the stationary and rotating configurations, the stationary peaks occurred at  $\theta \approx 90^\circ$  and  $\theta \approx 270^\circ$ , whilst the peaks on the rotating wheel occurred at  $\theta \approx 60^\circ$  and  $\theta \approx 270^\circ$ . This offset of  $30^\circ$  observed upstream from the top of the rotating wheel, represents an earlier region of separation with the application of rotation.

Lift coefficient was also measured by Stapleford and Carr [34]. As would be expected, the lift generated by the stationary wheels at the highest clearance is very small ( $C_L \approx 0$ ), but with wheel movement closer to the ground, lift coefficient increased ( $C_L = 0.74$  and  $C_L = 1.57$  at 0.25in and zero ground clearance respectively). The drag force coefficient also increased along a similar pattern,  $C_D = 0.9$  and  $C_D = 1.15$  at 0.25in and zero ground clearance respectively. At maximum ground clearance on the rotating wheel configuration,  $C_L$  was first found to be negative ( $C_L \approx -1.0$ ), subsequently changing to a positive lift ( $C_L = 0.6$ ) with ground clearance reduction to zero. An increase in drag was also measured for the rotating wheel configuration when compared to the stationary configuration with  $C_D \approx 1.1$  throughout the tested ground clearances. Whilst for the stationary case, as the ground clearance was reduced, a significant increase in drag was observed, as  $C_D \approx 0.7$  at maximum ground clearance, to  $C_D \approx 1.15$  at zero clearance.

From their results, Stapleford and Carr [34] constructed a representation of the aerodynamic characteristic flow field around both the exposed stationary and rotating wheel. Initially considering the case of the stationary wheel in free air, Figure 19(a), the flow around the wheel is symmetric about the front stagnation point (Figure 19 – S). Separation regions are identified at approximately  $120^\circ$ , on both the upper and lower surface of the wheel from the stagnation point forming the boundaries of the rear wake. As a result of the symmetric flow field around the wheel, the lift force is negligible. Once the stationary wheel is in contact with the ground, Figure 19(b), an obvious conclusion is that, the flow travelling beneath the wheel is prevented; therefore the flow must travel entirely around the top or sides of the wheel, causing the wake to be extended from the upper separation position on the wheel down to the ground plane. The asymmetry created in the flow field, as a result of the wheel in contact

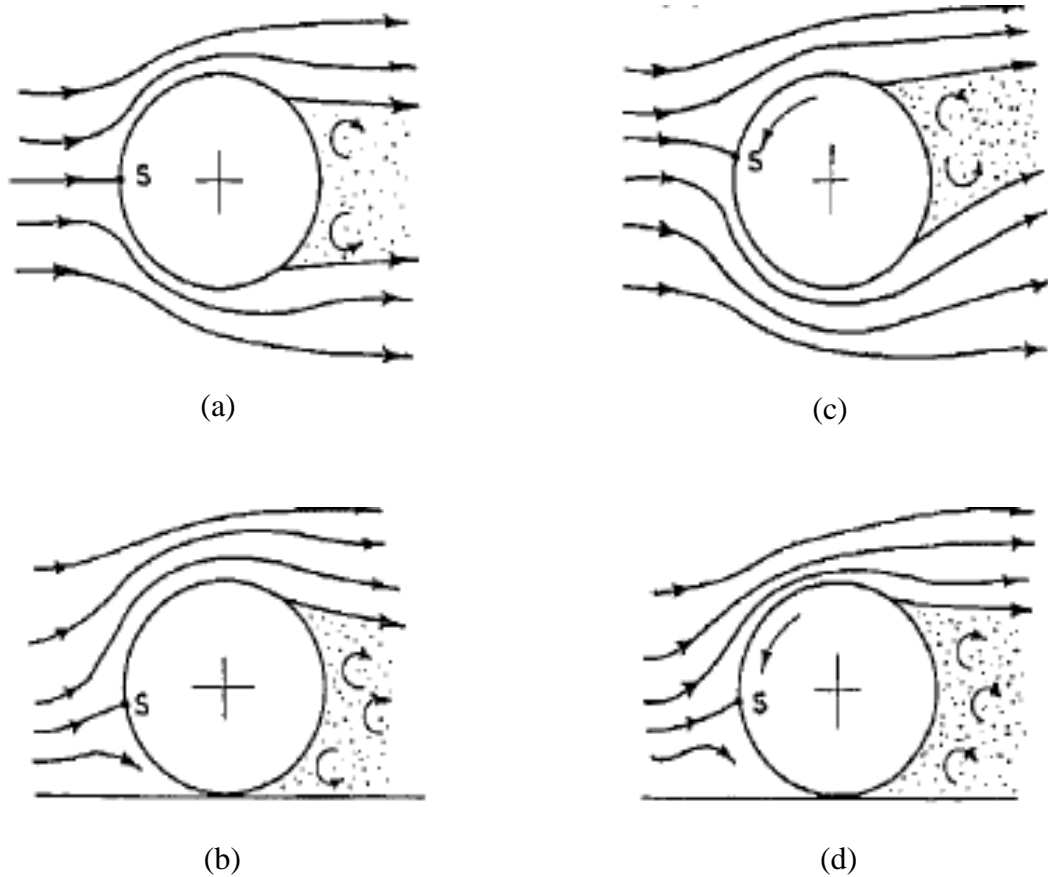


**Figure 19 – Flow pattern around stationary and rotating wheels in free air and in contact with the ground [34]**

with the ground, indicates an increase in suction pressure over the top surface of the wheel whilst reducing that on the lower surface. Subsequently the positive pressure around the front stagnation region extends towards the frontal lower side of the wheel, resulting in a positive lift force. The increased wake region behind the wheel was also suggested to increase the drag force. For the case of the rotating wheel in free air, Figure 19(c), the most noticeable difference compared to the stationary wheel in free air (Figure 19(a)), is the wake being considerably displaced by an up-wash angle. Additionally, the accelerated flow on the lower half induced by the rotation of the wheel along with the reduced flow velocity on the upper half, creates a pressure differential which is the result of the experienced downwards negative lift. The rotating wheel in contact with the ground, Figure 19(d), however, does not significantly differ when compared to the stationary configuration of a wheel in contact with the ground (Figure 19(b)), as the observed characteristic difference is the reduction in velocity on the upper surface of the rotating wheel.

Fackrell [22] conducted a study on isolated wheel aerodynamics, testing three different tread widths and two wheel profiles, denoted A, B, C and 1, 2 in [22]. The wheels comprising a

Wheel No.	Total Width Dia.	Tread Width Dia.	X-Sect Area sq.ft.	Tread x Dia. sq.ft.	Coefficients Based on X-Sect. Area		Coefficients Based on Tread x Dia.		Contribution From Hub		
					$C_{D1}$	$C_{L1}$	$C_{D2}$	$C_{L2}$	$\Delta C_{D1}$	$\Delta C_{D2}$	$\Delta C_{L2}$
A 1	.50	.26	.91	.48	.52	.28	.97	.53	.06	.12	-.01
B 1	.66	.41	1.19	.77	.63	.40	.98	.61	.03	.05	0
C 1	.81	.56	1.48	1.05	.70	.43	.97	.61	.02	.02	0
A 2	.46	.26	.85	.48	.51	.28	.90	.49	.08	.14	-.02
B 2	.61	.41	1.13	.77	.58	.44	.85	.65	.03	.05	0
C 2	.76	.56	1.42	1.05	.70	.43	.94	.57	.01	.01	0

Figure 20 – Force coefficients on different wheel geometries tested in [22]

diameter of 0.416m were tested in a wind tunnel with a free stream velocity of 18.6m/s corresponding to a Reynolds number of  $5.3 \times 10^5$ , based on wheel diameter. Both stationary and rotating wheels were analysed, with the angular velocity of the wheel and the moving ground set equivalent to the free stream velocity. Drag and lift coefficients were obtained for these tests, with some selected results shown in Figure 20. Common to the investigation were

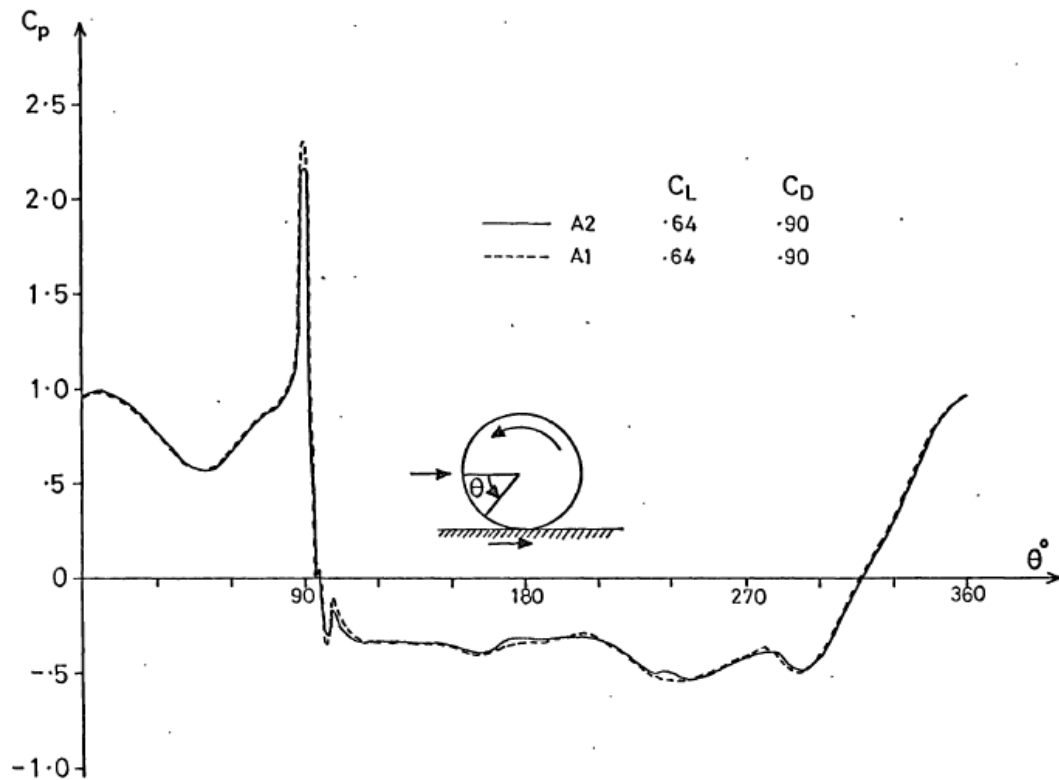


Figure 21 – Centreline pressure distribution around rotating wheels A1 & A2 [22]

that, for the most part,  $C_D$  and  $C_L$  increased with wheel width effectively giving larger drag forces with increasing aspect ratio. Wheel shapes A & C show similar force coefficient magnitudes even though they comprised different tread widths. Results for data obtained for the B-profile differed by up to 10% and were to be treated with caution as improvements were continuously made as the experiments progressed, as it was the first wheel tested. The contribution of hub force coefficients were presented separately in Figure 20 and showed the hub configuration from the ‘A2’ wheel, contributed the most drag force to the overall wheel drag ( $\Delta C_D = 0.08$ ) compared to the other wheel configurations.

After publishing this seminal work on the topic, comparisons of Fackrell’s work were made to Morelli [33] and discovered that his results were significantly different, concluding that Morelli’s [33] methodology was not representative of the real fluid flow of an isolated wheel in contact with the ground (principally via inaccurate modelling of the contact patch between the wheel and ground plane). Pressure distributions presented by Fackrell [22] around the surface of the A1 & A2 wheel are shown Figure 21. From these results, the centreline pressure coefficient was measured at a value greater than two near the contact patch ( $\theta = 90^\circ$ ) and found to result from the extra energy introduced to the flow via the suction of air into the contact patch through the converging boundaries of both the rotating wheel and moving

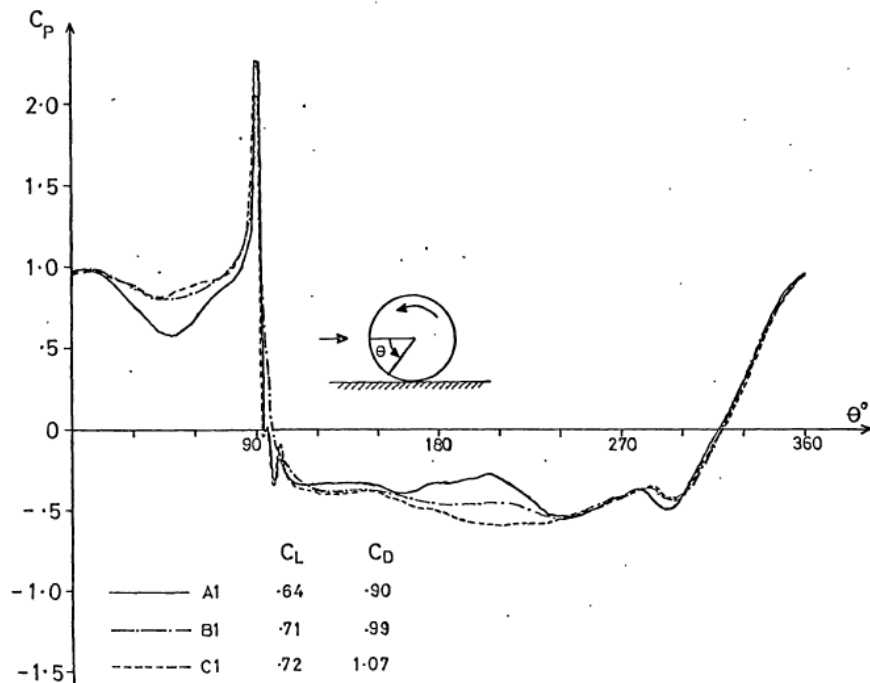


Figure 22 – Pressure distribution around wheels A1, B1 & C1 (Different wheel width, same edge profile) [22]

ground. The influence of wheel width, shown in Figure 22, was also found to have minimal effect on the values of  $C_p$  on the centreline of the wheel but become more prominent closer to the wheel edges. Separation was defined as the first point at which large scale pressure fluctuations begin (positions was measured at approximately  $\theta = 280^\circ - 300^\circ$ ). Separation was also found to take place slightly further upstream for B & C than that observed for wheel A. From comparing centreline pressure distributions around all wheel configurations, (Figure 22), Fackrell found that a lower pressure exists over the lower front face of the narrower wheel (A), with the widest wheel (C) found to have a lower base pressure. The influence of rotation was also analysed and compared to the stationary case. Although wheel B was not the most accurate wheel modelled in [22], Fackrell suggested any errors present would not invalidate any generalised conclusions made. When comparing the stationary and rotating  $C_p$  distributions shown in Figure 23, the influence of rotation resulted in a reduction in drag and lift forces (stationary:  $C_D = 1.18$ ,  $C_L = 1.16$  and rotating:  $C_D = 1.03$ ,  $C_L = 0.74$ ). A large

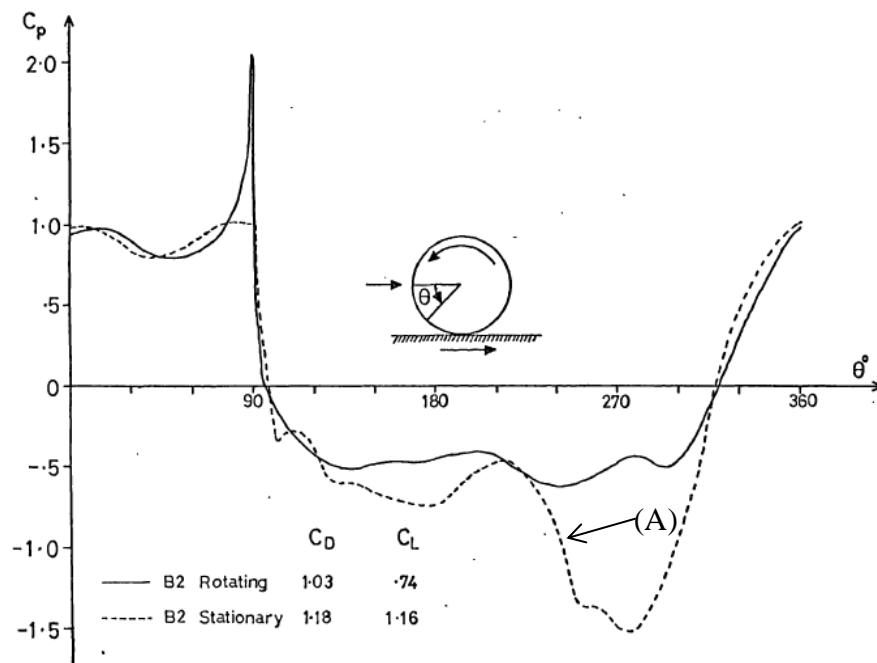


Figure 23 – Centreline Pressure distribution around stationary and rotating wheel B2 [22]

region of low pressure at the rear of the stationary wheel was seen, Figure 23 - (A), which contributes to a larger drag force. Separation on the rotating wheel was found to occur earlier on the rotating wheel [22, 35] at  $\theta \approx 280^\circ$ , as opposed to the stationary wheel ( $\theta \approx 220^\circ$ ), caused by the presence of a reversed layer of fluid on the wheel's surface. This was later confirmed by total head contour plots taken within this top region at the centreline of the wheel (Figure 24). Additionally, Figure 25 shows smoke visualisation obtained over the wheel, confirming the earlier separation suspected on the rotating wheel (D) together with the flow remaining attached further downstream on the stationary wheel (E). Total head contours in Figure 24, also shows a wider effective wheel wake for the rotating wheel on the upper half of the hub (B). This bulge feature of the rotating wheel configuration is due to the flow inside the upper hub opposing the direction of the free stream flow travelling alongside the wheel, creating increased viscous interaction between the flows. Conversely, the lower hub surface for the rotating wheel moves in the same direction as the free stream flow, resulting

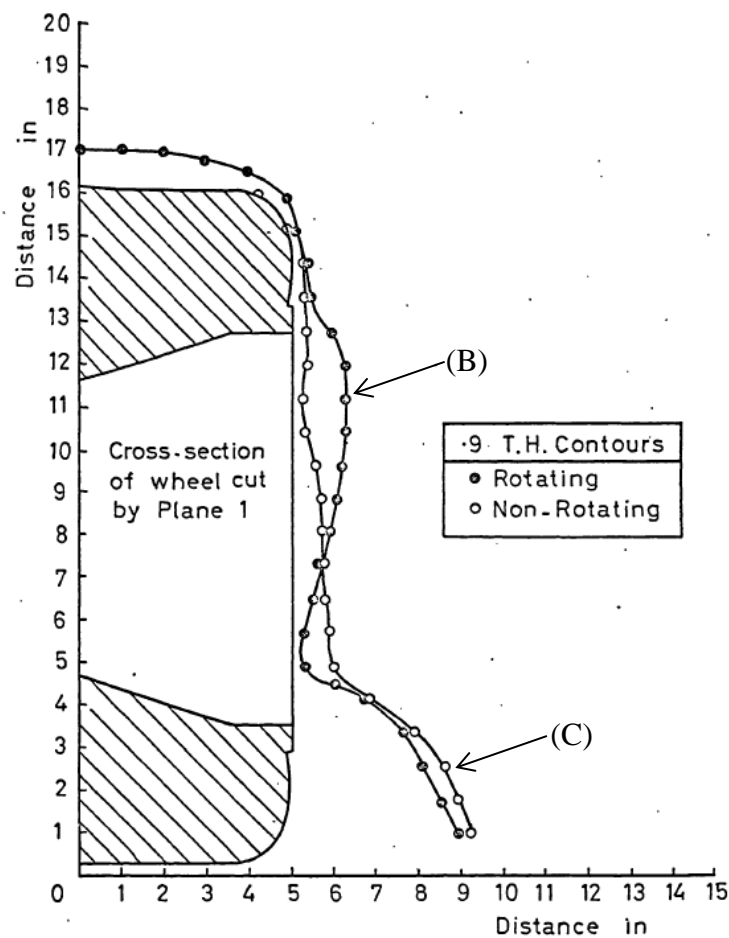
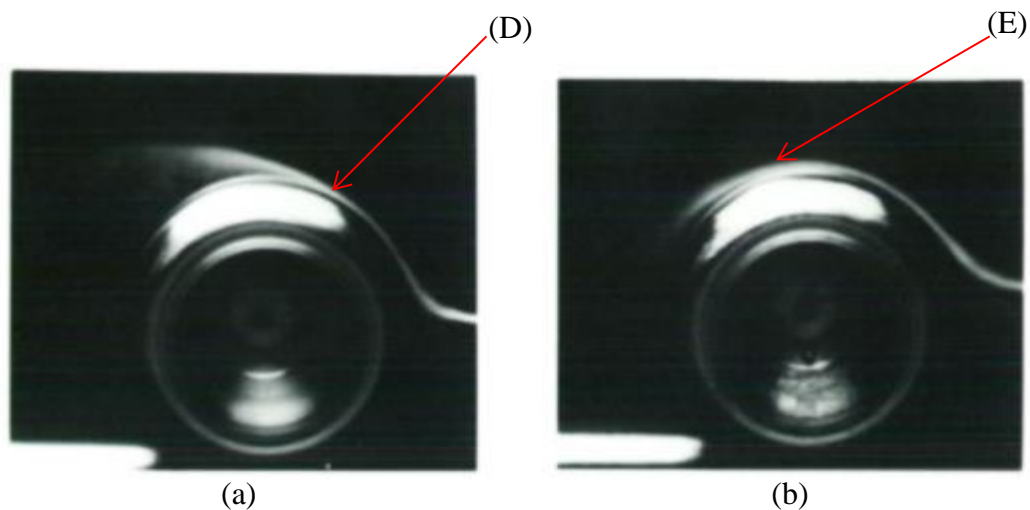


Figure 24 – Total head contour at Plane 1; 1.7 inches from the centre of the wheel, stationary & rotating [22]

in a total head contour and consequent wake positioned closer to the wheel. However, for the stationary wheel, a more uniform contour is seen alongside the hub due to the reduced interaction between the free stream flow and the air within the hub cavity. Analysing further, the total head contour results show a large displacement away from the lower section of the wheel (closer to the ground, Figure 24-C), particularly for the stationary wheel as a result of the air travelling out from beneath the front of the wheel rolling up to form a horse-shoe vortex around the wheel lower surfaces. Contour plots of total head even further downstream [22], also displayed a higher wake profile for the upper half of the rotating wheel whilst maintaining approximately, a wake width coincident of the actual wheel width. This wake widens in the rear lower half of the wheels as is convected downstream.



**Figure 25 – Smoke Visualisation of flow past wheel, (a) side view on rotating wheel, (b) side view on stationary wheel [22]. Flow direction: Right to Left**



Several seminal conclusions on rotating wheel flows were made from this work. Primary of these was the insights gained into the separation flow physics of a rotating wheel in contact with the ground. Figure 26 [22, 35] details this physics, providing a pictorial representation of the earlier separation evident on a rotating wheel (at 'A') due to the attached flow on the rotating wheel interacting with the free stream flow travelling in the opposite direction, effectively 'lifting' the separation position above the surface of the wheel. Also detailed in Figure 26 on the lower surface of the wheel ('B'), are viscous effects on the converging surfaces of the wheel and the ground plane, creating a high pressure region which Fackrell called a 'jetting phenomenon', where the flow travelling around the lower wheel surface and the free stream interact and get 'jetted' or 'pumped' at both sides of the wheel.

Cogotti [36] also investigated the influence of different ground clearances on aerodynamic forces and surface pressures of both stationary and rotating isolated wheels. Detailed in this work, a pair of isolated exposed wheels (diameter and width of 0.485m and 0.135m respectively), were installed on steel rims attached to an AC motor. The motor rotated at equivalent free stream velocity of 38m/s, corresponding to a test Reynolds number of  $1.1 \times 10^6$ , based on wheel diameter. Four ground clearances were tested for both the stationary and rotating wheel, from 50mm clearance to in contact with the ground. Results showed that as the ground proximity/clearance decreases, the air flowing between the lower surface of the

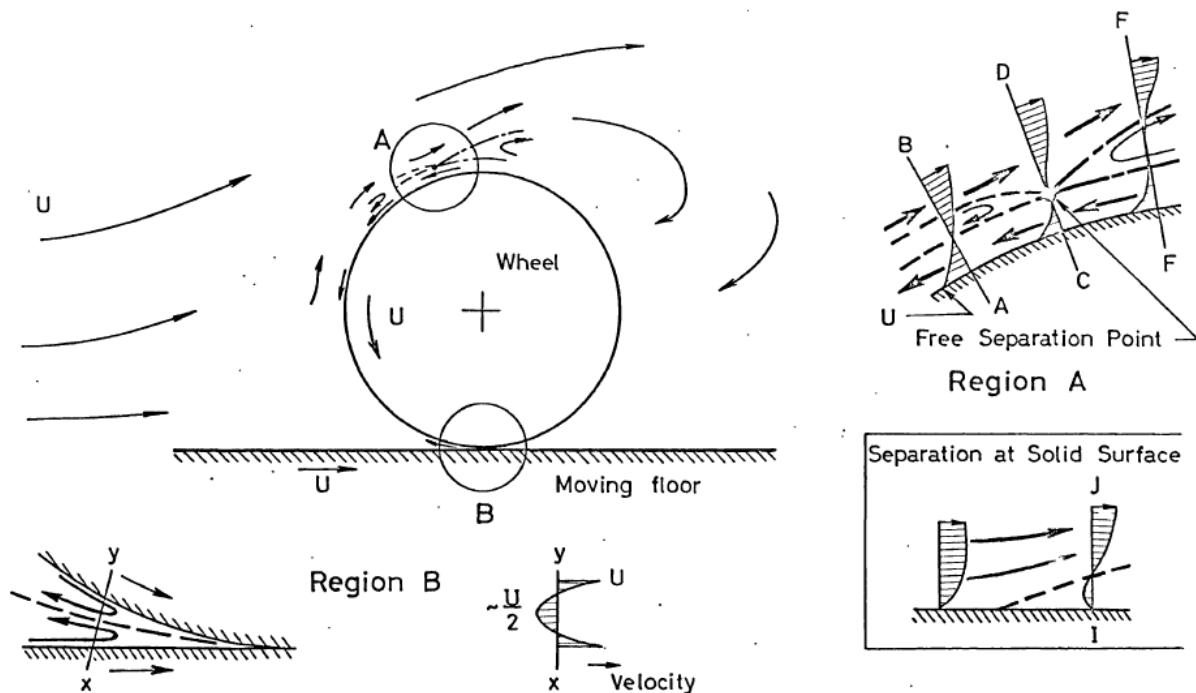


Figure 26 – Details of the separation point and 'jetting' flow [22]

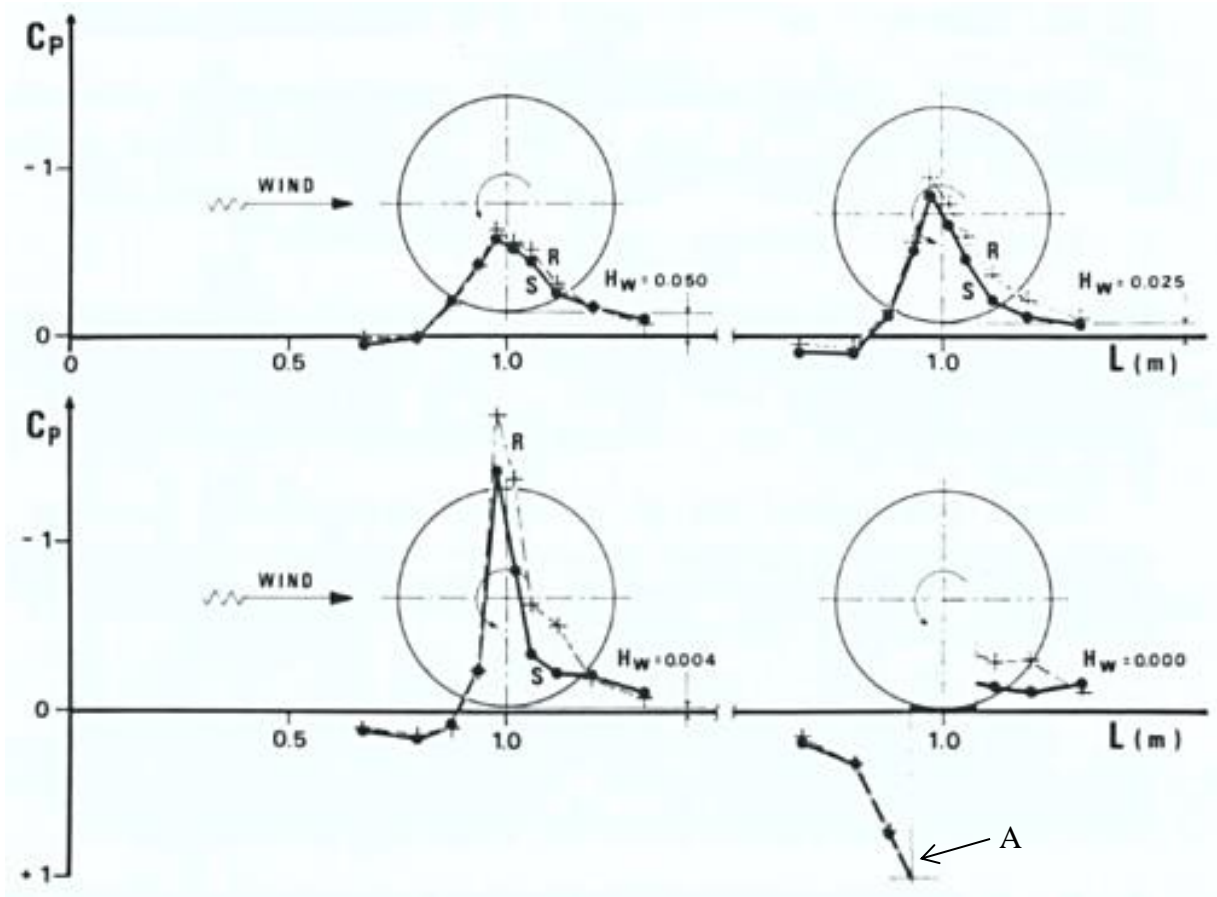


Figure 27 – Pressure distributions under a rotating wheel at different ground clearances [36]

wheel and the ground is accelerated, with a corresponding decrease in  $C_p$  under the rotating wheel (Figure 27). However, results also show that when the ground clearance is reduced to zero (in contact with the ground), a positive pressure peak (A), is observed due to the development of a secondary stagnation point within the contact patch region. The contact patch was tested by sealing the gap between the bottom of the wheel and the ground using foam and pads, however, there remains some questions as to the viability of this methodology, particularly since the characteristics of the positive pressure peak observed at this contact patch was found to depend on the quality of sealing of the gap in this region.

For the stationary isolated wheel case, Cogotti [36] also found drag and lift force coefficients to be  $C_D = 0.48$  &  $C_L = 0.04$  at a ground clearance of  $H/D = 0.10$ ; however rotating wheels produced a larger drag and a net negative lift ( $C_D = 0.54$ ,  $C_L = -0.14$ ), in-line with other published work [34], although the stationary wheel in direct contact with the ground produced more drag than the rotating wheel (Stationary:  $C_D = 0.59$ , Rotating:  $C_D = 0.58$ ). Yet, this result was found to be dependent on installed fairings around the rims and hub, as Morelli [33] had also previously discovered that the drag coefficient would be reduced by

fairing the wheel rim. Cogotti [36] confirmed this with an investigation using faired rims and obtaining lower drag forces of  $C_D = 0.54$  and  $C_D = 0.49$  for the stationary and rotating wheel respectively. With the wheel in contact with the ground, the negative lift force experienced, with a small gap for the rotating wheel, changed to a positive lift characteristic ( $C_L = 0.18$ ), distinctly different however from the stationary wheel case, which generates a larger lift ( $C_L = 0.27$ ) than the rotating case, which was also found to be dependent on the quality of sealing between the wheel and the ground plane [34].

In an attempt to theoretically categorise the isolated wheel configuration, Cogotti [36] also considered the wheel as a cylinder, treating the body through ‘the theory of vortices associated with lifting bodies’ [21]. As a result, Cogotti displayed the resultant motion of these dominant vortices (Figure 28), illustrating that for the stationary wheel in free air, ((a)

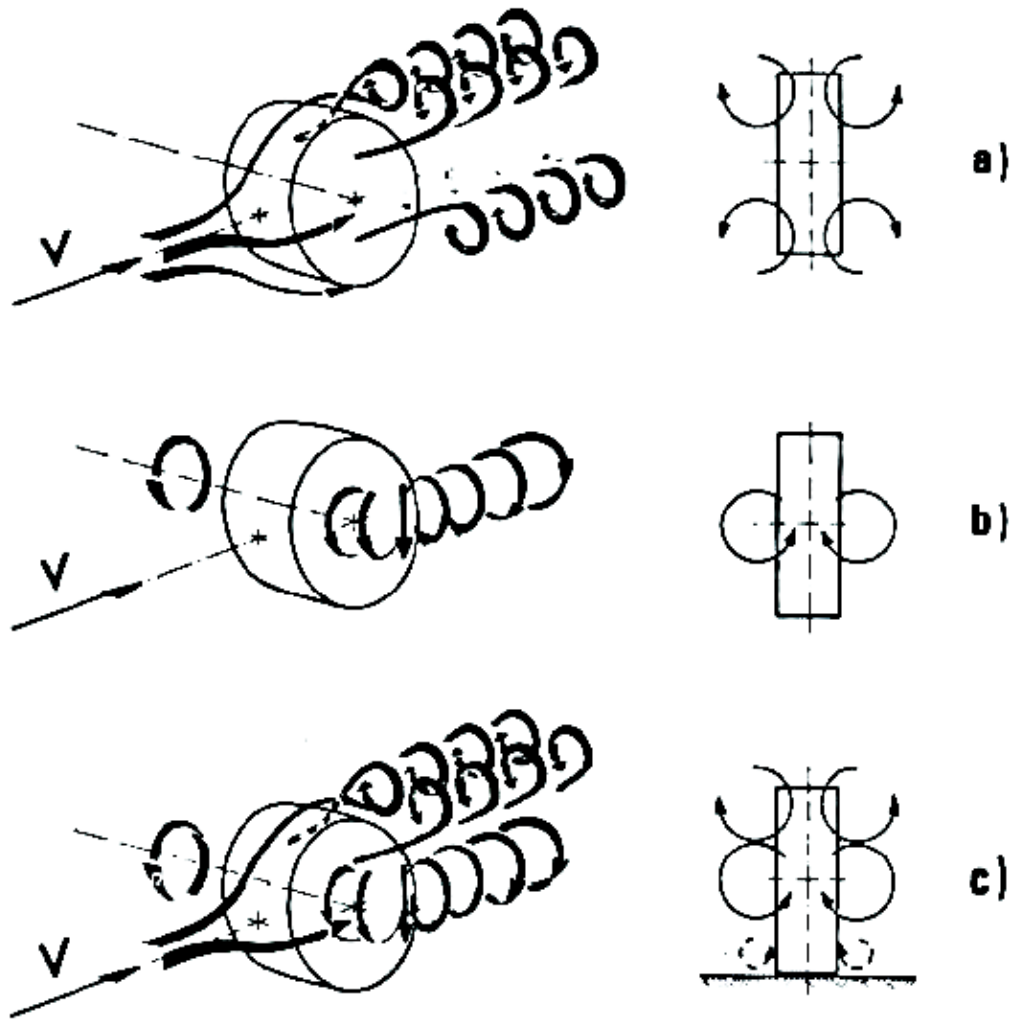


Figure 28 – Rear near wake pattern, (a) stationary wheel, (b) rotating wheel, (c) rotating wheel in contact with the ground [36]

in Figure 28), separation occurs on all four edges of the wheel forming two pairs of counter rotating vortices, symmetrical about the vertical and horizontal centreline of the wheel. With rotation applied, ((b) in Figure 28), the four vortices predicted to occur on the stationary wheel, are replaced by two mid region vortices. With ground clearance reduction to zero (wheel being in contact with the ground (c)) the two counter rotating vortices are seen to develop more near the contact patch, with the four upper vortices still present. Unfortunately, later work performed by McManus & Zhang [29], showed that this was indeed too simplified a characterisation of this flow field and that the real flow is distinctly different.

Waschle et al [37] conducted experimental and numerical investigations to make comparisons of velocity, pressure distributions and aerodynamic force measurements around both, a stationary and rotating isolated wheel in contact with the ground. The experimental work, obtained using Laser Doppler Anemometry (LDA), was used to compare results obtained via two CFD codes; STAR-CD™ and PowerFLOW™.

A scaled model of an isolated front wheel of a Formula-1 car was used in this investigation, comprising a wheel diameter of 215.8mm and tread width of 80.0mm, tested in a wind tunnel with a free-stream velocity of 45m/s ( $Re_n = 5.37 \times 10^5$ ). The wheel was held in the wind tunnel by a steel support, with the wheel configuration consisting of an aluminium rim with 5 openings, a tyre and a brake disk. The numerical solutions were also conducted with an inlet velocity equivalent to the experimental set up. The computational grid consisted of a hexahedral mesh consisting of 6.7million cells. The simulations in STAR-CD™ used two approaches: firstly using the standard  $k-\epsilon$  model and secondly, using a two layer approach which uses the  $k-\epsilon$  model to resolve the far field and using a one equation model for modelling the near wall flow. These simulations were performed at steady state, therefore obtaining the last iteration after convergence to be represented as the averaged flow field, which was then compared with the time averaged measurements. However, PowerFLOW™ used the RNG- $k-\epsilon$  turbulence model, with simulations obtained in transient conditions computed for 0.15 seconds in real time, which converts to 20,000 time steps.

For the stationary wheel in contact with the ground, results from all four methods showed two strong visible ground vortices, as well as a strong central downwash in the rear wake of the wheel, as has been shown in Figure 29 and in agreement to the findings in [29]. However, the PowerFLOW™ data indicated a downwash 8% larger in magnitude compared to the experiments, as shown (A) in Figure 29 and illustrated by the intensity of the velocity vectors

directed downstream, compared to the other three methods. Separation does not occur along the centreline of the stationary wheel and was thought to be due to the three dimensional flow around the wheel. Central vortex core positions were located lower than on the experiments, by  $\approx 15\text{mm}$  (PowerFLOW™) and  $\approx 20\text{mm}$  (STAR-CD™), although regions of back flow (shown by the lighter regions in the contour plots) were predicted to be in good agreement between the methods.

The application of rotation showed large differences in the flow field compared to the stationary case. The ground vortices still exist, but are much weaker (as indicated by the intensity of the velocity vectors between Figure 29 and Figure 30), although observed closer together due to the moving ground, representing the jetting vortices due to the diverging boundaries as found by Fackrell [22]. Separation is observed on the top surface of the rotating wheel, forming a wake on the upper half of the wheel which is taller in comparisons to the stationary rear wake, with the width of the wake remaining within the projected profile of the wheel. The two layer approach using STAR-CD™ was found to agree mostly with the experimental data (Figure 30); however the wake in the upper region appeared to be slightly

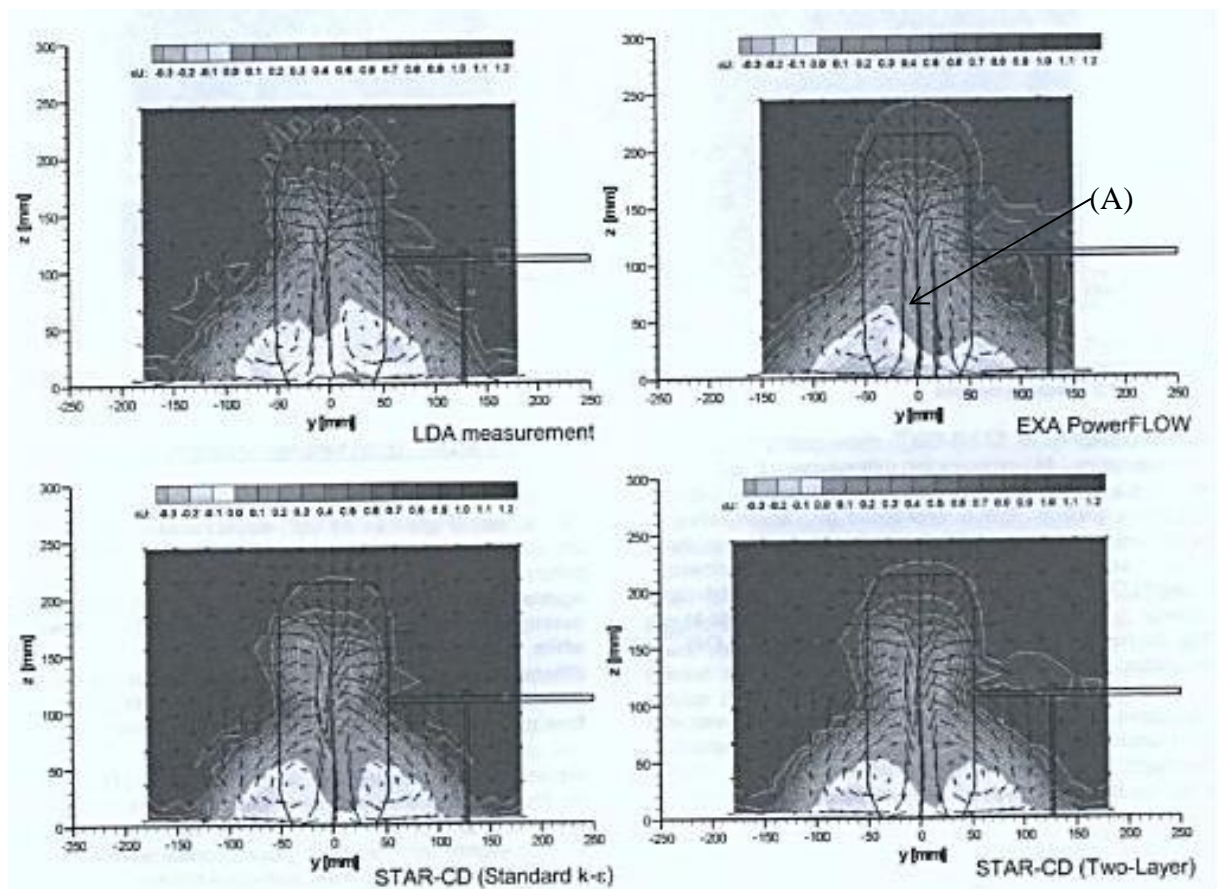


Figure 29 - Comparisons of velocity field in the rear wake of the stationary wheel at  $x = 150\text{mm}$ , illustrating velocity vectors and contours of the velocity component in streamwise x-direction [37]

wider by up to 10mm. At the cross section  $x=420\text{mm}$  of the rotating wheel, the results from PowerFLOW™ shows better agreement to the experimental result with regard to velocity magnitude and position of the ground vortices. In the centre plane, for the rotating wheel, a wake is present on the upper rear region of the wheel due to the flow separating on the upper surface. The strong downwash that was observed behind the stationary wheel was replaced by small velocities. Both of the CFD codes compare well to the LDA measurements, even though similar differences are observed between the two codes. In general, the two layer model proved to be the most beneficial when modelling the rotating wheel, as differences to the experimental measurements were minimal. The effect of drag and lift was also measured by the two CFD solvers and the experimental configuration. The STAR-CD™ two layer approach gave the closest comparison ( $C_D = 0.620$ ) to the experimental drag coefficient of 0.612, whilst the STAR-CD™  $k-\varepsilon$  and the PowerFLOW™ slightly under and over estimates the drag coefficient, with  $C_D = 0.576$  and  $C_D = 0.628$  respectively. However, the lift coefficients showed PowerFLOW™ providing better agreement to the experiments, with  $C_L=0.526$  and 0.530 respectively. On the rotating case, PowerFLOW™ also compared closest

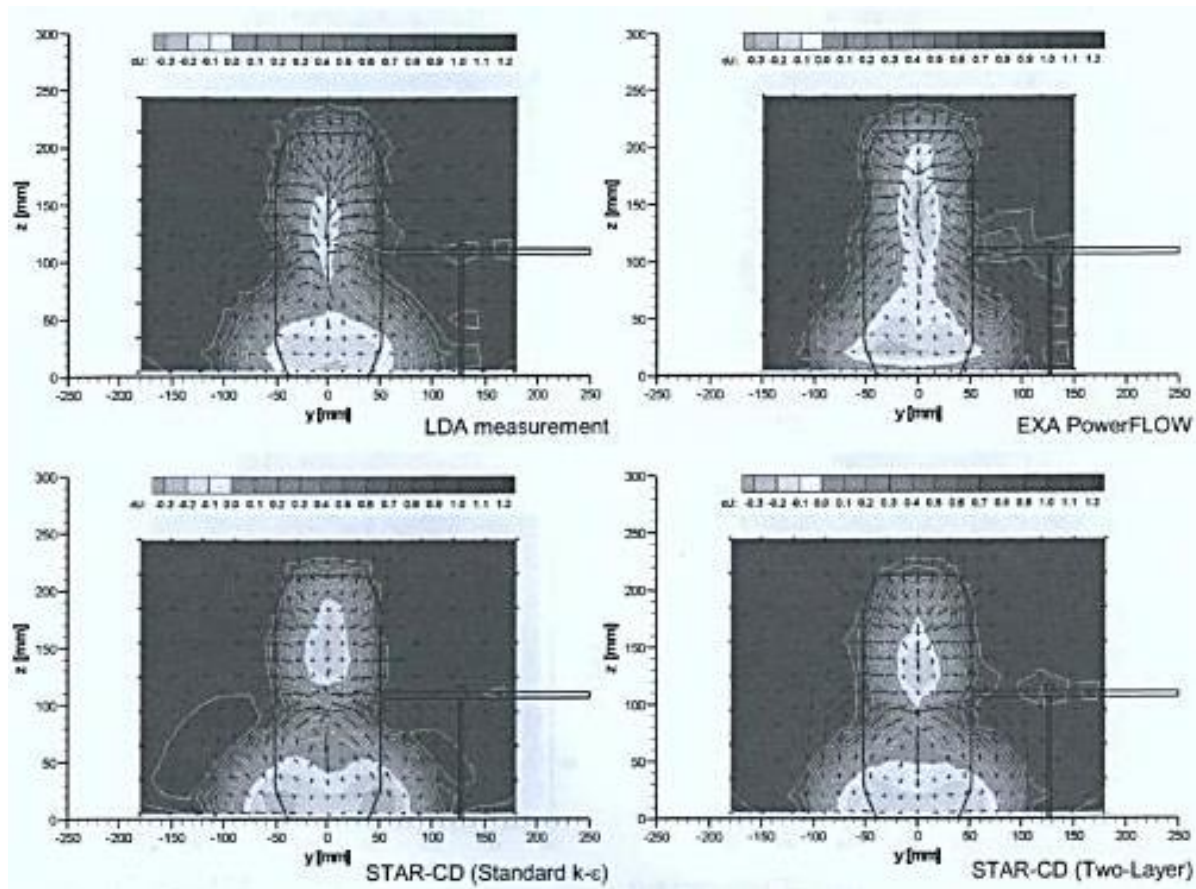


Figure 30 - Comparisons of velocity field in the rear wake of the rotating wheel at  $x = 150\text{mm}$ , illustrating velocity vectors and contours of the velocity component in streamwise  $x$ -direction [37]



to the experimental results, with  $C_D=0.540$ ,  $C_L=0.311$  and  $C_D=0.566$ ,  $C_L=0.315$  respectively, indicating a rotating wheel produces less drag and lift compared to a stationary wheel in contact with the ground.

A study of the flow field around an isolated wheel in contact with the ground was also investigated by McManus & Zhang [29]. The computational study captured the aerodynamic flow field around both stationary and rotating wheels using URANS transient simulations. These simulations were conducted on the same wheel geometry 'A2', as used in Fackrell's experimental wheel configuration [22], to provide experimental validation of their methodology.

Overall results showed a combination of complex vortical flow structures and multiple separation reattachment features. For the stationary wheel the flow was found to separate on the upper rear edges of the wheel (A) (Figure 31), and then reattach at (B) through the interaction of flow moving on to the central surface of the wheels from the sides (shown in (D)). This entrainment encourages attached flow on the central region of the wheel, which is

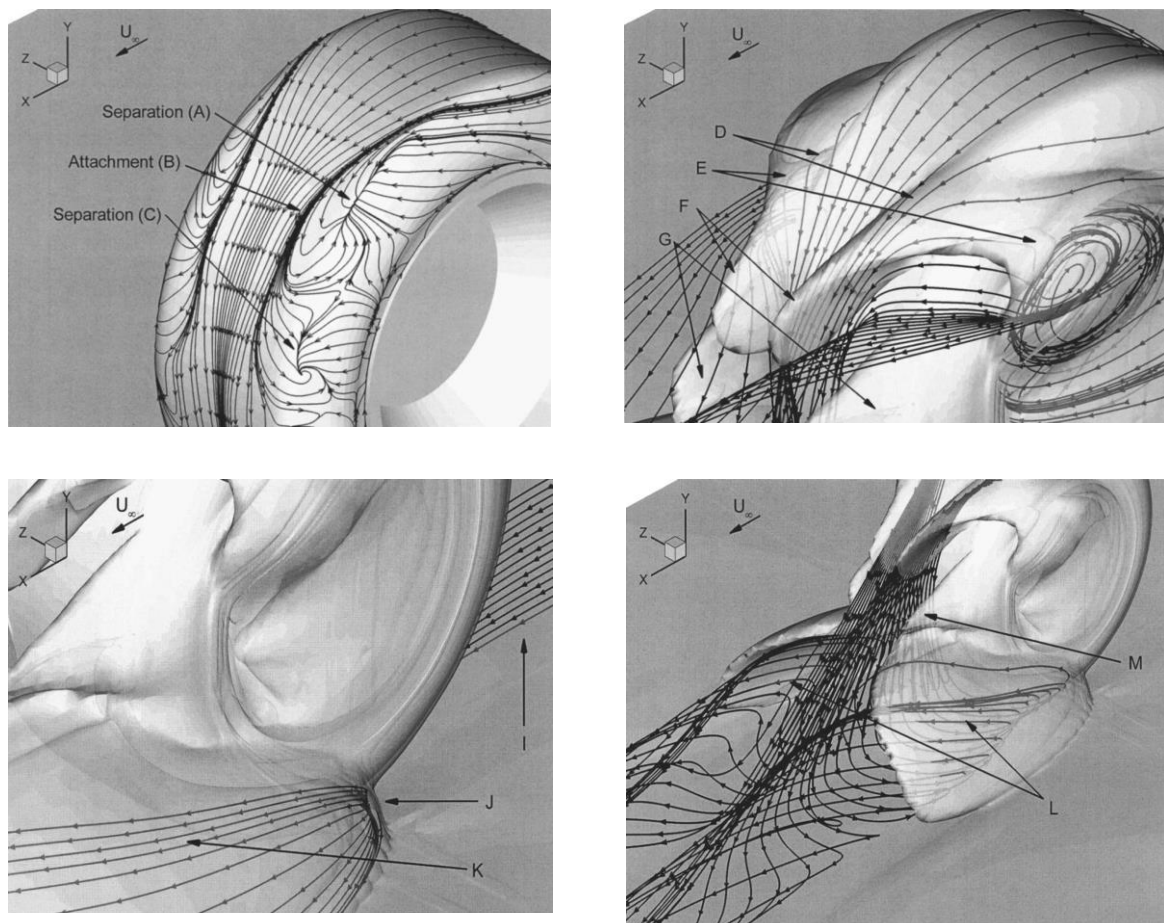


**Figure 31 - Streamlines and iso-surfaces of vorticity magnitude in the rear wake of the stationary wheel [29]**

directed, thereafter, straight down towards the ground. Trailing vortices are also seen when the flow rolls over the wheel edge, in the range of  $10^\circ - 30^\circ$  from the horizontal (G in Figure 31).

Within the hub region, airflow is of a low velocity, with a complex interaction with the main flow traveling from around the sides of the wheel. The results of these interactions were found to form arch shaped shear layers, which extend from the hub cavity to the upper sides of the wheel, forming a subsequent wake region at E. A small circulation that occurs in the separated region (C) is where the rotation in the surface flow appears from.

Large regions of separation were also found on the lower sides, on each side, of the stationary wheel (L) as the flow in front of the wheel is accelerated around the space between the ground and the wheel, causing a high velocity flow to be pushed sideward in front of the line of contact (J). This flow phenomenon is then decelerated after entering the mainstream flow field and is restricted from vertical propagation.

Flow features in this lower region, for the case of a rotating wheel, were found to be similar to the stationary wheel. Comparing McManus & Zhang's [29] findings in this region to that of predicted by Fackrell [22], expectations were that the positive pressure peaks would increase the velocity of the sideward flow from beneath the wheel, increasing the separation region with the subsequent formation of a horseshoe vortex. As this vortex was not found by McManus & Zhang [29], they proposed that this increase in sideward velocity was the result of other oncoming flow interactions. Additionally suggesting, the flow travelling from under

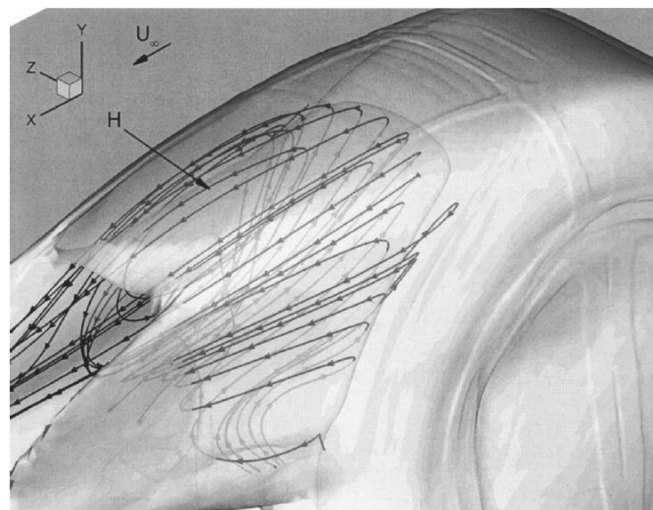


**Figure 32 – Iso-surface of vorticity magnitude on the upper rear wake of the rotating wheel [29]**



the front of a rotating wheel is deflected by the free stream velocity, with the flow travelling from under the front of a stationary wheel deflected by the low velocity boundary layer flow. As a result, the separation region formed around the stationary wheel is constrained less, allowing greater transverse growth than for the rotating wheel case. On the upper rear wake, the flow was observed to separate further towards the top of the wheel, subsequently forming an arch shaped vortex, shown H in Figure 32. This is a result of the attached flow on the rotating wheel, interacting with the separated shear layer on top of the wheel, causing recirculation in the flow.

Perhaps the most fundamental finding from this work and in agreement with others [22, 34], was the generation of a pair of counter rotating longitudinal vortices, formed in the lower near wake of the stationary wheel, from the downwash over the rear surface of the wheel and its interaction and roll-up with the ground. These vortices were shown to extend upstream to cover the near wake region at the rear of the wheel and extend laterally downstream, as they get weaker due to the low momentum and vorticity. These characteristic vortical structures also exist in the rear wake of the rotating wheel case, however for this case they are formed due to the areas of recirculation within the wake of the lower separation region (L).

Other results presented in McManus & Zhang [29] also illustrated surface pressure distributions. As displayed in Figure 33, their results for  $C_p$  were in reasonable agreement with published literature for the stationary wheel, although this agreement deteriorates at the contact patch (illustrating a discrepancy of approximately 4.5 degrees between the CFD & experimental results, Figure 33(a)), as the pressure falls before reaching the stagnation point upstream of the line of contact. Due to the curvature of the wheel on the upper surface, the flow is thereafter accelerated and separates at  $\theta = 232^\circ$  (S-A) or  $\theta = 210^\circ$  (RKE model). From Fackrell's experimental results [22], separation was observed at  $\theta = 210^\circ$ , providing

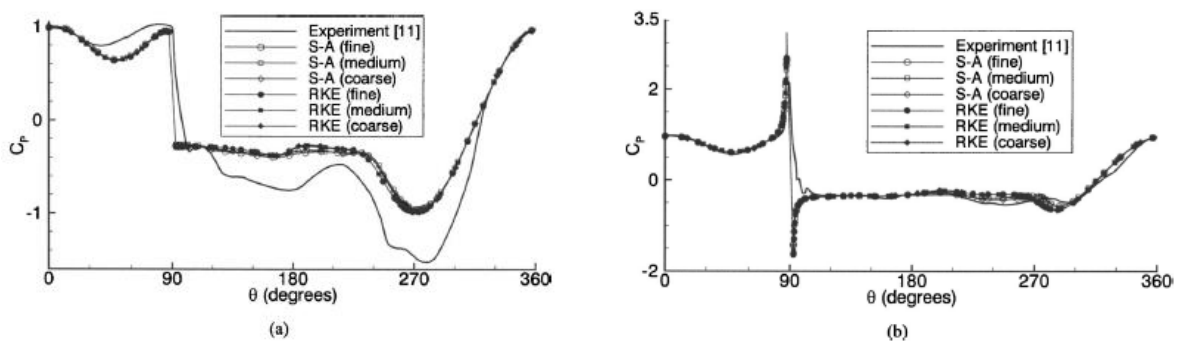
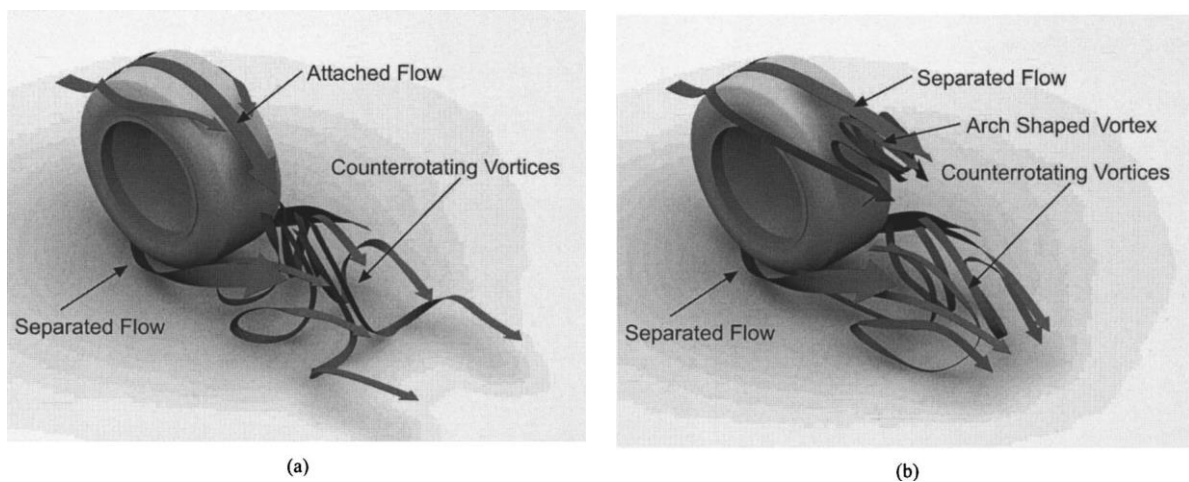


Figure 33 – Comparisons of surface pressure distribution on the centreline of (a) stationary & (b) rotating wheel to Fackrell's [22] experiment. [29]

confidence to the methodology used. Streamlines along the rear surface of the wheel also indicated that separation only occurs near the rear extremity of the wheel, with the flow travelling down the central region of the wheel remaining attached (Figure 31). For the rotating wheel, the experiments from Fackrell [22] indicated flow stagnation below the front of the wheel at  $\theta=5.6^\circ$ , in agreement with the predicted  $\theta = 4.2^\circ$  from S-A & RKE results [29]. For this special rotating configuration, at angular positions closer to the ground, the pressure falls and then reaches a pressure peak at the line of the contact patch. The pressure peak observed is the ‘pumping’ or ‘jetting’ described earlier, created by the boundary layer interaction on the rotating wheel with the moving ground, as McManus and Zhang [29] found pressure peaks 36% higher than that observed from Fackrell’s experiments. The separation position for the rotating case [22] predicted  $\theta = 280^\circ$  experimentally, whilst both S-A & RKE methods found separation to occur at  $\theta = 270^\circ$  and  $\theta = 255^\circ$  respectively; with reasoning by McManus & Zhang [29] suggesting that the slight difference in these results (when comparing to [22]), is due to the fact that the wheel used in the experimental measurements had a 33% difference in width compared to the wheel used in their computational results. Having performed their computational analysis and compared it to some experimental results, Figure 34 shows the proposed computational flow field around both the stationary and rotating wheel configurations. These shows the dominant result presented in McManus and Zhang and separates the fundamental differences in attached flow and central downwash, as well as the arch shaped & counter rotating vortices observed behind the rotating wheel. Comparing force coefficients with [22], McManus & Zhang [29] have found that the forces on the rotating wheel are less than that observed on the stationary wheel, as shown in Figure 35, showing similar results between the two computational methods with agreement to [22].



**Figure 34 – Flow characteristics on general isolated wheel, (a) stationary (b) rotating [29]**

Case	Stationary		Rotating	
	$C_L$	$C_D$	$C_L$	$C_D$
S-A (Fine)	0.349	0.523	0.152	0.475
S-A (Medium)	0.342	0.513	0.146	0.473
S-A (Coarse)	0.346	0.520	0.164	0.467
RKE (Fine)	0.357	0.482	0.156	0.434
RKE (Medium)	0.356	0.483	0.156	0.436
RKE (Coarse)	0.356	0.483	0.160	0.437
Experiment [11]	n/a	n/a	0.28	0.51

Figure 35 - Time-averaged force coefficients from [29] with a comparison to Fackrell's [22] experimental results

Axon et al [38] has also performed work on an isolated wheel in contact with the ground. Using CFD primarily, the wheel was modelled as being deformable through trimming the wheel at the bottom and creating vertical boundaries down to the ground plane. In much the same way as McManus and Zhang [29], the aim of this study was to create a CFD model of a known wheel geometry ('B2' from [22] in this case) so direct comparisons could be made. However, unlike McManus & Zhang [29], Axon et al [38] did not include the hub in this CFD model, which also consisted of a slightly different wheel edge profile when compared to

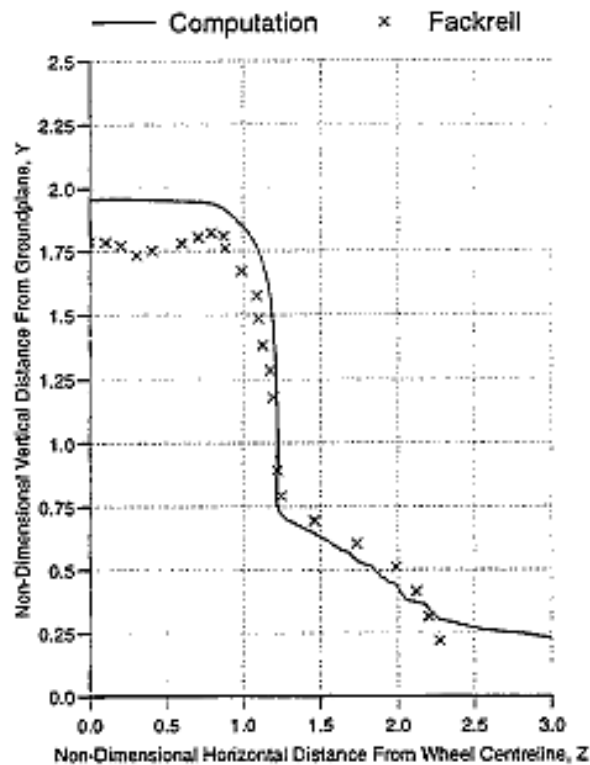
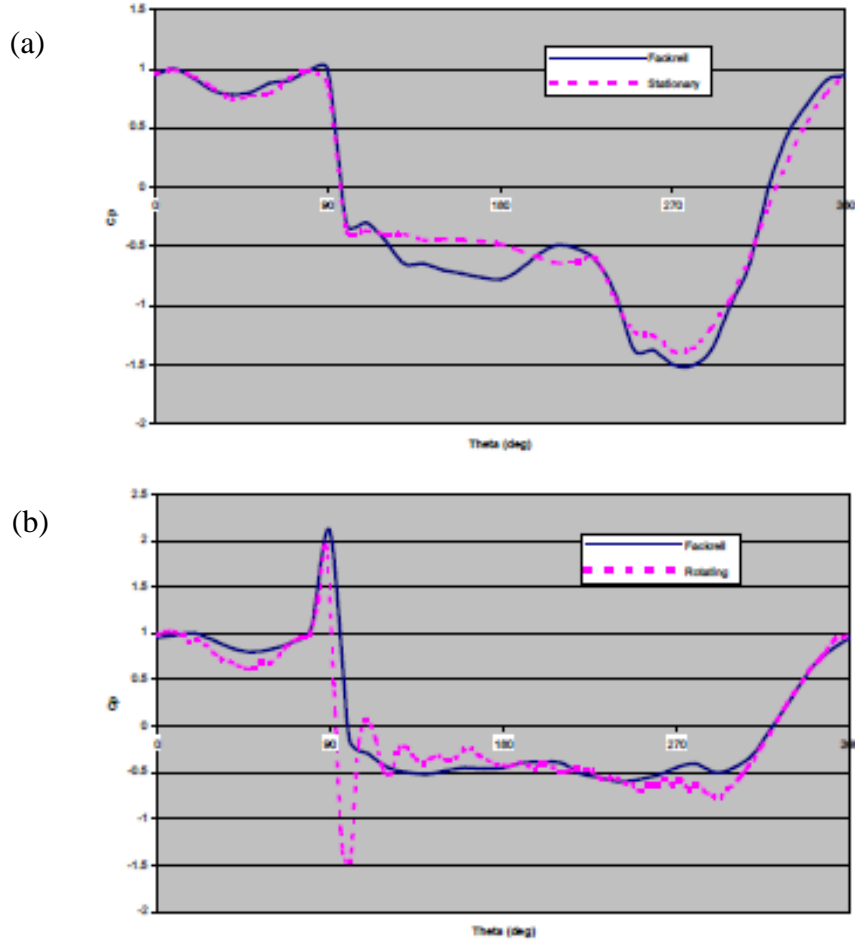


Figure 36 – 90% total head contour behind stationary wheel at a plane  $x = 0.699$  [38]

the ‘B2’ wheel in [22]. For the rotating wheel case, maximum pressure was found on the centreline of the wheel just before the contact patch, with the peak found to be sensitive to grid density. Comparisons of areas of separation at the top of the wheel were found to be poor, with an error of  $\pm 30^\circ$  when compared to the experimental results, and an additional area of poor comparison found on the edge of the wheel. They did, however, assume that this was due to the difference in wheel edge profile, which is known to affect surface pressures substantially. The pressure distribution over the top of the stationary wheel was under predicted; still the general trend was in very good agreement with experimental results in [22]. Wake measurements (Figure 36) also showed a good comparison to [22] near the ground plane. On the upper half of the wheel, the computational wake is seen to be much taller than observed in [22], due to the under prediction of peak pressure over the top of the wheel. With the drag force coefficient for the rotating wheel case being generally in good agreement with the experimental results, lift however, was over predicted by 8.2% and was thought to be due to the slightly later separation point. In general agreement with others [22, 29], the rotating wheel was found to produce less lift and drag than the stationary wheel.

Mears et al [39] also conducted an experimental study to understand the surface pressure and wake physics around a stationary and rotating pneumatic tyre. The wheel chosen was based on a racing car wheel model with an aspect ratio of 0.54, in comparison to Fackrell’s ‘B1’ wheel profile [22]. Overall, the surface pressure distribution along the centreline of the wheel was found to be in good agreement with Fackrell’s work [22], although the base pressure region of the stationary wheel was somewhat under calculated by Mears et al [39], as shown in Figure 37(a), and was thought to be due to differences in wheel edge profile, aspect ratio and Reynolds number. A larger lift force was experienced for the stationary wheel configuration compared to the rotating wheel, which was characterised via a stronger negative pressure peak at the top of the stationary wheel. Generally, surface pressure along the centreline of the rotating wheel, Figure 37(b), agreed reasonably well with [22], showing both similar areas of separation. In agreement with [22], a pressure peak of  $C_p \approx 2.2$  was found within the contact patch region of the rotating wheel configuration in [39], with similar reasoning as already explained for Fackrell [22]. A strong negative peak was found by [39] immediately after the line of contact; and although further investigation regarding this negative peak was suggested to be carried out by [39], this peak was not observed in Fackrell’s [22] experiments, yet his theoretical prediction suggested that this negative peak should exist. Flow separation positions at the top of the rotating and stationary wheel were



**Figure 37 - Centreline Pressure distribution, (a) stationary (b) rotating wheel [39]**

observed at  $\theta \approx 290^\circ$  &  $\theta = 230^\circ$  respectively, and were found to be in general agreement with other work. Pressure contour plots in [39], and illustrated in Figure 38, showed that the wake behind the stationary wheel is lower and wider, than the wake behind the rotating wheel which is higher and narrower, also found by [22], showing that this was due to the earlier separation from the rotating wheel. Vortices in the wake of the stationary wheel were also observed to be stronger than the vortices formed on the rotating wheel, however, the vortices formed behind the rotating wheel were somewhat closer together and higher in vertical position than those found for the stationary case [39] due to an up-wash effect caused by the rotary motion of the wheel. Vortices for the rotating wheel also indicate a weaker rotational velocity in the flow when compared to the stationary case, due to the weaker vortices positioned behind the rotating wheel. Generally two counter-rotating vortices are visible in the lower rear wake of both the stationary and rotating case, with both configurations in agreement with McManus and Zhang [29].

Using the same wheel geometry and model described above, Mears et al [40] also carried out a subsequent investigation to analyse the flow field, specifically around the pneumatic tyre used previously in [39]. Overall, lift and drag measurements showed general agreement to the results obtained by Fackrell [22], showing a decrease in lift and drag for the rotating wheel (from surface pressure distribution:  $\Delta C_D = -0.17$ ,  $\Delta C_L = -0.18$  and from load cell data:  $\Delta C_D = -0.07$ ). Centreline surface pressure distributions were similar to that observed in [39], as the same model was used; however additional pressure tapping locations were added to the wheel in [40]. Surface pressure distributions for the stationary and rotating wheel at the location of tapping 5, indicated that a stagnation region was not seen at this location for either the stationary or rotating wheel as there is a cross flow present across the wheel, due to tapping 5 being located more towards the sidewall of the tyre tread. Local pressure on the rotating wheel decreases to  $C_p \approx 0$  as the flow approaches the contact patch region, before reaching a positive pressure peak of  $C_p \approx 1.2$  upstream of the contact patch (also referred to the ‘jetting phenomenon’ [22]). However, downstream of the contact patch, a pressure distribution similar to that on the centreline of the wheel is observed and was thought to be due to the cross flow not affecting the highly unsteady flow in this area behind the wheel. The pressure distribution at tapping 9, located on the side edge of the wheel, was also analysed and indicated  $C_p$  similar to that expected of the jetting phenomenon, at  $90^\circ$ . The peak was not as extensive as observed on the centreline of the wheel or as discussed previously on tapping 5, and was thought to be because tapping 9 is not in contact with the ground plane, therefore the air that is pushed through between the bottom of the wheel and the ground plane, must travel down the side of the wheel. For the stationary case (Figure 39(a)), accelerated flow is present over the top of the wheel, resulting in a strong downwash (A) with a velocity magnitude of

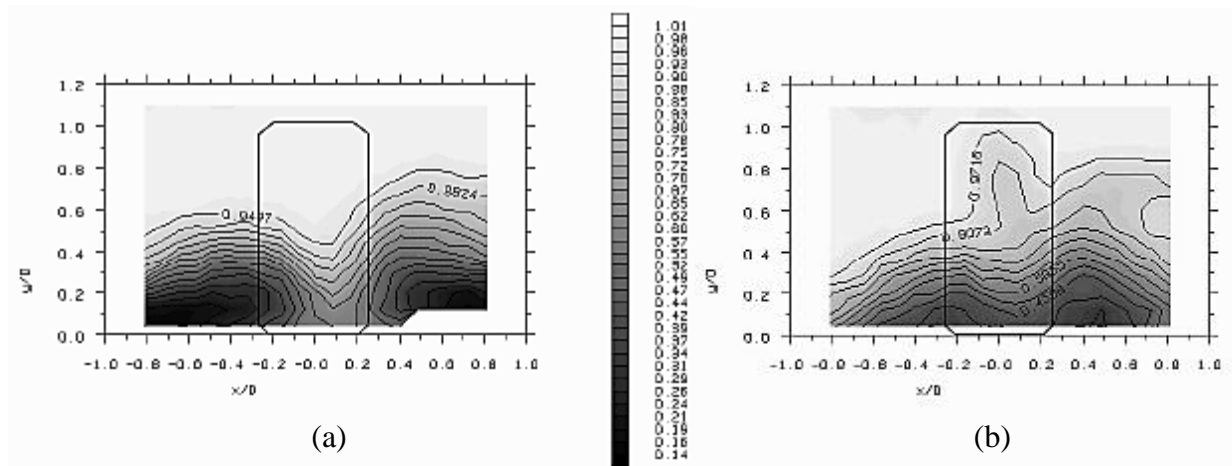


Figure 38 - Pressure contours at  $z = 2.5D$ , (a) stationary (b) rotating wheel [39]

18.5m/s at the back of the wheel, also observed in [29]. Separation was found to occur on the stationary wheel at  $\theta = 225^\circ$ , creating a separated shear layer that rolls up into a vortex in the rear wake of the wheel, resulting in reversed flow characteristics as shown in Figure 39(B). For the rotating case, Figure 39(b), the ‘jetting phenomenon’ can be seen with a slight downwash (C) comprising a velocity magnitude less than 4m/s. Additionally, an up-wash (D) is present due to the air being entrained in the direction of wheel rotation. When analysing the upper rear wake, vector plots on the stationary wheel (Figure 40(a)) show attached flow before separation, subsequently forming a vortex as described earlier. The rotating case, Figure 40(b), shows an earlier separation (E) compared to the stationary wheel (as discussed earlier and shown in all other studies comparing stationary and rotating wheel configurations), thereafter causing recirculation of the flow on the wheel surface (E). Overall, with comparisons made to instantaneous velocity vector plots obtained at different time intervals, it has been suggested by Mears et al [40] that the flow in the rear wake of a stationary wheel appears to be more unsteady than for the rotating case.

With reference to previous work carried out by Mears et al. [39, 40], Mears & Dominy [41] carried out another experimental & CFD study, on the same wheel geometry already used in [39, 40]. Using the  $\kappa$ - $\epsilon$  turbulence model to obtain a steady state solution, an unstructured tetrahedral volume mesh consisting of 3.1 million cells was used for the CFD mesh, with the moving ground and wheel edge peripheral velocity set to 14.7m/s and its equivalent angular velocity, respectively.

Comparing the lift and drag force coefficients to the previous work by Mears et al. [39, 40],

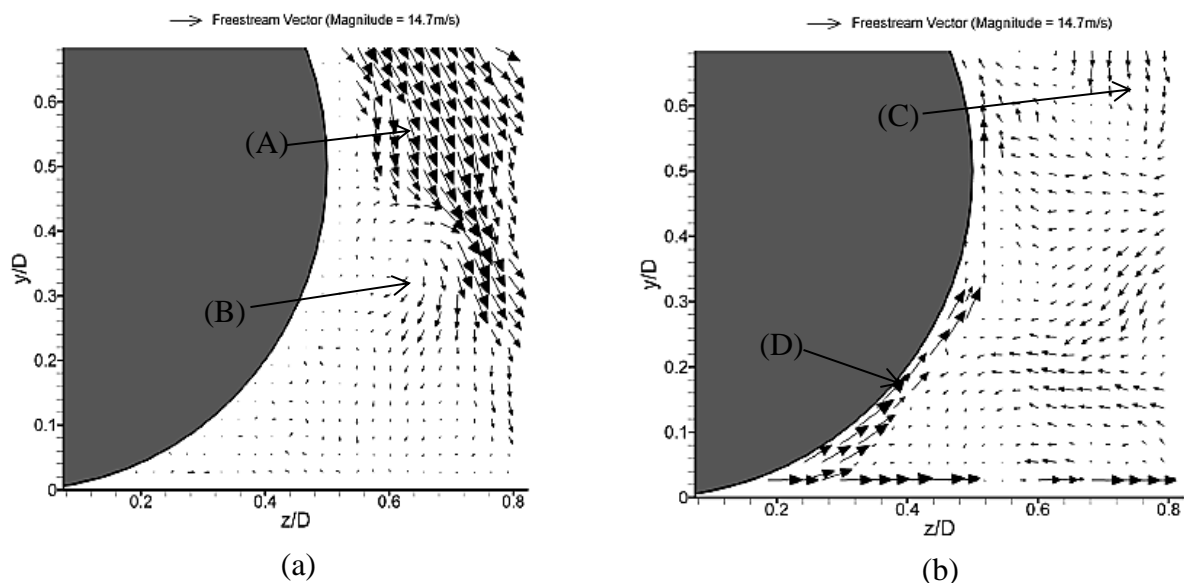


Figure 39 - Velocity vector plot on the centreline of the lower rear (a) stationary (b) rotating wheel [40]

$C_D$  was found to be in good agreement. However, there were differences in results for  $C_L$ , due to the differences in relative separation positions measured and presented by the methods used. Centreline surface pressure distributions taken both, experimentally and from CFD are shown in Figure 41 for comparison. Generally, there is good agreement between the results near the contact patch, indicating a pressure peak of  $C_P = 1.32$ , considerably lower than the experimental pressure peak of  $C_P = 1.9$ . A low pressure peak of  $C_P = -0.6$  &  $C_P = -1.45$  was observed in the CFD and experimental pressure behind the contact patch respectively, with this region of low pressure thought to be due to the presence of the two diverging boundaries of the wheel and the moving ground plane, pulling air out from the contact patch. This observed rear jetting motion opposes the jetting phenomenon discussed earlier at the front of the contact patch, as a suction of air into the contact patch causes a higher pressure peak. Comparing the separation positions for the CFD & experimental results, results for the CFD were at  $\theta \approx 245^\circ$  and experimentally at  $\theta \approx 290^\circ$  respectively. The earlier separation due to the rotation on the wheel observed experimentally, is somewhat in agreement to Fackrell's experimentally measured position at  $\theta = 280^\circ$  [22]. Although separation was computationally observed further downstream on the wheel, a similar result was found by McManus & Zhang [29] when comparing their computationally obtained separation position to [22]. Asymmetry in the wake behind the wheel on the experimental set up was attributed to the support sting, where the wake was observed to be much wider than observed on the CFD results,

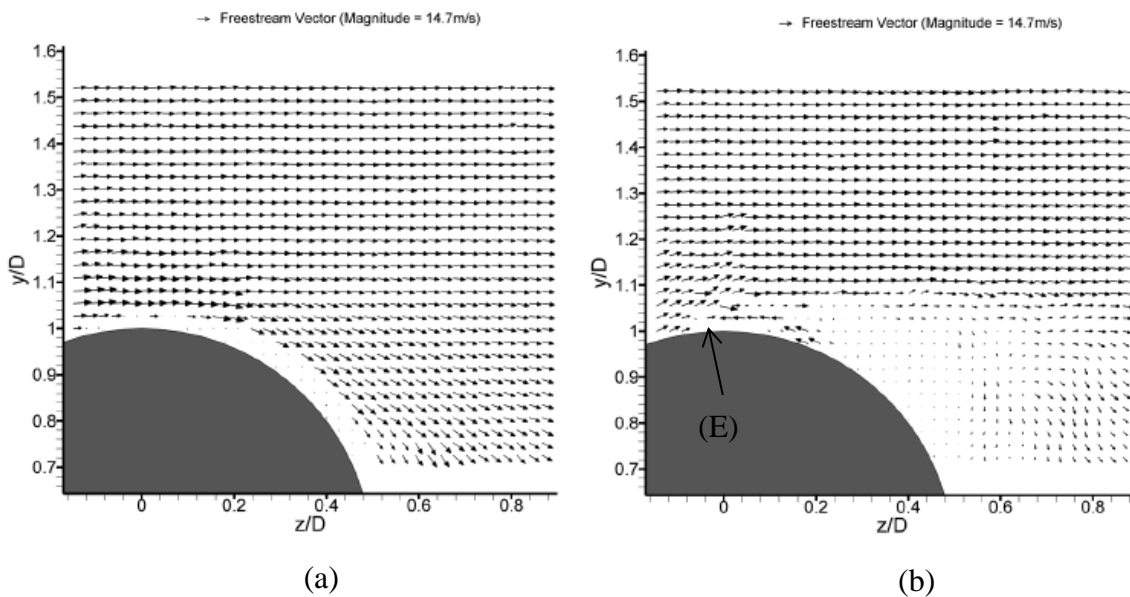


Figure 40 - Velocity vector plot on the centreline of the upper rear (a) stationary (b) rotating wheel [40]



surprisingly; however the pressure gradients across the wakes were in good agreement. Velocity vector plots for the experimental and CFD results were generally in good agreement, although flow vectors were found to differ slightly due to the difference in flow separation positions obtained between the two methods.

Using Fackrell's work, again as a benchmark, Ramachandran & Doig [42] carried out CFD investigations using RANS, URANS, LES and DES on the 'A2' wheel configuration [22]. After carrying out initial simulations using steady state RANS, they found that the 'lip' or 'rim' of the hub had minimal effect on the flow field, deciding thereafter, not to model the 'lip' on their model, to reduce the mesh density and computational expense. The contact patch was also modelled off the surface by 1.2mm to reduce the skewness of the cells in that area. Two structured grids of different densities (3.48 million cells and 6.79 million cells) were created using the STAR-CCM+ grid generation software. However, after a grid refinement study based on lift and drag coefficients, it was decided to use the coarse mesh only, as a small error (1.7% for lift and 2.7% for drag) was present with this mesh, compared to the finer mesh proposed. Free stream velocity of 18.6m/s was used which also corresponded to the peripheral speed of the rotating wheel. Both the RKE model & Kw-SST models were employed for the RANS method, but the RKE was ultimately used as it was decided that this model gave more accurate results. For URANS and DES the KW-SST &

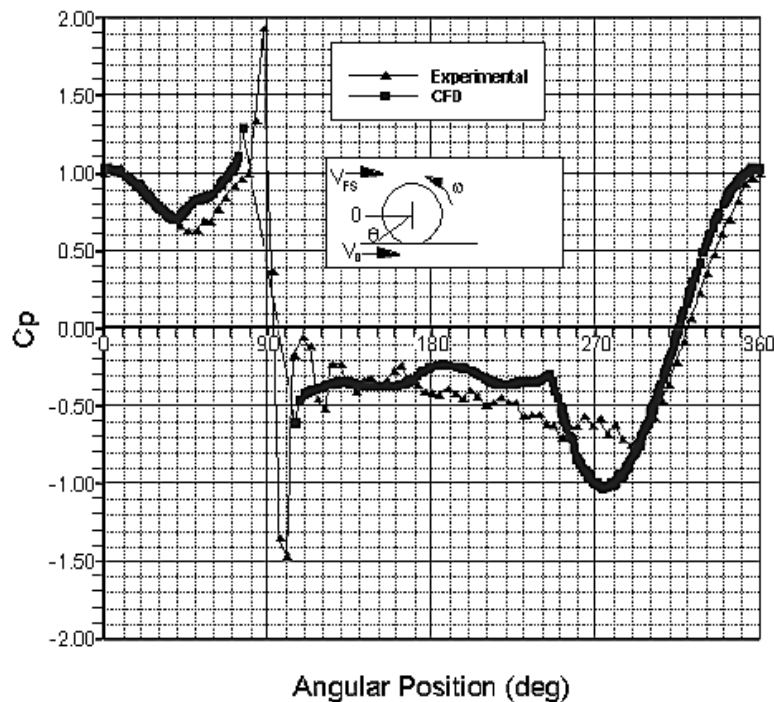
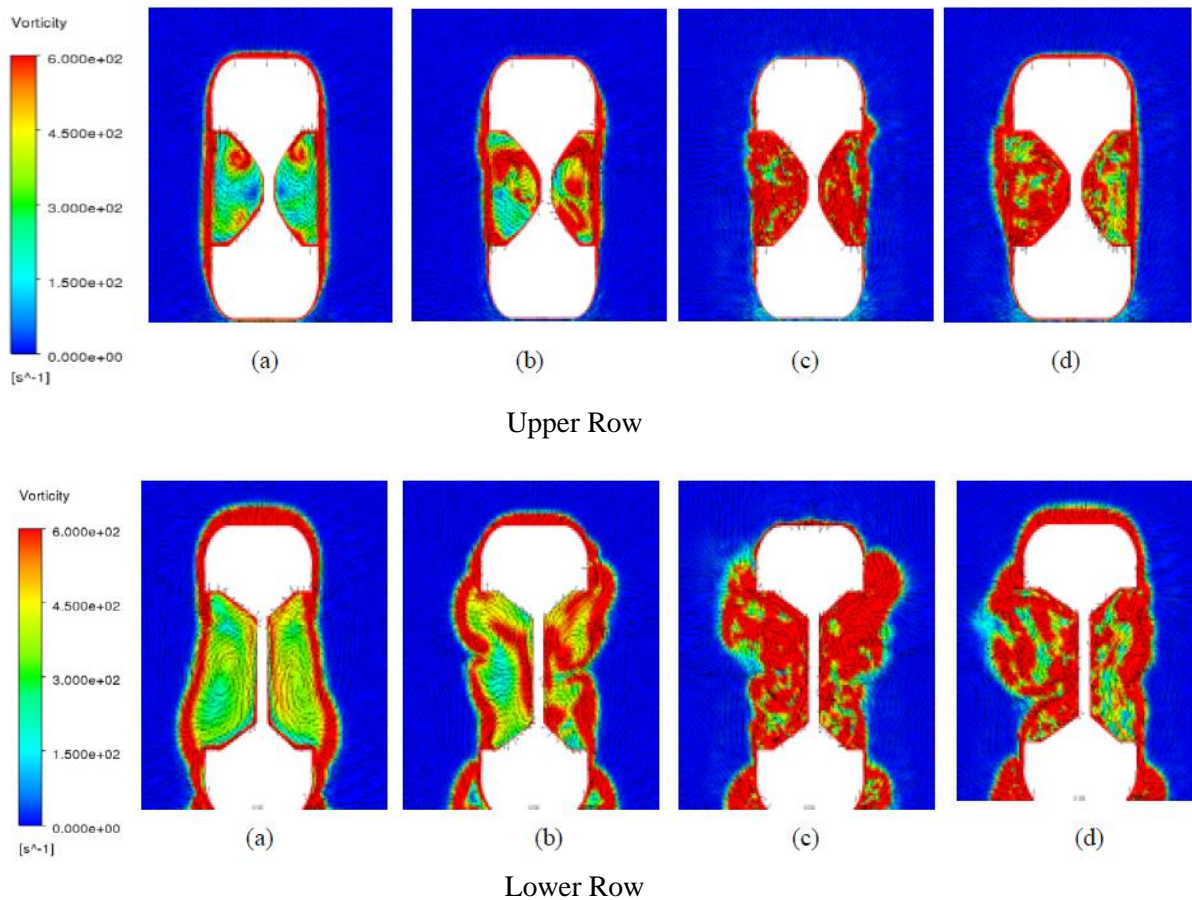


Figure 41 – Centreline Pressure distribution, experimentally [40] & CFD, [41]

Spalart-Allmaras models were used respectively. Overall, the centreline pressure coefficient for all simulations, under predicted the pressure peak at the contact patch when compared to Fackrell's  $C_p$ , with this difference attributed to how well the contact patch was modelled through the geometry and grid resolution. Base pressure behind the wheel was found to be within the range  $-0.5 < C_p \leq -0.1$ , and well predicted by all methods, however differences occurred at areas of separation with the different CFD models used. RANS, URANS & DES predicted separation to be within Fackrell's experimental range of  $\theta = 280^\circ$ - $290^\circ$ , at  $290^\circ$ ,  $289^\circ$  &  $293^\circ$  respectively, with corresponding pressure coefficients of  $-0.41$ ,  $-0.6$  &  $-0.38$  respectively, to Fackrell's  $C_p$  of  $-0.5$  at his measured separation location. LES predicted separation further downstream at  $\theta = 275^\circ$ , with  $C_p = -0.94$ . These variations in  $C_p$  & separation locations indicate the necessity for LES to have a much larger grid resolution within the boundary layer. Drag force coefficients measured, were in good agreement with each other resulting in the range of  $C_D \approx 0.61 - 0.68$ , with the anomaly of  $C_D \approx 0.52$  from the steady state RANS, indicating that it may not be suitable to model an unsteady flow field



**Figure 42 – Vorticity plots for (a) RANS (b) URANS (c) LES (d) DES; upper row:  $z/d = 0.22$ , lower row:  $z/d = -0.04$  [42]. Flow travelling towards  $-z/d$ .**

using a steady state solver. Lift coefficient showed values, for the sRANS, URANS, LES & DES models, at  $C_L \approx 0.07, 0.19, 0.28$  and  $0.1$  respectively, with the largest value observed by the LES method thought to be caused by the much later separation position. The jetting phenomenon on a rotating wheel proposed by Fackrell [22] is clearly seen in [42], showing the separation location adjacent to the surface of a rotating wheel, with the rotation of the wheel causing a strong shear flow to travel in the opposite direction. Vorticity contour plots from Ramachandran and Doig [42] (Figure 42), show the pair of upper hub vortices found in the investigation by McManus & Zhang [29], with symmetry on each hub; however, URANS solutions predicted the vortices being located more towards the centre of the hub, with the LES simulation indicating much more mixing within the hubs. Further downstream from the centreline of the wheel, Figure 42 (lower row), the flow has developed to displace towards the centre of the hub, what was referred to as a ‘blow out’ effect. Another difference in the flow field observed near to the ground plane was the increased levels of vorticity, resulting in a wider wake apart from the steady state RANS. The flow is dispersed after interacting with the contact patch, with separation further downstream the wheel using the LES method. From Figure 43, wake physics predicted by LES was found to be shorter than the wakes obtained by the other three methods, with the ‘blow out’ effect found to affect the upper wake. For the URANS & LES simulations, a larger ‘blow out’ region, corresponding to the wider upper wake downstream on both sides of the wheel can also be seen, whilst vorticity levels on the DES was observed to be smaller corresponding to a weaker upper wake. Overall, the authors were able to identify the deficiency in using the steady state RANS solver, as the URANS, LES & DES methods, provided a better understanding of the flow field in the unsteady wake region behind a wheel.

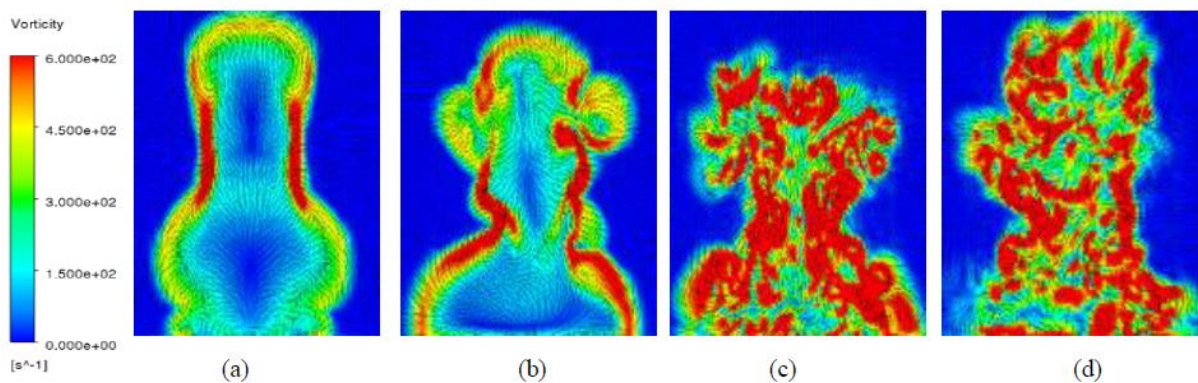
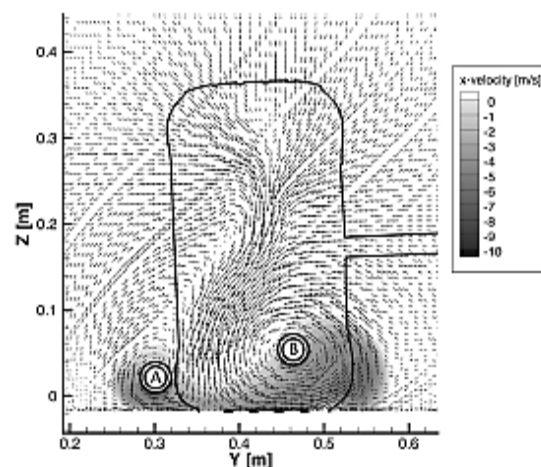


Figure 43 – Vorticity plots at  $z/d = -0.52$ , for (a) RANS (b) URANS (c) LES (d) DES from [42]. Flow travelling towards  $-z/d$ .

A 60% scaled isolated rotating formula 1 wheel has also been used to investigate wake physics of a wheel in contact with the ground [30]. As all previous studies that have been to date, carried out on idealised wheels without the effect of modelling the tyre tread, Axerio-Cilies & Iaccarino [30] presented work which included this influence. Four wheel geometries were tested; a simplified wheel geometry with wheel fairings; a full wheel geometry with outer ducts, inner passages and brake assembly; a full wheel geometry with exterior brake ducts and spokes; and simplified wheel, with a Reynolds number of  $5.0 \times 10^5$  based on wheel diameter (0.3948m). These four geometries were denoted CI, CII, CIII and CIV respectively. Both experimental and CFD investigations were carried out at a free stream velocity of 18.4m/s in a wind tunnel fitted with a moving belt. CFD simulations were carried out using hybrid structured-unstructured grid containing tetrahedral cells in the boundary layer, with hexahedral cells extending further out to the far-field domain (mesh sizes from 9 - 27 million cells). As already discussed from earlier work, results also indicated a counter rotating vortex pair dominated the rear lower wake behind the rotating wheel, which in agreement with McManus & Zhang [29], were found to originate from the front of the contact patch, due to the ‘jetting’ phenomenon. Generally, the wake was also found to be narrower and taller, with a larger area of recirculation behind the wheel compared to a stationary wheel. This is also observed in other studies [22, 39], and was a result of separation occurring on top of the rotating wheel compared, to the further downstream separation position expected on a stationary wheel. This flow mechanism also forms two vortices at each shoulder of the tyre. The influence of the support sting and wheel camber was also found to import a degree of asymmetry in the rear wake at  $x/d=1.14$ , (Figure 44), generating a larger vortex on the right side (B) with the downwash region translating from right to left.



**Figure 44 - Time-averaged URANS velocity vectors at  $x/d = 1.14$  in the wake of CI wheel configuration [30]**

From comparisons of the experimental PIV measurements (CII configuration), to results from CFD, the upper two vortices (C, D) were found to be in the same location and of the same intensity in both results, Figure 45. The strong left vortex of the counter rotating vortex pair was found to overpower the right vortex, dominating the lower wake region. The downwash region was observed to be pushed towards the right side and then towards the centre of the tyre as it propagates further downstream. This was thought to be due to the cross flow of air moving towards the centreline of the tyre entrained by the top left vortex.

As this configuration was modelled with the brake duct (Figure 46), the brake duct was found to ‘inhale’ a lot of the air forming a low pressure region, hence a stronger cross flow (B). As the air exits near the top of the right side of the hub (C), a strong asymmetric recirculation occurs resulting in a strong downwash (D) towards the right side of the wheel, as the vortex on the left dominates the majority of the rear wake (A). Nearly all the turbulence models used for this comparison over predicted the intensity of the lower left vortex, apart from the unsteady RKE model which found the cross flow to reduce the vortex intensity, observed through comparison to the experimental PIV data. The steady and unsteady RKE models, predicted the separation at the top of the wheel to be at  $\theta = 270^\circ$ , corresponding directly to their measured experimental separation location at  $\theta = 270^\circ$ . The stagnation region was also found to be equally well predicted, at  $\theta = 6^\circ$  (using both the RKE models compared to the experimental set up). As this study was the first study to publish the pressure change along the tread of the tyre on a fully loaded racing wheel, the addition of modelling the tread and the load was found to have a significant effect on the contact patch. They found that the

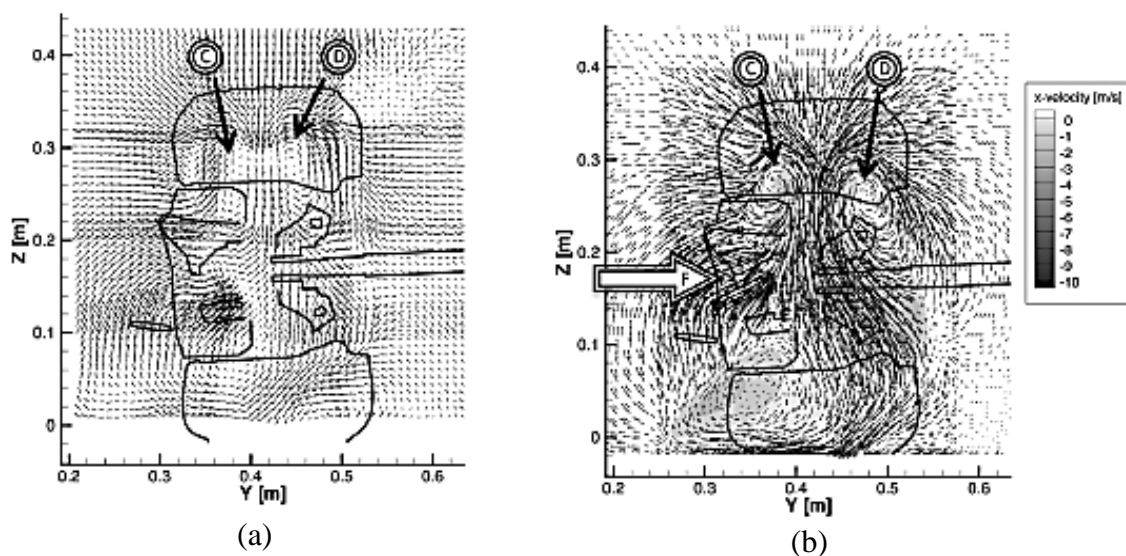


Figure 45 - Velocity vectors in  $x/d=0.57$  plane in the wake of CII wheel configuration, (a) PIV (b) CFD [30]

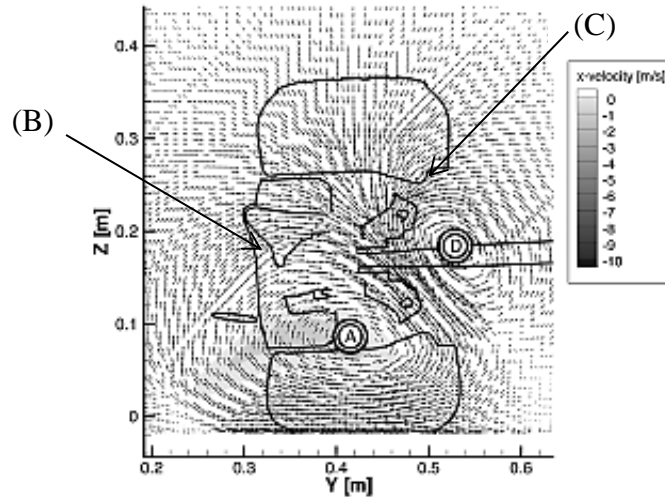


Figure 46 - Time-averaged URANS velocity vectors in  $x/d=1.14$  plane in the wake of CII wheel configuration [30]

negative pressure peak, also observed by previous authors, on the ‘rotating wheel has approximately 12% less drag, 72% less upward lift and 50% less side force compared to a stationary wheel’ [30]. Figure 47 indicates the flow pattern along the centre plane of the wheel with streamwise velocity profiles. At the front of the wheel, as the stagnation region is approached, the increase in pressure causes the flow to decelerate. The formation of the shear layer causes the air to slow down, as it flows over the top of the tyre. At the top of the wheel, a negative streamwise velocity, results in the formation of the arch-shaped vortices, confirmed by McManus & Zhang [29]. Further downstream, the streamwise velocity appears to merge with the free stream velocity.

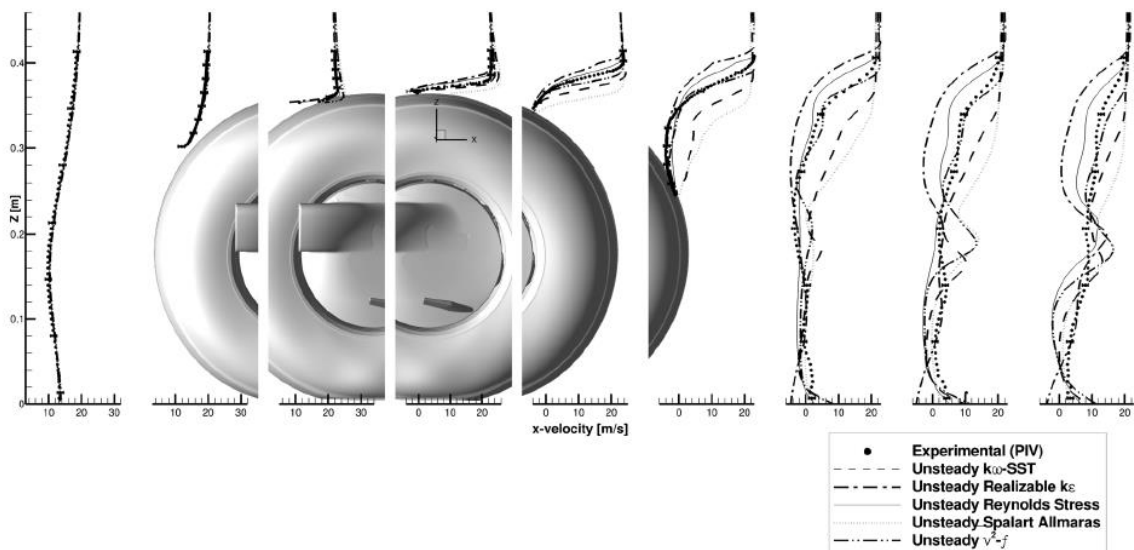


Figure 47 – CII streamwise velocity profiles for centre plane from experimental and CFD URANS simulations [30]



Overall, by investigating the flow field around a wheel configuration corresponding to real world conditions with the inclusion of tyre treads, the existence of the pair of counter rotating vortices was confirmed and found to be asymmetric, due to the air travelling through the hub creating a cross flow, which ultimately reduces the intensity of the vortex found on the right side of the wheel. From the six different turbulence models tested, the KW-SST model was closest at determining the experimental vortex core locations; however if the velocity fields from each turbulence model were translated so that the co-ordinate origin of each simulation lies on a particular vortex core, the RKE model was found to be most accurate at predicting the strength and intensity of the vortices. The inclusion of modelling the treads on the wheel, as well as on the contact patch geometry, was also found to affect the drag by up to 3%.

Saddington et al [10] also carried out Laser Doppler Anemometry (LDA) measurements in the near wake of an isolated formula one wheel rotating in contact with the ground, with a free stream velocity and Reynolds number of 30m/s and  $6.8 \times 10^5$  respectively. Measurements taken at various streamwise locations also showed a near wake consisting of two lower ground vortices and one central region of recirculation, as illustrated in Figure 48.

From these results, the size of the two lower vortices also indicated asymmetry due to the presence of the support sting, as was also found in [30]. Four regions of vorticity were clearly visible in their results, with line integral convolution images at  $x/d = 0.6$ , presented in Figure 49(a), showing two upper and lower vortices, with the upper two vortices dissipating quickly and merging with the two lower vortices slightly below the horizontal centreline of the wheel

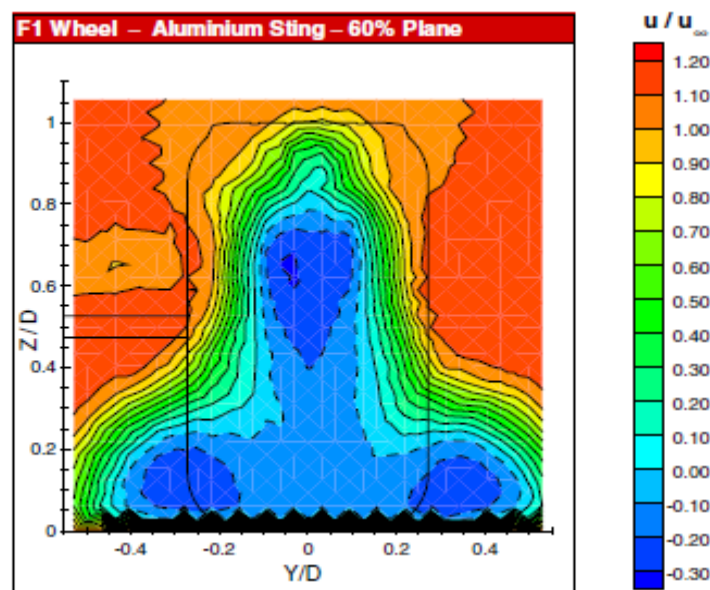


Figure 48 – Contours of mean streamwise velocity at  $x/d = 0.6$  [10]

by  $x/d = 0.75$  (b). All four separate vortex positions were found within the projected area of the wheel outline and separated by a central downwash region.

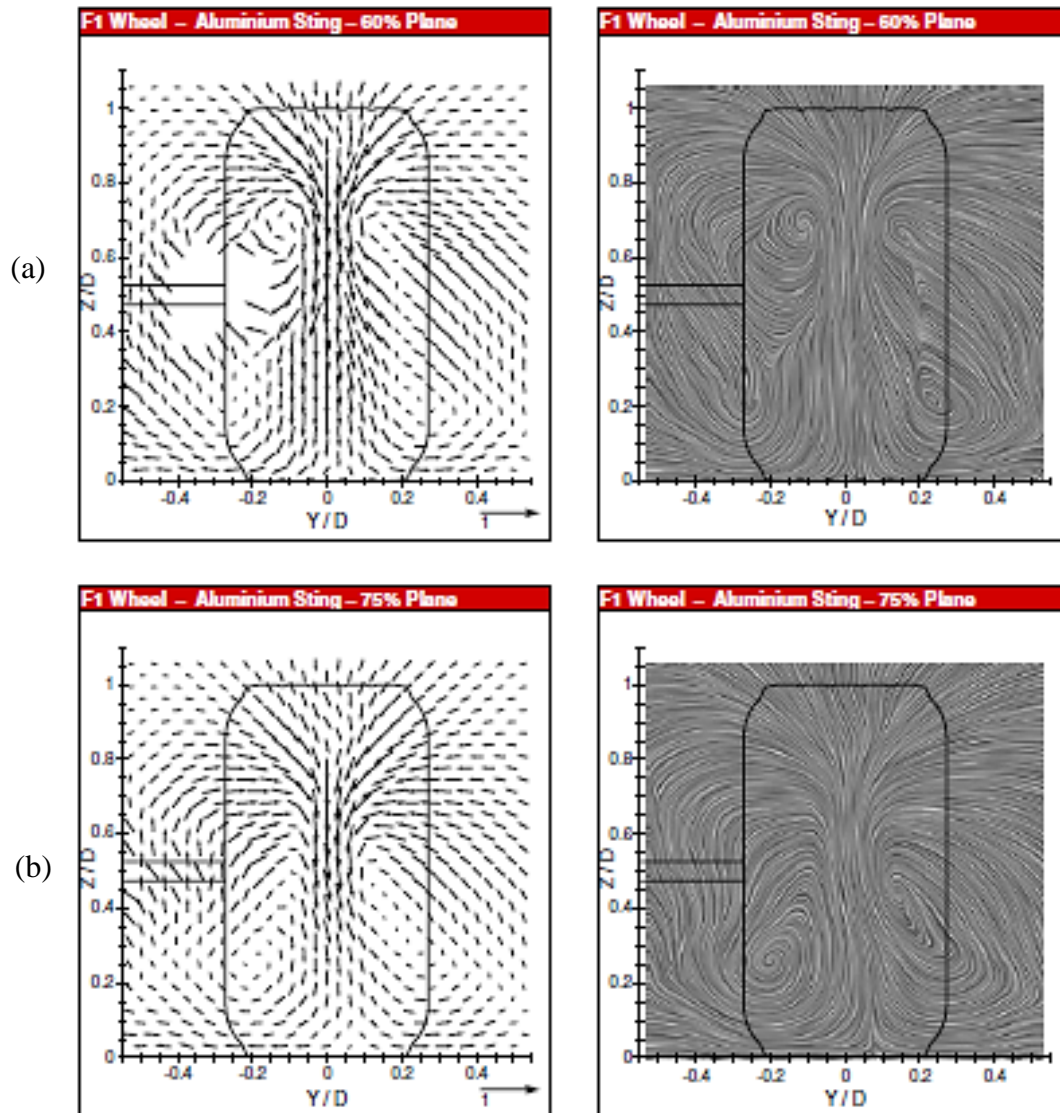


Figure 49 – Velocity Vectors (left) & line integral convolution image (right) from [10]

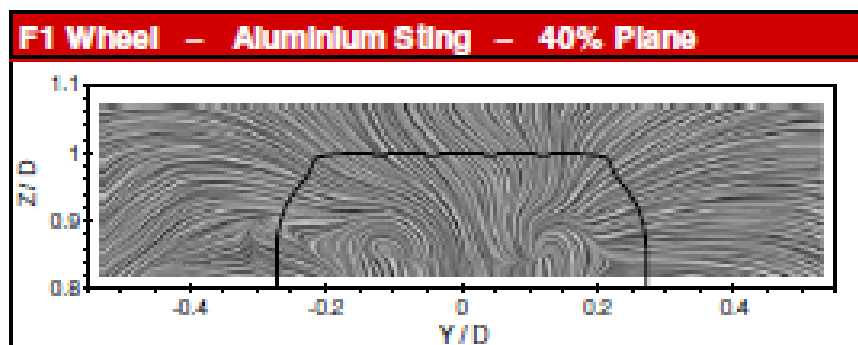


Figure 50 – Line integral convolution image from [10]



Measurements were taken on a plane intersecting the wheel, at  $x/d = 0.4$ , in an attempt to identify the origins of the two upper vortices. Results presented in Figure 50, clearly show the origins of the two upper vortices at the top of the wheel, positioned within the projected wheel outline, suggesting that they are formed immediately downstream of flow separation and roll up around the shoulders of the wheel.

In a subsequent investigation, Knowles et al [43] investigated how the presence of a formula one car affects the wake behind a formula one wheel. LDA was used, with measurements taken in two planes downstream of the wheel at  $x/d = 0.75$  &  $x/d = 1$ , under the same condition as used in [10]. Streamwise velocity contours obtained from the two planes behind the wheel showed the effect the car has on the wake, Figure 51. With the car present, the

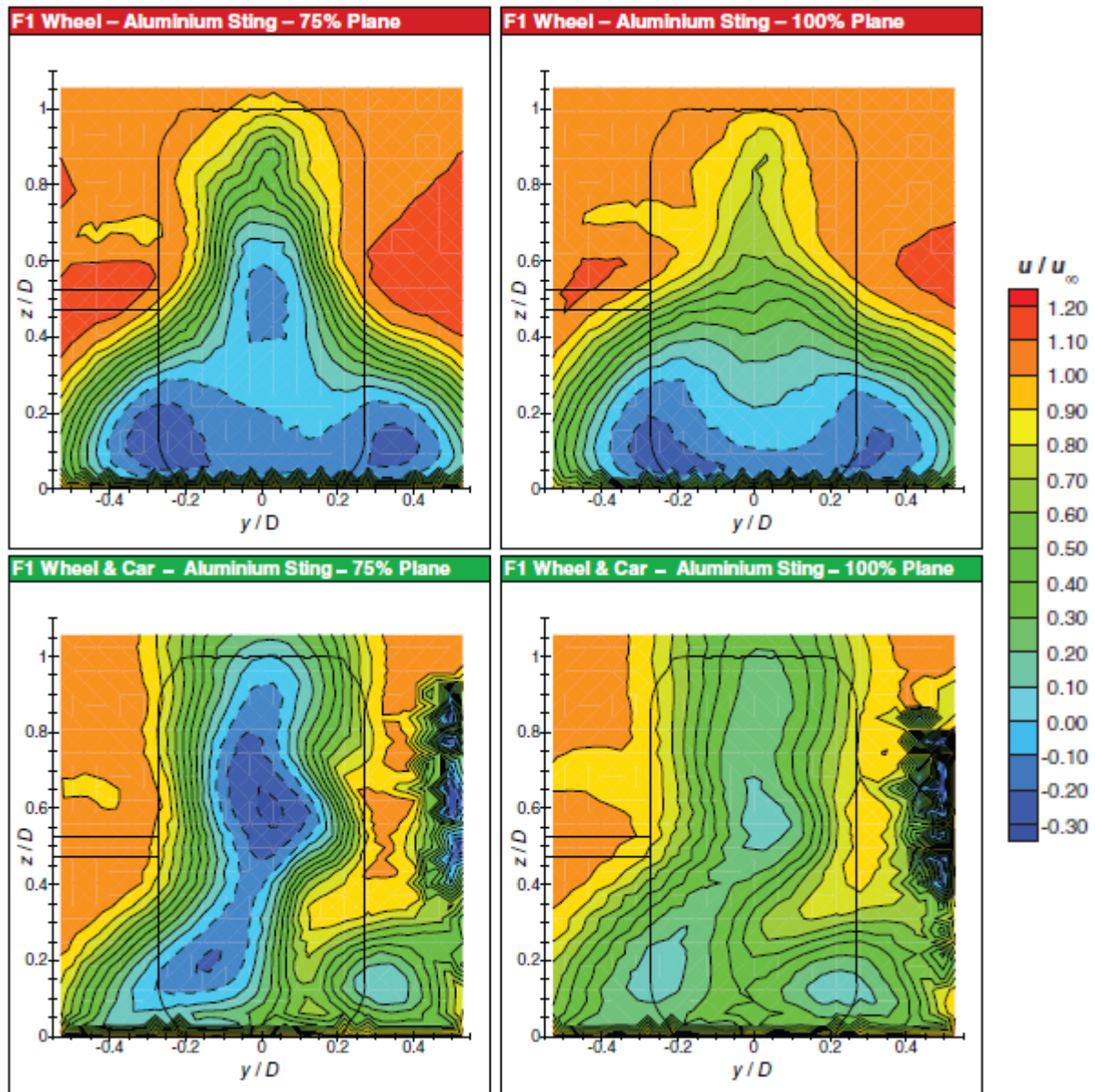


Figure 51 – Contours of mean streamwise velocity at  $x/d = 0.75$  and  $x/d = 1$  [43]

wake is taller, indicating separation occurs further upstream on the wheel when modelled with the car. Areas of recirculation (indicated by the dashed lines) in Figure 51, are shown to be affected by influence of the car. The central region of recirculation observed in the wake behind the isolated wheel was thought to be due to the entrainment of flow into the region by the upper vortices. However, with the inclusion of the car, the central wake region was replaced by a strong recirculation, spanning the central vertical axis, within the projected wheel outline. The downwash, initially observed for the isolated wheel case, has been replaced by a ‘side wash’ directed towards the centre of the wheel, also observed in [30], creating the low velocity reversed flow due to the earlier separation, reducing the entrainment effect, as the two upper vortices observed on the isolated wheel case are no longer visible with the car present. However with the influence of the car, a single smaller trailing vortex

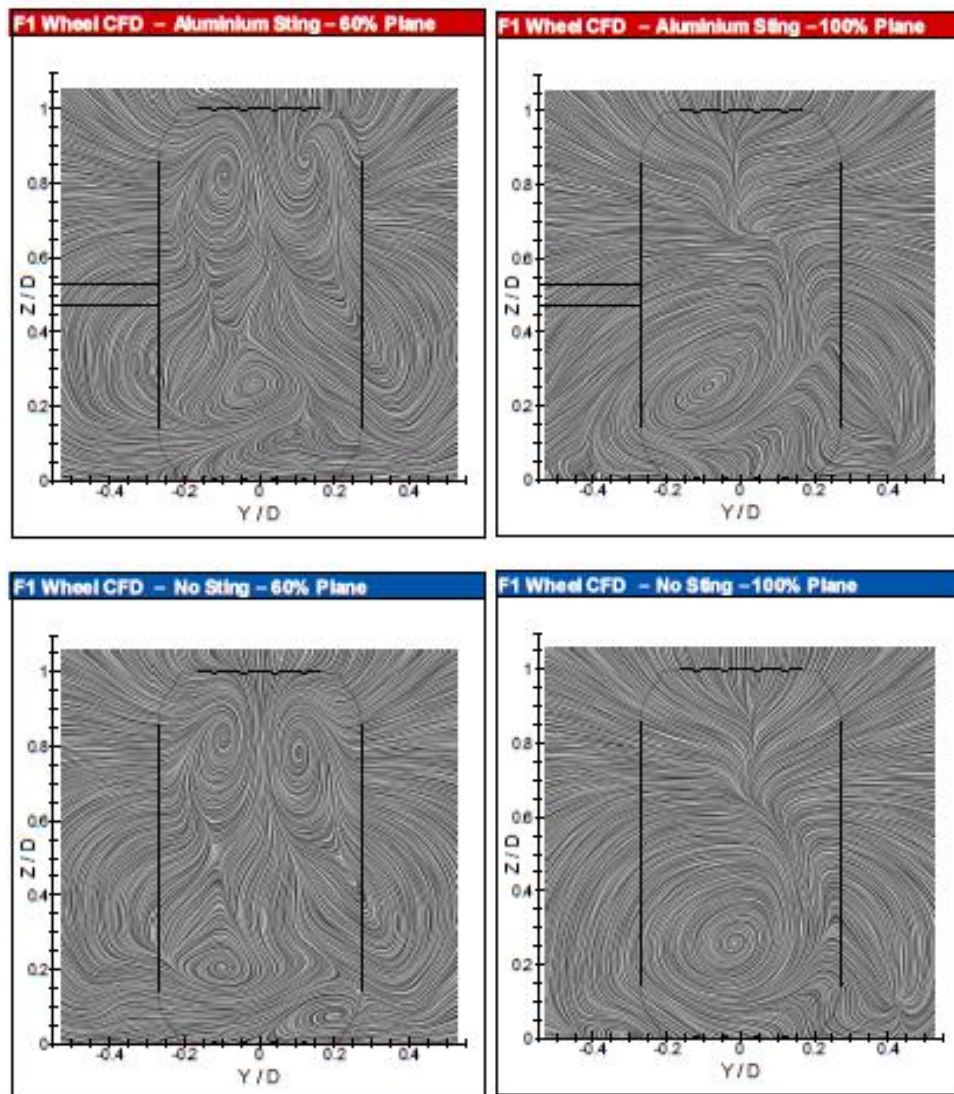


Figure 52 – CFD Line integral convolution images at different planes downstream F1 wheel with & without sting from [31]

appears on the bottom right of the wheel. Although the origins of the vortices, behind an isolated wheel, had been shown to be within the projected profile of the wheel in [30], the smaller vortex observed on the lower right has its origin just outside of the profile, leading the authors to speculate that this vortex was not generated from the wheel. This assumption was reinforced by the work carried out by van den Berg [44], as this vortex was on the likely path of the front-wing end-plate vortex. Therefore, overall analysis of their results showed that the recirculation regions in the rear wake of a wheel, with the influence of the car, occurs along the vertical axis as opposed to the streamwise axis for the isolated wheel case; also showing that the car body has a strong interference effect on the wheel wake flow.

Knowles [31] subsequently described the findings of these results in more detail and also conducted a computational investigation to make flow-field comparisons. The computational method involved modelling the wheel and the support sting, using a grid size of 1.5 million cells with the wheel modelled in contact with the ground. The grid, which consisted mainly of tetrahedral cells, was simulated with a ground plane given a moving wall boundary condition comprising a free stream velocity of 30m/s. Using the RANS standard k- $\omega$  model, simulations were run until the monitors of drag, lift and mass flow rate reached a convergence criteria of up to three orders of magnitude, with first order schemes used to stabilise the flow before switching the simulation to the second order schemes, in a similar methodology to [30]. From the results in [10, 43], generally, good agreement was observed between the experimental and computational results. Centreline velocity profiles were, in general, well correlated though the asymmetry observed in the near wake from the experimental results was found to be less prominent in the computational results. Overall, the computational results under predicted the centreline streamwise velocity at  $z/d > 0.25$  and over predicted the centreline streamwise velocity at  $z/d < 0.25$ , when compared to the experimental results. Comparison of the near wake for changes in streamwise velocity magnitude between the CFD & experimental data, suggested that the major difference between the two results was the prediction of the reversed flow regions on the bottom of the wheel (initially seen by the two blue low velocity regions in Figure 48), with the CFD results capturing two upper vortices (Figure 52). Further downstream, the upper vortices were found to merge into the general wake structure, forming a large area of reversed flow behind the wheel. This enhanced the increasing skewness of the central downwash as the flow propagated downstream, as well as reducing the asymmetry in the planes further downstream. Pressure coefficients obtained computationally were also compared to work carried out

experimentally by Hinson [45], who had obtained pressure data on a similar configuration. The centreline surface pressures were in very good agreement, with pressure peaks being observed upstream and downstream of the contact patch and showing flow separation in the region  $\theta \approx 270^\circ$  &  $\theta \approx 295^\circ$  (upstream from the top of the tyre), for the experimental and computational results respectively. One major difference was that the CFD base pressure was predicted slightly lower ( $\Delta C_P \approx -0.5$ ) than observed in the experiment. This pressure data showed a similar trend to the pressure data obtained by McManus & Zhang [29], although lower peak values of  $C_P \approx 2.1$  &  $C_P \approx -1.3$  (upstream and downstream respectively) were found at the suction region near the contact patch.

MacCarthy [12] has studied the aerodynamic effects on exposed racing car model wheels. Experimental tests were carried out in both water and in air, with solid and pneumatic wheel diameters ranging from 0.2-0.327m, corresponding to a range of aspect ratios from 0.38 - 0.61, at a  $Re \approx 4.7 \times 10^5$ . Results of the stationary and rotating wheel in contact with the ground in the water, shows the ‘jetting’ action previously observed by authors. The rotating wheel shows a more unsteady flow field than the stationary wheel, with large clusters of dye, representing vorticity, found on the rear surface of the rotating wheel, due to the earlier separation of the flow causing a low velocity wake to propagate downstream from that region. Two small clusters of dye were also found in the upper rear corners of the stationary wheel and were thought to be due to a pair of upper vortices being present, however, the central clustered region observed on the rotating case, was not present on the stationary case.

PIV results obtained in the rear wake of the 38% pneumatic tyre, showed the dominating two upper shoulder counter rotating vortices originating from the shoulders of the wheel. Two weaker vortices are also seen on the lower region of the rear wake. With PIV data being obtained further downstream in to the wake, it was shown that, at a data plane 1.5D downstream, the upper two vortices merge with the two lower vortices at around the wheel mid-height. At up to 4D downstream, the weaker lower vortex pair, had shown to deteriorate at a slower rate but was still perceptible. Symmetry in the rear wake was observed up to a distance of one diameter downstream of the wheel; however after this region, the positive circulation of the vortical structures was evidently higher than the negative circulation, which was confirmed in the PIV data obtained 2.5D downstream, showing a highly skewed flow characteristic towards the bottom right of the wheel (when looking directly behind the wheel). A suggestion for this resulting asymmetry was the presence of the support arm.

MacCarthy [12] also investigated the influence of wheel yaw. Four yaw angles of  $\pm 6^\circ$  and  $\pm 2^\circ$  were applied to the wheel, with vorticity in the near wake of the wheel yawed at  $-6^\circ$  indicating the most dominant feature to be a shoulder vortex, located at the upper right corner of the wheel. The central downwash was also found to be highly skewed in that region with these findings being similar to the wheel yawed at  $6^\circ$ , but with wake characteristics skewed to the opposite side to the findings at  $-6^\circ$  yaw. Velocity magnitude plots for all three angles in the positive yaw direction are shown in Figure 53. It is evident, that as the yaw angle increases, the velocity of the downwash is reduced with results further downstream showing the larger region of circulation present on the right side, as the vortex decays slower than observed on the right. A larger drag force was also found with the larger yaw angle due to the flow being more likely to separate in the adverse pressure gradient on the leeside, resulting in a larger wake and lower base pressure. The effect of covering the hubs had also shown to reduce the overall drag on a rotating wheel, as the flow remains attached on these surfaces travelling in the same direction as the flow. Velocity vector contour plots obtained of the flow field with the hub covers on and off, shows a larger lateral spread of velocity vectors indicating an increase in wake size, which also corresponds to an increase in drag force. The reduction in peak vorticity, at higher yaw angles, on the upper rear wake indicating weaker upper vortices was suggested to be the reason a lower lift force was experienced with increasing yaw angle. Results of drag coefficients obtained for different configurations are shown in Figure 54, and shows the immediate reduction in drag by up to 24% by sealing the hub cavities. Direct comparisons were also made to Fackrell's 'B2' wheel [22] ( $C_D = 0.58$ ). Although the wheel used in both investigations were of the same aspect ratio and wheel edge profile, the design of the central hub was reported to be the reason for the difference in drag, as Fackrell's hub was solid and smooth as opposed to the spoked design used in [12], resulting in the change in drag coefficient to  $C_D = 0.63$ .

However, the configuration with the 'spokes blocked' was thought to be the most similar configuration tested, when compared to Fackrell's wheel, therefore, analysing drag coefficients (Fackrell's B2 wheel:  $C_D = 0.58$  and Spokes blocked:  $C_D = 0.59$ ) showed that the results are in good agreement.



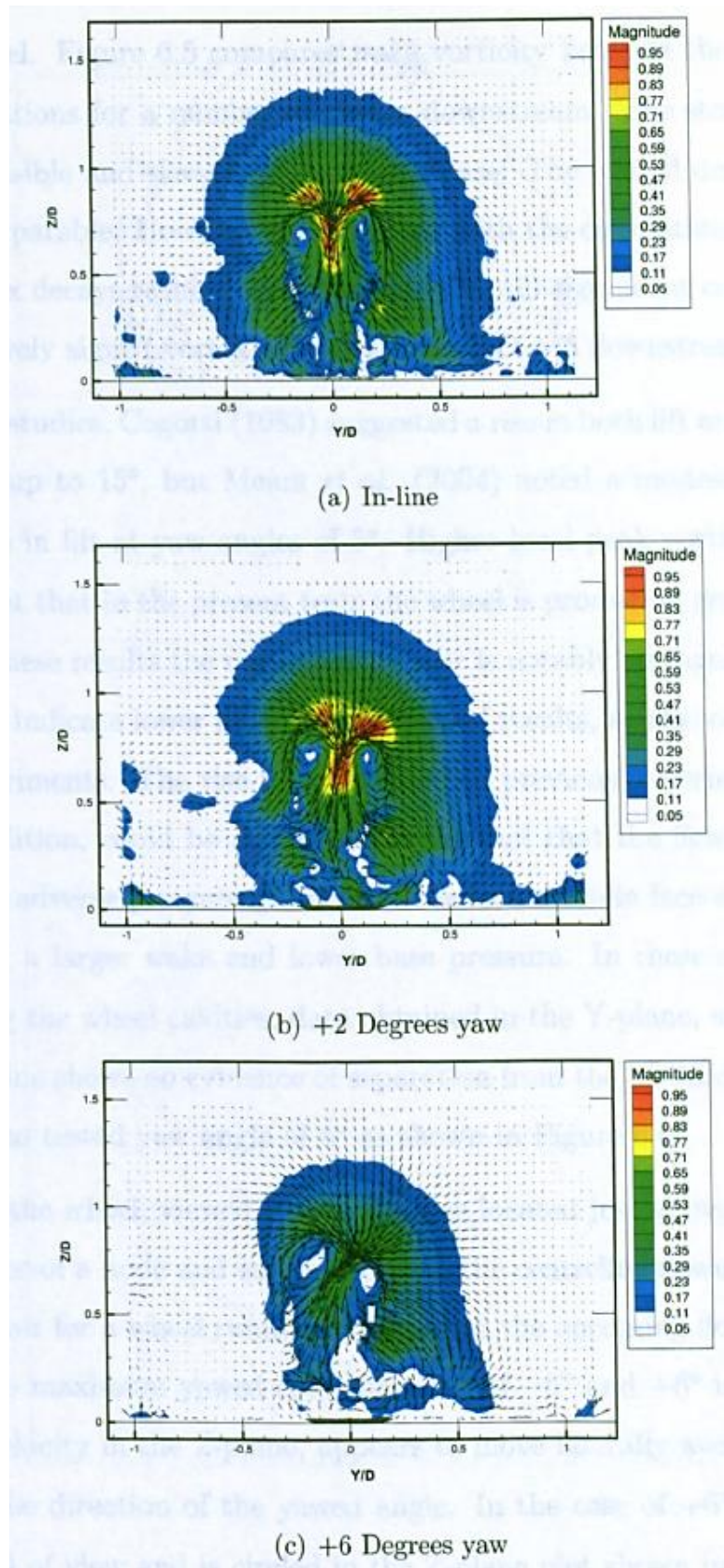


Figure 53 – Contours of velocity magnitude with velocity vectors at different yaw angles from [12]

Strouhal numbers ranging from 0.17-0.26 were obtained for three different stationary wheel configurations, with Reynolds number within the range of  $1.3 \times 10^5 < Re < 6 \times 10^5$ , which corresponds well to  $St=0.24$  for a typical Von Karman vortex shedding from a 2D cylinder and to those measured by previous authors. In order to investigate the instabilities around a stationary wheel in contact with the ground and the influence of aspect ratio and Strouhal number, a double wheel-width configuration was created by attaching two wheels together and bridging the gap to create a large smooth tread surface. A lower spectral peak frequency of  $St = 0.19$  was obtained for the double width configuration, as opposed to the single wheel ( $St = 0.24$ ), showing agreement to those observed by Bearman [46]; therefore indicating that the spectral peak frequency is higher on lower aspect ratio wheels. Overall, aerodynamics around an isolated stationary wheel in contact with the ground experiences a higher drag force compared to the rotating case. Separation is observed to occur upstream of the top and off the shoulders of the rotating wheel. Sizes of the hub cavity and support stings (if any present), can influence the size of the vortices in the rear wake, subsequently having an influence on the drag, as shown in Figure 54. The influence of yaw angle promotes the skewness in the rear wake of the wheel in the direction of the yaw angle.

Experiment	$C_D$
No Hubcaps	0.63
Hubcaps on	0.51
Brake disc hubcap	0.54
Outer rim hubcap	0.54
Spokes blocked	0.59
Fackrell's B2 wheel AR=0.61	0.58
Other research based on representative racing wheels	0.60

Figure 54 - Drag coefficients for a rotating wheel using different hub sealing arrangements [12]

## 2.3 Aerodynamics & Aeroacoustics of Aircraft Landing Gear

The Landing gear of an aircraft combines various parts and components, of different shapes and sizes, (wheels, struts, linkages, hydraulic lines, etc.) and can therefore be referred to as a cluster of bodies which, in its entirety, has proven in the past to be one of the hardest to analyse and investigate effectively, as well as being one of the largest contributors to unwanted noise. Although the work of this thesis centres predominantly on a component of aircraft landing gear, it is thought to include a review of the current aerodynamic and aeroacoustic understanding of aircraft landing gear. The following section includes both experimental and computational work, to try and understand how the flow field around landing gears differ from individual wheel components.

Lazos [7] experimentally analysed the mean flow characteristics around a four wheel landing gear, using a simplified scaled model of a Boeing 757 landing gear, entailing the wheels (diameter and width of 0.305m and 0.113m) and struts. Digital particle image velocimetry (DPIV) data was obtained on a plane bisecting the inline wheels, at a free stream velocity of 29m/s, and fiduciary points [7] were used on one of the wheels to accurately map oil mist visualization images. Fifty pressure taps were also fitted around another wheel, whilst a servomotor was used to allow data to be measured around the full 360 degrees circumference

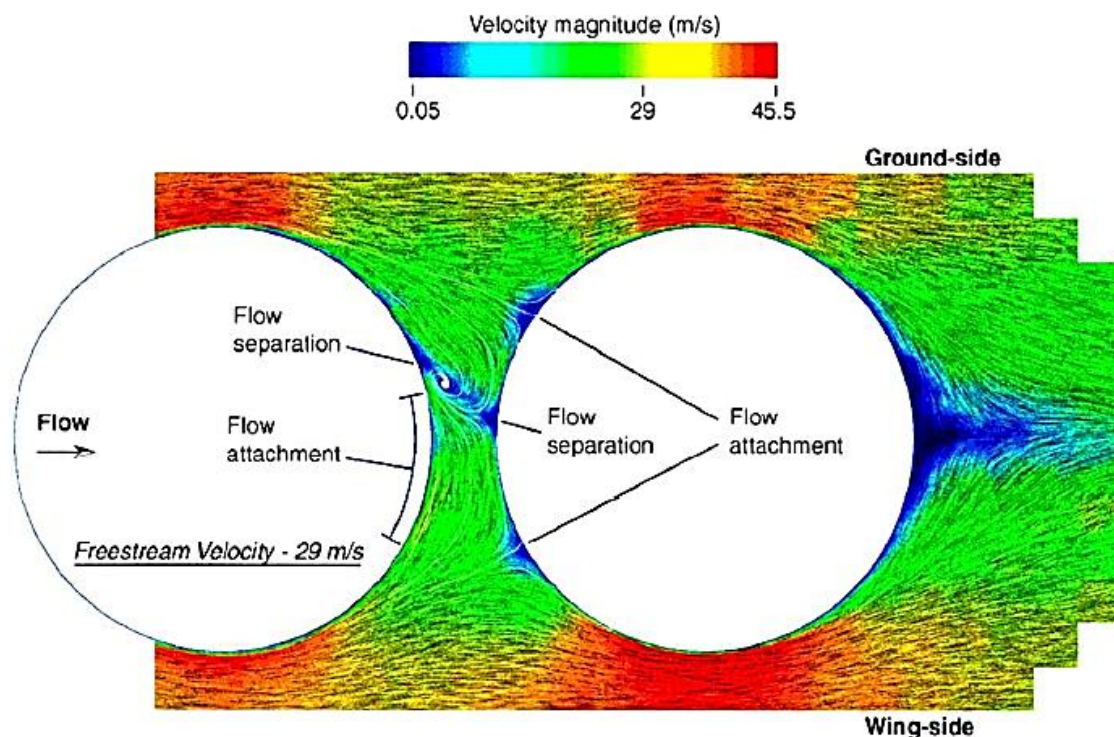


Figure 55 – Velocity magnitude contours inplane bisecting inline wheels from [7]



of the wheel. Overall, the results obtained, indicated that the flow conditions were significantly unsteady with significant areas of separation, reattachment locations and complex aerodynamic interactions (Figure 55). Considering surface pressure on the circumferential centreline of the front wheel (Figure 56), a flow stagnation region is observed at the front of the wheel with  $C_p = 1$ , before accelerating around the top and bottom surfaces of the wheel reaching a negative pressure peak ( $C_p = -1$ ). A pressure recovery is then observed until separation occurs on the rear surface of the wheel, where pressure peaks are observed at  $134^\circ$  and  $148^\circ$  (Figure 56); with flow attachment between  $-150^\circ$  to  $-190^\circ$ .

Differences in these separation positions clearly indicate separation on the ground side occurs  $14^\circ$  ahead of that observed on the wing side, and was suggested to be due to the geometric asymmetry of the centre support strut which, subsequently, contributed to the asymmetric flow features observed on the rear wheel. Illustrated in Figure 55, are the present asymmetric flow features on the rear wheel, including the magnitude of flow velocity on the wind and ground sides and the locations of flow attachment. A  $5^\circ$  offset is present between the two regions of flow attachment located on the rear wheel, at  $30^\circ$  on the wing side and  $-35^\circ$  on the ground side. Flow attachment on the wing side, closer to mid-wheel height on the wheel, allows the flow to enter into the gap between the wheels, shifting the location of separation on the rear wheel towards the ground side, allowing the separated flow to roll up into a vortex behind the

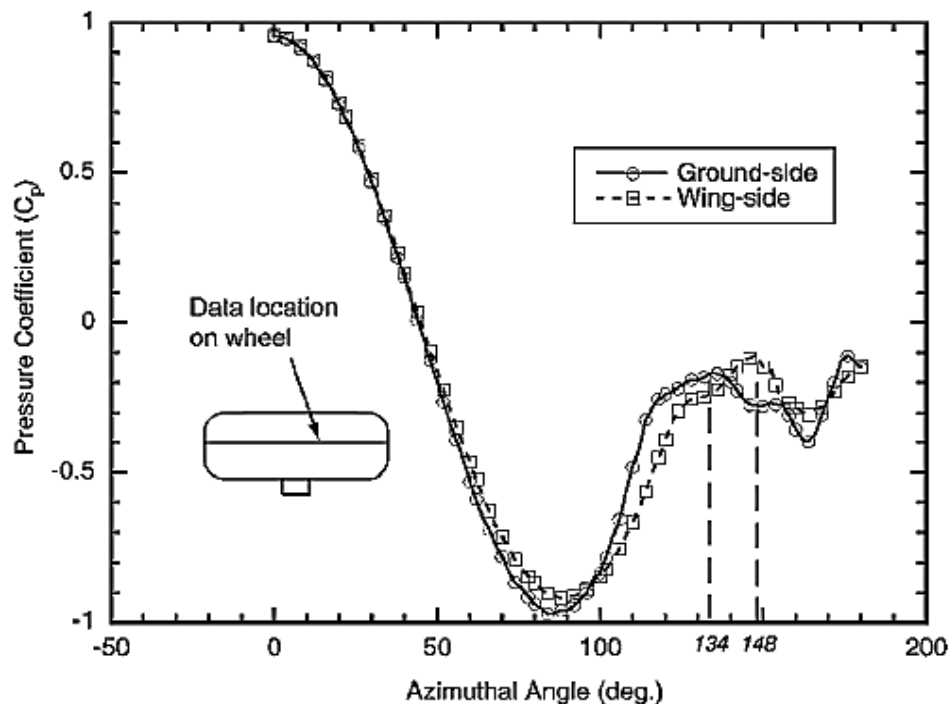
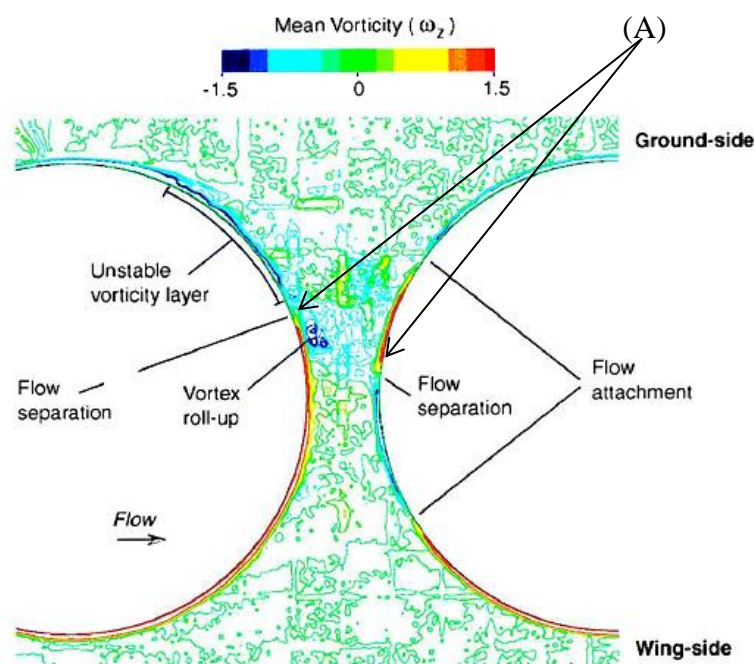


Figure 56 – Mean centreline pressure on front (fore) wheel, from [7]

front wheel. Contours of mean vorticity obtained in the same data plane bisecting both the front and rear wheels (Figure 57), correlates well to what Lazos [7] had already described, confirming the flow very nearly remaining attached, with a mean positive vorticity, on the wing side of the front wheel up to approximately  $200^\circ$  from stagnation, as well as the formation of the mid-wheel vortex. Away from the wheel surfaces, vorticity levels were found to be very close to zero, with changes in vorticity magnitude indicating regions of separation, Figure 57-A. A wavy, discontinuous region of negative vorticity is observed on the upper rear surface of the front wheel (approximately  $-115^\circ$  from the front stagnation position), indicating an unstable vorticity region causing the flow to remain attached to the wheel at times with separation to otherwise occur. This highly unstable wake, contains turbulent eddies that will eventually scrub against the wheel surface due to the rotation of the vortex, and is therefore able to produce significant ground directed noise.



**Figure 57 - Mean vorticity in mid-plane of wheels [7]**

To identify the position of the vortices between the wheels, datasets from three different positions were obtained by the DPIV data (Figure 58), showing changes in vortex position between the wheels. The vortex has a downstream shift, as the shear layer on the ground side of the wheel begins to separate, however, once it is completely separated the vortex is positioned directly in front of the rear wheel, as has been shown in Figure 58(c). The observed mid-wheel vortex was suggested to be a possible noise source, as if the vortex was resting against the wheel surface in a stationary position, it would scrub turbulent eddies

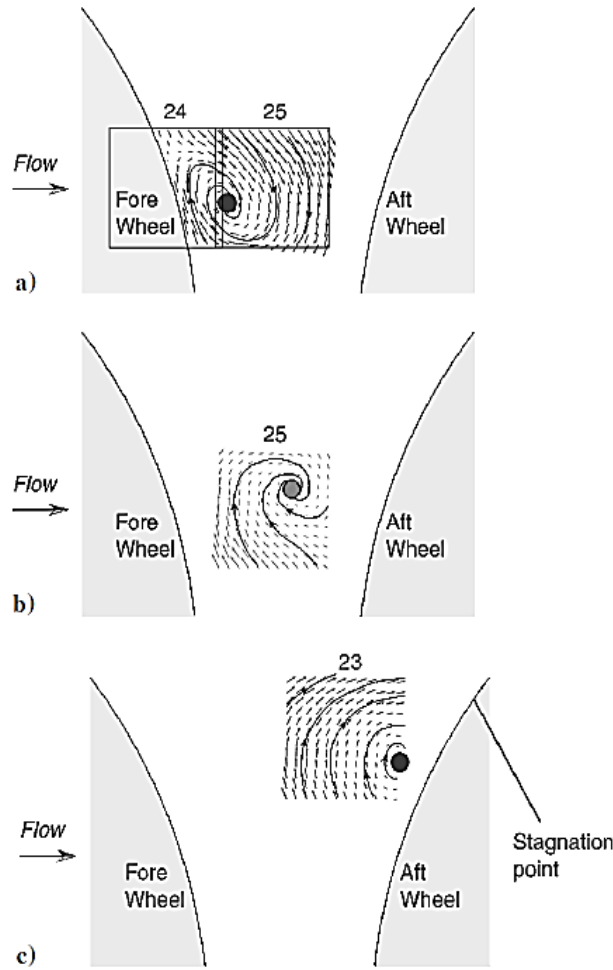


Figure 58 – Change of positions of vortex between wheels from [7]

against the surface of the wheel. Also if the vortex was to move, the collision of the vortex with the wheels would also generate noise. In addition, with separation locations, vortex formation position (Figure 57) and vortex translation (Figure 58) being located more towards the ground side, the potential noise generated was suggested to be directed downwards towards the ground.

To computationally validate these findings by Lazos [7] and to further understand the flow-field, Hedges et al [9] used the same, but simplified geometry of the 31% scaled Boeing 757 main landing gear model, using DES and URANS with the Spalart-Allmaras turbulence model. DES was employed, as it was found to be a more computationally efficient method than LES, when modelling the highly unsteady separated regions.

For the URANS results, a grid consisting of approximately 2.5million cells was developed, with simulations initially started using the steady RANS (SRANS), to allow the flow to develop quickly across the domain up to three or four orders of magnitude, before employing URANS with a normalised time step of 0.03. Time averaging was turned on after

approximately 10 time units, so that sufficient time was given for any initial fluctuations to stabilise.

Pressure coefficients along the horizontal centre line of the front and rear wheel are shown in Figure 59 from a top view. These illustrations were obtained by producing line plots of  $(1 - C_p)/10$ , as they indicate the magnitude of  $C_p$  on the surface by showing regions of low pressure as the curve appears to be ‘pulled’ away from the surface, whilst high pressure regions are indicated as the curve appears to ‘press’ against the surface. It can be seen from Figure 59-C, that the stagnation occurs at maximum  $C_p$  in front of the wheel, as would be expected. All three computational methods are in agreement in this region. As the flow travels around the sides of the wheel,  $C_p$  is reduced to a minimum as the flow is accelerated around the sides of the wheel (Figure 59-A). URANS simulations seemed to over predict this, generally, with DES showing best agreement with experimental results. For the majority of the rest of the wheel,  $C_p$  comparisons between CFD and experimental results were well correlated, with DES predicting closer results than URANS. The greatest differences observed were found to be in the region between the wheels, as would be expected, due to the instability within this region [7]. DES simulations were also found to be more accurate when visualising the contour plots in [9], although URANS simulations had also revealed the same flow features with small spatial discrepancies. Comparisons of the numerical simulations to experimental lift and drag coefficients, were poor with values of the computational  $C_D$  differing by up to 45% to the experimental, however, the authors suggested that this could be improved by carrying out a grid and time step refinement study, to ensure the correct grid is used in order to capture the flow features more accurately. Moreover, instantaneous and time

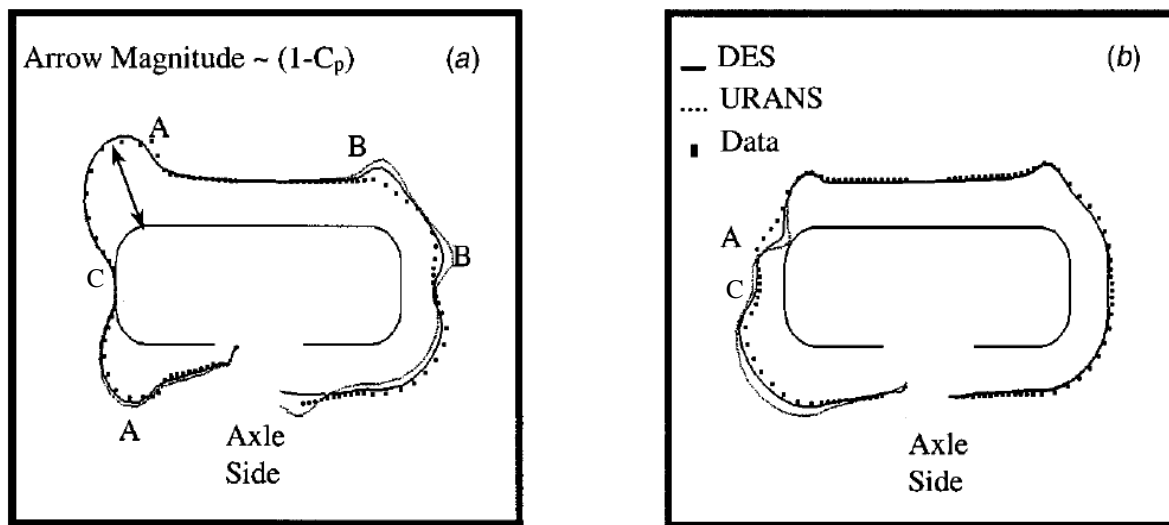


Figure 59 –  $C_p$  around the wheel when placed in the top view, (a) Front wheel, (b) rear wheel [9]

averaged velocity magnitude plots of the two CFD models were compared. The DES time averaged plots were also found to show eddy like features, as a result of separation off the shoulders of the wheels, a flow characteristic that the URANS simulations did not pick up due to the use of turbulence closure modelling. Overall the time averaged results for both numerical tests were very comparable. Instantaneous and time averaged vorticity magnitude, shown in Figure 60, was also analysed. The DES simulation in Figure 60(a) showed strong vortical structures downstream of the configuration, a characteristic that the URANS simulations (b) also predicted, however, some features were less oscillatory and ‘damped out’, as a result of using the URANS method.

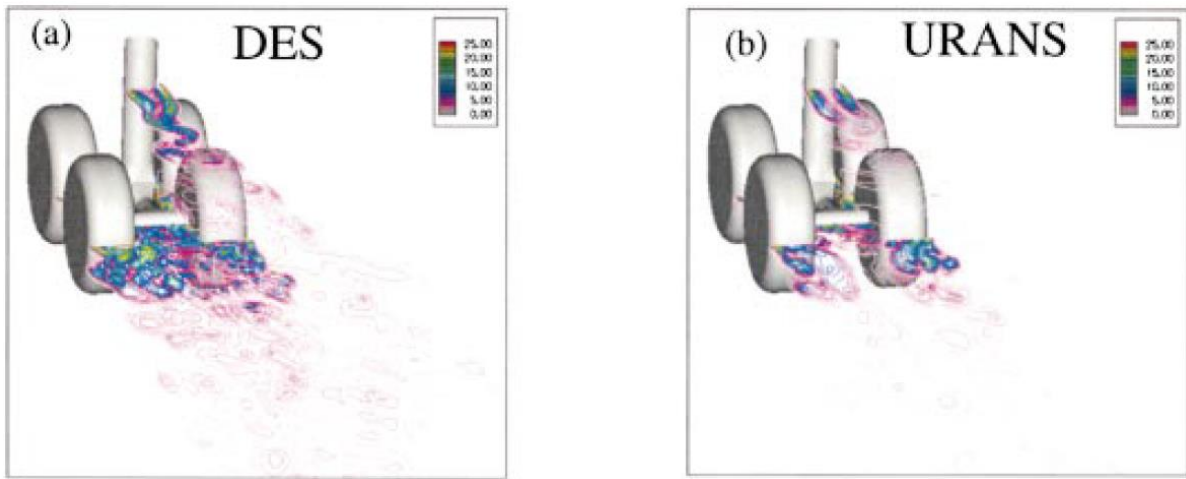


Figure 60 – Instantaneous vorticity magnitude, (a) DES, (b) URANS [9]

Further landing gear experiments were carried out at the NASA Langley Research Centre by Lazos [8], with the main aim, to improve computational modelling of the flow-field around landing gear. Tests were carried out on a scaled model of a simplified four-wheel main landing gear configuration of a Boeing 757, with the dimensions of the model and free stream velocity identical to that previously used by Lazos [7] and Hedges et al. [9]. The tests commenced at a Reynolds number of  $6 \times 10^5$ , based on the wheel diameter, with data obtained via DPIV. The results from the tests were then used to make comparisons with the computational fluid dynamics results, which were also performed. The area where the vortex was previously observed, in between the wheel in [7], shows a region of high turbulence intensity, with maximum and minimum transverse velocity components of 60 and -48m/s respectively. This highly turbulent region is skewed towards the ground side of the

configuration, leading to a suggestion by the authors that it may be of significant contribution to ground directed noise. The asymmetry in this mid region was also found to be due to the obstruction of the flow by the centre support strut, which contributes to the flow interaction between the ground and wing side. The flow through these areas, were expected to be of significance on fully functional landing gears, due to the stronger pressure gradients created by flow interactions with the gear elements in this region.

Following the work of Lazos [7], Li et al [47] performed URANS computations on a modelled representation of a Boeing 757 main landing gear, inclusive of four wheels, 2 diagonal struts, an oleo strut, a side door attached to the oleo strut and yokes and pins that assembled the landing gear structure. A structured grid consisting of 13.3 million grid points was used for the simulations, which were computed using the two equation  $k-\omega$  turbulence model. Reynolds number and wheel diameter were  $1.23 \times 10^6$  and 0.094m respectively, with detailed analysis of velocity contours for each modelled component. From this work, centreline pressure for each wheel showed that the flow does not stagnate directly at the front centres of the two front wheels (Figure 61), because of the asymmetry in the configuration caused by the struts and door. High pressure regions (red colour in contour plot) were, therefore observed on the front strut and oleo strut, with the stagnation on the two front wheels being pushed slightly inboard towards each other. Low pressure regions (green) on the curvature of the front two wheels indicate the low pressure regions, where acceleration in the flow occurs, with stagnation not occurring on the front of the rear wheels as this region



**Figure 61 – Instantaneous pressure contours [47];  
red = high pressure, green = low pressure**



lies within the wake of the front two wheels. Instantaneous centreline pressure data was taken on all four wheels at 13 different instances of time. Graphs shown in [47] for values of  $C_p$  against azimuthal angle, show the classical flow around a circular object for the first half of the two front wheels (i.e. from stagnation to the top and bottom of the wheel respectively). For the 13 curves plotted (each representing a point in time), results of  $C_p$  show minimal differences to one another for the front left wheel. However, the ground side of the front right wheel shows variations in the pressure plots, indicating that the flow has either reached an unsteady state or is oscillating at a very low frequency. Overall, the flow for the front two wheels reaches a minimum pressure between  $\theta = 80^\circ - 90^\circ$ , in-line with classical circular cylinder theory, recovering thereafter for the front left wheel until approximately  $\theta = 140^\circ$  on the wing side (upper surface) and  $\theta = 130^\circ$  ground side (lower surface) respectively. Pressure recovery was found to cease earlier on the front right wheel, with these differences in the flow field around the two front wheels, explained to be a result of the asymmetry in the model configuration. Once the flow reaches the two rear wheels, as mentioned previously, stagnation does not occur due to the front surfaces being exposed in the rear wake of the two front wheels, and unsteady separation occurs at approximately  $\theta = 110^\circ - 130^\circ$ . Conversely, the pressure distribution on the left wheel for all 13 time instances was found to remain fairly constant; however the rear right wheel was found to show oscillatory fluctuations on the ground side. The reason for this, as suggested by the authors, was caused by the impingement of the wake from the front right wheel, to the rear right wheel. These measurements of pressure distribution were generally in good general agreement when compared to the work carried out by Lazos [7]; however Lazos's experiments showed a slight decrease in pressure in the rear half of the wheels.

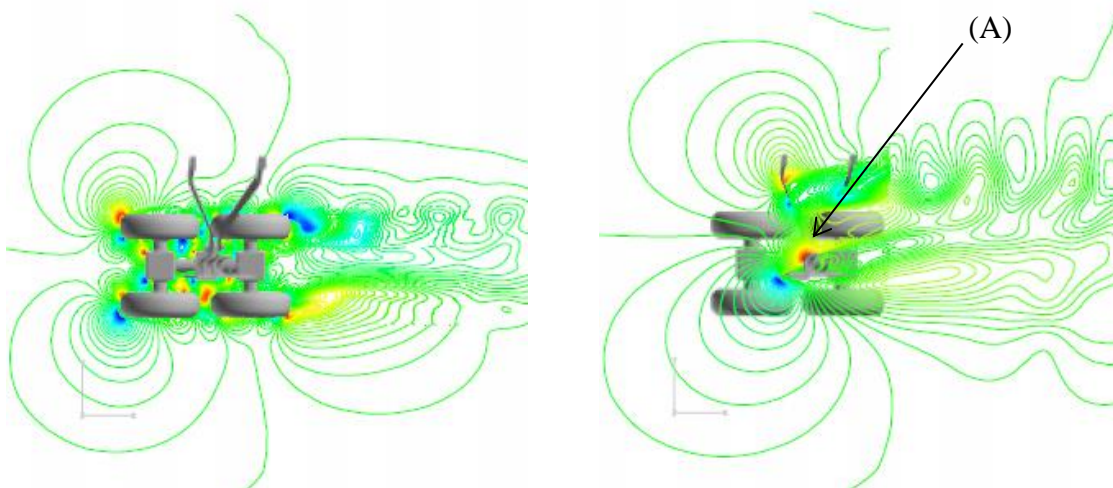
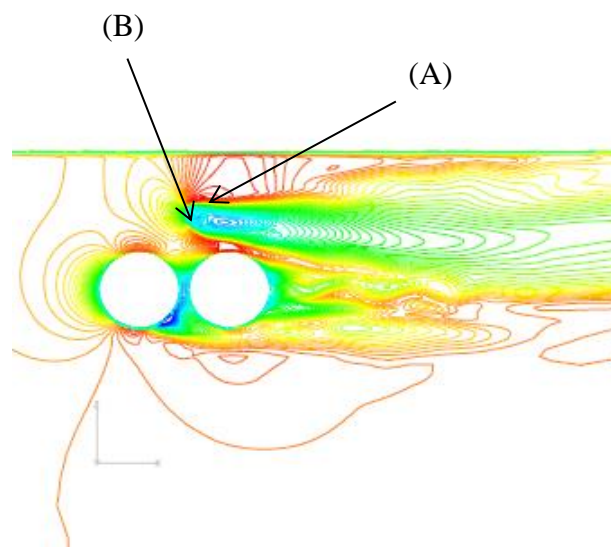


Figure 62 – Spanwise velocity contours (blue: -0.12 and red: 0.12), left:  $z=0$  plane, right:  $z= 1.3$  plane [47]

Top view velocity contour plots at two planes, horizontal mid-plane and a cut further up, are also shown in Figure 62. As mentioned earlier, a more energetic flow pattern is observed behind the rear right wheel when compared to the left side because of the wake from the strut, accelerating the flow on the right rear side. A vortex was found, in [47], to form at the top (A) and bottom (B) of the door, with areas of reversed flow being present between these two positions. Considering streamwise velocity contours (Figure 63), the lower vortices were observed to merge into the surrounding flow field, whilst the upper vortex propagates into the streamwise wake region.



**Figure 63 – Streamwise velocity contours,  $y = 0.463$  plane (blue: -0.1 and red: 0.25) [47]**

Further comparisons were made to Lazos's [7] work by Venkatakrishnan et al [48], who carried out an experimental investigation on a rudimentary four wheel landing gear. This rudimentary landing gear was similar to the configuration used by Lazos [5] and consisted of a four wheel truck arrangement including the vertical post, truck and wheels comprising a diameter 0.406m. Experiments were conducted at a free stream velocity of 40m/s, corresponding to a Reynolds number of  $1 \times 10^6$ , with the flow field around boundary layer tripped wheels analysed using oil flow visualisations (Figure 64) and contours of pressure distribution. The stagnation pressure region was also seen to be shifted inboard towards each other in a similar result to [47], coinciding not in the exact centre of the two front wheels. A region of low pressure is observed on the outboard edge of the front wheel representing flow acceleration, however, this only occurs on the outboard face of the wheel dissimilar to that



observed on a single isolated wheel. The presence of the truck on the inboard of the configuration was thought to be the cause of this, with pressure in the central region remaining high. The flow on the rear of the front wheels was found to separate and reattach on to the front face of the rear wheels. This reattachment shows a stagnated region biased towards the wing side of the configuration and is thought to be caused by the presence of the vertical strut decelerating the flow, creating asymmetry between the top and bottom halves of the rear wheels. Comparing  $C_p$  plots to those provided from [7], the maximum  $C_p$  on the front face of the wheels centreline does not reach a classical stagnation value of one. This is confirmed by the pressure contour plots, showing the stagnation point being shifted more towards the inboard side of the configuration. The position of this stagnation region was also found to be offset from the centreline of the wheel by 4%, after obtaining pressure data around the circumference of the wheel passing through the centreline of this stagnation point.

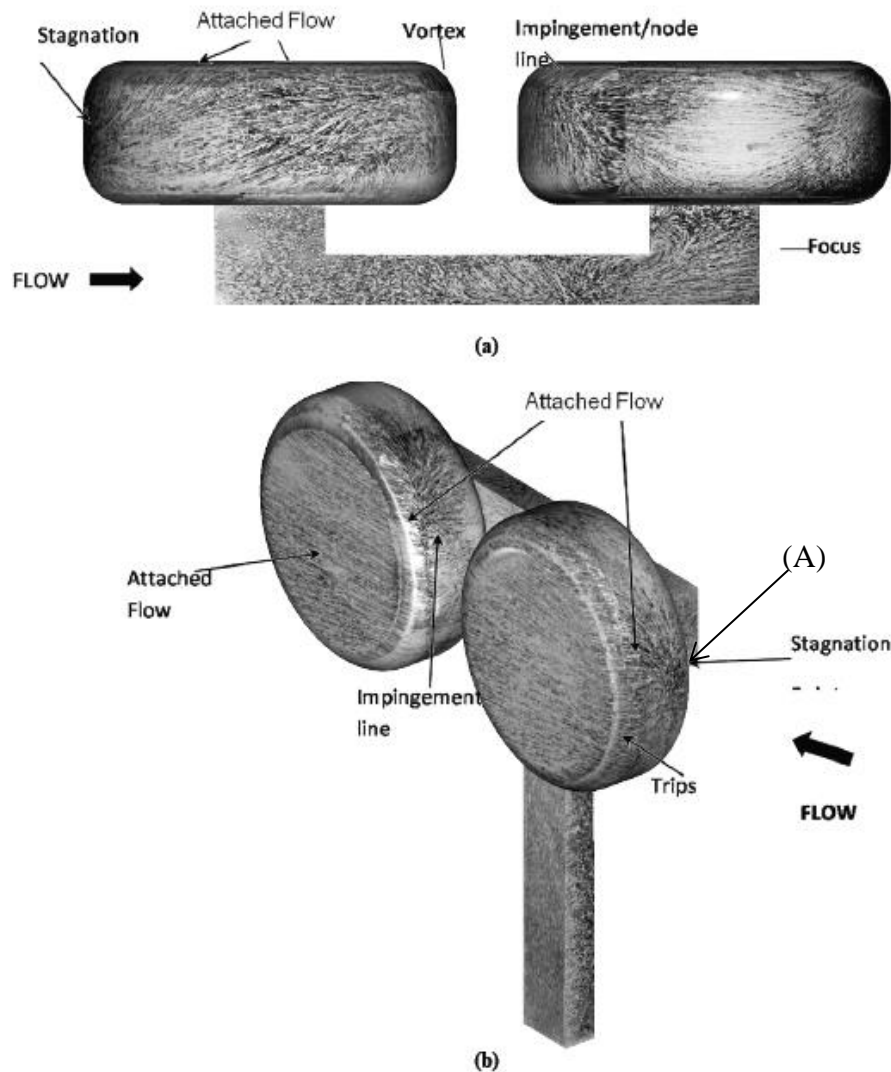


Figure 64 – Half landing gear model showing oil flow visualisation data – (a) top view, (b) isometric view from front [48]

Although the graph comparing  $C_p$  to that obtained in [7] are of similar nature, significant differences are observed after separation on the rear surface of the front wheels, as  $C_p$  across the rear surfaces are observed to be higher in [7]. This was suggested to be due to the difference in Reynolds number, trip/untripped wheel configuration and difference in the strut geometry. Complex flow features were found when observing the flow on the rear surface of the front wheel, such as the presence of a focus (A) and saddle (B), at  $\theta = 150^\circ$  &  $\theta = 165^\circ$  respectively, (Figure 65). The formation of the focus was determined to be caused by the high speed flow from the inboard side of the wheel, separating along a negative open bipartition which terminates at the focus. The saddle is therefore formed upon meeting the negative open bipartition lines, after the flow from the outboard side separates and reattaches. As the flow travels further downstream, a node (C) was observed at  $\theta = 190^\circ$ , leading to a stagnated region of up to  $\theta = 220^\circ$ , because of the open bipartition lines from the wing-side moving towards the node [48]. Similar features were also found in a computational study which compared the aerodynamic flow field around a rudimentary landing gear using Partially-Averaged Navier-Stokes (PANS) methods and LES [49]. The focus and saddle points observed in [48] are also known as critical points; those being defined as the “points at which all the spatial derivatives of the velocity are zero” [49]. These points can be classified into three main groups, (Figure 66); nodes, foci and saddles, where the former two groups can be stable or unstable. Streamlines compared on the rear surface of the front wheel also showed

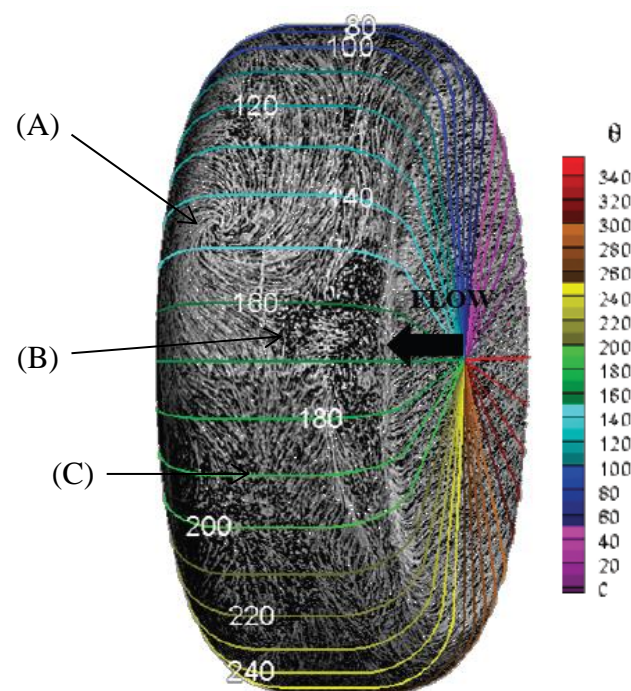


Figure 65 – Surface flow visualisation on rear surface of front wheel [48]

these critical points. When comparing the three different methods (experimental, PANS & LES), the stable focus was found in the range of  $143^\circ \leq \theta \leq 150^\circ$  and the saddle point in the range  $160^\circ \leq \theta \leq 165^\circ$ . Comparison of these features by Krajnović et al [49] to those observed in [48], are in good agreement. However, the differences in these positions between the different methods in [49] were suspected to be caused by poor spatial resolution in the near-wall region. Drag & lift force coefficients were also obtained for this configuration. By calculating force coefficients obtained on the wheels from the surface pressures, as well as force balance data, it was observed that the contribution of  $C_D$  &  $C_L$  from the truck and strut were 43.3% & 72.5% of the total  $C_D$  &  $C_L$  respectively. Overall, the authors [48] found that the truck and strut were significant contributors to the total lift and drag.

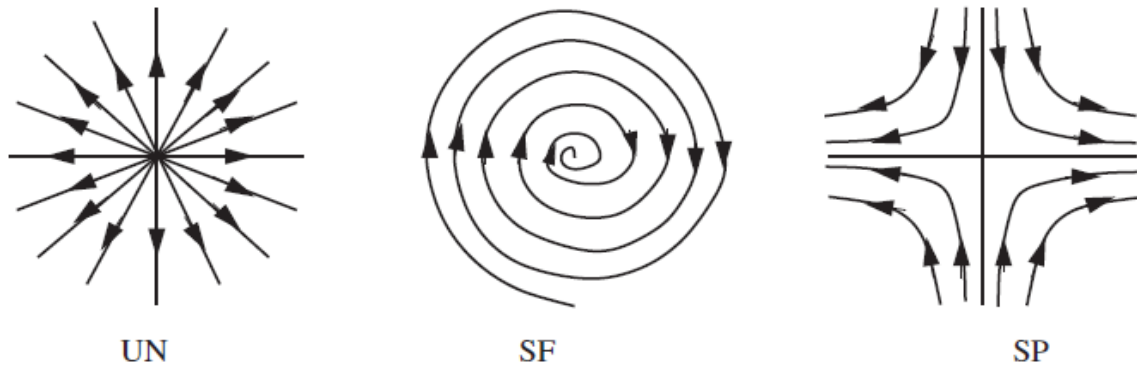


Figure 66 – Schematic representation of an unstable node (UN), stable focus (SF) & saddle point (SP) [49]

Guo [5] also investigated the effect of local flow variations on a landing gear, from CFD results obtained from Boeing's CFD database which had been accumulated over several years for different aircraft configurations. Data for full scale nose and main landing gear configurations, for the Boeing 777 & 737, were analysed to identify how flow velocity around wing mounted and fuselage mounted landing gear affects the overall generated noise. Around a wing mounted landing gear, the local flow velocity was found to be up to 25% lower than the free stream velocity because of the circulation region close to the high lift systems, such as the wings and flaps, encouraging the flow to be less than the free stream. This reduction in velocity corresponds to an approximate 6dB reduction in noise levels. The same gear installed in a wind tunnel was found to generate 6dB more noise. Therefore, it was found that the local flow velocity around a wing mounted landing gear increases as the distance of the flow from the wing/flap surface increases. Other strong influences that are known to affect the local flow around a landing gear, and specifically for wing mounted landing gears, are the angle of attack. Guo [5] discovered that as the angle of attack is

increased, the local flow velocity beneath the wing decreased significantly, due to the larger region of circulation producing more lift on the wing.

The flow around the fuselage mounted gear has a similar but opposite trend, as the flow travels much faster than observed for the wing mounted gear. The flow velocity on the lower surface of a fuselage travels within a very close range to the free stream speed because of the flat unobstructed surface. Whilst the flow travels past the nose cone of the fuselage, the flow stagnates shortly downstream of the nose point, where flow velocity is at minimum. Further downstream of the nose point, the flow accelerates along the lower surface of the fuselage, increasing the velocity in the region of the nose gear; opposing what was observed on a wing mounted gear, as the velocity reaches a maximum closest to the fuselage and reduces as the distance from the fuselage increases. With applied angle of attack, the flow velocity was observed to exceed the free stream velocity, depending on the angle of attack and the location of the nose gear.

Dobrzynski et al [50] carried out experiments obtaining wake measurements, in an attempt to improve noise prediction around landing gears. Experiments were carried out in a wind tunnel with velocities up to 70m/s, on a scaled fully extended central landing gear with the landing gear doors present. Wake characteristics showed the largest area of low velocity present behind the main leg, above the axle between the two doors. High turbulence intensity was found to occur downstream of the main gears, reaching values of up to 35%, additionally values of up to 23% were also observed above the tyres. Downstream of the wheel, vortex shedding peaks were found to occur off the main fitting, however, overall results showed that small changes upstream of the gear had no major influence on the characteristics of the gear wake. Khanal et al [51] also conducted a computational study to obtain a deeper understanding about the aeroacoustics on a single wheel. Noise levels generated from certain components of landing gear were found to be reduced by making them streamlined. Unfortunately due to the bulky nature of wheels and their purpose, streamlining the wheels is not possible, resulting in the wheels being a significant contributor to noise. Due to the expense in computing resources required by LES to achieve a highly accurate simulation of an unsteady flow field, a hybrid method was used. The results presented in [51] are not sufficiently detailed, however, still outlines key features observed in the flow field. Iso-surfaces illustrated in Figure 67, show a highly unsteady flow field in the wake of the wheel, with large amounts of vortex shedding. Acoustic measurements taken from around the wheel, displayed in Figure 68, show peaks in amplitude at low frequencies, typically less than 200Hz

all around the wheel. Khanal et al [51] suggested that this was due to the flow over large bodies emitting noise at low frequencies, whilst smaller bodies are responsible for noise at higher frequencies. Therefore, low frequency noise generated from aircraft wheels indicate that the wheels are large contributors towards noise generated from a landing gear.

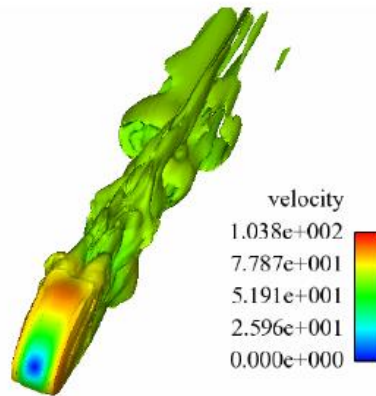


Figure 67 – Iso-surface of Vorticity [51]

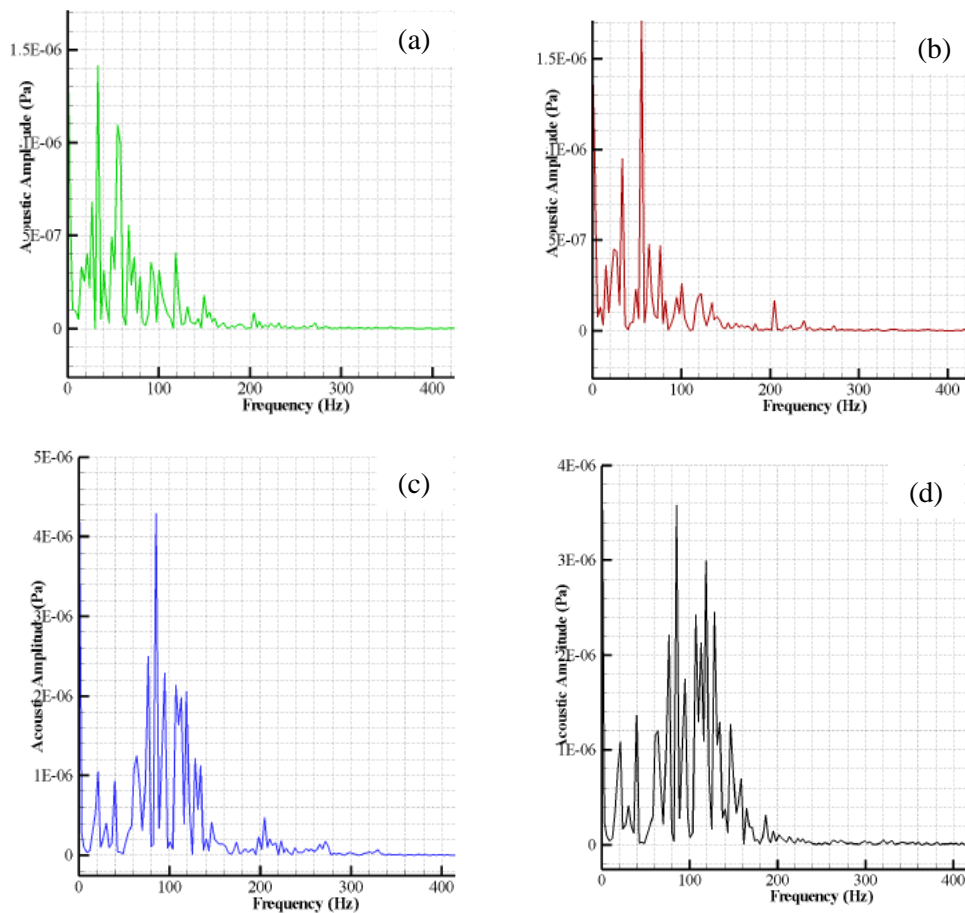


Figure 68 – Acoustic Signals, (a) Directly above the wheel, (b) Directly below the wheel, (c) Upstream of the wheel, (d) Downstream of the wheel [51]

In conclusion, a detailed understanding of the flow physics was obtained from this literature review to aid this present computational study in terms of the strategies that could be used and to provide insight into the flow physics when trying to understand the aerodynamic flow field around a single wheel in free air.

### **3. Computational Methodology & Set-Up**

A computational approach was used for this investigation, and this chapter outlines the reasons for using this approach and provides a detailed description of the methodology used. Justification for the decisions made throughout this methodology is also validated by making comparisons to the available literature where possible.

#### **3.1 Introduction to CFD**

Computation Fluid Dynamics (CFD) is a technique used to model and analyse fluid flow around objects. By using mathematical models and numerical methods, it provides qualitative and quantitative predictions of the real fluid flow from virtual simulations. CFD technology is more commonly used nowadays due to its speed and ability to provide data for multiple variables from just a single simulation. It is also used in research areas where experimental investigations are difficult, and may not even be possible to carry out, (and although CFD should not be used as a substitute for experiments), by accurate modelling and use of appropriate models and conditions, a detailed real life scenario can be analysed.

The procedure for using CFD comprises of four stages;

1. Identifying the problem to model, with an idea of what variables are required to be analysed
2. Creating a grid/mesh
3. Simulating the grid/mesh with correct operating conditions with the most appropriate numerical models
4. Carrying out post-processing analysis

All of the four stages mentioned above, were met and completed in order to obtain results for this study.

#### **3.2 Description & Justification of selected Wheel Geometry**

The wheel geometry chosen for this study is the ‘A2’ configuration used in Fackrell’s [22] experimental investigation, and the same used for the computational results in [29, 42]. The decision to choose this configuration was driven by the need to provide a solid foundation of experimental and computational data for subsequent validation and verification of the

computational methodology and subsequent flow-field dynamics. The A2 wheel (Figure 69) has a diameter and width of 0.416m and 0.191m respectively, corresponding to  $AR = 0.46$ . This wheel also contains both hub details approximating a simplified landing gear hub configuration (although usually more asymmetric) as well as a tyre width to diameter ratio (aspect ratio) indicative of a landing gear wheel.

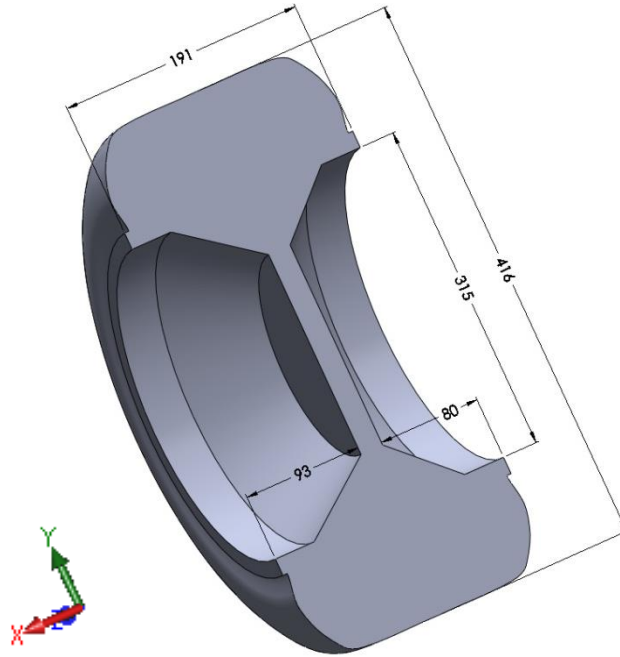


Figure 69 - Cross-sectional view of wheel showing dimensions (mm)

### 3.3 Computational Method & Grids

The geometry of the wheel was carefully measured from Fig. 2-1 & Fig. 2-2 in [22] using a digital calliper measuring instrument. These extracted measurements were drawn on SolidWorks™ CAD software which, in the end, provided a computational geometry of the wheel. To create the initial grid, the CAD geometry of the wheel was exported in to Pointwise™; which was used to create all grids. Pointwise™ grid generation software allows users to generate 2-dimensional (2D) and 3-dimensional (3D) grids and meshes before exporting them into CFD packages to be simulated. As the full 3-dimensional flow field is required to be analysed in this study, the grids created in Pointwise™ are all 3D.

The grids can either be structured, unstructured or hybrid. These are defined by the shape of the cells used; unstructured grids consist of triangular tetrahedral cells whilst structured grids



consist of all hexahedral cells. A hybrid grid combines both structured and unstructured blocks. A review comparing the differences between structured and unstructured grids [52] showed that structured grids are known to be superior to unstructured grids due to their quality and control. Using a structured grid provides users control over the generating the exact grid required. An advantage of using a structured grid is the time and memory it requires, as a volume can be filled with fewer hexahedral cells as opposed to tetrahedral cells subsequently lowering the cell count of the grid. As a result, the computational time and memory usage is reduced; therefore it is a key factor when generating large scale grids, similar to that needed for this investigation. Improved resolution and alignment is also achieved by using a structured grid. Fluid flow that experience strong pressure gradients, particularly in the regions of boundary layers and wakes, require high quality cells with high aspect ratios which can be stretched, however, the use of stretched tetrahedral cells causes difficulties in the generation of the solutions due to problems such as cell skewness, although the use of tetrahedral cells can be an advantage when attempting to mesh very small confined spaces. Additionally, CFD solvers were found to produce results with higher accuracy when the grid is aligned with the geometry and flow direction, and a hexahedral mesh would automatically provide this due to their six sided cell volume blocks as opposed to the tetrahedral meshes which provide no such alignment. With these differences between the two grid types showing a bias towards the use of a structured grid, together with previous investigations using structured meshes [29, 38, 9], it was decided to use a structured hexahedral grid for this study.

Certain variables need to be considered to obtain good quality grid such as skewness & volume of the cells. Skewness is the stretching of cells; the less skewed the cells are, the higher the grid quality is. During the process of grid generation, cell skewness was maintained below the default skewness value of 0.8 set in Fluent™ (the CFD solver used in this study) for 3D models [53]. The volume of the cells (also referred to as Jacobians in Pointwise™ [54]) had to be kept at a positive value as negative Jacobian cells would indicate twists in the grid or negative cell volumes caused by overlapping domains which will eventually cause problems when trying to simulate the grid.

Different topologies can be applied when creating grids; two of the commonly used topologies are the block topology (also known as a C-grid) and the circular topology (also known as an O-grid) as illustrated in Figure 70. The block topology (a) consists of creating volume blocks around the geometry propagating to the far field. However, due to the near

field blocks touching the geometry with just the corners of the blocks at a certain point (illustrated A), differences in near wall cell size are produced as a result of the adjoining corner of the blocks (B) having to satisfy the near wall spacing constraints as well as the corresponding connector distribution to the connector present on the opposite side of the domain. Therefore, when simulated, discontinuities in the results are observed due to the

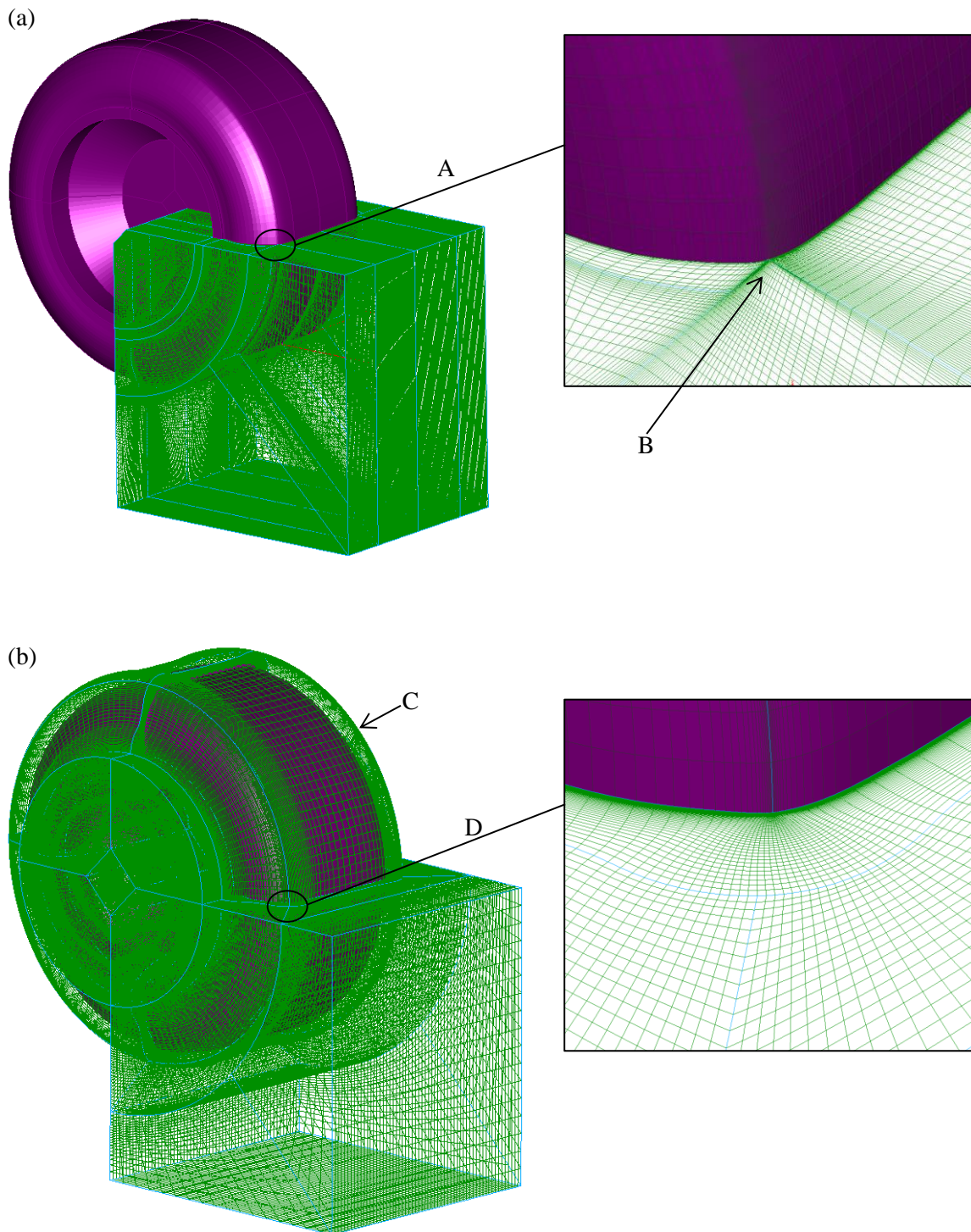


**Figure 70 - Representation of (a) block topology - 'C' grid and (b) circular topology - 'O' grid**

large variances in cell size. Using a block topology was also found to be more challenging when trying to keep the Jacobians and the skewness at an acceptable level because of the circular shape of the wheel geometry. On the other hand, the circular topology, Figure 70(b), involves creating a circular boundary layer off the geometry (C), by conducting a normal extrusion of the wheel surface and extending it in to the near field and subsequent far field using the block topology. This provides greater control of the internal volume mesh as well as maintaining smooth gradual increases in cell wall distance from the wheel surface (D). Therefore a multi-block topology, consisting of a circular topology for the boundary layer region and a block topology propagating to the far field domains, was used.

The imported geometry was presented in Pointwise as a database, and connectors were created on the database surface. The dimensions of the connectors were chosen according to the size (length) of the connector and by deciding on how dense the corresponding section of the wheel, where the connector is placed, has to be. After the connectors had been created appropriately on the database, the connectors were deleted leaving behind just a 2D plane consisting of the edge profile. A 2D normal extrusion on the wheel's edge profile was conducted up to 10-20mm away from the surface of the wheel at a growth rate of 1.1 so a  $y^+ \approx 1$  was achieved, corresponding to the first cell wall distance off the surface to be approximately 0.005mm. A near field boundary was created on the same 2D plane to form a rectangular outer domain which was then rotated  $360^\circ$  about the projected centre of the wheel to fully obtain the near-field mesh including the boundary layer mesh and surface mesh of the wheel. Subsequently, the near field mesh was extruded outwards in all three coordinate directions to create the far field boundary. The distance & length of the far-field boundary were chosen to closely correspond with the far field computational domain used by McManus & Zhang [29]. The skewness of the grids was kept as low as possible but definitely below the threshold value of 0.8, whilst also making sure that all Jacobians were positive; criteria that have to be met for a good quality grid.

The geometrical axis was identical to the coordinate (x, y, z) axis; x in the spanwise direction (positive x directed right to left when looking downstream from the inlet), y in the vertical direction with positive y directed towards the top of the domain and z in the downstream direction with positive z directed downstream from the inlet.

Majority of wheel in contact with ground studies described in the literature [22, 29, 39, 30], used free stream velocities in the range 15 – 18.6m/s, through focusing primarily on race car

wheel configurations. Free stream velocities for wheel configurations used for investigations based on landing gear used higher speeds ranging from 29m/s – 40m/s [48, 7] , with additional free-air and a ground clearance study using 40m/s [32] and 38m/s [36] respectively. As the speed of a large passenger aircraft on approach is known to be in the range of 130-140 knots, corresponding to approximately 65-70m/s; a speed of 70m/s was considered and attempted at first with a preliminary simulation but, as expected the simulation took approximately a month to obtain  $\approx 0.5$ s of data. Therefore a longer simulation time was required for convergence to be reached. Considering time and computational constraints playing a vital role in this study, using a velocity of  $\approx 70$ m/s was not practical. Therefore it was decided to reduce the velocity to correspond to the range used in previous studies for landing gear and free air studies as more direct comparisons can be made. As a result, a final free stream velocity of 40m/s was chosen corresponding to a Reynolds number of  $1.1 \times 10^6$  based on wheel diameter. Turbulence intensity of 0.2% was used, corresponding to that used by McManus & Zhang [29], with a hydraulic diameter equivalent to the diameter of the wheel of 0.416m, since the hydraulic diameter is considered as the characteristic length of obstruction in external unbounded flows [55]. Atmospheric pressure condition with gauge pressure of zero was defined for the pressure outlet, with a symmetry condition on all other remaining sides of the far field domain. The symmetry condition is used to negate the need to resolve the boundary layers on these far field walls. A symmetry boundary condition is summarised as a plane with zero normal velocity and with zero normal gradients for all variables, and as the wheel was placed at the centre of the computational domain, the flow pattern is expected to mirror symmetry [53]. Due to the free stream flow only entering from the inlet, and the far fields boundaries placed at a significant distance from the wheel (dimensions provided in Section 3.3.7 and Section 3.3.7), the walls were measured to produce a negligible effect on the flow field, as the flow was expected to be of a steady state by the time it reached the far field walls. The wheel was modelled as a smooth, no slip wall (Figure 71). This is a default condition in Fluent™ for walls in viscous flow and indicated that the fluid sticks to the wall and if moving, moves with the same velocity as the wall [53]. This enables the components of velocity on the walls to be set as required; a zero velocity stationary wall for the stationary wheel condition and a moving wall for modelling the influence of rotation.

The surface mesh on the wheel, illustrated in Figure 71 also shows denser regions in the mesh (A & B) due to a finer grid being required to resolve the boundary layer. Considering the

flow field around a single wheel from the literature, it has been shown that complex flow characteristics such as separation, recirculation and wake flow dynamics are prominent features that determine the aerodynamic flow field. For that reason, it is important to predict accurately these positions. One of the factors that affect the prediction of separation position was suggested to be the wheel edge profile [22], with differences of  $\pm 30^\circ$  when comparing CFD data [38] to experimental results [22]. Subsequent to separation position, the flow was shown to roll up over the shoulders of the wheel forming vortices [42, 10, 9, 12], with a similar characteristic shown on the shoulders of a cylinder [28], therefore, in an attempt to minimise errors and to accurately predict separation positions and the locations of vortex formation, a finer mesh was applied around the shoulders of the wheel (A). In addition, flow interaction on sharp edges will cause recirculation within the flow, therefore a denser mesh was applied in the regions where two wheel surfaces meet (i.e. hub and rim regions illustrated (B) in Figure 71).

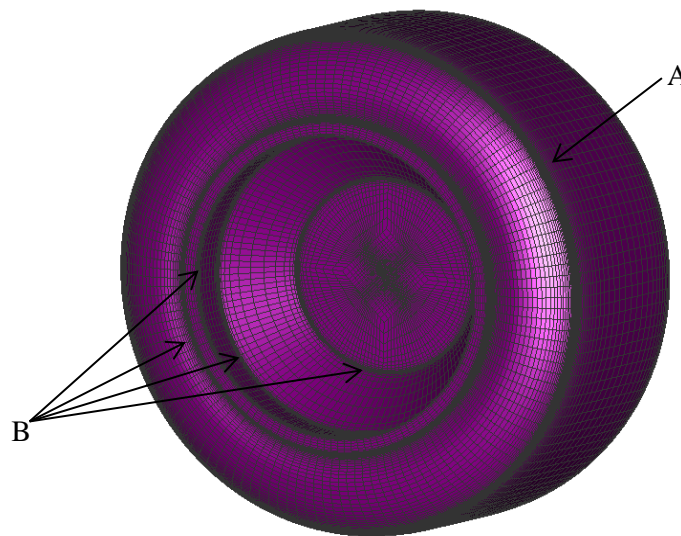


**Figure 71 – Surface mesh on wheel**

### 3.3.1 Numerical Methods & Turbulence Models

Turbulence is known to be an unsteady random motion, observed in fluids [53]. Although turbulence is initially described via the Navier-Stokes equation, resolving these equations using Direct Numerical Simulation (DNS) would exceed the computational capabilities currently available as the cost required for a DNS solution is proportional to  $Re_n^3$ . Therefore, averaging is required to reduce & simplify parts of the turbulence spectrum. The most commonly used method involved eliminating the turbulent structures to obtain averaged velocity and pressure fields, and is known as the Reynolds-Averaged Navier Stokes (RANS) equations. The governing incompressible RANS equations for continuity and momentum [53] are defined as:

$$\frac{\partial \bar{u}_i}{\partial x_i} = 0 \quad \text{Equation 5}$$

$$\frac{\partial \bar{u}_i}{\partial t} + \bar{u}_j \frac{\partial \bar{u}_i}{\partial x_j} = -\frac{1}{\rho} \frac{\partial \bar{p}}{\partial x_i} + \nu \frac{\partial^2 \bar{u}_i}{\partial x_j^2} - \frac{\partial}{\partial x_j} (\overline{u'_i u'_j}) \quad \text{Equation 6}$$

From the equations, variables are defined,  $\rho$  is the air density,  $p$  is the air pressure,  $\nu$  is the kinematic viscosity,  $u_i$  is the velocity in the  $i$ th direction (i.e.:  $i = 1, 2, 3 = u, v, w$ ) and  $u_j$  is the velocity in the  $j$ th direction (i.e.:  $j = 1, 2, 3 = u, v, w$ ). The directional tensors,  $x_i$  and  $x_j$ , are defined for the  $i$ th and  $j$ th directions (i.e.:  $i = 1, 2, 3 = x, y, z$  and  $j = 1, 2, 3 = x, y, z$ ). Mean and fluctuating quantities are indicated by the over-bar and the prime, respectively [29]. As a result of this averaging process, additional terms are introduced to the transport equations known as Reynolds Stresses,  $\overline{\rho u'_i u'_j}$ , which require an appropriate turbulence model in order to be resolved. The quality of the simulation depends on the selected turbulence model, and with no single turbulence model specifically designated for classical problems, special consideration needs to be given to the flow physics, level of accuracy required and available time and computational resources available, as all these variables differ from each turbulence model.

A few other turbulence models that were of interest when deciding which model to use are subsequently described.

The one equation Spalart-Allmaras [56] model solves a modelled transport equation for the kinematic turbulent viscosity ( $\tilde{\nu}$ ), shown in Equation 7.

$$\frac{\partial}{\partial t}(\rho \tilde{\nu}) + \frac{\partial}{\partial x_i}(\rho \tilde{\nu} u_i) = G_\nu + \frac{1}{\sigma_{\tilde{\nu}}} \left[ \frac{\partial}{\partial x_j} \left\{ (\mu + \rho \tilde{\nu}) \frac{\partial \tilde{\nu}}{\partial x_j} \right\} + C_{b2\rho} \left( \frac{\partial \tilde{\nu}}{\partial x_j} \right)^2 \right] - Y_\nu + S_{\tilde{\nu}}$$

**Equation 7 – Spalart-Allmaras transport equation**

This equation combines the production of turbulent viscosity ( $G_\nu$ ) and the turbulent viscosity destruction term ( $Y_\nu$ ). The destruction term occurs in the near wall regions, where viscous damping and wall blocking effects are dominant [55].

Initially the Spalart-Allmaras model was created for aerospace applications as it has been proven to provide good results when modelling boundary layers subjected to adverse pressure gradients. Although, this model is becoming more popular in other areas of engineering, the quality of the results start to deteriorate as errors are produced when modelling the free shear layers formed after separation due to the swift changes in length scales [53].

The three k- $\epsilon$  models (standard, RNG and realizable k- $\epsilon$ ) have also been analysed in this study. These models are all two equation models based on the turbulent kinetic energy (k) and the turbulent dissipation rate ( $\epsilon$ ). All three models are similar to one another but the differences occur in the method of calculating the turbulent viscosity.

#### 1. Standard k- $\epsilon$ model (k- $\epsilon$ )

The standard k- $\epsilon$  model was the first from its group to be created, hence the most basic. Solving two separate equations allows the model to determine both turbulent length and time scale. This model is used in many engineering applications due to its robustness, low economical expense, along with providing results to a reasonable level of accuracy for turbulent flows. Whilst deriving the standard k- $\epsilon$  model, it was assumed that the flow being modelled is fully turbulent and that the effects of molecular viscosity are negligible, therefore, only making this model valid for fully turbulent flows. As this is the oldest model in its group, modifications were made to enhance its performance resulting in the creations of the two most recent versions of the k- $\epsilon$  model as described below.

## 2. RNG k-ε model (RNG)

This model was created using a statistical technique called the ‘renormalization group theory’. It is a refinement of the standard k-ε model, as the equation for turbulent dissipation rate (ε) includes an additional term which improves its accuracy. The accuracy of predicting swirling flow is also improved and also enables this model to be used for flows at low Reynolds numbers, if the near wall region is modelled appropriately. This allows a more accurate and reliable modelling solution for a wider range of flows [55].

## 3. Realizable k-ε model (RKE)

‘Realizable’ means that this model is consistent with the physics of turbulent flows as the model satisfies certain mathematical constraints on the Reynolds stresses. The Realizable k-ε model has two significant features that differentiate it from the standard k-ε model; it uses an alternative formulation for turbulent viscosity and it contains a modified transport equation for the turbulent dissipation rate (ε) [55]. The transport equations for the RKE model are shown below:

$$\frac{\partial}{\partial t}(\rho k) + \frac{\partial}{\partial x_j}(\rho k u_j) = \frac{\partial}{\partial x_j} \left[ \left( \mu + \frac{\mu_t}{\sigma_k} \right) \frac{\partial k}{\partial x_j} \right] + G_k + G_b - \rho \varepsilon - Y_M + S_k$$

**Equation 8 – Turbulence Kinetic energy transport equation (k)**

$$\frac{\partial}{\partial t}(\rho \varepsilon) + \frac{\partial}{\partial x_j}(\rho \varepsilon u_j) = \frac{\partial}{\partial x_j} \left[ \left( \mu + \frac{\mu_t}{\sigma_\varepsilon} \right) \frac{\partial \varepsilon}{\partial x_j} \right] + \rho C_1 S_\varepsilon - \rho C_2 \frac{\varepsilon^2}{k + \sqrt{\nu \varepsilon}} + C_{1\varepsilon} \frac{\varepsilon}{k} C_{3\varepsilon} G_b + S_\varepsilon$$

**Equation 9 – Rate of dissipation transport equation (ε)**

Out of all the k-ε models, the RKE model has been proven to provide the best performance when analysing separated flows with complex secondary flow features [53, 55]. It has been additionally validated for flows that contain boundary layers with adverse pressure gradients, flows involving rotation, separation and recirculation [57]. Ramachandran & Doig [42] also used the RKE model in their investigation due to its accuracy. Axerio-Cilies & Iaccarino [30] tested six different turbulence models for their investigation on a wheel in contact with the ground, and found that the KW-SST model was closest at determining vortex core locations; however the RKE model was found to be most accurate at predicting the strength and intensity of the vortices.

Large Eddy Simulation (LES) was also of interest due to its enhanced accuracy. The LES model resolves the large eddies directly, whilst modelling the small eddies allowing a coarser



mesh to be used with large time step when resolving the larger eddies. However, a mesh in LES is significantly finer and larger in size than those used in RANS simulations, therefore LES simulations are required to be computationally simulated for a longer period of time to obtain a near steady solution. This subsequently, increases the computational expense in terms of memory (RAM) & CPU time when compared to RANS calculations [55].

Due to the both computational expenses and time constraints present for this study, using a LES approach was not a practical solution, therefore the URANS method was chosen with the Realizable  $k$ - $\epsilon$  model due to its advantages over the other models. It has been validated for enhanced performance in capturing separated flow regions and boundary layers containing adverse pressure gradients together with flows involving rotation and recirculation, making the decision more bias towards this model as these are known to be prominent flow features around a wheel, which are to be thoroughly analysed and discussed from the results acquired from this study. The RKE model was used by other authors [29, 42, 30] who have conducted similar studies due to the advantages mentioned. McManus & Zhang [29] used both the RKE & S-A turbulence models in their computational investigations, and although both predicted similar results, the S-A computations were found to predict better surface pressures and separation positions. However, the S-A computations were found to have a larger dependency on the grid, as opposed to the RKE model. Additionally, Mahon & Zhang [58] have conducted a computational study analysing the pressure and wake characteristics of an aerofoil using six different turbulence models: one equation Spalart-Allmaras model, standard  $k$ - $\epsilon$  model, standard  $k$ - $\omega$  model,  $k$ - $\omega$  SST model,  $k$ - $\epsilon$  RNG model, and the Realizable  $k$ - $\epsilon$  model. Conclusions from their study have stated that the RKE model was the most accurate when predicting the flow field in the near wake. Unsteady Reynolds-Averaged Navier-Stokes (URANS) was chosen due to its capability to provide a time dependent unsteady solution, therefore, not assuming that the simulation is of steady state. As the flow over a bluff body is known to be unsteady with a highly oscillatory flow in the rear wake region, the unsteady solver would predict these unsteady flow characteristics more accurately [53].

### **3.3.2 Solver Settings**

URANS simulations were computed on a cluster with a Linux based operating system. Boundary layer modelling was implemented through the use of the enhanced wall treatment due to the complex flow structures expected. As previously used in [29, 30], the  $y^+$  value was

maintained at less than 2.0 over the entire wheel, ensuring that the wall adjacent cells are within the viscous sub-layer.

URANS simulations were computed using the Pressure-Based segregated algorithm with absolute velocity formulations in transient conditions. The Pressure-Velocity coupling method, SIMPLEC, is used in this study as it aids convergence [53]. Accuracy is a significant factor in this study as resolving the boundary layer in highly separated flow regions can be affected by errors and inaccurate modelling. As a result, an upwind spatial discretization was used, yielding second order spatial accuracy rather than first order, although first order will reduce the computational time. However, a combination of both first and second order schemes was used in this study and will be described in the subsequent section. In addition, the gradient discretization used was the Least Squares Cell Based. The least squares method is comparable in accuracy to the Green-Gauss Node based but requires less computational time [55]. Under-Relaxation factors are used in the pressure-based solver to control the convergence at each iteration. Default values for these factors were already set in Fluent™ (Density = 1.0, Pressure = 0.2, Momentum = 0.5, Turbulent Kinetic Energy ( $k$ ) = 0.5, Turbulent dissipation rate ( $\epsilon$ ) = 0.5), and are optimised to work for a large number of cases, therefore, it is recommended to begin the simulations with the default values and to only reduce them if the residuals start to show unstable or divergent behaviour [53]. Therefore the under-relaxation factors were unchanged and kept at their default values as the solutions eventually reached a converged state.

### 3.3.3 Convergence

Before starting the simulations, the entire computational domain was initialized to the free stream conditions at the inlet boundary, which was chosen, as the initial flow variables were required to be computed based on the initial free stream velocity of 40m/s [53]. All results obtained from the URANS solver were obtained using a time step of  $6 \times 10^{-5}$ s representing a non-dimensional time step of 0.005, based on free stream velocity and wheel diameter, however a time step study was subsequently carried out (Section 3.3.6 in this thesis) to provide confidence in the time step size. For each time step, residuals were allowed to converge to a minimum standard of three orders of magnitude at 20 iterations per time step. This determines the numbers of iterations that are carried out within a time step before moving to the next and if the convergence criteria are met before the maximum number of iterations within the time step are completed, the solution will progress to the next time step

[53]. Computational discretization was performed initially using first-order schemes for pressure, momentum and turbulence quantities to minimise computational expense [30], before enacting second-order discretization schemes after an initial development period. An initial start-up from first order also yields convergence reducing the simulation time [53], also used in [29, 30]. After this initial first-order development period, the flow was allowed to further develop (in second-order), with residuals required to converge to five orders of magnitude, for an additional 17.3 non-dimensional time units before data sampling for mean flow statistics was initiated. The solutions were considered to be converged, once the mean flow quantities were stabilised, showing no significant changes with additional time units, represented by the force coefficients and residuals illustrating regular oscillating patterns [30]. Mean flow quantities were thereafter calculated after 173 subsequent non-dimensionalised time units corresponding to a total of approximately 2 seconds of data. Drag, lift and side force coefficient monitors were set to record the data in +z, +y and +x directions respectively.

### **3.3.4 Boundary Refinement Study**

A boundary refinement study was carried out to find the most appropriate distance at which the far field boundary distance has negligible effect on the results, so that the boundaries were large enough to minimise their influence on the results as well as keeping them as small as possible to minimise the number of grid cells, which will subsequently reduce computational expense.

This study was conducted on the grid comprising of the largest blockage, as this grid comprises the far field boundaries closest to the walls of the wheel, therefore the grid with the wheel yawed at  $15^\circ$  was chosen. An initial grid was created with boundary and mesh conditions similar to those used by McManus & Zhang [29], due to the same wheel geometry being modelled. The far field boundary distance was enlarged by 0.5 & 2.0 times the original distance in all three coordinate directions. Simulations were completed and the values of  $C_D$  &  $C_L$  were plot on a graph (Figure 72). The mean drag obtained from the results shows  $C_D = 0.49$  for both the initial and ‘2.0x’ grid, whereas the grid with a boundary distance enlargement of 0.5 indicated  $C_D = 0.51$ . Average lift coefficient is observed as negligible ( $C_L \approx 0$ ) for all test cases. Boundaries on the initial grid were placed at 18d downstream and 6d upstream the centre of the wheel, with the total test section horizontal width and vertical height of 4.5d and 6d respectively. For comparison purposes of the rear wake region,

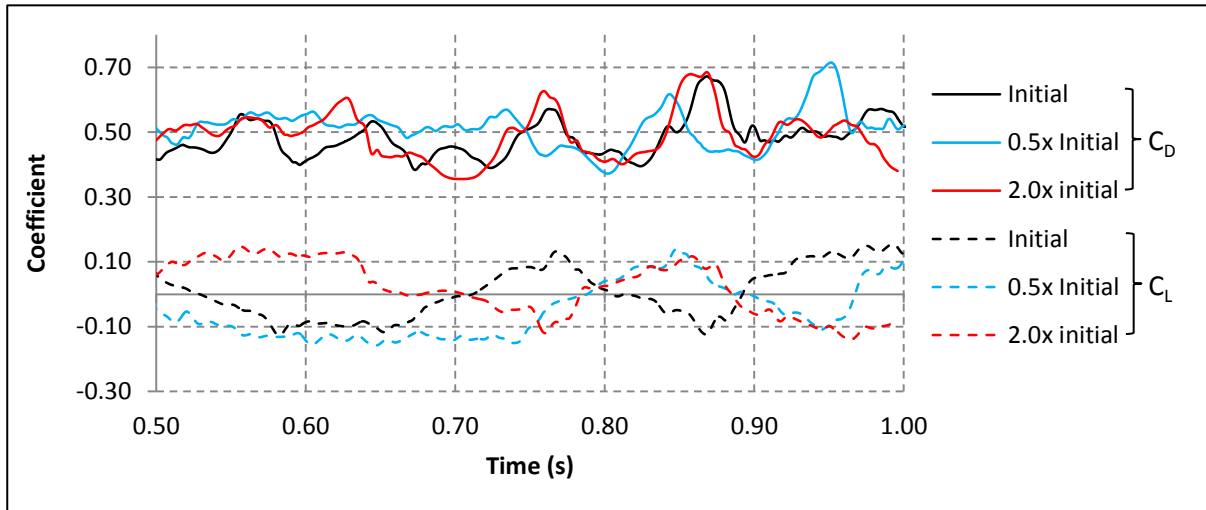


Figure 72 - Force coefficient against real time, for different far-field boundary distances

boundary distances downstream the centre of the wheel were placed  $15d$  [29],  $16d$  [31], and  $20d$  [41], showing that the downstream distance of  $18d$ , from the initial grid in this study, is of sufficient distance and in range to similar computational studies carried out. Vertical boundary distances were also in range, with other studies showing boundary distances of  $2.9d$  [29],  $5d$  [31] and  $10d$  [41]. It is important to note that although vertical boundary distances as small as  $2.9d$  were used by McManus & Zhang [29], the present study is conducted with the wheel positioned at the vertical centre of the computational domain (free-air), as opposed to previous studies investigating a wheel in contact with the ground. Horizontal domain boundary distances had a length of  $10d$  [31, 41], although a width of  $3.66d$  was used by McManus & Zhang [29]. This study used a horizontal boundary distance of  $4.5d$ , which is of a similar length to that used by McManus & Zhang [29]. However, as McManus & Zhang [29] did not experience any boundary interference with their reduced horizontal boundary length, with results from Figure 72 showing almost negligible effects with increasing boundary distances, the horizontal boundary distance of  $4.5d$  was kept unchanged. Therefore, the initial grid was used for the final study, also resulting in the computations being more computationally efficient.

### 3.3.5 Mesh Refinement Study

A mesh refinement study was also carried out to find the most appropriate sized grid that will identify key features in the flow field to a reasonable level of accuracy, whilst keeping the computational time to a minimum. As has been mentioned previously, a larger and more refined grid will provide better results but with a significant computational expense, therefore, it is vital that an appropriate sized grid is chosen due to the computational and time

limitations present for this study. To perform an accurate mesh refinement study, the grids have to be refined in all three coordinate directions, keeping the denser regions (where key characteristics, such as separation, are expected) dense so flow features can be accurately observed. Grids of 3, 4, 5 and 6 million cells were created and simulated. After plotting the acquired data of  $C_D$  &  $C_L$  for each grid on a graph, the trend (as expected), was observed to be highly oscillatory (Figure 73). Lift coefficient (dashed curves) averaged to approximately zero for all cases. All grid sizes showed variations in  $C_D$  in the region  $0.33 < C_D < 0.35$ . The overall average of the data for each grid size indicated  $C_D = 0.35$ , with both the individual five and six million cell grids showing this value.

Earlier investigations used a structured - 2.9 million [29], structured – 2.5 million [9], unstructured – 3.1 million [41], hybrid – 9.1 million [30] and hybrid – 1.6 million [31] grids. All the grids from these previous studies are comparable in size to the grid consisting of 5 million cells in this study. Grids that are noticeably lower in grid size which were used for simulation, comprised of a simplified wheel geometry [41, 9], or used a hybrid mesh type [31], both requiring less cells to produce an acceptable grid. Although a hybrid grid structure was used in [30], the grid size totalled to 9.1 million cells as a result of smaller but complex wheel components (such as brake ducts, fairings, calliper) being included in configuration.

With a need to finalise the mesh size, the grid consisting of 5 million cells was chosen, as the mean drag calculated from Figure 73 corresponds to this grid size. Even though the 6 million grid is more refined, giving the same average value of  $C_D$ , a higher computational time would be required if this grid was to be used.

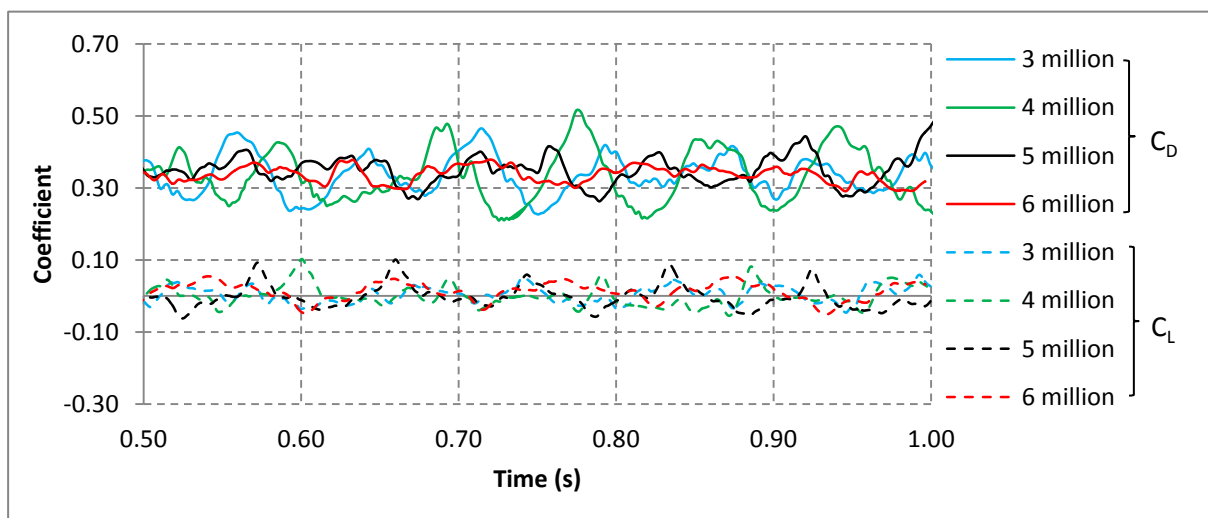


Figure 73 - Force coefficient against real time, for different sized grids

### 3.3.6 Time Step Study

Similar to McManus & Zhang's [29] computational procedure, a time step of 0.01 (non-dimensionalised by wheel diameter and free stream velocity) was used with the initially tested free stream velocity of 70m/s. Although the free stream velocity was reduced to 40m/s after preliminary tests, the time step size ( $\Delta t = 6 \times 10^{-5}$ ) was unchanged when using the revised free stream velocity (though the revised non-dimensionalised time step was 0.0057), as the flow characteristics should be captured more accurately with a smaller time step. However, a time step study was completed with additional simulations, conducted with a time step size of  $\Delta t = 1 \times 10^{-4}$  and  $1 \times 10^{-5}$ . After plotting drag and lift coefficients for each test case (Figure 74), it was observed that, similar to the mesh and boundary refinement trends, the largest and smallest time step peaked between  $0.25 < C_D < 0.5$ , with the initially tested time-step showing a trend in between. Averaging this data showed  $C_D = 0.35$ , therefore indicating using the initial time step size  $\Delta t = 6 \times 10^{-5}$  (or 0.0057 non-dimensionalised by wheel diameter and free stream velocity) would be suitable. Additionally a similar trend was observed for the lift coefficient, as the average of the lift coefficient data obtained produced  $C_L \approx 0$ . Therefore a non-dimensionalised time step of 0.0057 was used for the remainder of this study. Earlier investigations used time steps of 0.01 [29], 0.0046 [30] and 0.005 [47], (all non-dimensionalised by wheel diameter and free stream velocity). The larger time step (0.01) used by McManus and Zhang [29], is due to the lower Reynolds number used in their study. However, time steps similar to that chosen for this study were used in previous studies [30, 47], showing that using a larger time step was found to be too coarse for capturing the unsteadiness in the wake [30].

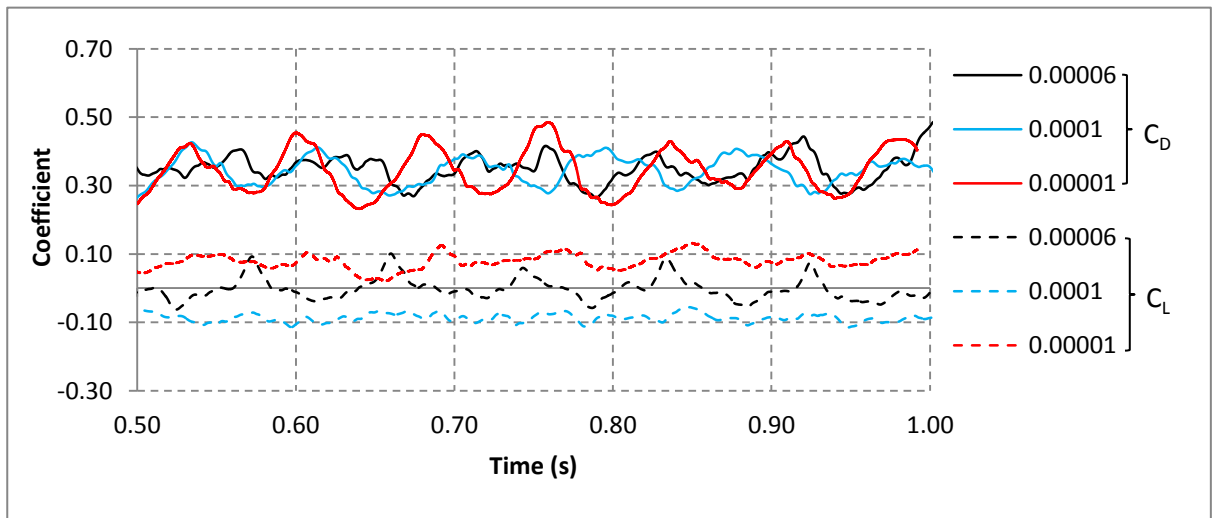


Figure 74 - Force coefficient against real time, for different time-steps

### 3.3.7 Final Computational Grid

On completion of the refinement studies, the final computational grid used as a baseline for this study comprised 80 blocks, positioned both within the near-field (32 blocks), Figure 75, and far-field (48 blocks). The distribution of grid points from a single block to its adjacent block was carefully analysed, to make sure that there was no significant jump/increase in cell distributions (as shown in Figure 70(b)), as discontinuities in the flow field can be seen if the solver is not able to calculate the flow accurately between cells. Boundary conditions were kept the same as described in section 3.3. A schematic of the final computational domain is detailed in Figure 76.

For all simulations, the wheel centre was positioned at the geometric centre of the height and width of the domain, positioned at a distance  $z_2 = 6d$  downstream from the inlet plane.

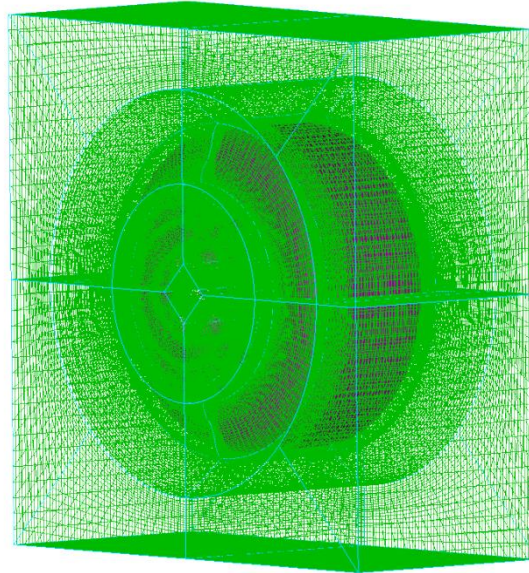


Figure 75 - Near-field computational grid

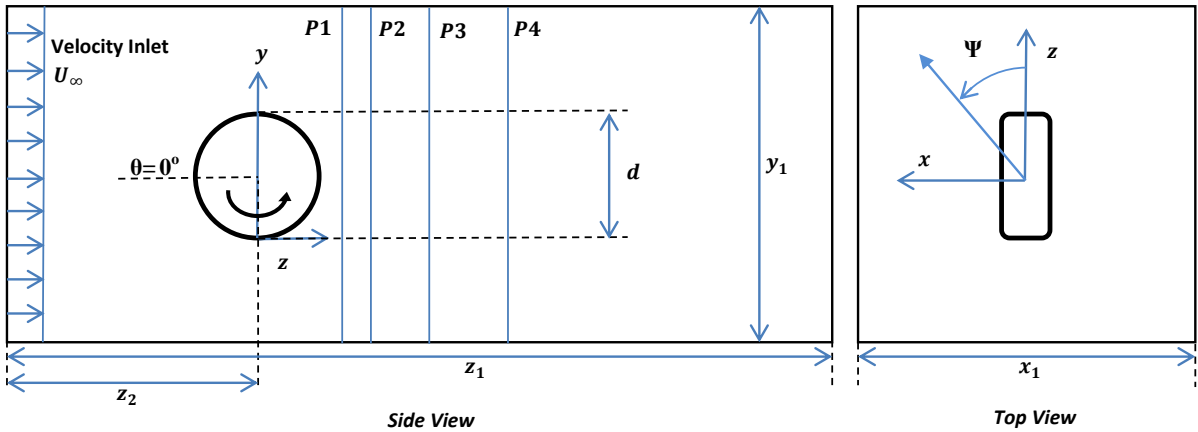


Figure 76 – Geometry of computational domain



Therefore a final computational domain with measurements  $z_1 = 24d$  in length,  $x_1 = 4.4d$  in width and  $y_1 = 6d$  in height, comprising of 5 million structured hexahedral cells was selected. Figure 77 shows the final baseline computational grid. Data acquired for this investigation from planes P1, P2, P3 & P4, as shown in Figure 76, are taken at distances of  $0.75d$ ,  $1.0d$ ,  $1.5d$  &  $2.5d$  from the centre of the wheel respectively.

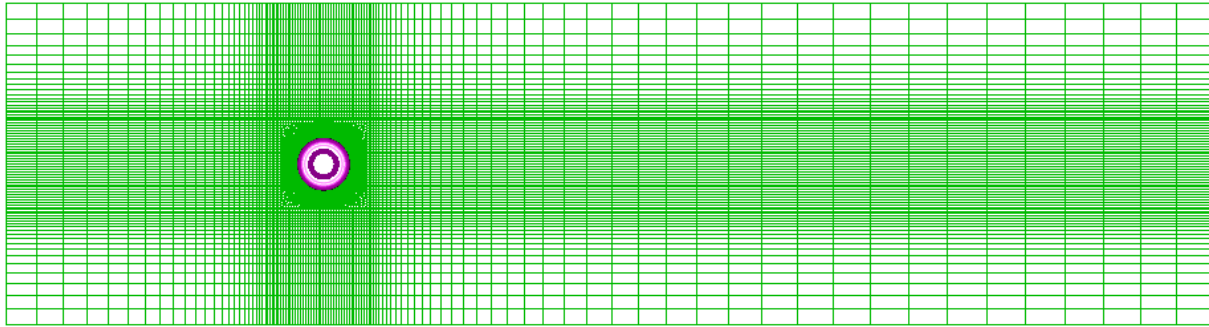


Figure 77 – Side view (+x) of computational grid

### 3.3.7.1 Modelling Yaw

Yaw angles between  $\Psi = 0 - 15^\circ$  at  $5^\circ$  intervals were selected to analyse the typical crosswind approach conditions of an aircraft. For the grids incorporating wheel yaw, the blocks, domains and connectors in the near-field region of the baseline grid ( $\Psi = 0^\circ$ ), including the wheel, were selected and rotated with centre of rotation positioned to the geometric centre of the wheel, anticlockwise by an angle ( $5^\circ$ ,  $10^\circ$  or  $15^\circ$ ) about the y axis representative of the yaw angle required, in the mesh generation software Pointwise™. The far-field mesh was

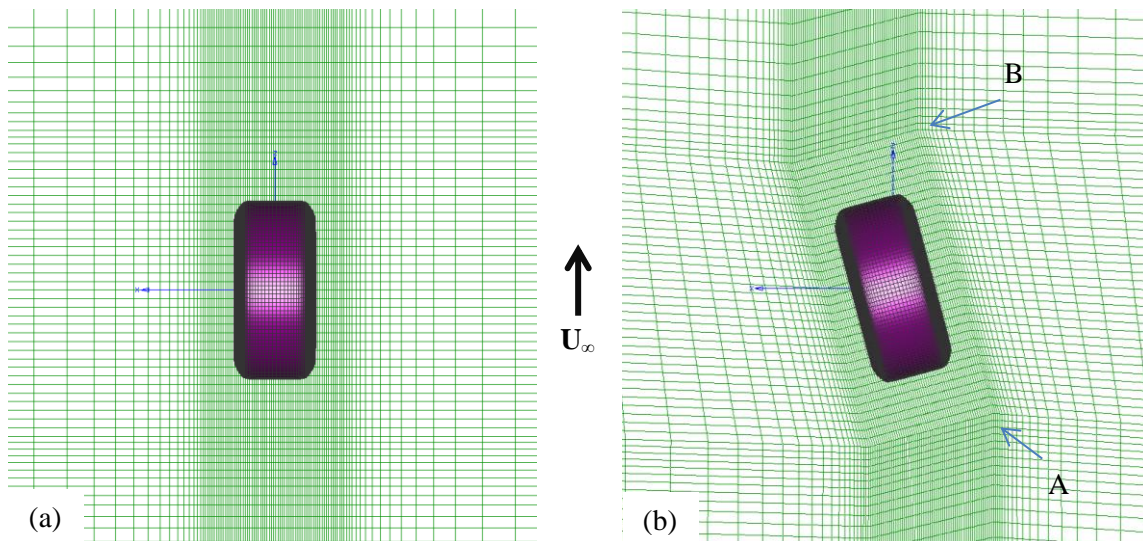


Figure 78 – Top view of Computational grid including wheel showing applied yaw angle, (a) no yaw (b)  $15^\circ$  yaw



automatically reformed around the yawed near-field blocks, to complete the computational domain, maintaining the integrity, dimensions and quality of the grid. Top view computational grids of the zero yaw and 15° yawed configurations are shown in Figure 78, clearly illustrating (on the 15° yaw case) the intersection between the near-field and the far-field blocks upstream (A) and downstream (B) of the wheel. Rotating both the near-field blocks and the wheel, ensures the grid spacing around and on the wheel surface is maintained and corresponds to that of the zero yaw case as much as possible, therefore once simulated, the influence of applied wheel yaw, only, could be observed.

### 3.3.7.2 *Modelling Rotation*

The effect of rotation on the wheel was modelled, in Fluent™, by changing the boundary condition on the wheel to ‘moving wall’. Thereafter, the angular velocity ( $\omega$ ), axis and direction of rotation were required. The angular velocity ( $\omega$ ) was calculated from Equation 10 and set to 192.31rad/s, equivalent to the free stream inlet velocity  $U_\infty=40\text{m/s}$ . The wheel was rotated in the direction of  $\theta$  (anticlockwise as shown in Figure 76) about the centre (x-axis) of the wheel.

$$\omega = \frac{U_\infty}{r} \quad \text{Equation 10}$$

In order to model the combined effect of yaw and rotation, the wheel had to be yawed with rotation applied on the wheel before simulation. Yaw was implemented on the wheel as has been described in the previous section of this chapter, however the application of rotation was changed as this is a 3D problem. With a yaw angle applied on the wheel, the centreline wheel axis had shifted, consequently changing the rotational axis (parallel to the centreline of the wheel). Referring to Figure 79, the coordinate axis for an un-yawed wheel, from a top view, is marked by the +x & +z axis. Once a yaw angle ( $\Psi^\circ$ ) is applied, the geometric axis of the wheel is also yawed, providing the revised geometric axis to be marked  $x'$  and  $z'$ . As the application of rotation on the wheel surface in Fluent™ requires a rotational axis and direction, this information was entered in the form of a ‘point and normal’ of rotation. Due to the yaw angle being applied on the wheel by rotating the wheel about the wheel centre, this point would not change and would also lie on the rotational axis ( $x'$ ) of the yawed wheel

configuration; therefore this point was kept unchanged. However, to obtain  $x$ ,  $y$ ,  $z$  coordinates for the normal, the initial geometric axis (Figure 79 – solid arrows) need to be resolved in to their horizontal and vertical components (Figure 79 – dashed arrows) representative of the applied yaw angle. Resolving these values mathematically would provide  $x' = \cos (\Psi)$ ,  $y' = 0$ ,  $z' = -\sin (\Psi)$  for the normal direction vector, thereafter specifying the angular velocity ( $\omega = 192.31\text{rad/s}$ ), rotation would be applied on the wheel.

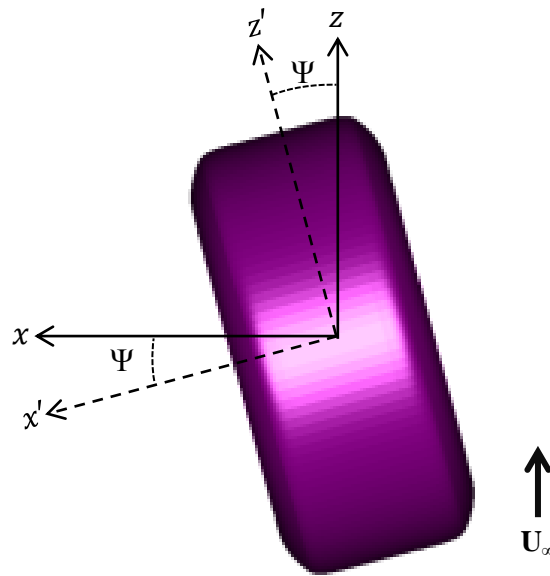


**Figure 79 - Representation of rotational axis on a wheel with applied yaw angle**

## 4. Validation of Computational Methodology

Before presentation and discussion of the results from the computational analysis, where available and appropriate, both experimental and computational results available in the current literature will be compared to the baseline case of the isolated, non-yawed, wheel in

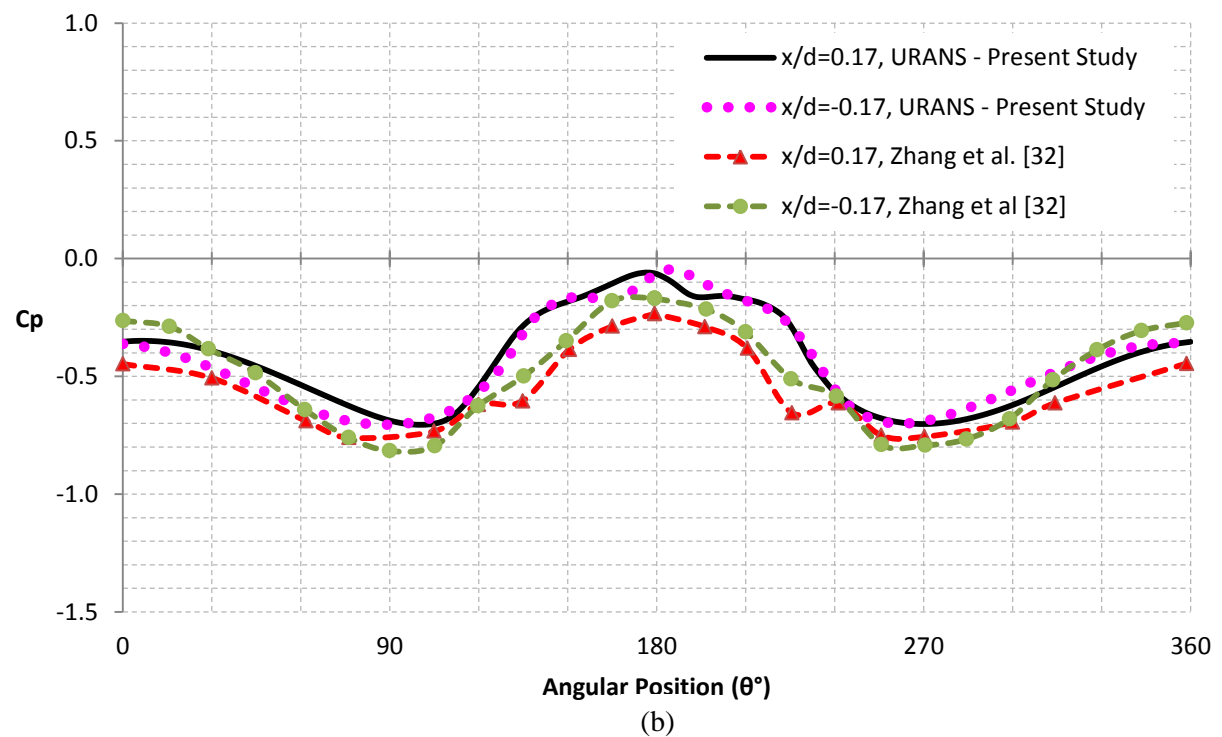
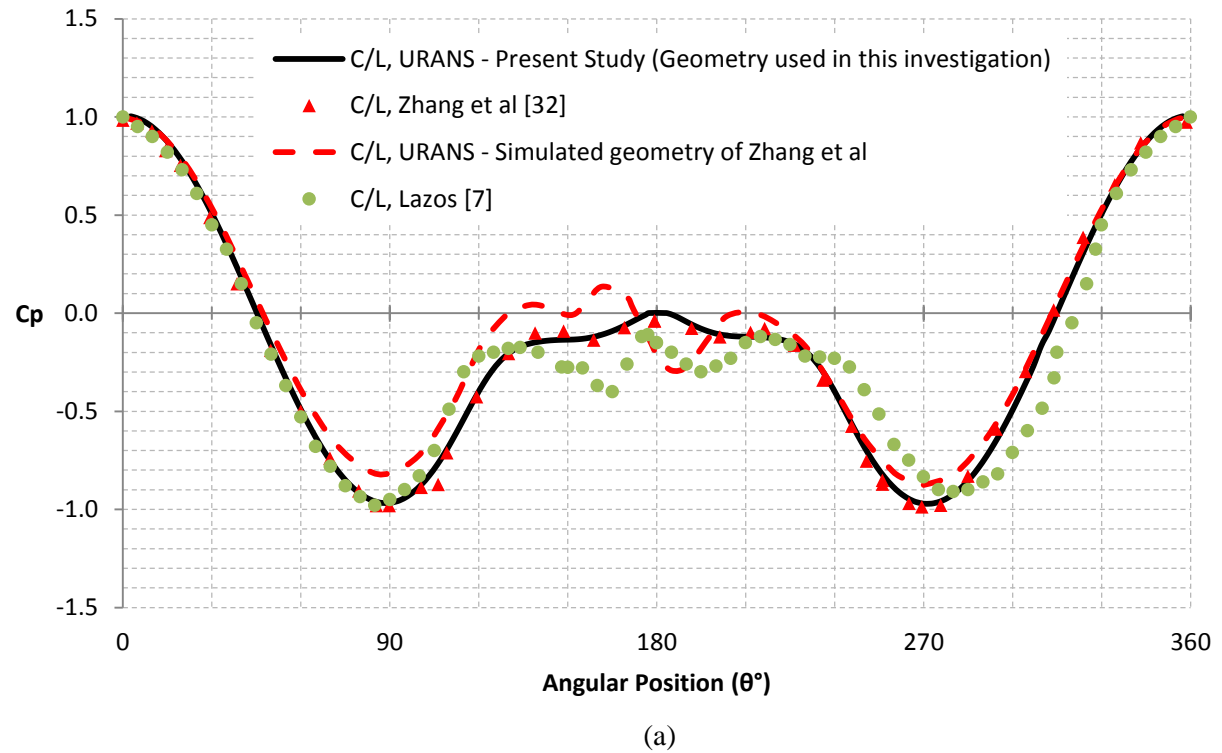


Figure 80 – Comparison of centreline mean pressure coefficient with experimental literature, (a) centreline  
(b)  $x/d = \pm 0.17$

free-air, to validate and verify the computational methodology. Where possible, this validation involves the use of both mean surface data as well as near-field wake data, however, particularly for the latter, limited data exist for comparison.

As an initial comparison, Figure 80(a) shows the mean surface pressure coefficient along the centreline of the wheel obtained from the current URANS study, plotted against centreline experimental data manually extracted from the two studies by Lazos [7] and Zhang et al [32]. The illustrated graphs for comparisons indicate excellent agreement to [32] over most of the wheel centreline circumference with maximum deviations found to be typically less than  $\Delta C_p \approx 0.05$ , although Zhang et al [32] involved a dedicated experimental investigation of an isolated wheel with asymmetric hub detail. Agreement with Lazos [7], which was extracted from the front wheel of a four wheel landing gear model, is much less correlated, but nevertheless, does show general qualitative agreement with that of the isolated wheel flow cases presented. For both comparisons, it is evident that the URANS solution tends to predict higher mean pressure coefficients within the wake region surrounding  $\theta = 180^\circ$  than those obtained experimentally. This trend has been identified in other studies comparing both URANS to higher-order computational methods as well as experimental studies [9]. Flow separation is predicted to occur where pressure recovery ceases [22, 29]. Comparing the data from Figure 80, flow separation along the centreline tends to occur earlier ( $\theta \approx 140^\circ$  &  $220^\circ$ ) on the current URANS results with more asymmetric wake behaviour, indicating these regions are in agreement with [7, 57], and that the influence of the subsequent rear wheel is significant on the aerodynamics of the front wheel of a landing gear. Similarly separation was observed at  $150^\circ$  &  $220^\circ$  in Zhang et al [32],  $148^\circ$  &  $226^\circ$  in Lazos [7]. From the upper rear wake analysis by McManus & Zhang [29], separation was observed at  $232^\circ$  &  $225^\circ$  from the S-A & RKE models respectively. Comparison of these separation locations to those observed in this present URANS study are in very good agreement with near exact agreement with the experimental study [32] and up to variations by 3% when compared to [7]. Differences between the previous studies [7, 32] are expected as these separation locations were extracted from a wheel from a four wheel landing gear configuration and a wheel in contact with the ground respectively. The presence of support struts/axles was also found to complicate the wake characteristics for this configuration [7]. Comparing experimental mean pressure coefficient data, Figure 80(b), at  $x/d = \pm 0.17$  from the wheel centreline, results also shows reasonably coherent correlation between the two sets of isolated wheel data. This is particularly evident in regions on the wheel where attached flow is expected to occur in the

regions of  $\theta < 120^\circ$  and  $\theta > 220^\circ$ . Off-centreline surface pressure is known to be very sensitive to wheel profile [22] and from Figure 80(b), the qualitative differences evident, together with differences in hub detail are thought to be the main factors responsible for the observed differences in the data.

The wheel geometry used for the experimental investigation in [32] was also drawn on CAD software and subsequently simulated in an attempt to validate the computational methodology used in the present study. The boundary conditions and computational domain were identical to that used for this present URANS study. Centreline surface pressure distribution obtained from the simulation Figure 80(a), shows general agreement with the experimental work. The overall trend of the curve is also generally over-predicted by the URANS computations, though this has also been observed when comparing URANS to experimental results [9]. Computationally modelling this geometry provided separation angles of  $\theta = 132^\circ$  &  $\theta = 209^\circ$ , showing general agreement with the experimental study with variances of up to 13%. Overall, results between the computationally modelled geometry of [32], the experimental data and the present URANS study are in general agreement. Discrepancies are present in the wake region; however the wheel geometries are different as the present URANS study comprises of two near-identical hub cavities which would essentially demonstrate a symmetrical flow-field on either sides of the wheel.

Additional surface pressure data measured on the centreline of the front wheel of a four wheel rudimentary landing gear configuration (Figure 81) are used for comparisons of this study. Venkatakrishnan & Karthikeyan [48] had also used the work of Lazos [7] to compare their pressure data and is shown in Figure 81. As both of these studies used a four wheel landing gear configuration, stagnation at  $\theta = 0^\circ$  did not reach the expected value of unity, as stagnation was shown to occur slightly inboard of the wheel centreline towards the centre of the configuration [7, 47]. In agreement with Lazos [7], the pressure distribution on the ground side showed generally lower values for  $C_p$  due to the presence of the truck on the wing side obstructing the flow field. Overall, the pressure distribution obtained in [48] was in good agreement up to  $\theta \approx 100^\circ$  on the top and bottom surfaces of the wheel from the front stagnation region of the wheel. Beyond this point, significant differences are observed between the two investigations on the rear surface of the front wheel and were thought to be caused by the lower Reynolds number of  $6 \times 10^5$  used in [7] with untripped wheels, as opposed to  $1 \times 10^6$  used in [48] with tripped wheels, resulting in larger base pressures for laminar flows at lower Reynolds numbers than for turbulent flows. Comparing this pressure

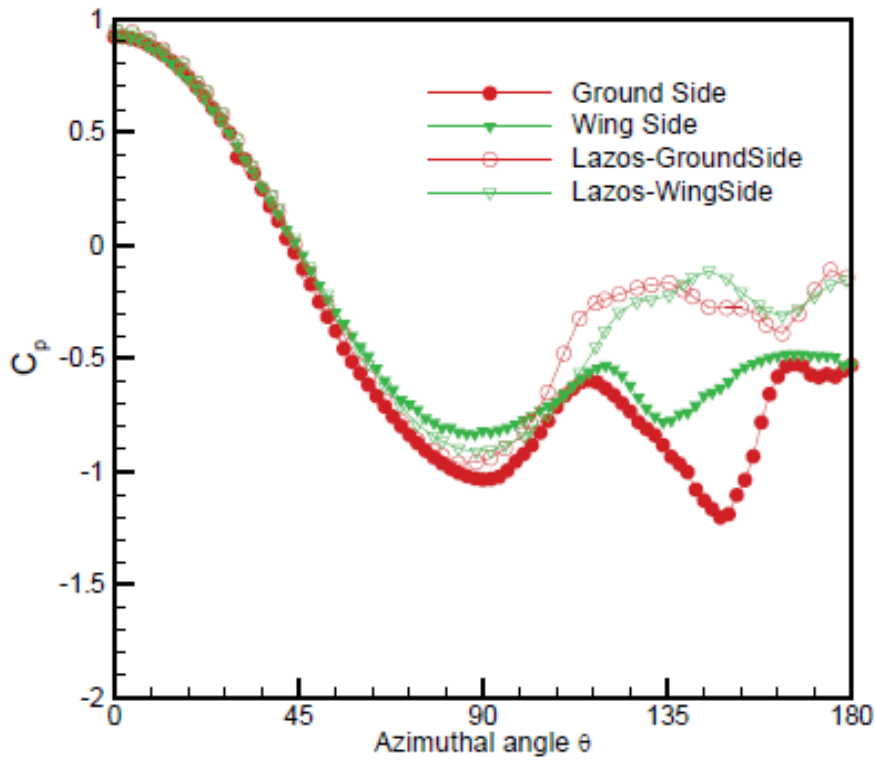


Figure 81 - Centreline pressure data on front wheel [48]

distribution with that observed in this study Figure 80(a), similar to Lazos [7] the general trend is also in agreement on the front face of the wheel up to  $\theta \approx 100^\circ$ . Separation was found to occur earlier in [48] at  $115^\circ$  and  $240^\circ$ , and with a subsequent negative peak  $C_p$  of -1.2 observed at  $148^\circ$  on the ground side indicating flow acceleration. The presence of the truck, especially in [48] consisting of a rectangular shape with sharp corners, as opposed to the circular shape in [7], was considered to significantly affect the flow field in the wake of the wheel.

Pressure distributions obtained on the front stationary wheel by Stapleford & Carr [34] are shown in Figure 18(a), although direct comparisons will not be possible due to the difference in ground clearances, as their maximum ground clearance was 2.0 inches compared to the ‘free-air’ configuration used in this study. However, Figure 18(a) does show general agreement to that observed in this study, Figure 80(a). Negative pressure peaks from [34] reached approximately  $C_p = -2.0$  at the top and bottom of the wheel, indicating increased flow acceleration probably due to the effect of the ground. Separation was predicted to occur at  $120^\circ$  from stagnation on both top and bottom surfaces of the wheel indicating an angular position of  $\theta = 120^\circ$  and  $\theta = 240^\circ$ , with a base pressure just below unity showing general agreement with the present study.

Further comparisons made to the pressure distributions obtained from the work conducted by Li et al [47], show better agreement to the current study than the work by Stapleford & Carr [34]. Figure 82(a) shows the pressure distributions along the centreline of the front left wheel taken at 13 different selected time instances, as indicated by the visible thickness in trend line (A). Similar to other landing gear investigations providing results for surface pressure distribution, a stagnation  $C_p$  slightly less than unity is observed due to the flow stagnating towards the centre of the configuration. Subsequently, a pressure distribution similar to [7, 32, 34] is observed. Separation is observed in [47] at  $\theta = 140^\circ$  &  $230^\circ$  (B), respective to the defined azimuthal angle used for this study, and were found to be in very good agreement with [7, 32] and this present URANS study, although showing general agreement with [48, 34]. Base pressure in the rear wake (C) was also shown at a value very close to zero, showing good agreement to [32] and the present URANS study, although slightly higher ( $\Delta C_p \approx 0.2$ ) than that observed by Lazos [7] as shown (D) in Figure 82(b). This decrease in pressure with angular position in the rear wake is suggested due to the differences in landing gear configurations between the computational [47] and experimental work [7], and therefore was not used for quantitative validation, but to validate the  $C_p$  trend within the flow-field.

Comparisons of mean drag coefficient between the two isolated wheel studies (Table 1) also show reasonable agreement. Results of drag coefficient reported in [32] for both the wheel and support sting without artificial boundary layer tripping ( $Re_n > 1 \times 10^6$ ) were reported as  $C_D \approx 0.29-0.3$ . Overall drag coefficient for the present URANS study, modelling the wheel only at  $Re_n = 1.1 \times 10^6$ , was measured at  $C_D = 0.35$ . If consideration is given to the influence of the

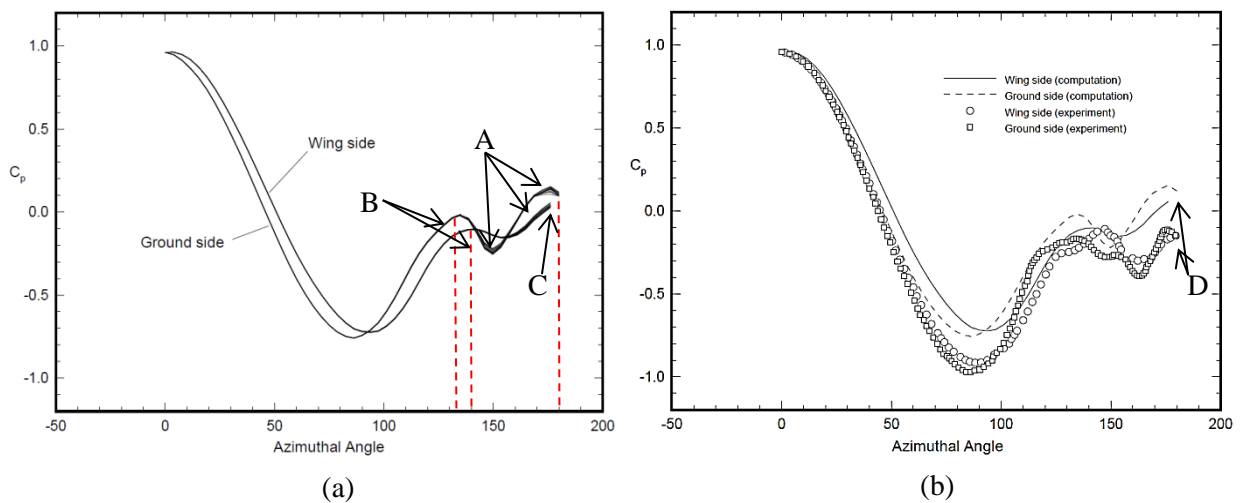


**Figure 82 - Surface pressure distribution along the centreline of the front left wheel; (a) single front left wheel, (b) with comparisons to Lazos [7], from [47]**

sting drag supporting the wheel from [32] whose individual drag was estimated at  $C_D = 0.11$  (un-tripped), inferred overall wheel drag coefficient reduces to  $C_D \approx 0.19$ . It should be noted however, that in accounting for this difference, the A2 wheel profile used in the present study, has near-symmetric, wholly evacuated hub detail allowing the generation of further flow stagnation regions within the inside of the hub region. This will be discussed in subsequent sections. Allowing the flow to enter this region and stagnate would further increase the overall drag of the wheel, with previous studies showing differences in exposed and covered hub detail representing as much as a further 27% increase in drag [33, 59]. Additionally,  $C_D = 0.26$  from the computationally modelled geometry from [32] showing general agreement to both results presented in Table 1. However, deducting the drag contribution from the hub of the A2 wheel (stated in [22] of  $C_D = 0.08$ ) from the present URANS coefficient, an overall drag coefficient of  $C_D = 0.27$  would be obtained showing good agreement to the URANS computational geometry used in the experimental study [32].

	$C_D$	$Re_n$
<b>Zhang et al [32] – Wheel with Sting</b>	0.29	$1.3 \times 10^6$
<b>Present URANS study</b>	0.35	$1.1 \times 10^6$
<b>Simulated geometry of Zhang et al</b>	0.26	$1.3 \times 10^6$

**Table 1 - Drag force coefficient with comparisons to [32]**

Moreover, it should also be noted that the hub detail, described in the experimental study [32] and shown in Figure 83, on the ‘boss’ side (a) has no perceivable evacuated area, exposing the flow field to a much more streamlined wheel side producing less internal stagnated regions of flow, and conceivably, less aerodynamic drag. This reasoning is also supported from estimates of individual wheel drag coefficients extracted from ‘no hub’ landing gear wheels ( $C_D \approx 0.15$ - $0.16$  [9]). Inherently, these configurations are much more streamlined inhibiting free stream flow impingement onto downstream internal hub surfaces. Additionally, although URANS computations are used for general comparison and does show good agreement, this method was also observed to over-predict drag coefficients up to 9.7% when compared to experimental results modelling the turbulent flow past a cylinder. However, drag force predictions using LES & DES showed variances up to 1.2% due to their capabilities in capturing small and finer detail within the flow-field [18, 60], however due to time and resource constraints, it was not possible to model an LES or DES solution for this study.



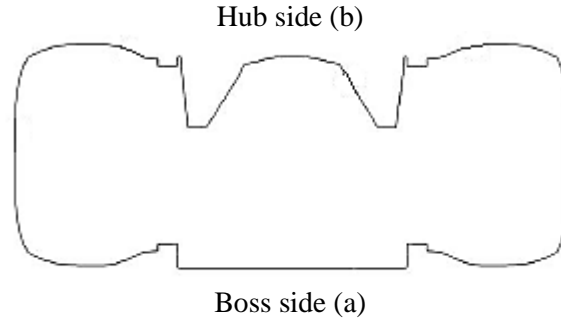


**Figure 83 - Wheel geometry used in [32], indicating 'hub side' & 'boss side'**

Qualitative comparisons of the general wake dynamics observed from the current study also show general agreement with other published literature. Figure 84 provides baseline wake information representative of the centreline, non-dimensional, streamwise velocity at wheel mid-width. Considering Figure 84(a) initially, the baseline wake characteristics are similar in general topology to the isolated wheel experimental investigation by Zhang et al [32] presented in Figure 84(b) and the rear wheel wake characteristics of the four-wheel complete landing gear study presented by Lazos [7]. Characteristics of this wake are the contours of non-dimensional streamwise velocity magnitude emanating from directly behind the wheel with very low flow velocity experienced at wheel mid-height. URANS results from the present study, calculated within the inner-most region of the wake, were very close to zero, with results observed in the literature reporting a similar magnitude both behind an isolated wheel [32] and within the wake of the rear wheel of a four-wheel landing gear [7]. Contour plots of non-dimensional streamwise velocity at mid-height ( $y/d = 0.5$  – Figure 85) also show

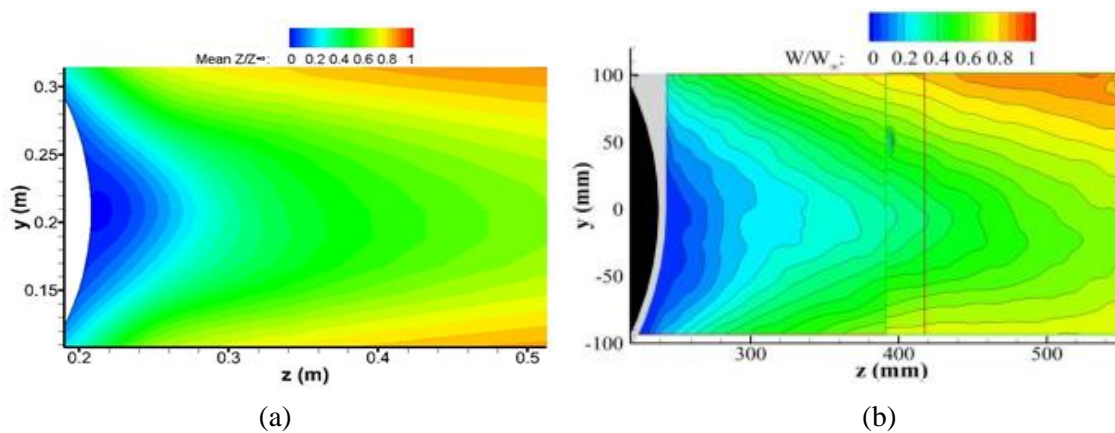


**Figure 84 – Contour plots of streamwise velocity on wheel centreline plane  $x/d=0$ ; (a) present study, (b) from [32]**

general qualitative agreement with similar topology presented for both the ‘simple’ and ‘complex’ hub configurations presented in Zhang et al [32]. Evident in both of these comparative cases, are a pair of near symmetric regions of flow velocity behind the wheel. Non-dimensionalised mean y-velocity in the near wake centreline plane of the wheel is shown in [32] for both the simple and complex hub. Comparison of this data from the simple hub configuration (closest in wheel configuration to the wheel used in this study) illustrated in Figure 86(b), to the data obtained in the same centreline plane in this study Figure 86(a), shows very good agreement in shape and magnitude. Negative & positive y-velocity in the centreline rear wake indicates the flow travelling vertically downwards & upwards respectively, due to the combined down-wash, up-wash and recirculation of the counter rotating vortex pairs formed behind the wheel. The four vortices observed in this URANS study correspond to those found by Zhang et al [32] and to Cogotti’s [36] theory for the formation of counter-rotating vortex pairs behind a stationary wheel, Figure 28(a).

Comparison of rear surface flow features from [48], as discussed earlier in the literature, shows similar features to those observed in this study. As illustrated in Figure 87, surface streamlines show a stable focus (SF) on the upper rear section of the wheel in both configurations, indicating good agreement in both topology and position. The predicted position of this focus in [48] was at  $\theta = 210^\circ$  (note that Figures in [48] were presented with angular position measured clockwise from the inlet, therefore for comparative reasons, these angular positions are re-defined as  $360^\circ - \theta$ , corresponding to the angular position used in this

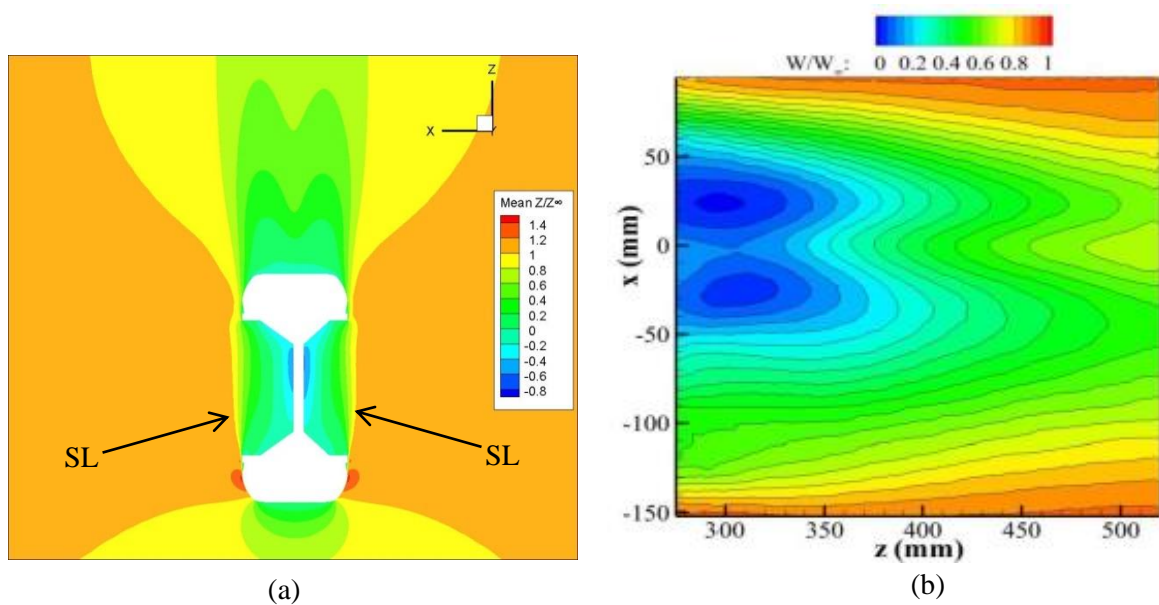


**Figure 85 – Contours plots of streamwise velocity on wheel centreline plane  $y/d=0.5$ ; (a) present study, (b) from [32],**

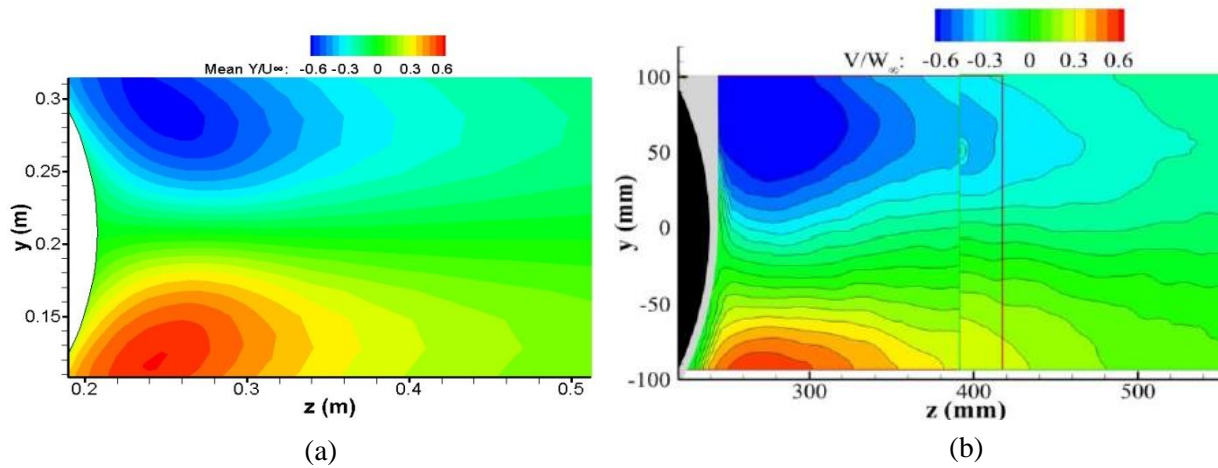


Figure 86 – Contour plot of y-velocity on wheel centreline, at  $x/d=0$ ; (a) present study, (b) from [32]

study). The position of SF in this present URANS study is at  $\theta \approx 226^\circ$ . Additionally a saddle point (SP) was located in this study at  $\theta \approx 190^\circ$  compared to those from the experimental results [48] being predicted at  $\theta = 195^\circ$ . These positions are in good agreement with maximum difference in focus (SF) position  $\approx 8\%$  and saddle point position (SP)  $\approx 2.7\%$ . An unstable node (UN) is observed on the rear surface of the wheel in [48] at  $\theta = 170^\circ$  and is also observed in this present study at  $\theta \approx 180^\circ$ , comprising a difference of 6% in position. These small deviations in the angular positions of these characteristics were suspected to be due to

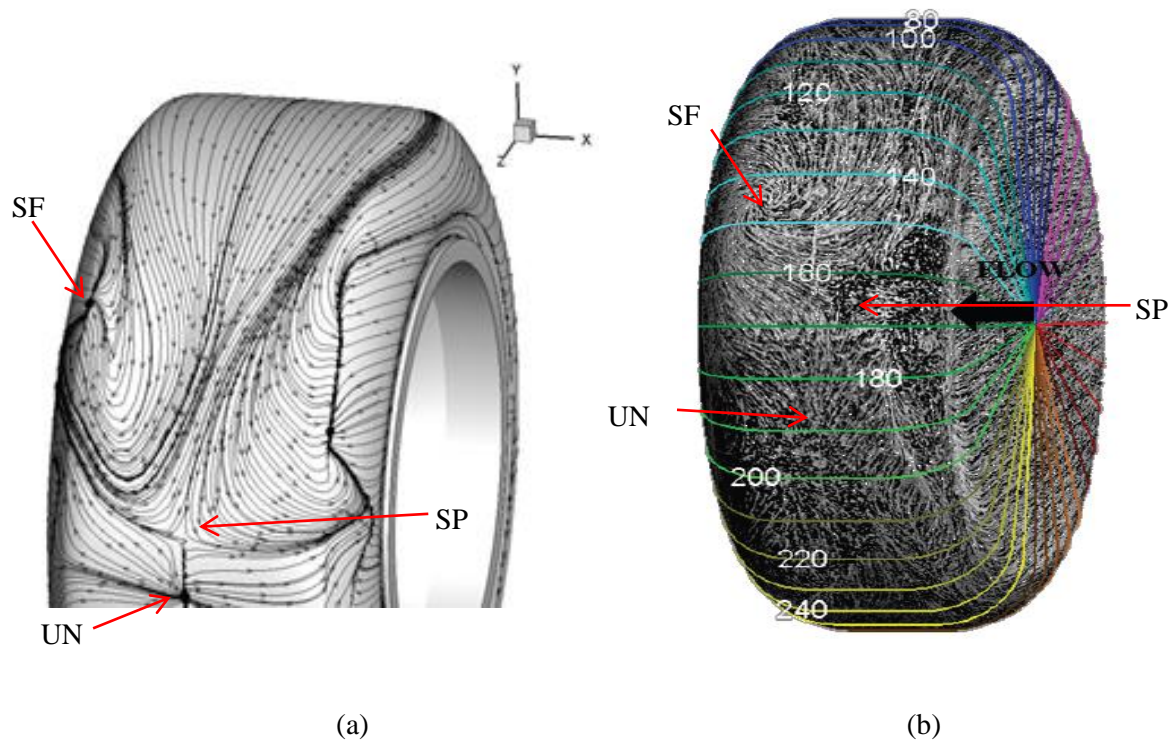
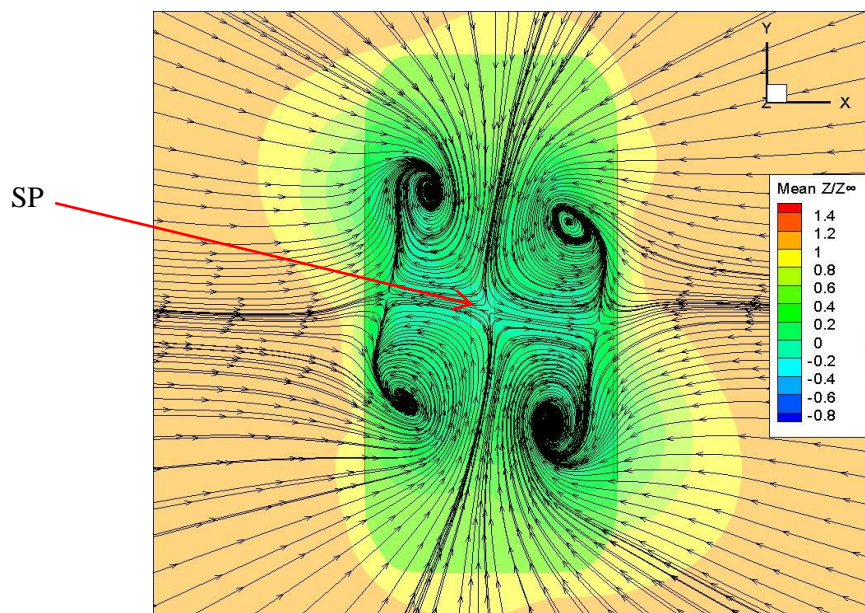


Figure 87 – Streamlines on the upper rear surface – (a) present URANS study, (b) front wheel [48]

the difference in geometry. The wheels in the experimental study [48] were modelled without hub cavities; therefore the flow could travel along the sides of the wheel without interacting with the hub flow. However, hub flow has been shown to affect the flow in the wake region influencing vortex position and overall drag force [22, 12].

A stable focus (SF) and saddle point (SP) were also discovered on the rear surface of the front wheel of a rudimentary four wheel landing gear [49], and were predicted in the regions of  $210^\circ \leq \theta \leq 217^\circ$  and  $195^\circ \leq \theta \leq 200^\circ$  respectively, showing good agreement to the positions observed in this study and in [48]. The configurations modelled in the literature [48, 49] are models of a full rudimentary landing gear configuration, therefore the presence of additional components such as additional wheels, truck assembly and struts would ultimately affect the overall flow-field, causing unsteadiness and asymmetry in the flow field [30, 10, 48, 12]. Additionally, as described in the literature, the flow stagnation region is shifted slightly inboard towards the centre of landing gear configuration [47, 48, 49] and is therefore a contributor to the overall asymmetry of the flow-field as opposed to the near symmetric flow-field around the front of a single isolated wheel, as analysed in this study. A saddle point can also be seen vaguely near the centre behind the wheel in Figure 12 by Zhang et al [32], although there is no reference to this position in their work. The saddle point is assumed to be a region where the three-dimensional derivatives of velocity are zero [49]. With reference to Figure 88, it can be seen that this saddle point is the region where the up-wash and downwash from the upper and lower half of the wheel, respectively, meet and get dispersed to the sides of the wheel eventually forming vortical structures.



**Figure 88 - Streamwise velocity contours with streamlines behind the wheel at plane  $z/d=0.5$**



The observed rear wake (Figure 88) is found to be asymmetric, both about the horizontal (x) and vertical (y) centreline axis. The asymmetry about the vertical (y) centreline was predicted to be due to the asymmetric hub depths, as one hub is marginally deeper than the other. However, the asymmetry observed about the horizontal (x) centreline was predicted to be due to the ‘skewing’ of the flow, to either side of the vertical centreline, directly behind the wheel due to the high Reynolds number. Additionally, due to the highly oscillatory nature of this rear wake, another reason for this asymmetry about the horizontal centreline could be due to the limited amount of unsteady data available for time-averaging.

Overall, the computational methodology was validated by comparing surface pressures, separation positions and drag force coefficients, for a quantitative comparison. Additionally, rear wake data was also compared to the available literature for a qualitative comparison, with both the quantitative and qualitative comparisons showing good agreement when compared to the literature. To provide further confidence in the methodology, the wheel geometry used by Zhang et al in their experimental investigation was also extracted and modelled computationally using the current methodology, and results also showed general agreement.

## 5. Results & Discussion

In order to understand the flow field around an isolated wheel in free air with applied yaw and wheel rotation, it is essential, as a first step, to understand the fundamental flow physics around a stationary wheel in free air with zero yaw and zero rotation. This chapter is split into four sections, first outlining the baseline flow case of the stationary isolated wheel, subsequently followed by the remaining three sections outlining the effect of yaw, rotation and both variables combined. Results obtained from the computational simulations for each flow case include mean surface pressure data, wake physics and aerodynamic forces with comparisons made to the literature where possible. A discussion will also be provided at the end of each section comparing the different flow cases for each variable.

### 5.1 Characterisation of the baseline flow case (zero yaw, zero rotation)

Primarily, the fundamental flow physics on a un-yawed, non – rotating, stationary isolated wheel is analysed. Results obtained from the URANS simulation on the flow case discussed within this section include non-dimensional vorticity magnitude, together with mean velocity direction and magnitude, mean surface pressure distribution and force coefficients. The results obtained for the two latter variables are also used in discussions in the previous chapter.

The general flow field around a single isolated wheel in free air [47, 32, 7], indicates the flow stagnating at the front face of the wheel before accelerating around the two sides, top and bottom surfaces of the wheel. Subsequently, the flow travels into the hub cavities on either sides of the wheel and impinges on the rear hub surfaces, causing the flow to circulate within the hub until the air is drawn out due to the entrainment around the sides of the wheel before separating. This causes the air to roll up over the shoulders of the wheel forming four streamwise vortices that propagate downstream into the unsteady wake region.

#### 5.1.1 Surface Pressure Characteristics

The centreline surface pressure distribution for this baseline flow case, Figure 80(a), has already been presented and discussed in the previous chapter to validate the computational methodology. Contours of mean surface pressure on the wheel and on a plane obtained at wheel mid-height ( $y/d = 0.5$ ) are presented in Figure 89. At the cross-sectional plane (c) and discussed in conjunction with (a), (b) and Figure 85(a), there is a substantial region of

stagnated air (A) located on the front surface of the wheel at  $\theta = 0^\circ$ . From this position, the flow accelerates up to 37% in excess of the free-stream velocity reaching a maximum velocity of 54.7m/s and  $C_P = -0.97$  around both the top and bottom of the wheel. Prominent on either side of this main front stagnation region (A), is a crescent shaped region of suction pressure (B) in Figure 89(c), with  $C_P = -1.34$ , where the flow, upon being fully retarded by the front face of the wheel, accelerates up to 47% of the free-stream velocity to a maximum of 58.7m/s around both sides of the wheel edges. Subsequent to these regions of flow acceleration, a separated shear layer forms over the wheel hubs, SL in Figure 85(a), with the flow found to impinge onto the back inner face of the exposed, evacuated hubs indicated C in Figure 89(c), reaching a mean pressure magnitude of  $C_P = 0.35$ . This is a near-symmetric

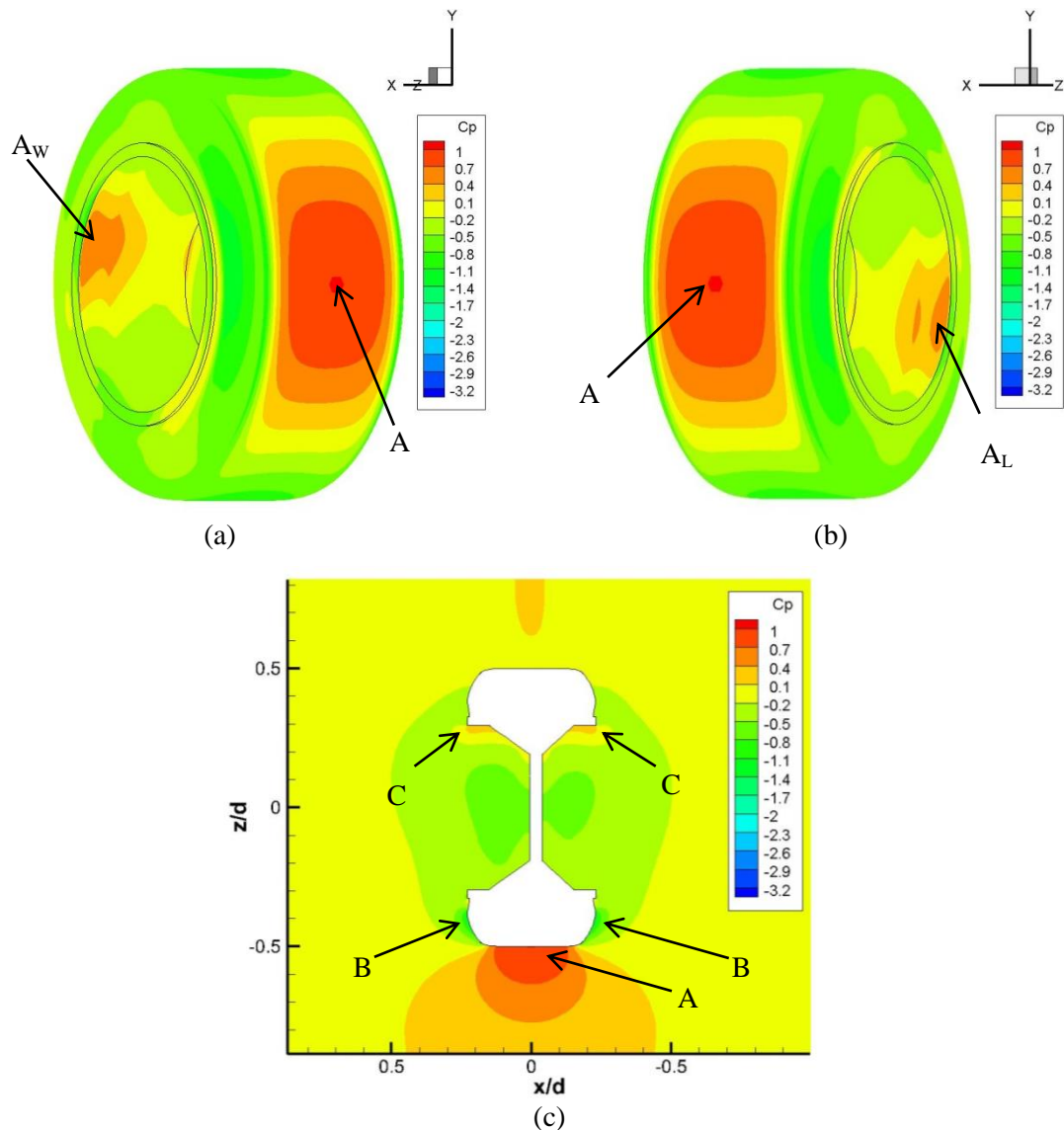


Figure 89 – Contours of mean  $C_P$  for  $0^\circ$  yaw + no rotation, (a) wheel surface looking downstream from left, (b) wheel surface looking downstream from right (c) cross-sectional plane at  $y/d=0.5$

characteristic over both sides of the wheel. The transfer of this flow momentum to the wheel through this physical mechanism is what would be expected to increase the drag force compared to the more streamlined hub configurations discussed in the literature review [22, 36, 33, 12]. After passing over the evacuated hubs, the flow reattaches to the rear side edges before being entrained within the wake behind the wheel.

### 5.1.2 Wake Physics

Considering the vorticity plot shown in Figure 90, the wake structure seems to be dominated by a primary interaction of intense down-flow from the top of the wheel and up-flow from the bottom of the wheel indicated D & E respectively in Figure 90(a), both originating from the wheel centreline  $x/d=0$ . In both cases, maximum mean flow velocity magnitude was found to be near symmetric. Results also indicate that as a consequence of these two distinct flows

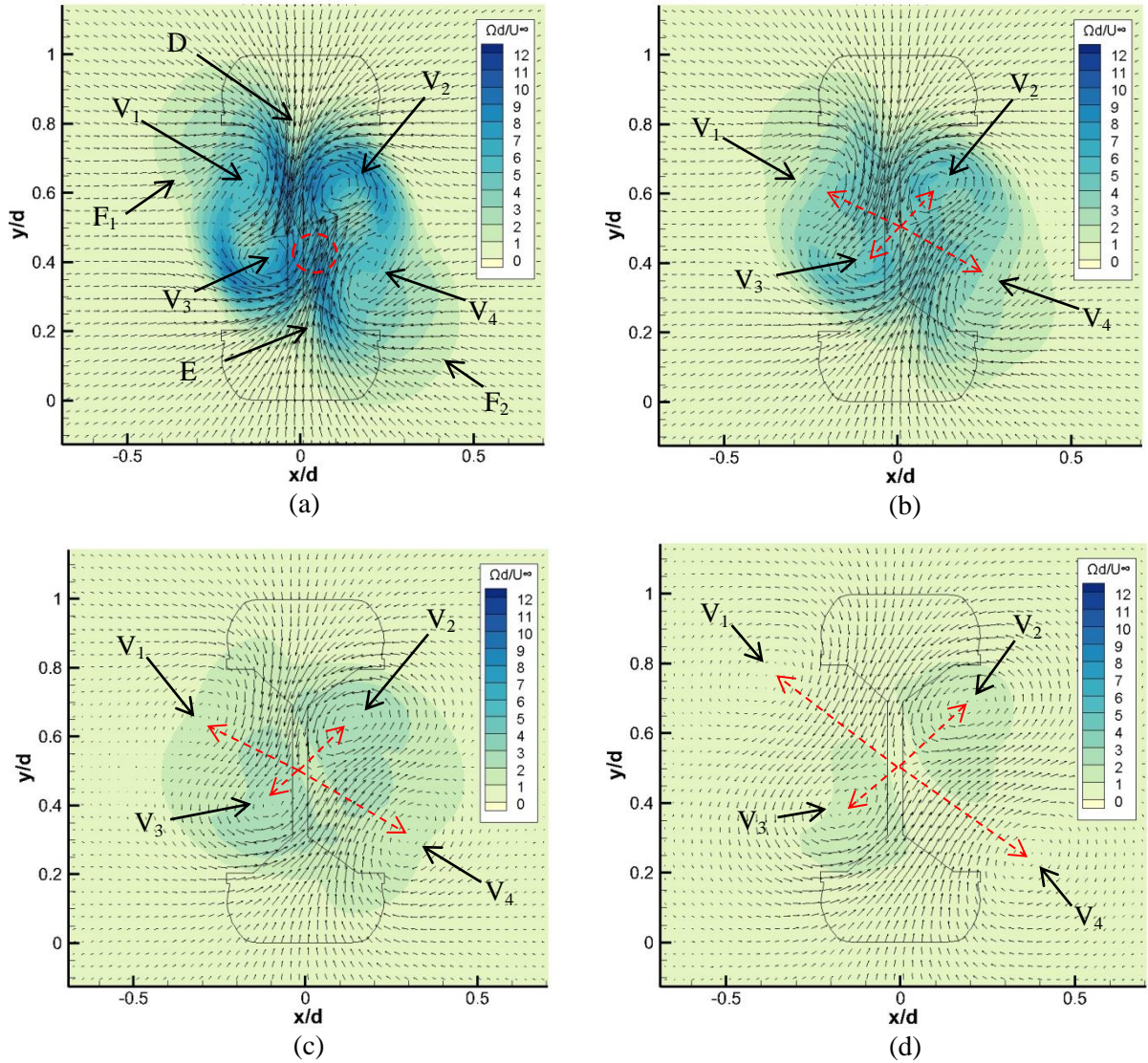


Figure 90 – Non-dimensional vorticity plots for 0° yaw; (a)  $z/d=0.75$ , (b)  $z/d=1$ , (c)  $z/d=1.5$ , (d)  $z/d=2.5$



over the top and bottom of the wheel and their interaction with the wheel side-flow, four distinct and separate vortices are formed and are observed to propagate downstream. The physical mechanisms for the generation of these separate vortical structures are fundamental to the resulting flow field in several distinctive ways [30]. As is shown in Figure 90(a), the four vortices generated play a significant role in entraining the flow from the top and bottom of the wheel, delaying flow separation and producing a much smaller wake size than would be experienced from larger aspect ratio configurations. This is a common characteristic of finite length bluff-bodies with high inherent vorticity and typically results in a drag reduction with decrease in aspect ratio [20]. Although significant, this entrainment mechanism still remains of insufficient intensity to remove the generation of a separated wake completely (full base pressure recovery), and as is evident in Figure 84(a), there remains a region of very low velocity flow on the rear surface of the wheel, defining a separated wake. Similar characteristics of the wake flow behind both an isolated wheel in free air [32], as well as the rear wheels of complete landing gears [47, 7], are detailed in the literature. Wake flow physics from [32] shows this low velocity region on the rear surface of the wheel (Figure 84(b)), and indicates that it is the central region between the positive and negative vertical velocity regions on either side of the wheel centreline recirculating due to the vortex structures. The flow around the rear wheels of landing gear configurations [47, 7] shows a velocity defect on the ground side of the wheel and a higher velocity on the outboard side of the wheel, caused by the blockage effects from the central support truck, creating a shear layer after flow separation, resulting in the low velocity flow in the central rear wake region behind the wheel. Another important characteristic of these vortices is that they are generated as Counter-Rotating Vortex (CVP) pairs, both within the upper ( $V_1, V_2$ ) and lower halves ( $V_3, V_4$ ) of the wheel wake. Vortices  $V_1$  and  $V_2$ , generated initially from either side of the top half of the wheel are shown to propagate downwards with the intense entrained flow (D) over the top of the wheel favouring a bias in vortical position towards the left of the wheel centreline. Conversely, vortices  $V_3$  and  $V_4$ , initially developed on either side of the bottom of the wheel, are entrained from the intense up-flow (E) with vortical position bias towards the right side of the wheel centreline. From flow-field interrogation, vortex core position and vorticity magnitudes were analysed by determining the centre of curl of the velocity vectors at the vortex core [30]. As evident from Figure 90 at data planes further downstream (b) (c) (d), the upper left vortex  $V_1$  & the lower right vortex  $V_4$  appear to dissipate into the free stream quicker than vortices  $V_2$  &  $V_3$  with almost negligible vorticity

magnitude of  $\Omega d/U_\infty \approx 0.5$  for  $V_1$  and  $V_4$  at  $z/d = 2.5$ . Considering vortex core vorticity magnitude at  $z/d = 0.75$ , Figure 90(a), vortex core vorticity magnitudes for  $V_2$  &  $V_3$  are stronger than  $V_1$  &  $V_4$  by up to 34%. The downwash (D) from the top of the wheel being skewed to the left, in essence pushes vortex  $V_1$  outwards and away from the wheel in the horizontal and vertical direction allowing more space on the upper right side for vortex  $V_2$  to be entrained in to the gap.

Similarly on the lower half of the wheel, vortex  $V_4$  is also pushed outwards by the intense up-wash (E) from the bottom of the wheel as is skewed to the right, again with increasing skewness further downstream whilst  $V_3$  is entrained in to the central gap on the lower left side. Overall, the higher intensity of  $V_2$  &  $V_3$  keeps these two vortices entrained into and near to the central region of the wheel by the skewed downwash and up-wash respectively, whilst this downwash & up-wash simultaneously push vortex  $V_1$  &  $V_4$  further away from the wheel, as shown by the red dashed arrows in Figure 90, with the size of the arrow indicating approximate vortex translation as described. Comparing vorticity magnitude between the nearest and furthest data plane used ( $z/d=0.75$  &  $z/d=2.5$ ) respectively, there is a rapid decrease in vorticity magnitude for each vortex;  $V_1$ :  $\Delta\Omega d/U_\infty \approx 5.4$ ,  $V_2$ :  $\Delta\Omega d/U_\infty \approx 5.4$ ,  $V_3$ :  $\Delta\Omega d/U_\infty \approx 5.5$ , and  $V_4$ :  $\Delta\Omega d/U_\infty \approx 4.4$ . Although, the change in vorticity magnitude is similar for all four vortices, the differences in vortex intensity between the vortices further downstream remain the same, i.e.  $V_2$  &  $V_3$  was found to be stronger than  $V_1$  &  $V_4$  at the closest plane to the wheel ( $z/d = 0.75$ ), and at the furthest downstream plane ( $z/d = 2.5$ ). Additionally, Figure 90(a & b) shows two large circular regions of vorticity on either side of the wheel ( $F_1, F_2$ ) causing asymmetry in the rear wake.

After further analysis of the flow field around the sides of the wheel, it was suggested that these large regions of vorticity are produced due to the location at which the flow is being entrained out of the hub cavities. With reference to Figure 89(a & b), two stagnated regions are present on the rear internal hub surface ( $A_W, A_L$ ), and are also shown in Figure 91(a & b) to be positioned in the corresponding region. Although near symmetrical pressure was observed on the rear hub surface on the  $y/d=0.5$  data plane (Figure 89(c)), contour plots of  $C_P$  on the wheel surface shows the internal hub impingement positioned at  $\theta = 195^\circ$  with  $C_P = 0.63$  and  $\theta = 161^\circ$  with  $C_P = 0.52$ , on the left ( $A_W$  in Figure 89(a)) and right ( $A_L$  in Figure 89(b)) hubs respectively when looking in the streamwise direction. Therefore, it is noticeable that the left impingement occurs above wheel mid-height ( $\theta=180^\circ$ ) whilst the right impingement occurs below wheel mid-height; this is also illustrated in Figure 91 (referenced

to wheel mid-height shown by red dashed line). After analysing flow patterns on either sides of the wheel, an upper wheel mid-height impingement ( $A_W$ ) causes the flow to circulate inwards and downwards, resulting in the flow leaving the hub on the lower half of the wheel ( $G_W$ ). The lower impingement ( $A_L$ ) shows the opposite, as flow stagnation occurs in the hub cavity below mid-height, therefore circulating inwards and upwards, resulting in the flow leaving the hub on the upper half of the wheel ( $G_L$ ). After computationally testing four different wheel configurations, Axerio-Cilies & Iaccarino [30] also found that the hub flow reduces the intensity of the outboard vortex causing asymmetry in the wake. The reduction in vortex intensity, on the corresponding side that the flow departs from the hub, can also be seen from the flow curvature between  $V_4$  &  $V_2$  on the left side from Figure 91(a), and similarly between  $V_1$  &  $V_3$  on the right side (b). This has also been shown and discussed earlier in the vorticity plots (Figure 90). Furthermore, Figure 91(a) shows a similar flow structures ( $H_W$ ) on the rear face of a stationary wheel that had been observed by McManus & Zhang [29] and shown in Figure 31(D), indicating regions of flow attachment onto the rear edge of the wheel as the flow is entrained in to the rear wake, and is also shown  $H_L$  &  $H_W$  in Figure 91. The analysis of the hub flow and internal hub impingement was also expected to affect the overall drag force [12].

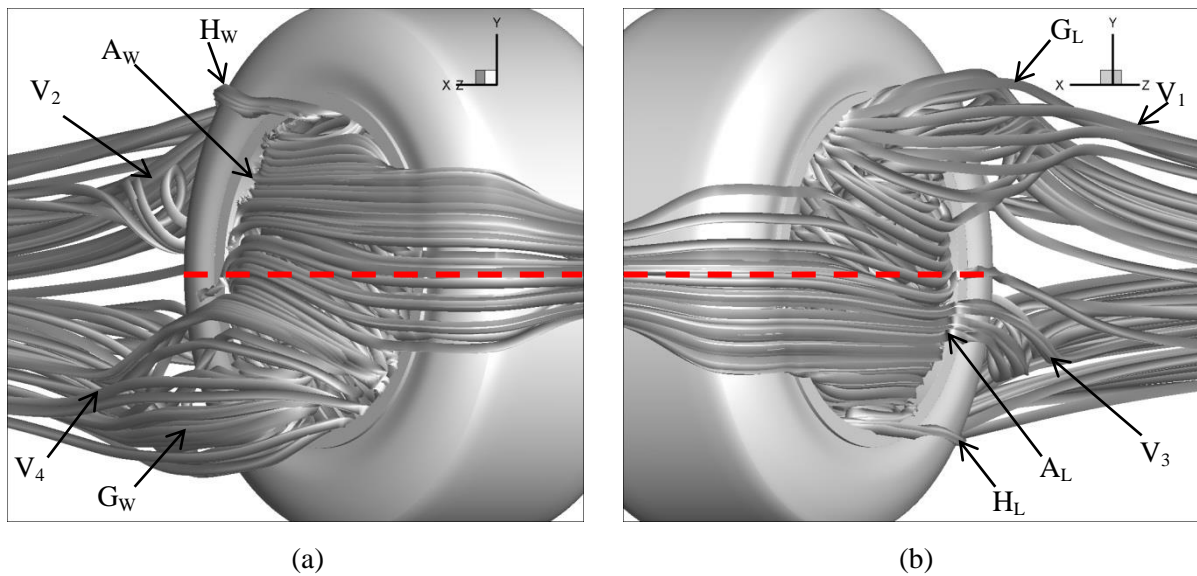


**Figure 91 - Streamlines showing hub flow on the, (a) left side (b) right side, when looking in the streamwise direction**

### 5.1.3 Aerodynamic Forces

Force coefficients obtained for drag, lift and side force, obtained were  $C_D = 0.35$ ,  $C_L = -0.01$  &  $C_X = -0.05$  respectively. As already has been discussed in the previous chapter,  $C_D$  was found to be higher than expected when compared to similar experimental configuration which obtained an overall  $C_D = 0.19$  for an isolated untripped wheel. This is thought to be due to the flow impingement within the exposed hub cavities on either side of the wheel. Investigations that were conducted with and without hub cavities [33, 12], showed that allowing the flow to travel in to the hubs, results in unsteadiness in the flow and increases the wake size, creating an overall increase in drag force. Fackrell [22] obtained pressure measurements at two holes inside the hub of the ‘A2’ wheel geometry, and found positive pressures in the regions  $140^\circ \leq \theta \leq 200^\circ$ , and suggested that these locations represent the flow entering the hub and circulating inside. The hubs were also found to be a large contributor to the drag, specifically with  $\Delta C_D = 0.08$  for the ‘A2’ geometry. Although this study by Fackrell [22] was conducted as a ‘in-contact with the ground’ configuration, if the same  $\Delta C_D$  was assumed to be present for this free air configuration which uses the same ‘A2’ geometry modelled computationally, an overall drag coefficient of  $C_D = 0.27$  ( $C_D = 0.35 - 0.08$ ) would be provided representing a wheel with no hub cavity, similar to the wheel configuration used in [32]. The drag coefficients would then be in good agreement with the free air configuration in [32], and the computationally modelled geometry used by Zhang et al [32] which provided  $C_D = 0.26$ . This reasoning is also supported by estimates of individual wheel drag coefficients extracted from ‘no hub’ landing gear wheels ( $C_D \approx 0.15$ - $0.16$  [9]). Inherently, these configurations are much more streamlined inhibiting free stream flow impingement onto downstream internal hub surfaces. Considering lift and side force, both were observed and expected to be very close to zero as the wheel is stationary and positioned at the vertical centre of the domain with a symmetrical flow-field on the upper and lower halves of the wheel. Side force was also very close to zero but  $C_X = -0.05$ , represents the side force acting in the negative x-direction (towards the right side of the computational domain when looking in the streamwise direction). This could be due to the slightly larger hub cavity on the positive x-side of the wheel, whereby the flow enters into a larger volume, essentially having a push towards negative x-direction. However, as this side force is almost negligible, it will be investigated in more detail with the application of yaw and rotation.

## 5.2 The Influence of Wheel Yaw

When a crosswind is present during the approach phase of an aircraft, the free-stream air is flowing at an angle to the aircraft, which can be interpreted as a yaw angle. Therefore, to simulate the typical crosswind approach conditions of an aircraft, yaw angles of  $\Psi = 5^\circ$ ,  $10^\circ$  and  $15^\circ$  were applied on to the single stationary wheel. The results will focus on the surface pressure distribution on the centreline of the wheel with subsequent wake analysis identifying the vortical structures and the influence of yaw angle on the rear wake. Aerodynamic forces will also be discussed for each case. Although insights into yawed wheel cases are limited, comparisons to the available literature with similar flow physics and configurations will be provided. For comparison purposes, identification of flow features/regions is denoted with a letter followed by ' for increasing yaw angles, (i.e. Flow feature/region being described in zero yaw case is denoted A, with the same feature/region denoted A', A'' & A''' for the  $5^\circ$ ,  $10^\circ$ , &  $15^\circ$  yaw cases respectively).

Initial results from the un-yawed case showed almost symmetric flow characteristics upstream of the wheel, flow stagnation ( $C_P = 1$ ) occurred on the central region of the front surface of the wheel before flowing around the wheel. Due to the curved profile on the wheel, the flow accelerated around the sides up to 58.7m/s with  $C_P = -1.34$ , and around the top and bottom up to 55m/s with  $C_P = -0.97$ . Upon passing the edges on the side of the wheel, the flow travels into the hub cavities and forms a stagnation region on the rear hub surface. Fackrell [22] also observed this flow characteristic to occur in the region  $140^\circ \leq \theta \leq 200^\circ$ , causing a subsequent circulation of the flow inside the hub. Impingement position on the rear surface of each hub was found to influence the direction of circulation of air within the hub hence, determining the location of exit; an upper impingement (above wheel mid-height) found the flow to circulate inwards and downwards and exit on the lower half of the hub whereas a lower impingement (below wheel mid-height) showed the opposite. The zero yaw case showed the positions of these impingements to be on either side of the mid-wheel centreline as has been discussed previously, therefore creating asymmetry in the near wake region. On the rear surface of the wheel, an intense up-wash from the bottom of the wheel and down-wash from the top of the wheel were present, skewing towards the positive and negative x- directions respectively. Overall, on the rear surface, four distinct vortical structures are formed due to the separated flow rolling up over the rear shoulders of the wheel. The asymmetry in the wake shows two of the vortices being up to 34% weaker in

magnitude, therefore being dissipated in to the free-stream much quicker than the remaining two stronger vortices. Changes in vorticity magnitude between the nearest and furthest data plane, showed a reduction in vorticity magnitude by  $\Delta\Omega d/U_\infty \approx 5$  for all four vortices, but their individual strengths were maintained (i.e. the stronger vortices ( $V_2$  &  $V_3$ ) observed at  $z/d = 0.75$  remained to be stronger than  $V_1$  &  $V_4$  at the furthest data plane of  $z/d = 2.5$ ).

### 5.2.1 Surface Pressure Characteristics

The application of wheel yaw shows a similar surface pressure distribution along the centreline of the wheel, with significant differences observed on the rear surface of the wheel,  $120^\circ \leq \theta \leq 240^\circ$ , as illustrated in Figure 92. Analysing the flow field from the most upstream point on the centreline of the wheel, differences in  $C_p$  at  $\theta = 0^\circ$  are also evident. This region initially represented the stagnation region for the zero yaw case providing  $C_p = 1$ , however the pressure at  $\theta = 0^\circ$  decreases to  $C_p = 0.99, 0.94, 0.87$  with increasing yaw angle at  $5^\circ, 10^\circ$  and  $15^\circ$  respectively, showing that an increase in yaw angle causes a shift in stagnation position on the front surface of the wheel. After the frontal region, the flow accelerates around the top and bottom surfaces of the wheel to a maximum velocity magnitude of 55m/s with negative peak  $C_p \approx -1$  on all yawed cases. Subsequently, a pressure recovery occurs until separation is observed, which is predicted to be, where pressure recovery ceases [47, 29]. A significant

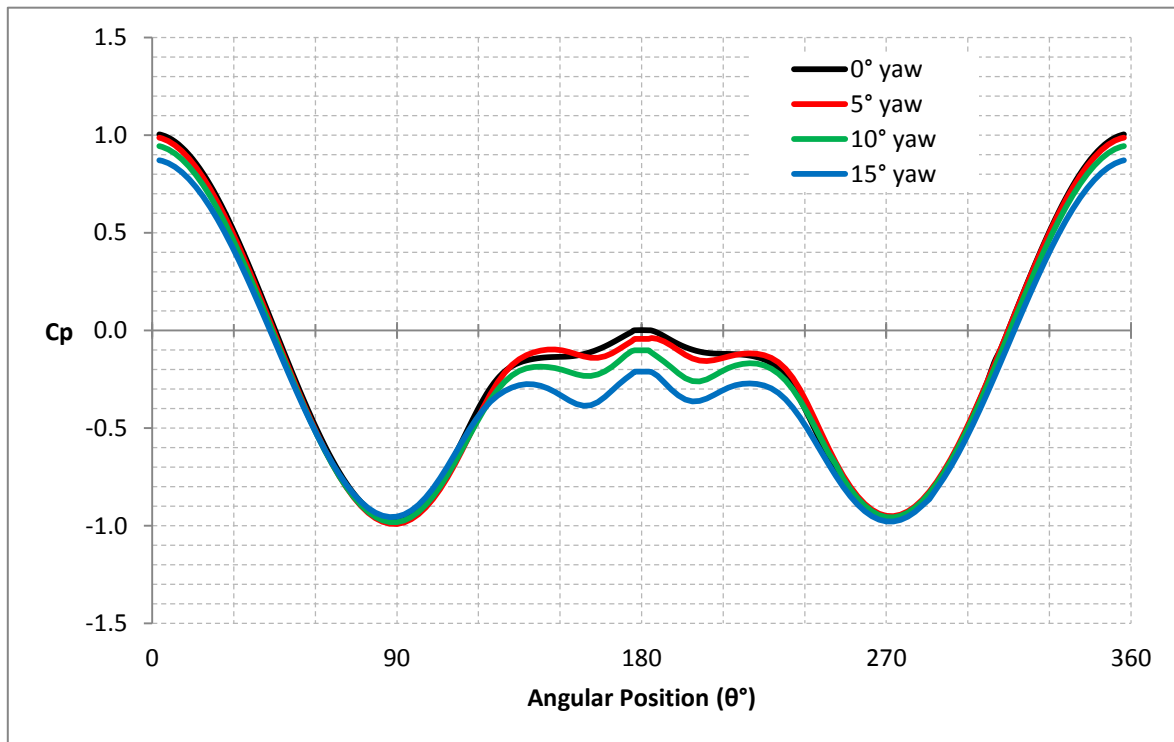


Figure 92 – Stationary wheel centreline mean surface pressure coefficient with added yaw angle

reduction in base pressure is also observed with  $C_P = -0.04, -0.10, -0.21$ , with increasing yaw angle to  $5^\circ, 10^\circ$  and  $15^\circ$  respectively, directly behind the wheel at  $\theta = 180^\circ$ . This was also a discovered characteristic behind a yawed cylinder, as the influence of yaw reduces the intensity of vortex shedding in the rear wake reducing the base pressure [26].

Pressure contour plots obtained on the wheel surface (Figure 93) and at a cross-sectional plane at wheel mid-height ( $y/d = 0.5$ ) from Figure 94, representing  $5^\circ, 10^\circ, 15^\circ$  yaw cases respectively, provides a more detailed understanding of the characteristic flow field around a yawed wheel. Considering the frontal region of the wheel, the earlier stated shift in stagnation position towards the windward side of the wheel is clearly evident ( $A', A'', A'''$ ) from the figures, and is shown to have a transverse displacement towards the windward edge of the front surface as applied wheel yaw angle increases with  $\Delta x/d = 0.04$  ( $5^\circ$  yaw),  $\Delta x/d = 0.08$  ( $10^\circ$  yaw),  $\Delta x/d = 0.11$  ( $15^\circ$  yaw), relative to the initial stagnation region at  $x/d = 0$  ( $0^\circ$  yaw). This would be expected as the flow would essentially interact first on the windward side due to the applied yaw angle.

Subsequent to the flow stagnation, the mean pressure distribution (Figure 94) shows an enhancement of negative pressure on the leeside of the wheel, together with an overall increase in pressure on the windward side. This is principally evident with the increase in suction region around the front leeside edge of the wheel from  $C_P = -1.34$  at  $0^\circ$  yaw ((B) in Figure 89(c)), to  $C_P = -1.9$  ( $B_1$ ),  $C_P = -2.6$  ( $B_3$ ),  $C_P = -3.0$  ( $B_5$ ). Corresponding velocity magnitudes of  $60\text{m/s}$  ( $B_1$ ),  $71\text{m/s}$  ( $B_3$ ),  $78\text{m/s}$  ( $B_5$ ) respectively, were also found indicating increasing flow acceleration around the front edge on the leeside of the wheel. This increase in negative pressure, occurs in unison with a decrease in negative pressure on the windward side of the model from  $C_P = -1.34$  at  $0^\circ$  yaw ((B) in Figure 89(c)), to  $C_P = -1.05$  ( $B_2$ ),  $C_P = -0.73$  ( $B_4$ ),  $C_P = -0.35$  ( $B_6$ ) with corresponding velocity magnitudes up to  $55\text{m/s}$  ( $B_2$ ),  $51\text{m/s}$  ( $B_4$ ) and  $46\text{m/s}$  ( $B_6$ ) respectively. The decrease in negative pressure and velocity is a result of relative exposure to the oncoming free stream. Together with the flow asymmetry found over the front edges of the wheel, there is also evidence of flow asymmetry within the flow stagnation regions impinging onto the rear face of the internal hub cavities of the wheel. Within these regions, there exists an increase in surface pressure within the windward side cavity, representing more than a 30% increase (at  $5^\circ$  yaw) over the results found at zero yaw,  $C_P = 0.44$  ( $C_2$ ) relative to  $C_P = 0.30$  (C) respectively. Conversely, a 13% decrease ( $C_P = 0.26$ ,  $C_1$  from Figure 94(a), relative to  $C_P = 0.30$ , C from Figure 89) is shown within the leeside cavity.

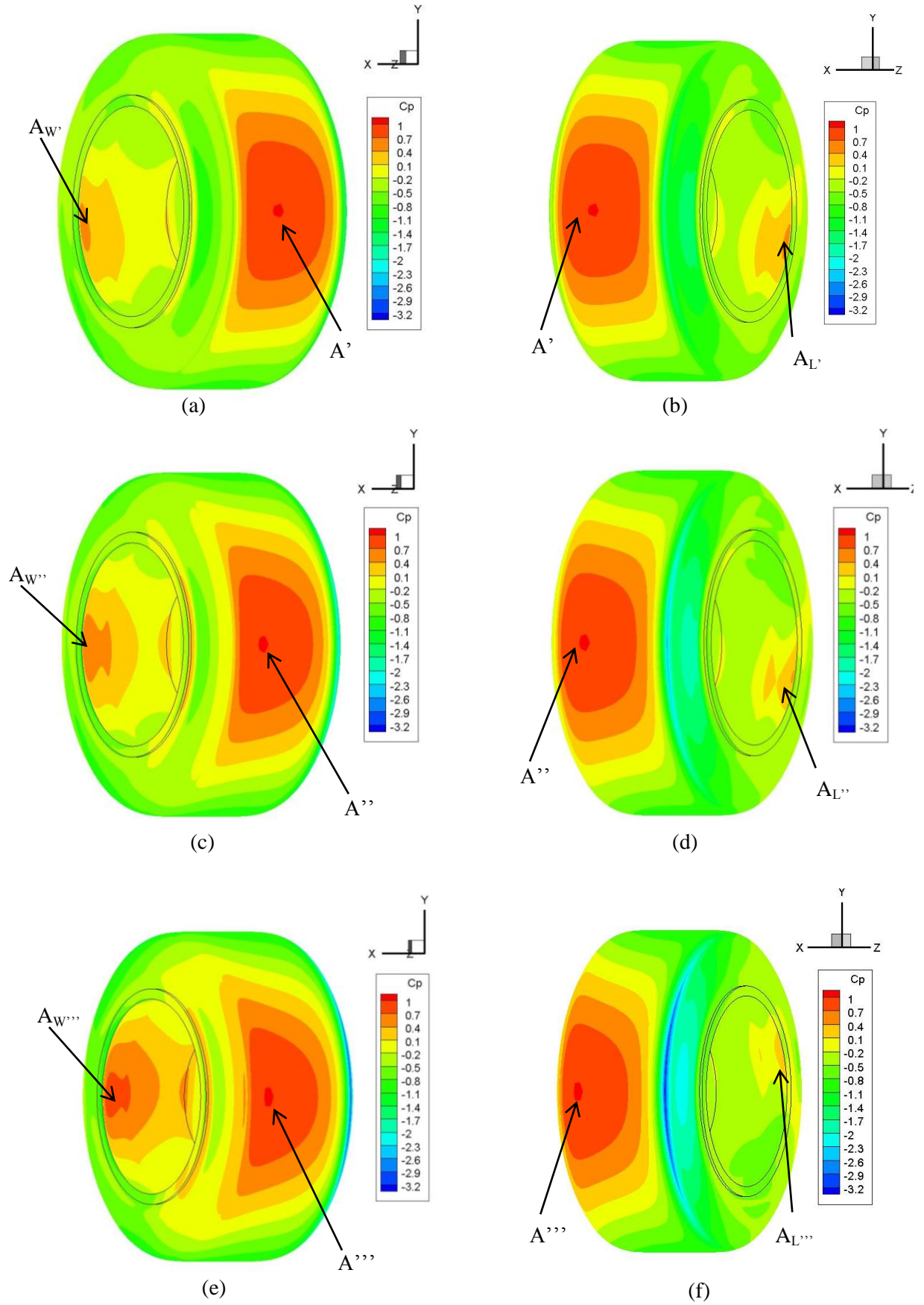


Figure 93 – Contours of mean  $C_p$  on stationary wheel surface when looking downstream: (a) 5° left, (b) 5° right, (c) 10° left, (d) 10° right, (e) 15° left, (f) 15° right



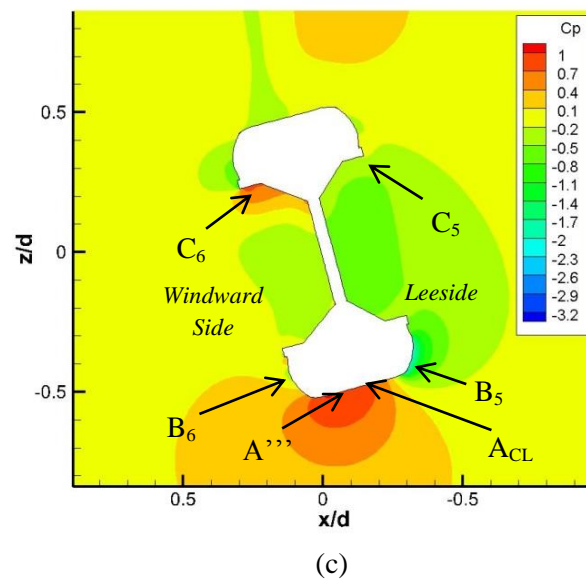
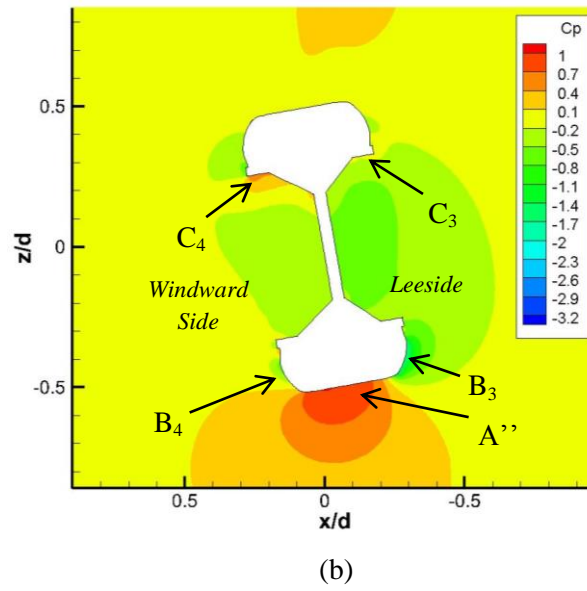
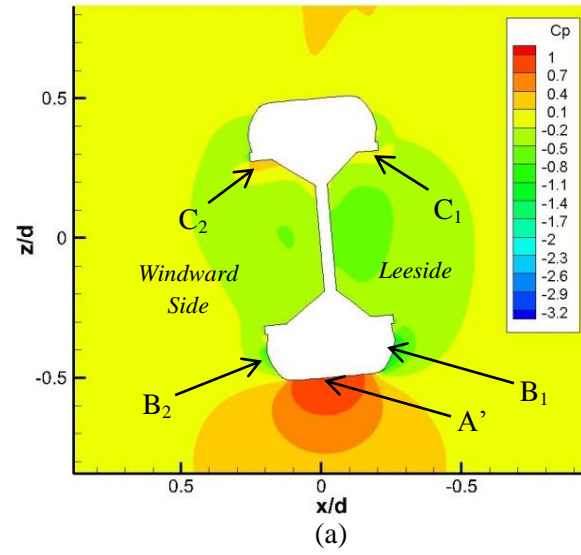


Figure 94 – Contours of mean  $C_p$  on stationary wheel at cross-sectional plane at  $y/d=0.5$ : (a) 5°, (b) 10°, (c) 15°

Similarly, this trend is followed with further increases in yaw angle, with leeside hub rear stagnation regions decreasing to  $C_p = 0.09$  ( $C_3$ ) at  $10^\circ$  yaw and  $C_p = -0.15$  ( $C_5$ ) at  $15^\circ$  yaw. On the windward side, the pressure increases to  $C_p = 0.58$  ( $C_4$ ) at  $10^\circ$  yaw and  $C_p = 0.77$  ( $C_6$ ) at  $15^\circ$  yaw. This would be expected as the leeside cavity is more sheltered and obstructed from direct exposure to the oncoming free-stream flow, minimising the area exposed to direct impingement, whilst the windward side cavity, particularly the rear surface, is more exposed as the yaw angle increases. However at  $15^\circ$  yaw, the single dominant flow stagnation region evident on the windward side rear face of the hub ( $C_6$ ), showed  $C_p = 0.77$ , approximately equivalent in magnitude to that observed at the front centreline of the wheel ( $A_{CL}$ :  $C_p = 0.87$ ). The impingement on the rear surface of the hub cavity on the leeside ( $C_5$ ), is almost negligible, with the oncoming free stream flow being obstructed to an extent where the flow reaches the back of the wheel before having the opportunity to impinge on the hub cavity resulting in low velocity circulation to persist in the hub cavity on this leeside. Overall, the flow asymmetry around the wheel continues to increase, as more of the windward side of the model becomes directly exposed to the oncoming free-stream.

### 5.2.2 Wake Physics

With the application of yaw, both significant and subtle changes in the physics of the flow-field are immediately evident. First, considering the  $5^\circ$  yaw case, it is clear, from Figure 95, that the most noticeable feature of the wake dynamics is that there is a clear bias and asymmetric distribution of vorticity favouring the windward side of the wheel. Significant changes in the number of distinctive vortical structures present as well as vortex core central magnitudes have also occurred. There is no direct evidence of the development of  $V_1$  &  $V_3$ , seen for the zero yaw case, however the  $z/d = 0.75$  streamwise location for the  $5^\circ$  yaw case signifies, that a fundamental shift in the distribution of wake vorticity to dominate a two-vortex wake has occurred. Together with this fundamental overall change in wake dynamics, the application of wheel yaw has also resulted in a characteristic change in the flow entrainment over both the top and bottom of the wheel. Outlined for the zero yaw case shown in Figure 90, the flow entrainment over the top and bottom of the wheel, was seen to undergo an interaction that resulted in the downwash (D) from the top, upon interacting with the up-flow (E) from the bottom, displacing to the left and right of one another prior to subsequent convection downstream. This skewness characteristic in the downwash, was also observed in [12] with the application of  $\pm 6^\circ$  yaw. However from Figure 95, the added vorticity generated from applied wheel yaw on the windward side, is shown to both intensify and fortify the

skewness of the entrainment over the bottom of the wheel (E' relative to E), with the entrainment from the top of the wheel previously moving towards the left of the wheel (D in Figure 90), now being straightened to move directly down the wheel centreline (D' relative to D). Effectively, it seems that the applied wheel yaw and the augmented vorticity produced bias towards the windward side of the model, resulting in further intensification of the resulting sideways flow entrainment to augment wake bias towards the windward side of the wheel.

Considering central core vorticity magnitude at  $z/d = 0.75$ , the application of  $5^\circ$  yaw on the wheel has increased the vortex core magnitude of  $V_2'$ , increasing from  $\Omega d/U_\infty = 6.60$  for  $V_2$  in Figure 90(a) to  $\Omega d/U_\infty = 6.77$  in Figure 95(a). Correspondingly, vortex core vorticity magnitude for  $V_4'$  has increased to  $\Omega d/U_\infty = 8.60$  from  $\Omega d/U_\infty = 4.96$  for  $V_4$ , suggesting that

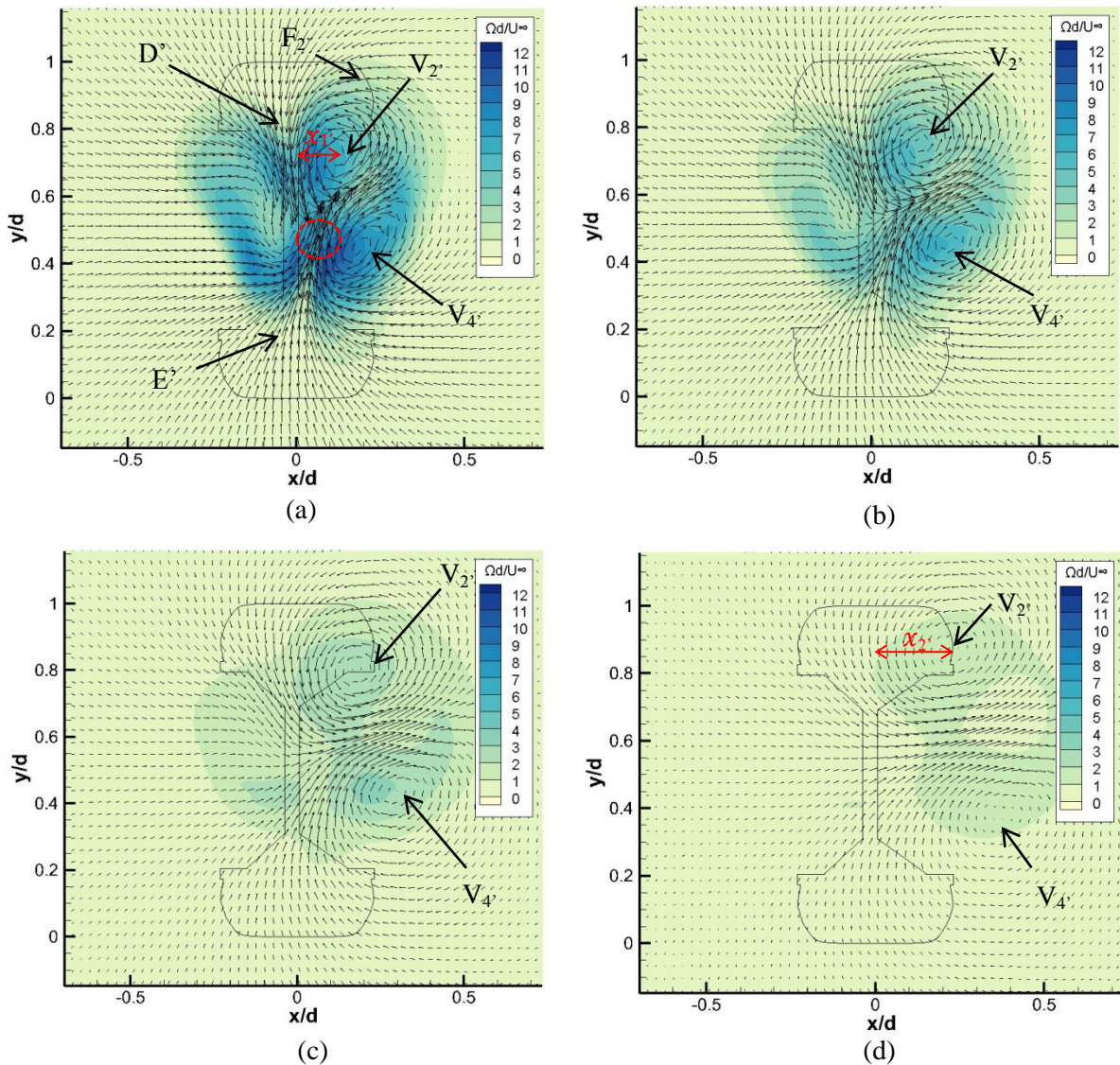
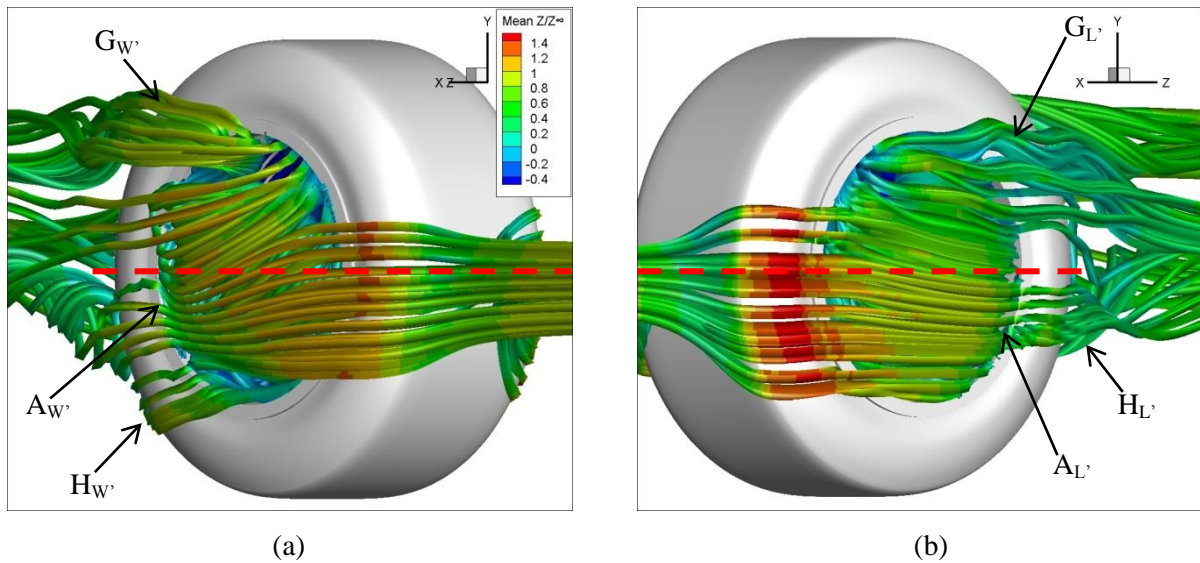


Figure 95 – Non-dimensional vorticity plots for  $5^\circ$  yaw; (a)  $z/d=0.75$ , (b)  $z/d=1$ , (c)  $z/d=1.5$ , (d)  $z/d=2.5$

the application of yaw has an effect on increasing the net core vorticity magnitude on the bottom half of the wheel wake relative to the top. This is thought to be caused by the 92% increase in transverse velocity from the upwash, relative to the zero yaw case (indicated by the red dashed circular region in Figure 95(a) and Figure 90(a)), creating a stronger curl within the flow in the region of  $V_4$ . This effect acts in unison with the attached flow on the lower half on the windward side ( $H_W$ ), separating and rolling up over the edge of the wheel forming a more intense vortex structure for  $V_4$ , as shown in Figure 96(a). Additionally, the larger vorticity but lower intensity region ( $F_2$ ) of  $V_2$  compared to  $V_4$  is suggested to be due to the effect of the low velocity recirculating flow in the hub leaving on the upper half of the wheel ( $G_W$ ,  $G_L$ ) and being entrained into the upper vortex ( $V_2$ ) reducing its intensity, also observed on the zero yaw case and in [30]. Similarly, on the leeside of the wheel, the flow entering the rear wake of the wheel originates from the upper hub region and the attached flow over the lower edge, which is subsequently entrained by the downwash and upwash respectively. The flow from the upper leeside hub ( $G_L$ ), is entrained into the upper vortex  $V_2$ , whilst the attached flow from the lower side of the hub ( $H_L$ ) is entrained by the upwash into  $V_4$ . The reason behind the hub flow leaving both hub cavities on the upper half, is due to the flow impingement below wheel mid-height at  $\theta = 174^\circ$  and  $\theta = 165^\circ$  for the windward side ( $A_W$ ), and leeside ( $A_L$ ) respectively, with corresponding pressure coefficients of  $C_p = 0.48$  and  $C_p = 0.46$  illustrated in Figure 93(a & b) and Figure 96.



**Figure 96 - Streamlines (coloured by mean streamwise velocity) showing hub flow on the 5° yaw wheel, (a) windward side (b) leeside, when looking in the streamwise direction**

It is also evident that through comparing Figure 90 and Figure 95, that the application of a  $5^\circ$  yaw angle has increased the transverse displacement of the two primary vortex structures ( $V_2$ ,  $V_4$ ), with vortex core positions relative to Figure 90(a) being displaced by  $\Delta x/d = 0.003$  and  $\Delta x/d = 0.002$  for  $V_2$  &  $V_4$ , respectively at  $z/d = 0.75$ . The central vortex core position was obtained, by using the bottom centre of the wheel as a reference point ( $x/d = 0$ ,  $y/d = 0$ ), allowing the vortex core to be predicted at the centre of the curl of velocity vectors [30]. At  $z/d = 0.75$ , there also appears to have been an increase in vertical displacement, with vortex core positions relative to Figure 90(a) being displaced by  $\Delta y/d = 0.10$  and  $\Delta y/d = 0.08$  for  $V_2$  &  $V_4$ , respectively. For the  $5^\circ$  yaw case shown in Figure 95, an increased asymmetric horizontal offset of vortex  $V_4$  relative to  $V_2$  is present; most probably as a result of the more efficient constructive interference over the bottom of the wheel than over the top as has been discussed earlier for Figure 90. The difference in offset between the two vortices, initially representing  $\Delta x/d = 0.07$  at  $z/d = 0.75$ , was found to increase to  $\Delta x/d = 0.15$  at  $z/d = 2.5$ . Similarly, the vertical positions of  $V_4$  relative to  $V_2$  were found to differ, with initial  $\Delta y/d = 0.27$  and  $\Delta y/d = 0.49$  at  $z/d = 0.5$  and  $z/d = 2.5$  respectively, indicating that the vortices propagate downstream with horizontal displacement in the  $+x$  direction and vertical displacement ( $+y$  direction for  $V_2$  &  $-y$  direction for  $V_4$ ). This tends to correspond to results obtained for the respective vortex core magnitudes with the bottom vortex ( $V_4$ ) showing increased intensity over the top vortex ( $V_2$ ). Additionally, and in similar trend to that found for the  $0^\circ$  yaw case, with subsequent propagation downstream from  $z/d = 0.75$  to  $z/d = 2.5$ , vortex core vorticity magnitudes for both vortices were found to dissipate rapidly from  $\Omega d/U_\infty = 6.77$  to  $\Omega d/U_\infty = 1.29$  for  $V_2$  and  $\Omega d/U_\infty = 8.60$  to  $\Omega d/U_\infty = 1.27$  for  $V_4$ , respectively.

Application of another  $5^\circ$  incremental increase in yaw angle to  $10^\circ$ , Figure 97, shows the dominant two-vortex wake structure, observed for the wheel at  $5^\circ$  yaw, continues to persist. The additional increase in yaw angle has continued to increase the central vortex core magnitudes of the two vortices  $V_2$  &  $V_4$  presented in Figure 97. There is also an increase in the transverse displacement of the dominant pair of vortices ( $V_2$ ,  $V_4$ ) towards the windward side of the wheel. This additional displacement caused through the additional increase in transverse flow entrainment is rather subtle, at the spanwise location of  $z/d=0.75$ , being marginally larger, than that observed for the  $5^\circ$  yaw case where  $x/d = 0.118$  ( $V_2$ ) and  $x/d = 0.188$  ( $V_4$ ) from Figure 95(a), and  $x/d = 0.168$  ( $V_2$ ) and  $x/d = 0.22$  ( $V_4$ ) from Figure 97(a). Propagating downstream from  $z/d=0.75$  to  $z/d=2.5$ , an increased displacement in the transverse



direction, is observed when analysing the central vortex core positions between the  $5^\circ$  and  $10^\circ$  cases (demonstrated for the transverse displacement of the upper vortex at  $5^\circ$  as  $\Delta x/d = x_{2'} - x_{1'}$ , and at  $10^\circ$  as  $\Delta x/d = x_{2''} - x_{1''}$ ).

Comparing  $\Delta x/d$  &  $\Delta y/d$  from  $z/d=0.75$  to  $z/d=2.5$ , the  $5^\circ$  configurations from Figure 95 indicates that the displacement in the upper vortex  $V_{2'}$  as  $\Delta x/d = 0.113$ ,  $\Delta y/d = 0.139$  with the lower vortex  $V_{4'}$  having  $\Delta x/d = 0.188$  and  $\Delta y/d = -0.081$  (*Note. negative value indicates displacement in the negative y direction*). However at  $10^\circ$  yaw (Figure 97), vortex  $V_{2''}$  has a displacement of  $\Delta x/d = 0.188$ ,  $\Delta y/d = 0.146$  and  $V_{4''}$   $\Delta x/d = 0.208$ ,  $\Delta y/d = -0.08$ . This indicates a marked increase in transverse displacement of the central vortex core positions over the five degree yaw case, although the vertical change in vertical displacement between the two cases are almost negligible as they both seem to be shifted vertically by approximately  $y/d = 0.08$ . Also evident from the results in Figure 97, is confirmation that

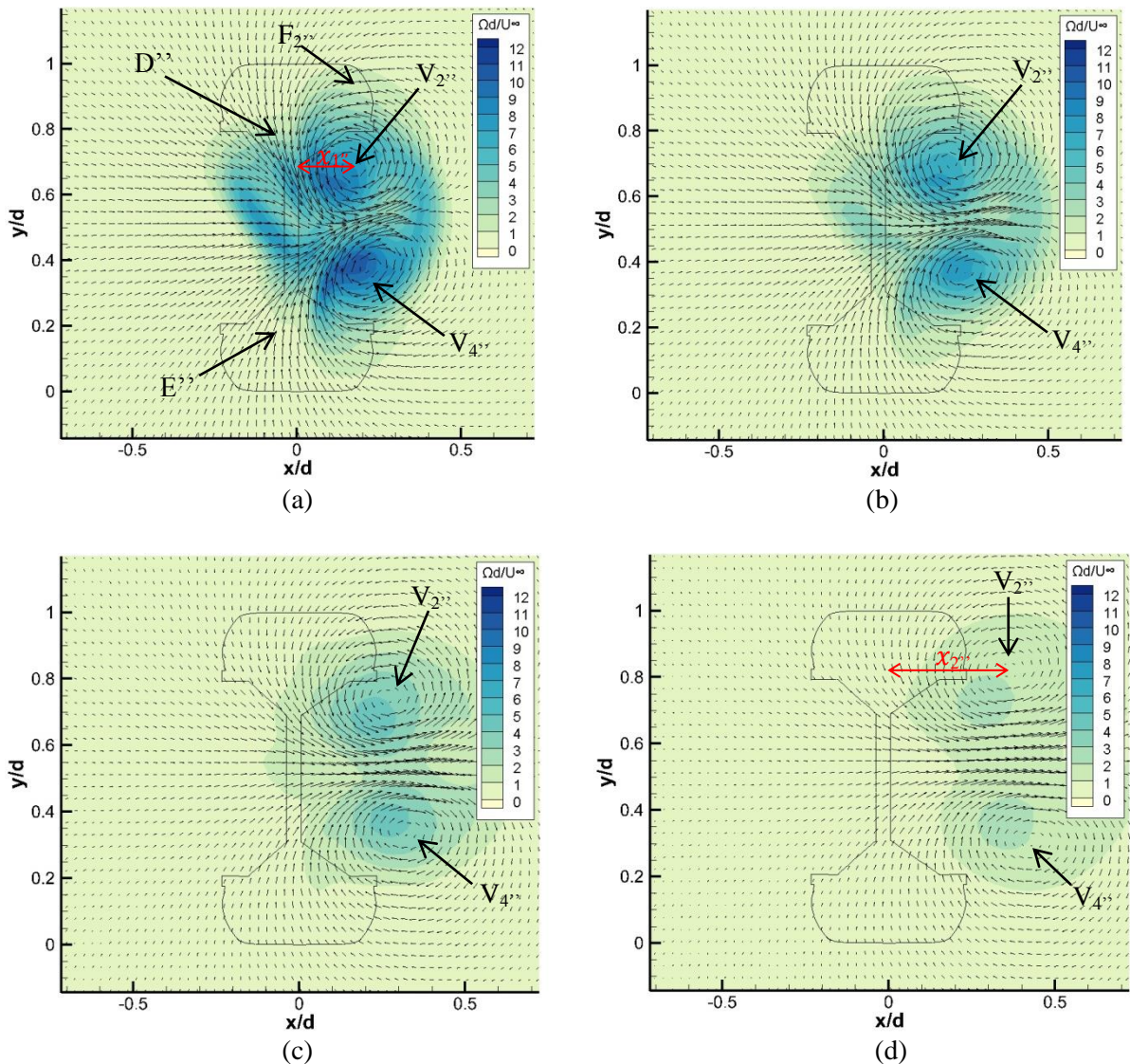
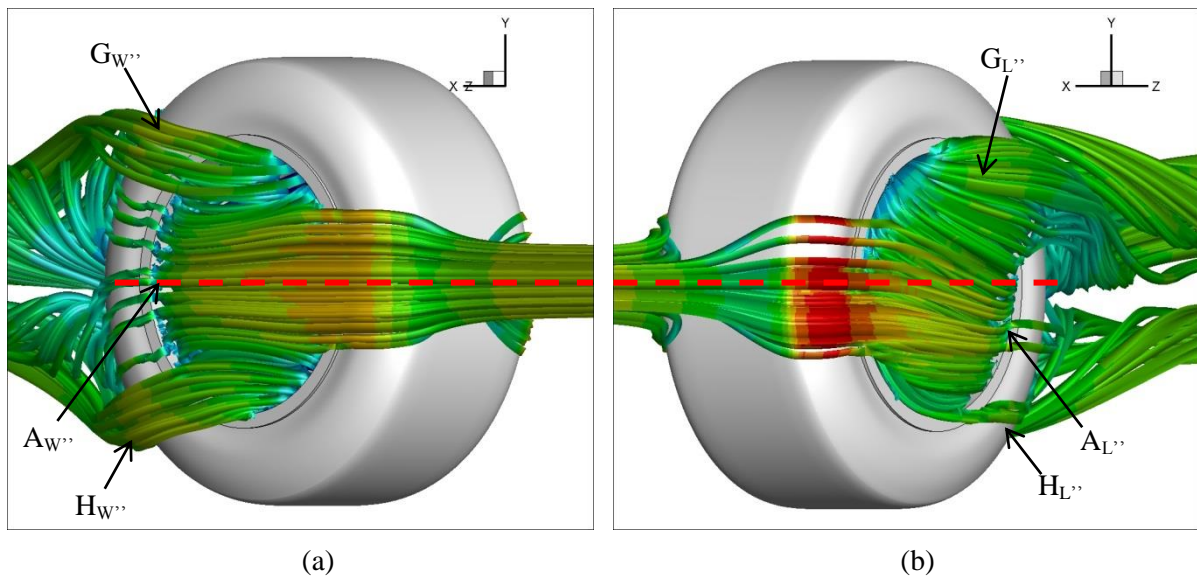


Figure 97 – Non-dimensional vorticity plots for  $10^\circ$  yaw; (a)  $z/d=0.75$ , (b)  $z/d=1$ , (c)  $z/d=1.5$ , (d)  $z/d=2.5$

with the increase in yaw angle to  $10^\circ$ , the downflow from over the top of the wheel ( $D''$ ) and the up-flow from the bottom of the wheel ( $E''$ ), has become noticeably more symmetric under these flow conditions; with the strength of the vorticity, particularly over the top of the wheel now being strong enough to not only entrain the downwash from the top of the wheel moving to the adjacent side of the upflow, as shown in Figure 95, but also to now fully entrain the flow towards the windward side of the wheel, with a similar degree of intensity ( $D'$  relative to  $D''$ ). Contrary to this near symmetry, there is still an offset in the transverse direction of the central vortex cores ( $V_{4''}$  relative to  $V_{2''}$ ) by approximately up to 30% at  $z/d=0.75$  with this offset reducing to approximately 21% further downstream. However this offset percentage is almost double for the  $5^\circ$  yaw case (Figure 95) with  $V_{4'}$  being positioned almost 60% more in the  $+x/d$  direction relative to  $V_{2'}$ . Furthermore, unlike this offset reducing further downstream as observed in the  $10^\circ$  yaw case, this offset remains about 60% further downstream on the  $5^\circ$  yaw case. With the application of  $10^\circ$  yaw, the degree of flow asymmetry around the wheel continues to increase as more of the windward side of the model becomes directly exposed to the oncoming free-stream, confirming and enhancing the flow characteristics already observed in the  $5^\circ$  yaw case.

At  $10^\circ$  yaw, central vortex core vorticity magnitude indicates  $\Omega d/U_\infty = 8.30$  ( $V_{2''}$ ) and  $\Omega d/U_\infty = 9.68$  ( $V_{4''}$ ) at  $z/d = 0.75$ , signifying a stronger lower vortex. The less intense vortex on the upper half ( $V_{2''}$ ) although again covering a larger region ( $F_{2''}$ ), was suggested to be due to the flow from the upper side of the leeside hub being entrained into the upper vortex. Considering Figure 93(c & d) and Figure 98, internal hub impingements are shown at



**Figure 98 - Streamlines (coloured by mean streamwise velocity) showing hub flow on the the  $10^\circ$  yaw wheel, (a) windward side (b) leeside, when looking in the streamwise direction**

approximately wheel mid-height on the windward side of the wheel,  $A_{W''}$ ;  $\theta = 179^\circ$  with  $C_p = 0.58$  and below wheel mid-height at  $\theta = 165^\circ$  with  $C_p = 0.40$  on the leeside of the wheel ( $A_{L''}$ ). The rise in impingement  $C_p$  on the windward side ( $A_{W''}$ ) by 21% (relative to  $C_p = 0.48$  ( $A_{W'}$ ) at  $5^\circ$  yaw) indicates the increased exposure of the rear surface of the hub cavity, allowing the flow to stagnate/impinge on, whereas the front of the wheel further obstructs the rear surface of the hub cavity on the leeside due, to the applied increased yaw angle minimising the area exposed to direct impingement. Referring to Figure 98, and considering the same theory used earlier to describe the effect of impingement location on the subsequent flowfield, the near mid-height impingement on the windward side of the wheel ( $A_{W''}$ ) results in the motion of the flow thereafter illustrated to be very near symmetric, with the flow leaving the hub on both the upper and lower regions, and re-attaching to the edge of the wheel ( $G_{W''}$  and  $H_{W''}$  respectively) before separating and forming vortices. However, on the leeside of the wheel, the flow impinges below wheel mid-height ( $A_{L''}$ ), forcing the flow to circulate into and upwards, inside the hub due to its geometry, resulting in the flow leaving the hub on the upper half ( $G_{L''}$ ) and being entrained into  $V_{2''}$ , reducing its intensity as has been observed on the  $5^\circ$  yaw case.

The wake dynamics for the wheel with an applied yaw angle of  $15^\circ$  continues to uphold the two-vortex dominant flow-field, evident for both the  $5^\circ$  and  $10^\circ$  yaw cases, as shown in Figure 99. The two vortices appear to be near symmetrical about the horizontal centreline of the wheel at  $y/d=0.5$ . With a similar trend to what was observed for the  $10^\circ$  yaw case, the central vortex core magnitudes increased with this further  $5^\circ$  increase in yaw angle, by 29% for  $V_{2'''}$  however reducing by 11.5% for  $V_{4'''}$ . Although, central core vorticity magnitude for the two vortices differed slightly by up to 23% at  $z/d=0.75$  ( $V_{2'''}: \Omega d/U_\infty = 10.70$ ,  $V_{4'''}: \Omega d/U_\infty = 8.68$ ), further downstream ( $z/d > 0.75$ ) the maximum difference in vorticity magnitude was of 7%, with both vortices comprising an identical vorticity magnitude of  $\Omega d/U_\infty = 2.26$  at  $z/d=2.5$ . The application of  $15^\circ$  yaw also demonstrates that the downwash and upwash is now fully able to entrain the flow over the top and bottom of the wheel respectively, providing a near symmetrical wake. Wheel mid-height ( $y/d = 0.5$ ) stagnation on the rear surface of the hub cavity on the leeside (Figure 94 -  $C_5$ ) is almost negligible for the  $15^\circ$  yaw case, with the oncoming free stream flow being obstructed to an extent, where the flow reaches the back of the wheel before having the opportunity to impinge on the hub cavity. Considering wheel surface pressure, Figure 93(e & f), internal hub cavity impingement occurs on the windward side ( $A_{W'''}\text{'}$ ) at  $\theta = 181^\circ$  with  $C_p = 0.79$  and a region of



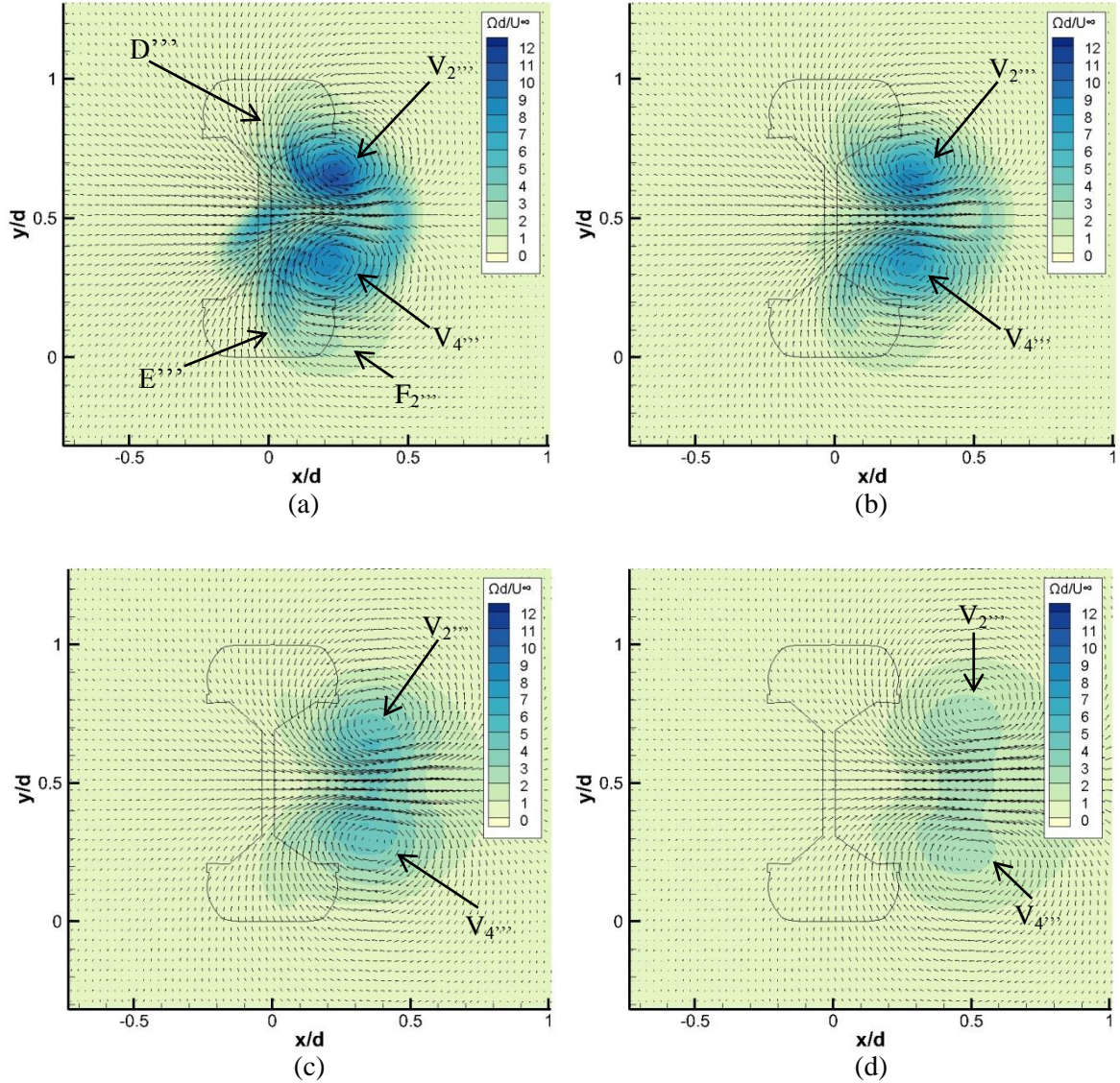


**Figure 99 – Non-dimensional vorticity plots for 15° yaw; (a)  $z/d=0.75$ , (b)  $z/d=1$ , (c)  $z/d=1.5$ , (d)  $z/d=2.5$**

maximum pressure reaching  $C_P = 0.33$  at  $\theta = 197^\circ$  on the leeside ( $A_{L'''}$ ). The further upstream region on the leeside hub at  $\theta = 197^\circ$ , located above wheel mid-height, explains the larger vorticity region  $F_2'''$  shown in Figure 99(a), due to the flow exiting the hub from its lower half (Figure 100 –  $H_{L'''}$ ), subsequently being entrained by the highly skewed upwash into the  $V_4'''$  vortex region. However, on the windward side of the wheel, the mid-wheel impingement ( $A_{W'''}$ ) accounts for the near wake flow characteristics being very near symmetrical about the horizontal wheel centreline,  $y/d = 0.5$ , as the flow re-circulates within the hub, leaving from both the upper and lower halves ( $H_{W'''}$  &  $G_{W'''}$ ).

The formation of the two vortical structures observed in the rear wake of all yawed cases are caused by the separated flow rolling up over the rear shoulders of the wheel [29, 22, 40]. Considering the graph of  $C_P$  against angular position for all yaw cases, (Figure 92), together

with the convention previously used in [34, 30, 29], predicting separation to occur where pressure recovery ceases; maximum separation angles were predicted for the current cases at  $\theta = 139^\circ$  &  $230^\circ$ ,  $\theta = 133^\circ$  &  $230^\circ$ ,  $\theta = 129^\circ$  &  $228^\circ$  for  $5^\circ$ ,  $10^\circ$ ,  $15^\circ$  configurations respectively on the lower and upper surfaces. Comparing the upper surface separation positions, the flow appears to separate approximately at  $\theta \approx 230^\circ$  for all three yaw angles. However on the lower surface, the maximum separation angle appears to be displaced further towards the bottom of the wheel by approximately  $4^\circ$  with an incremental increase of  $5^\circ$  yaw.

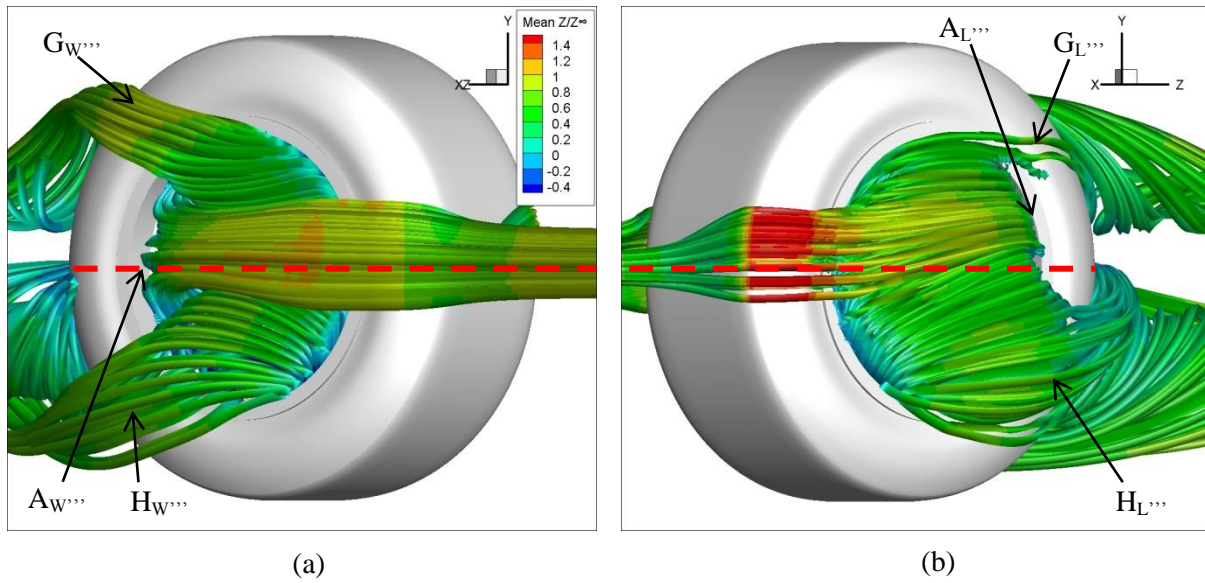


**Figure 100 - Streamlines (coloured by mean streamwise velocity) showing hub flow on the  $15^\circ$  yaw wheel, (a) windward side (b) leeward side, when looking in the streamwise direction**

### 5.2.3 Aerodynamic Forces

The aerodynamic force coefficients for the stationary wheel with applied yaw angle are displayed in Table 2. A 42% increase in drag, is observed with increasing yaw angle from  $0^\circ$  -  $15^\circ$ , which can be the resultant effect of several factors. The internal hub impingement was found to contribute to the drag as stated by Fackrell [22], therefore as the yaw angle increases, internal hub impingement  $C_p$ , particularly on the windward side, was found to increase by 68% from  $5^\circ$  to  $15^\circ$  of applied yaw. Additionally, an increase in yaw angle was also found to result in a larger lateral spread of velocity vectors in the wake region, which increases the wake size and subsequently, increasing the drag [12]. This was also found in the present results (illustrated in the vorticity plots Figure 95, Figure 97 & Figure 99) as the skewness of the up-wash and downwash intensifies with increasing yaw angle, with the  $5^\circ$  yaw case symbolising a 92% increase in transverse velocity towards the windward side,

relative to the zero yaw case. A lower base pressure in the rear wake is also found with increasing yaw angle (Figure 92), and is suggested in [12] to be caused by the flow separating due to an adverse pressure gradient at the back of the wheel. The lift coefficient remained very close to zero, however the side force decreased, directing the force towards the  $-x$  direction. This is predicted to be due to the windward side hub cavity being more exposed to the oncoming free stream flow, essentially having a push on the internal face of the hub towards the leeward ( $-x$  direction).

<b>Wheel Yaw Angle</b>	<b>Force Coefficient</b>		
	<b><math>C_D</math></b>	<b><math>C_L</math></b>	<b><math>C_X</math></b>
<b>0°</b>	0.35	-0.01	-0.05
<b>5°</b>	0.35	-0.07	-0.18
<b>10°</b>	0.39	-0.04	-0.35
<b>15°</b>	0.50	0.02	-0.52

**Table 2 – Stationary wheel force coefficients with applied yaw**

### 5.2.4 The effect of Yaw

With the application of yaw, the most noticeable difference was the four distinct vortical structures (observed with no yaw) being transformed into two distinct vortices. However, detailed analysis into the flow physics around each stationary yaw case, showed significant changes that were influenced by yaw angle.

From the most upstream position at the front central region of the wheel, a clear shift in front stagnation position is observed. Vertical displacement of the stagnation position is negligible, as the region remains within the front central midpoint region of the wheel, however changes in transverse position is noticeable, as can be seen in their individual pressure contour plots previously shown and discussed, (Figure 93 & Figure 94). Transverse displacement from the wheel centreline was measured and plotted on a graph (Figure 101), and showed  $\Delta x/d = 0.04$ ,  $\Delta x/d = 0.08$  and  $\Delta x/d = 0.11$  for the  $5^\circ$ ,  $10^\circ$  and  $15^\circ$  yaw configurations respectively, representing a horizontal linear displacement of  $x/d \approx 0.04$  towards the windward side of the wheel from the wheel centreline with each  $5^\circ$  incremental increase in yaw angle.

The flow travelling past the sides of the wheel upon stagnation shows an increase in acceleration around the leeside of the wheel as the yaw angle increases, acting in unison with a decrease in acceleration on the windward side of the front edge of the wheel. With no applied yaw, maximum velocity magnitude around the leeside indicates 59m/s and with  $5^\circ$  incremental increases in yaw angle to  $15^\circ$  yaw, the maximum velocity increases to 60m/s,

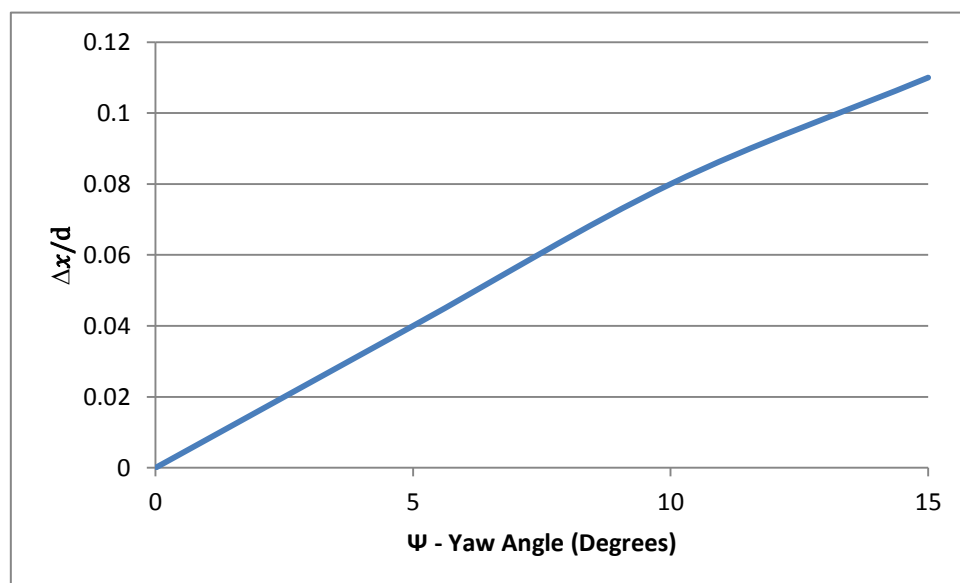


Figure 101 - Change in transverse displacement of stagnation region from stationary wheel centreline with increasing yaw angle

71m/s and 78m/s respectively. Similarly, on the windward side maximum velocity magnitude reduces from 59m/s at  $0^\circ$  yaw to 55m/s, 51m/s and 46m/s at  $5^\circ$ ,  $10^\circ$ , and  $15^\circ$  yaw respectively, indicating an approximate 9% decrease in velocity for each  $5^\circ$  addition of yaw. Moving further downstream towards the hub regions, the flow impinges on the rear surface of each hub. As has been previously discussed, the hub impingement influences the direction of flow within the hub, hence determining the location the flow departs the hub; these locations and flow patterns for each individual yaw case have been discussed previously under each of their respective sections. It is evident from the results that although impingement location varies at lower yaw angles ( $\Psi < 10^\circ$ ), after  $\Psi \geq 10^\circ$  the rear wake becomes somewhat steady with minimal asymmetry and internal hub impingement occurring in the wheel mid-height region, essentially stabilising the flow. Separation was predicted to occur from the centreline pressure graph (Figure 92) at  $\theta = 140^\circ$  &  $220^\circ$ ,  $\theta = 139^\circ$  &  $230^\circ$ ,  $\theta = 133^\circ$  &  $230^\circ$ ,  $\theta = 129^\circ$  &  $228^\circ$  for  $0^\circ$ ,  $5^\circ$ ,  $10^\circ$ ,  $15^\circ$  configurations respectively on the lower and upper surfaces. It was difficult to computationally predict the zero velocity regions on the wheel surface by identifying regions of backflow caused by flow separation due to the alignment of the velocity vectors with the wheel axis. This was also experienced by Smith et al [26], as they found regions of backflow on a yawed cylinder were defined by a position where the flow in the x-z plane was aligned with the cylinder axis, and not by the region of zero velocity. However from the centreline pressure data, separation location on the upper surface of the wheel increased by  $10^\circ$  with the application of yaw (relative to the un-yawed case), therefore occurring  $10^\circ$  closer to the top of the wheel but remained at that separation location of  $\theta \approx 230^\circ$  with increasing yaw angle between  $5^\circ \leq \Psi \leq 15^\circ$ . However, on the lower surface of the wheel, separation location decreased by up to  $4^\circ$  with each  $5^\circ$  incremental increase in yaw angle, therefore occurring closer to the bottom of the wheel with increasing yaw angle. The change in separation position on the lower rear surface of the wheel, can be expected due to the increasing yaw angle exposing the windward side of the wheel to the oncoming flow, therefore, as the low pressure flow rolls over the sides of the wheel, the interaction with the higher pressure region on the rear sheltered side creates an adverse pressure gradient resulting in flow separation.

Considering vortex core position and magnitude, the initially observed four vortices on the un-yawed configuration, transform into only two vortices with applied yaw angle. Central vortex core vorticity magnitude and position for the  $0^\circ$  yaw case has already been discussed earlier in this section, subsequently, followed by the individual yaw configurations. The wheel configurations with applied yaw angle show two vortices on the windward side of the

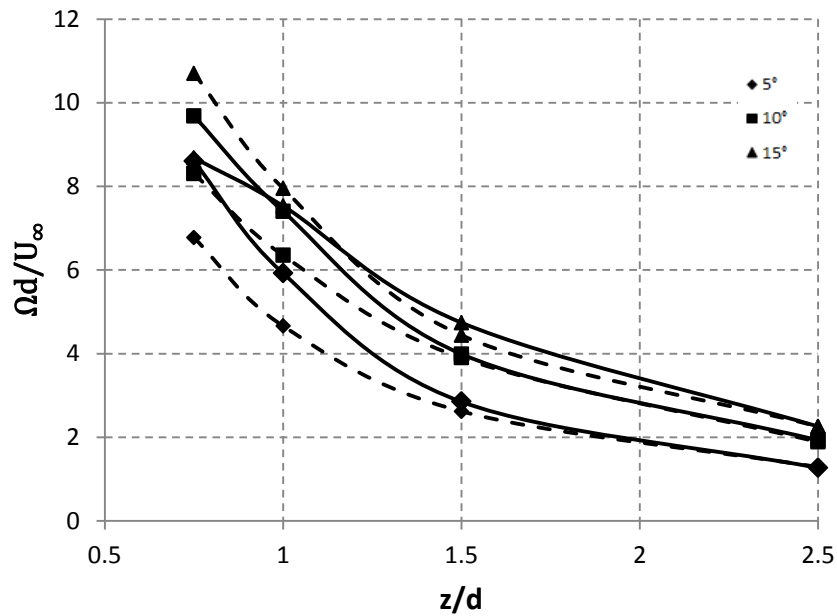


Figure 102 - Vortex core vorticity magnitude (on yawed stationary wheel) with downstream propagation into the rear wake; Upper vortex -  $V_2$  (dashed), Lower vortex -  $V_4$  (solid)

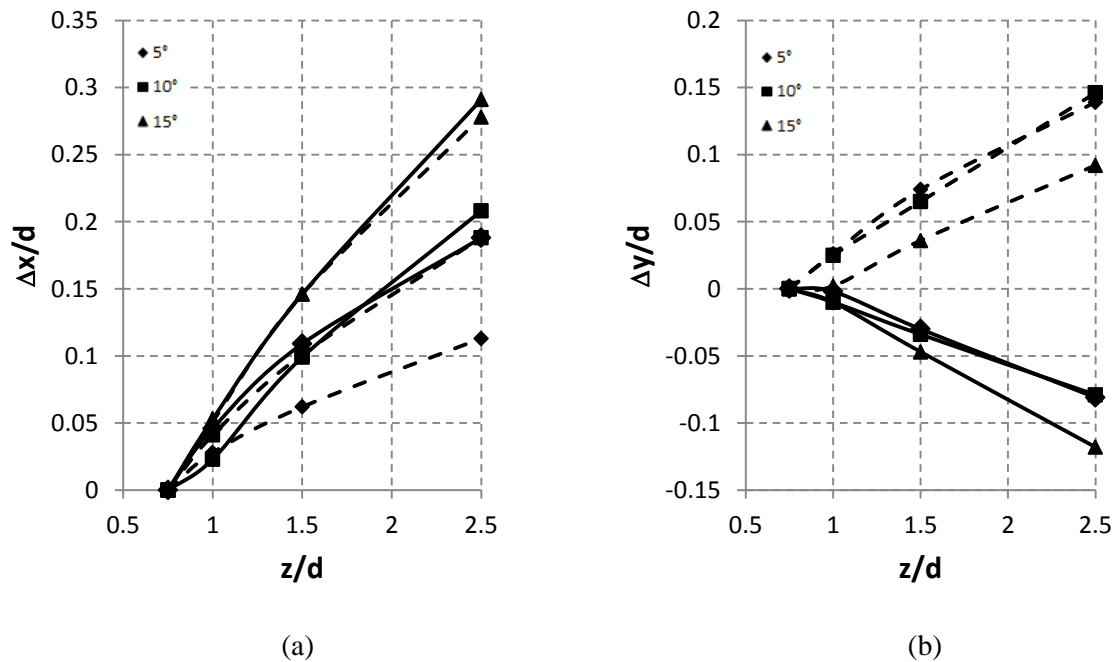
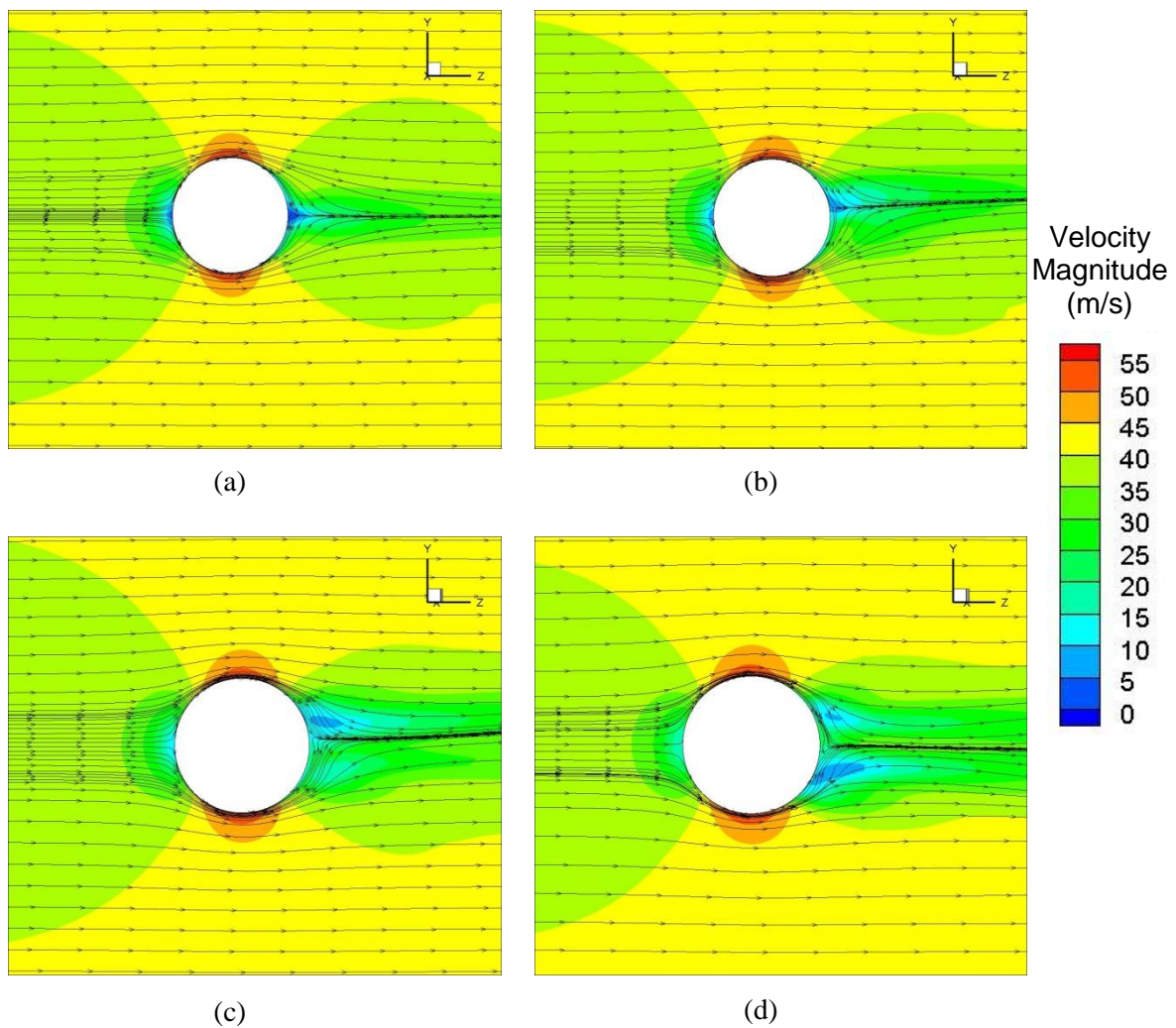


Figure 103 – Vortex core displacements (on yawed stationary wheel) relative to  $z/d = 0.75$  with downstream propagation;  $V_2$  (dashed),  $V_4$  (solid). (a) Transverse (b) Longitudinal



wheel. Central vortex core vorticity magnitude at  $z/d = 0.75$ , illustrated in the earlier vorticity plots and in Figure 102, indicate the lower vortex  $V_{4'}$  and  $V_{4''}$  for the  $5^\circ$  &  $10^\circ$  configurations respectively, to be stronger in magnitude than their respective upper vortex by up to 28% and 16% respectively. However, at  $15^\circ$  yaw, the upper vortex ( $V_{2'''}$ ) is stronger than  $V_{4'''}$  by up to 23%, although reducing to less than 5% for all cases with downstream propagation,  $z/d > 0.75$ . Both yaw angles, of  $5^\circ$  &  $10^\circ$ , show the same difference in magnitude of  $\approx 5\%$  between the two vortices after  $z/d \geq 1.5$ . Figure 103 illustrates the lateral and longitudinal central vortex core positions with downstream propagation referenced to  $z/d = 0.75$  ( $\Delta x/d = 0$ ,  $\Delta y/d = 0$ ). Considering the lateral displacement (a), an almost linear correlation is present showing an increase in relative horizontal displacement to the windward side of the wheel with increasing degree of applied wheel yaw. Interestingly, while the upper vortex ( $V_2$ ) moves with almost linear relative displacement with downstream propagation, the transverse displacement of  $V_4$ , exhibits some non-linear behaviour at lower yaw angles ( $\Psi \leq 10^\circ$ ). As described earlier, this result is suggested to be due to the asymmetric levels of constructive amplification discussed earlier resulting from the transverse flow physics (upper vortex  $V_2$ ) being unable to fully entrain the opposing wake flow from moving to the opposite leeside of the wheel which was found to be most prominent at  $\Psi = 5^\circ$ . The rear wake flow is dominated by the skewed up-wash and downwash, and is intensified by increasing transverse velocities near the centre of the wheel, therefore, being fully able to entrain the wake towards the windward side of the wheel at yaw angles  $> 5^\circ$ . An anomaly in the  $10^\circ$  lower vortex ( $V_{2''}$ ) at  $z/d = 1$ , shows a slight dip in  $\Delta x/d$ , at  $z/d = 1$ , and not being able to fulfil the linear trend observed at higher yaw angles; this is predicted to be as result of the highly oscillatory, unsteady near rear wake as an almost linear trend is shown further downstream  $z/d \geq 1.5$ . The upper and lower vortices at  $\Psi > 5^\circ$ , show an almost equal  $\Delta x/d$  as they propagate further downstream whilst the  $5^\circ$  yaw case shows a difference of  $\approx 66\%$  between the transverse displacement of the two vortices at the furthest downstream plane,  $z/d = 2.5$ ; also confirming the suggested observation that the increase in yaw angle essentially stabilizes rear wake flow field. These significant changes in transverse displacement with applied yaw, were found to occur with relatively small, but linear, changes in vertical displacement, as is shown from Figure 103(b), with results revealing both a relative insensitivity with very little defined trend or direct relationship relative to applied yaw angle. The size and shape of the rear wake are shown in Figure 104, which displays mean velocity magnitude contours and streamlines on the wheel's centreline plane. The rear wake on the  $0^\circ$  yaw case is relatively small in size

when observing the low velocity region due to separation being located more towards the rear, however, this low velocity region increases with increasing yaw angle. The asymmetry in the wake observed at 10° and 15° yaw, is due to the difference in vortex size and magnitude. As described earlier for the 10° yaw case, although the windward side hub cavity experiences flow impingement near wheel mid-height, the leeside cavity experiences impingement at 164.5°. With reference to Figure 98(b), this impingement location causes the flow to leave the hub on the upper half of the wheel and contribute to the upper vortex  $V_{2''}$ . Similarly, on the 15° case, the leeside impingement occurs at 196.7°, causing the flow to leave the hub on the lower side and contribute to  $V_{4'''}$ , as shown in Figure 100(b). These hub flow contributions to the vortical structures had shown to reduce the magnitude but increase the size of the vortices, therefore, resulting in the asymmetric rear wake indicating the low velocity regions to be the vortices that are weaker but larger in size. The increase in low velocity wake size contributes to the rise in drag coefficient as shown in Figure 105.



**Figure 104 – Contour plots of velocity magnitude on stationary wheel centreline cross-sectional plane; (a) 0° yaw, (b) 5° yaw, (c) 10° yaw & (d) 15° yaw, with velocity streamlines**



A larger wake region is expected to induce a larger drag force, due to the earlier separation forming the two shear layers which entrain the flow in the wake region [12]. Increasing yaw angle on the stationary wheel was found to intensify the lateral spread of velocity vectors in the wake of the wheel [12], as illustrated in the vorticity plots, resulting in a larger wake size subsequently increasing the drag force. Furthermore, Smith et al [26] also carried out tests on a yawed cylinder and observed a decrease in base pressure, was found to contribute for the increase in drag. In this investigation the same principle can be applied as a lower base pressure occurs as yaw angle increases (Figure 92), corresponding to an increase in drag coefficient. Lift is observed to fluctuate around the value of zero as the wheel is placed in the vertical centre of the domain, resulting in a near symmetric flow field on both upper and lower halves of the wheel. Side force shows a linear decrease with increasing yaw angle, representing a force directed in the negative x-direction respective of the wheel geometry and coordinate axis. An increase in side force is also shown by Morelli [33]; however, although a similar trend is experienced, direct comparisons were not made to the experimental results [33] as subsequent investigations by other authors proved that errors were present due to their methodology. An almost negligible (near zero) side force is present on the zero yaw case; this could be due to small fluctuations caused by the unsteady flow or due to the slight asymmetry between the hubs as the hub cavity on the positive side of the x-centreline is marginally deeper than the opposite side. Therefore as the flow travels into the marginally larger hub cavity comprising of a larger volume, a small side force could be induced in the  $-x$  direction.

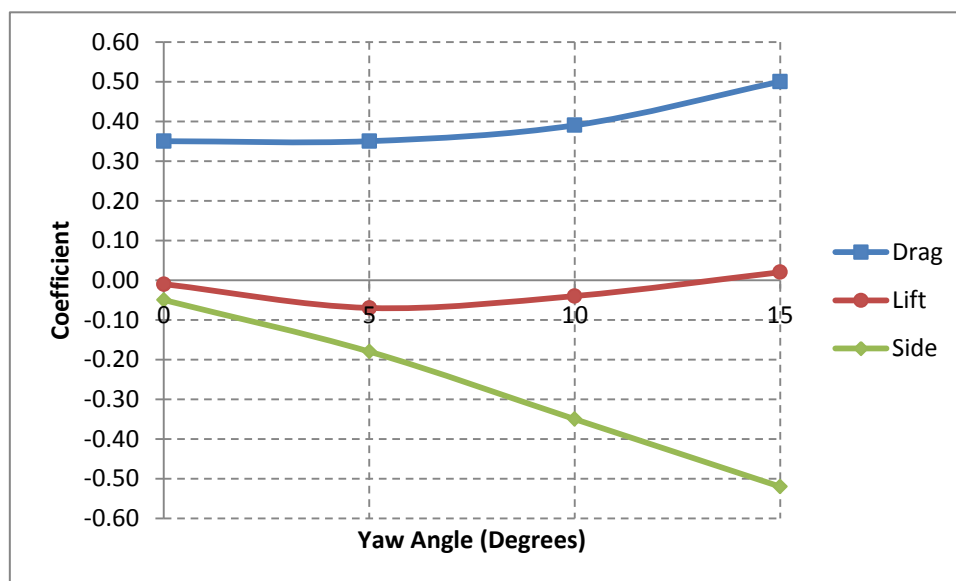


Figure 105 - Force coefficients for stationary wheel with applied yaw angle

### 5.3 The Influence of Wheel Rotation

Rotation was applied in order to understand the flow field around the wheel after an aircraft has taken off. Immediately after take-off, the wheels continue to spin forward into the oncoming free-stream flow at an equivalent speed to the aircraft's take-off speed, therefore rotational angular velocity of 192.31rad/s, equivalent to the modelled free stream flow of 40m/s was applied on the wheel. Time-averaged pressure on and around the wheel will be discussed with a detailed analysis of the wake physics and corresponding aerodynamic forces with comparisons made to the available literature. Similar to the yawed cases, identification of flow features/regions are denoted with a subscript (<sub>R</sub>) for the rotating cases, (i.e. Flow feature/region being described in zero yaw stationary case is denoted A, with the same feature/region denoted A<sub>R</sub> for rotating cases).

The general flow field around a rotating wheel shows a stagnation region on the front face of the wheel, before the flow accelerates around the wheel. Separation is found to occur earlier on the rotating wheel due to the attached flow on the wheel interacting with the free stream flow upstream at the top of the wheel, as illustrated in Figure 26 by Fackrell [22]. After the flow separates, a shear layer is formed on top of the wheel propagating in to the rear wake. Due to the wheel rotation, an intense up-wash is present on the rear surface of the wheel; however, after reaching and interacting with the upper shear layer, the flow is entrained in this region and recirculated forming two upper vortices.

#### 5.3.1 Surface Pressure Characteristics

Centreline mean surface pressure (Figure 106) for the rotating wheel, shows a different trend to that observed on the stationary wheel after the bottom of the wheel at  $\theta = 71.5^\circ$ . Initially considering the frontal region of the wheel, flow stagnation occurs at the front of the wheel with  $C_p = 1$ . The pressure reduces around the bottom of the wheel reaching a negative peak of  $C_p = -1.04$  at  $\theta = 90^\circ$  (A) with a corresponding maximum velocity of 56m/s. The negative pressure peak observed slightly lower, than on the stationary wheel, is predicted to be due to the 4% increase in velocity magnitude on the bottom surface of the rotating wheel, compared to the stationary wheel and caused due to the free-stream flow travelling in the same direction as the wheel rotation. A pressure recovery occurs until the flow detaches on the rear surface of the wheel at  $\theta = 145^\circ$  (B) and  $\theta = 264^\circ$  (D). At the former location of  $\theta = 145^\circ$ , located  $35^\circ$  below mid-height on the rear surface,  $C_p = -0.22$ . However, the pressure decreases to a value of  $C_p = -0.28$  directly behind the wheel at  $\theta = 180^\circ$  (C) where the, previously stated, up-wash

occurs with a mean velocity of 29.7m/s, before recovering at (D) to  $C_p = -0.18$  at  $\theta = 264^\circ$  where the flow separates. This separation location is  $6^\circ$  downstream from the top of the wheel. Centreline surface pressure obtained by McManus & Zhang [29] on the rotating wheel, predicted separation to occur at  $\theta = 270^\circ$  and  $\theta = 255^\circ$  for the Spalart-Allmaras & RKE computations respectively. Therefore it is clearly evident that the result from this study for the upper separation position is in good agreement. Separation on the lower half of the wheel was not observed by McManus & Zhang [29], although a lower base pressure was obtained. However, their study was conducted with the wheel in contact with the ground, therefore indicating a ‘pumping’ effect (as has been discussed in [29]) accelerating the flow outwards and downstream from the contact patch due to the diverging boundaries. With wheel rotation also inducing the up-wash velocity on the rear surface of the wheel, a consequent reduction in base pressure is observed on the rotating wheel in contact with the ground.

For comparison, the centreline surface pressure coefficient of the stationary wheel at zero yaw discussed earlier, is also plotted on the same graph, Figure 106, for direct comparisons. The graph clearly illustrates the difference in separation positions between the two configurations; the rotating wheel separates at an earlier angular position ( $\theta^\circ$ ) on the upper surface compared to the stationary case. This was also found by authors who have previously modelled both rotating and stationary wheels on the ground, whereby the rotating wheel is found to separate earlier than the stationary wheel, due to the reversed layer of flow on the wheels surface interacting with the free-stream flow (Figure 107 – D).

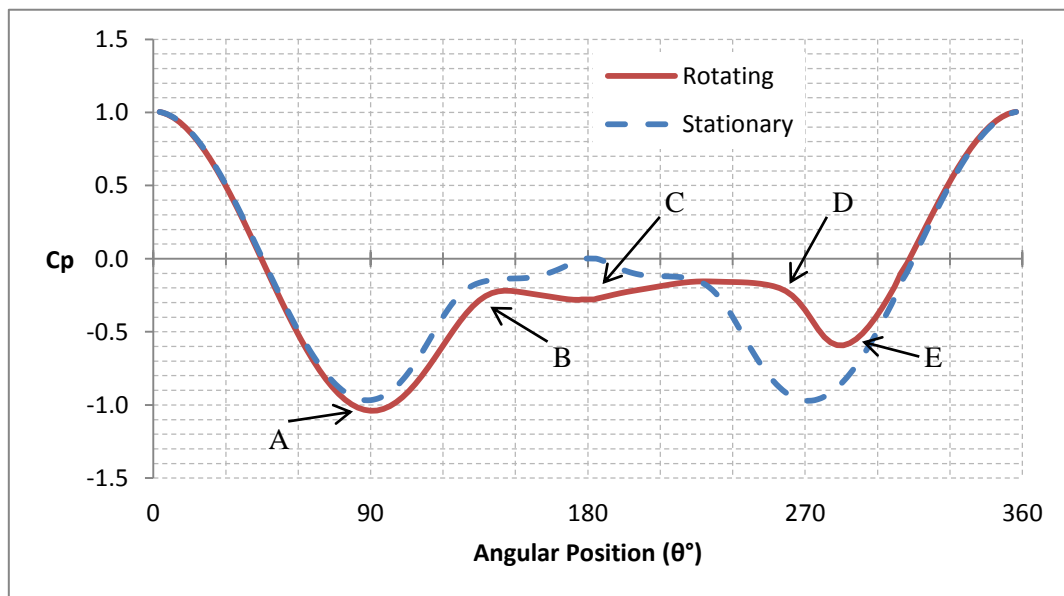


**Figure 106 – Centreline mean surface pressure coefficient on rotating wheel with no yaw**

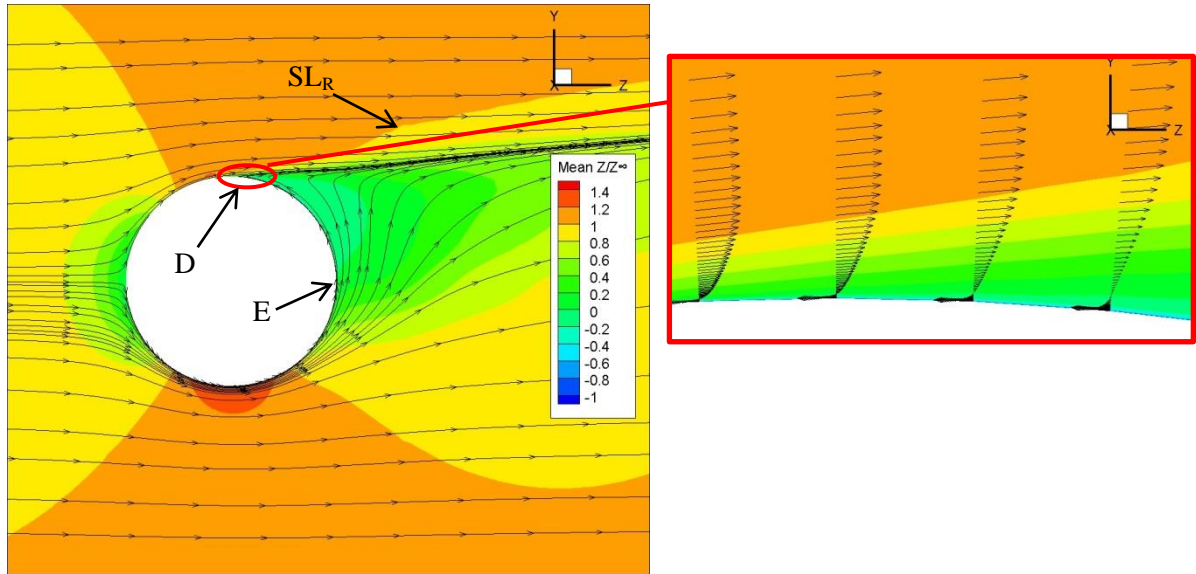


Figure 107 - Mean  $z$  velocity contours and streamlines on  $x/d=0$  plane, with 'D' showing a detailed illustration of the separation region

Between the separation regions on the rear surface of the rotating wheel, the average base pressure ( $C_p = -0.23$ ) remains lower than observed for the stationary case ( $C_p = -0.11$ ) as shown in Figure 106, and is thought to be due to the rotation on the wheel increasing the velocity directly behind the wheel, entraining the flow upwards, as shown E in Figure 107 and Figure 108.

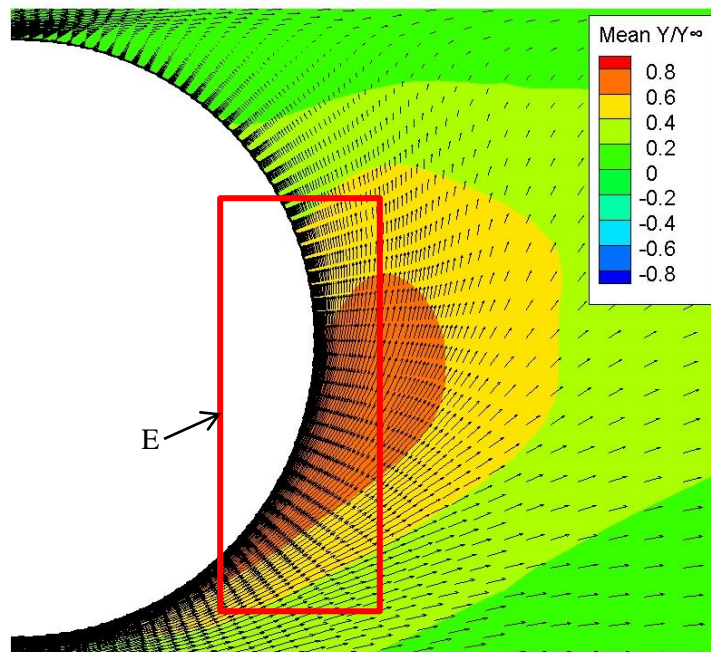


Figure 108 - Contours of mean  $y$  velocity with velocity vectors in  $x/d=0$  centreline plane

The contour plot of pressure on the  $y/d=0.5$  data plane, Figure 109(c), shows a similar pressure flow field to that observed for the zero yaw stationary case, showing the stagnation region at the centre of the front surface of the wheel ( $A_R$ ), before accelerating around both sides of the wheel reaching a maximum velocity of 57.5m/s. As the flow travels around the sides of the wheel, impingement regions are observed on the rear surface of both hub cavities causing the flow to circulate inside. However the direction of circulation is indicated by the location of the impingement. From the pressure contours on the wheel, Figure 109(a) (b), the flow was observed to impinge on the rear surface of both hub cavities above mid-height ( $A_{WR}$ ,  $A_{LR}$ ), at approximately  $190^\circ \leq \theta \leq 198^\circ$ , resulting in the flow circulating into the hub travelling downwards. As the circulated flow reaches the outer lower edge of the hub, the flow leaves and is entrained downstream by the free-stream flow travelling past the wheel,

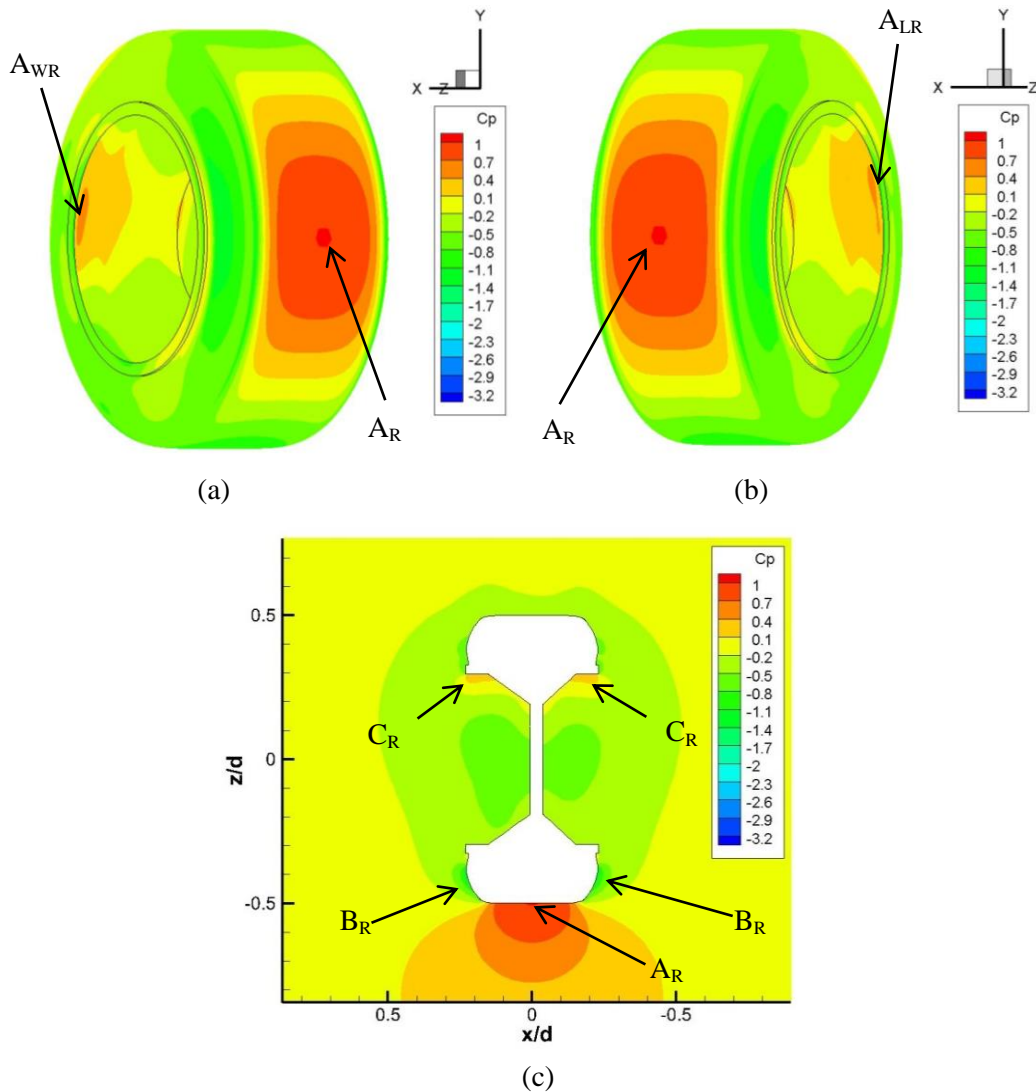


Figure 109 – Contours of mean  $C_p$  for  $0^\circ$  yaw + rotation, (a) wheel surface looking downstream from left, (b) wheel surface looking downstream from right (c) cross-sectional plane at  $y/d=0.5$



which is subsequently pulled upwards near the rear of the wheel due to the intense up-wash caused by the rotation, as has been described earlier and shown in Figure 108. The regions where the flow leaves the hub and rolls up around the lower shoulders of the wheel can also be identified in Figure 110(a)- $F_{1R}$ ,  $F_{2R}$  as regions of low vorticity. Further downstream into the wake, these regions of low vorticity are reduced until they are no longer visible at  $z/d = 2.5$  (d) as the flow is entrained upwards by the already stated, up-wash.

### 5.3.2 Wake Physics

The application of rotation on the wheel produces a pair of near symmetrical arch-shaped vortices ( $V_{1R}$ ,  $V_{2R}$ ) in the rear wake of the wheel as shown in Figure 110; in agreement with the flow physics observed on the upper rear surface of the rotating wheel by McManus & Zhang [29]. An intense up-wash ( $E_R$ ) is present on the lower half of the wheel caused by the

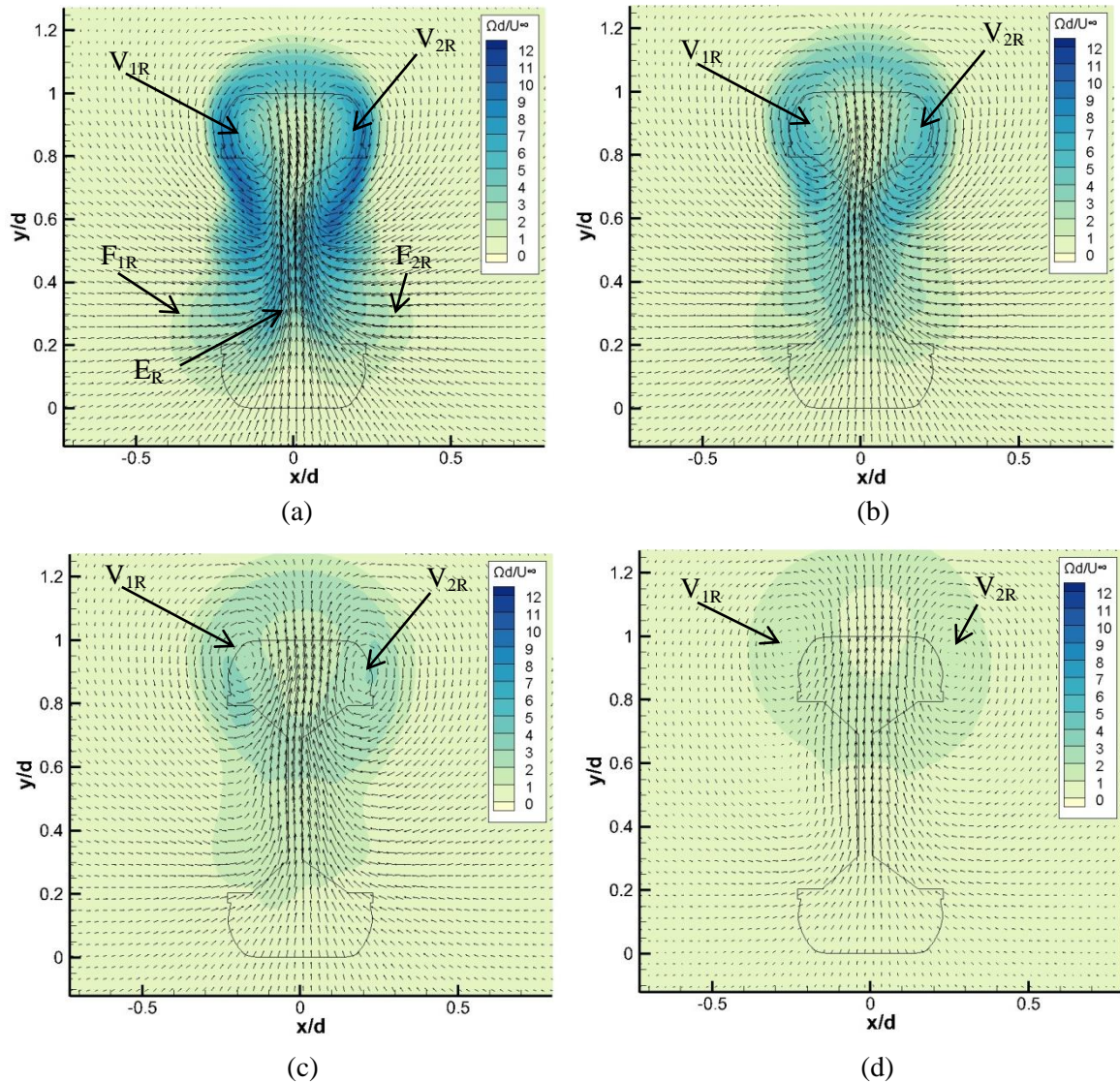


Figure 110 – Non-dimensional vorticity plots for  $0^\circ$  yaw + rotation; (a)  $z/d=0.75$ , (b)  $z/d=1$ , (c)  $z/d=1.5$ , (d)  $z/d=2.5$

rotation of the wheel entraining the flow in the direction of rotation. However, once this flow reaches the upper section of the wheel, it meets an adverse pressure gradient due to the separated shear layer on the upper surface of the wheel, previously identified in Figure 107, which directs the up-wash on the rear surface of the wheel to either side, forming two vortices. This vortex pair illustrates a counter-rotating motion as vortex  $V_{1R}$  rotates anti-clockwise and  $V_{2R}$  rotating clockwise (when viewed from behind the wheel); contrary to what was observed on the stationary case where the upper vortices  $V_1$  rotated clockwise in unison with  $V_2$  rotating anti-clockwise as shown in Figure 90, in agreement with the counter-rotating vortex pair found on the upper rear wake of a rotating wheel in contact with the ground [29, 12]. After analysis of the central vortex core position and vorticity magnitude, the two vortices were found to be near identically symmetrical about the  $x/d = 0$  centreline of the wheel. Central vortex core vorticity magnitude in the  $z/d = 0.75$  plane, Figure 110(a), revealed  $\Omega d/U_\infty = 5.05$  for  $V_{1R}$  and  $\Omega d/U_\infty = 5.64$  for  $V_{2R}$ , comprising of a difference in magnitude of 12% between the two vortices. However, at the furthest downstream data plane at  $z/d = 2.5$ , the difference in magnitude between the two vortices reduced to  $\approx 1\%$  ( $V_{1R}$ :  $\Omega d/U_\infty = 1.45$ ,  $V_{2R}$ :  $\Omega d/U_\infty = 1.47$ ) indicating near identical vorticity magnitude with downstream propagation. The magnitude of the two upper vortices appears to be smaller on the rotating wheel when compared to the stationary wheel ( $V_1/V_{1R}$ :  $\Delta\Omega d/U_\infty = 16\%$ ,  $V_2/V_{2R}$ :  $\Delta\Omega d/U_\infty = 17\%$ ), with a similar trend found in [39] which was suggested to be due to the earlier flow separation on the rotating wheel. Vertical vortex core positions at the  $z/d = 0.75$  plane shows,  $V_{1R}$ :  $y/d = 0.856$  and  $V_{2R}$ :  $y/d = 0.847$ , confirming the symmetry of the vortices with only a 1% difference in vertical position between the two. Comparing these positions to the upper vortex pair on the stationary wheel, it is also evident that the upper vortices on the rotating wheel are positioned higher up in the wake region by 37% and 39% for  $V_{1R}$  and  $V_{2R}$  respectively, representing a taller wake which is also expected on a rotating wheel, also observed in earlier studies [22, 29, 39]. Additionally, due to the earlier separation on the rotating wheel, the wake is constrained within the shear layers, more than on the stationary wheel, allowing greater transverse growth of the wake on the stationary wheel [22]. This was also observed in the current URANS study when calculating the transverse displacement of each vortex from  $z/d = 0.75$  to  $z/d = 2.5$  showing  $\Delta x/d = -0.12$  ( $V_{1R}$ ) and  $\Delta x/d = 0.10$  ( $V_{2R}$ ), for the rotating wheel and  $\Delta x/d = -0.22$  ( $V_1$ ) and  $\Delta x/d = 0.09$  ( $V_2$ ) for the stationary wheel, (note the negative symbol indicating displacement in the negative x-direction). Figure 111 shows a clear representation of the characteristic flow-field around a rotating wheel in free

air. The upper mid-wheel hub impingement ( $A_{WR}$ ) shows the flow being directed into the hub and circulating downwards until the flow leaves on the lower side of the hub, subsequently being entrained by the intense upwash ( $E_R$ ), as indicated by the coloured contours. The upwash forces this escaped hub flow to travel upwards until it interacts with the separated shear ( $SL_R$ ), subsequently, forming the two counter rotating vortices ( $V_{1R}$  &  $V_{2R}$ ) that propagate downstream into the wake.

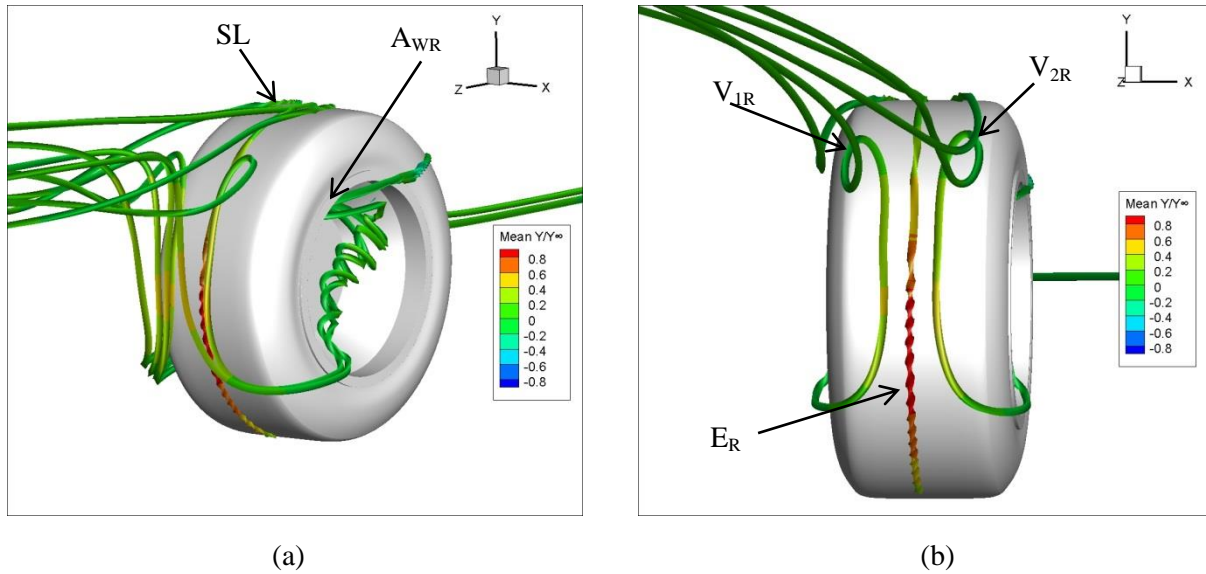


Figure 111 - Streamlines coloured by y-velocity

### 5.3.3 Aerodynamic Forces

Force coefficients for the rotating wheel shown in Table 3, are presented together with those obtained for the stationary wheel. Many earlier investigations studying the flow around both a stationary and rotating wheel in contact with the ground, had found the rotating wheel to produce less lift and drag than the stationary case [22, 29, 30]. However, in this case, with both the wheels placed in free-air, the opposite trend is observed as the rotating wheel indicates a larger lift and drag force. However, Cogotti [36] investigated the aerodynamic forces on a wheel at different ground clearances and had also found a larger drag force on the rotating wheel than the stationary ( $C_D = 0.54$ ,  $C_D = 0.48$ ) respectively. Although Cogotti's drag coefficient for the rotating and stationary wheel is 23% and 37% larger in comparison to the present results, this could be due to their maximum ground clearance being 0.05m compared to the present results obtained in a 'free-air' configuration. Additionally, the experimental configuration comprised of a motor to hold the wheel in position and would have caused an interference with the flow-field [36], as also shown in [30, 43] with the presence of a support sting. Although the motor was shielded by a fairing, Cogotti [36]



showed that a 13% difference in drag still persists on the stationary wheel. Lift force on the rotating wheel was experienced as a negative, and with the theory of the ‘Magnus effect’, this would be expected as the flow accelerates around the lower surface of the wheel at a higher velocity compared to the top of the wheel creating a pressure differential, subsequently directing the lift force towards the side of the wheel where the wheel rotation and free-stream flow are travelling in the same direction [20]. Stapleford & Carr [34] also suggested that a reduction in lift can be expected as rotation induces the velocity on the lower side of the wheel whilst decreasing the velocity on the upper surface, causing the rear wake of the rotating wheel to be displaced at an up-wash angle. This was also observed in the present results as shown in Figure 107.

	$C_D$	$C_L$	$C_X$
<b>Stationary</b>	0.35	-0.01	-0.05
<b>Rotating</b>	0.44	-0.25	0.01

**Table 3 - Force coefficients of stationary and rotating wheel**

### 5.3.4 The effect of Rotation

The effect of rotation showed both similarities and differences when compared to the stationary case and the literature. The most significant difference to the stationary case was the dominant two vortex wake created as a result of the up-wash, caused by the wheel rotation interacting with the separated shear layer on top of the wheel (Figure 110), as is observed in [22]. Flow stagnation was observed in the same region as for the stationary case, at the central most upstream point of the wheel. Upon stagnation, the flow travels around the sides of the wheel and enters the hub cavity before impinging on the upper hub surface causing the flow to circulate into and downwards inside the hub before being entrained out of the hub on the lower half of the wheel by the free stream flow and the wheel rotation travelling in the same direction (Figure 111). An intense upwash is present on the rear face of the wheel due to the wheel rotation, subsequently, entraining the flow behind the wheel to travel upwards towards the top of the wheel. On the upper surface of the rotating wheel, the flow was observed to separate earlier at  $\theta = 264^\circ$ , compared to the stationary case. The earlier separation was caused by the free stream flow and the direction of wheel rotation opposing one another on the upper surface [22, 29, 10]. This is also illustrated in Figure 107. Considering vortex core displacement and magnitude, change in vortex core magnitude with downstream propagation is shown in Figure 112 indicating that both vortices have a similar rate in magnitude reduction, with both vortices comprising of identical magnitude at the

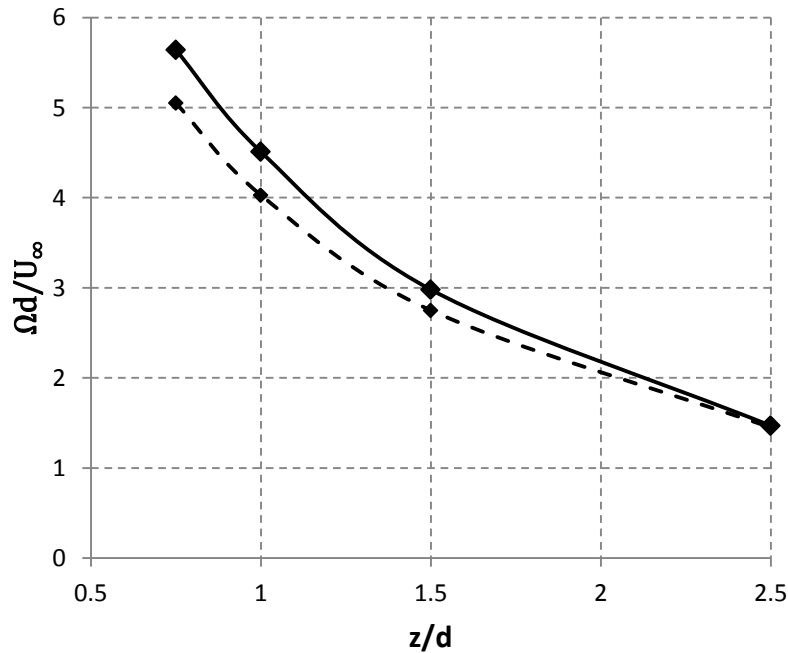
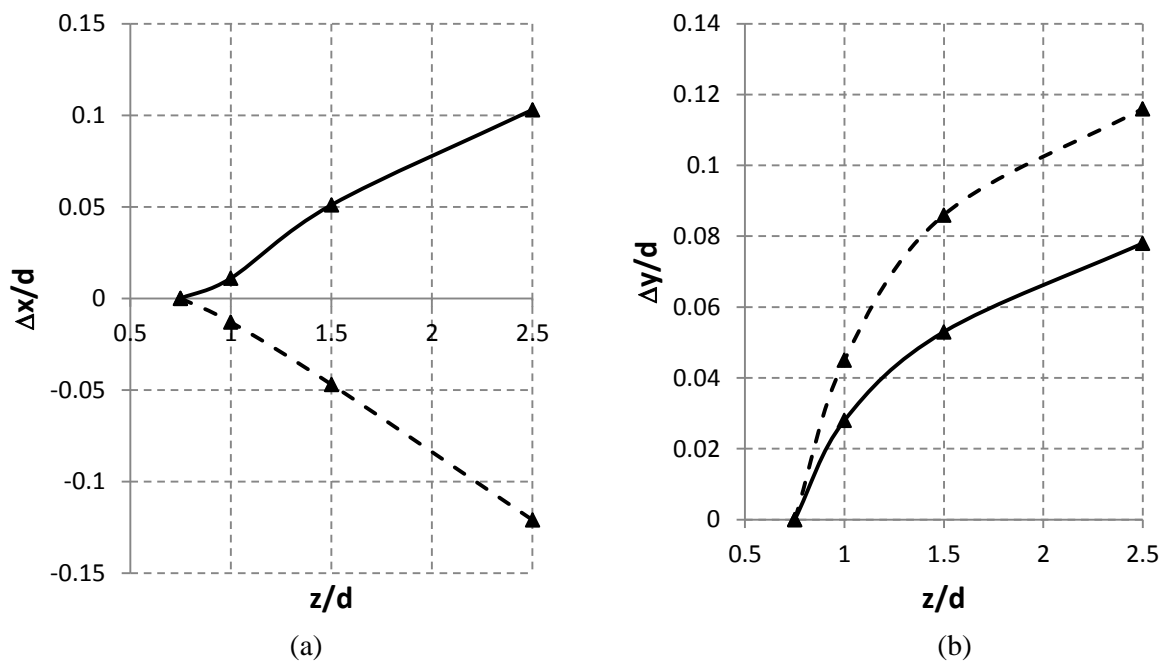


Figure 112 - Vortex core vorticity magnitude on rotating with downstream propagation into the rear wake;  $V_{1R}$  (dashed),  $V_{2R}$  (solid)

furthest downstream plane of  $z/d = 2.5$ . The transverse displacement of both vortices ( $V_{1R}$ ,  $V_{2R}$ ) consists of a linear relationship as both vortices are displaced almost equally on either side of the wheel centreline, as illustrated in Figure 113(a). However, a slight variance of  $\Delta x/d = 0.025$  occurs between the two vortices at the furthest plane downstream. Although this difference is very small (representing just 0.01m), it is predicted to be due to  $V_{1R}$  being weaker by up to 8% at  $z/d = 1.5$ , therefore dissipating faster into the freestream. The longitudinal displacement between the two vortices, Figure 113(b), showed the higher position of  $V_{1R}$  as has been observed previously.



**Figure 113 - Vortex core displacements (on yawed rotating wheel) relative to  $z/d = 0.75$  with downstream propagation;  $V_{1R}$  (dashed),  $V_{2R}$  (solid). (a) Transverse (b) Longitudinal**

Although most of the flow field characteristics are in agreement with previous investigations conducted on rotating wheels, a different trend is found when analysing the drag. Many investigations in the past that have considered both the stationary and rotating wheel providing results for aerodynamic force coefficients, were conducted with the wheel in contact with the ground, and have always shown to comprise of a higher drag force on a stationary wheel compared to the rotating wheel. However, in this study, a higher drag force was observed on the rotating wheel. Also described in the previous section are the results for the aerodynamic force coefficients obtained by Cogotti [36], and although his investigation was conducted with a ground clearance of 0.05m, the trend observed was similar to what is found in this study. Therefore the opposite trend found for wheels in contact with the ground,

is generally concluded to be due to the influence of the ground. A negative lift ( $C_L = -0.25$ ) was found (as expected) due to the pressure differential between the upper and lower surface of the wheel. Additionally, the rotation of the wheel resulted in the wake being displaced at an upwash angle, which has also been a proven factor in reducing lift [34]. Side force remained at zero as the flow around both sides of the wheel is near-identical.

## 5.4 The Influence of Wheel Rotation and applied Wheel Yaw

Combining wheel rotation and yaw angle provides a fundamental understanding of the flow physics around a landing gear wheel immediately after an aircraft takes off into a crosswind. The crosswind component is a typical representation of the added yaw angle and the wheel rotation represents the spinning of the wheels after take-off. Similar to Section 5.2, three yaw angles ( $\Psi = 5^\circ, 10^\circ$  and  $15^\circ$ ) will be modelled combining the application of wheel rotation (Section 5.3) with the wheel peripheral speed equivalent to the free stream velocity. As has been stated previously, flow features/regions are denoted with by ' for increasing yaw angles, combined with a subscript 'R' to signify rotation (i.e. Flow feature/region being described in zero yaw rotating case is denoted  $A_R$ , with the same feature/region denoted  $A_{R'}$ ,  $A_{R''}$  &  $A_{R'''}$  for the  $5^\circ, 10^\circ$ , &  $15^\circ$  combined yaw and rotation cases).

### 5.4.1 Surface Pressure Characteristics

Centreline wheel surface pressure on the combined yaw and rotation cases (Figure 114), shows the stagnation region on the front face of the wheel to be offset from the initially observed location of  $\theta = 0^\circ$  with  $C_p = 1$  for the zero yawed case. At this angular position, the front stagnation region appears to be insensitive to the application of rotation on the yawed wheel as the central front region ( $\theta = 0^\circ$ ) of Figure 114 is in very good agreement with that

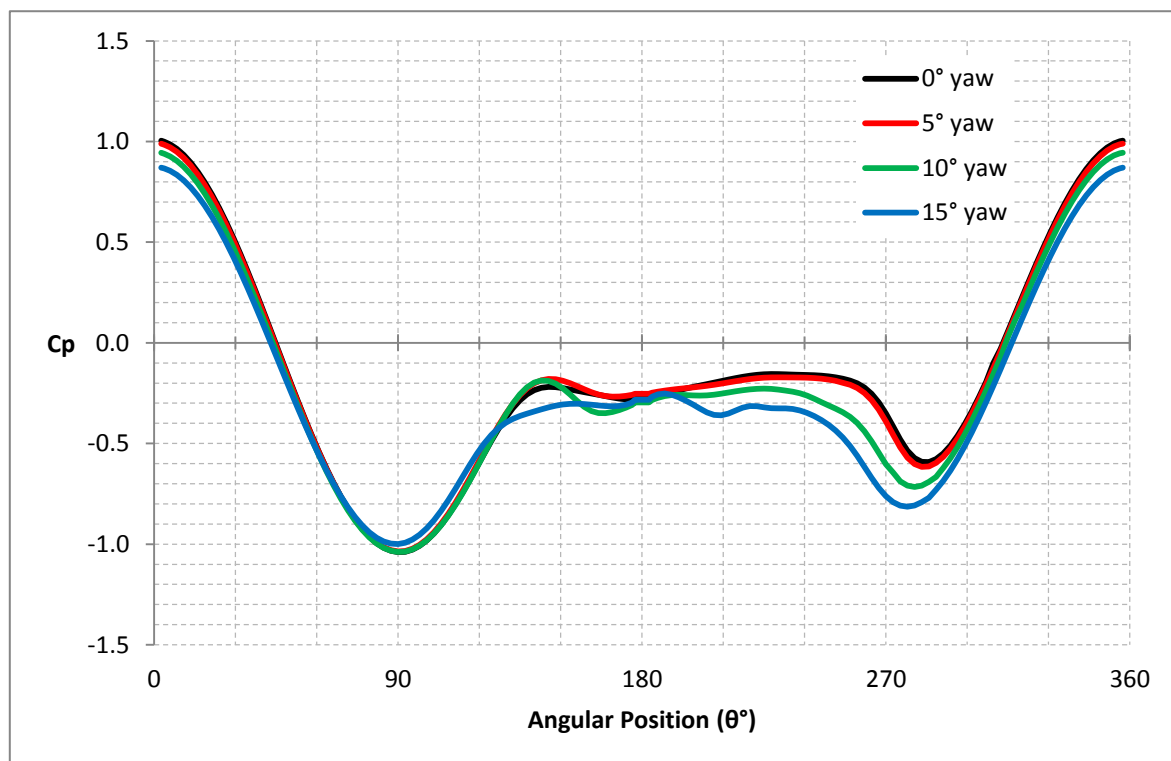
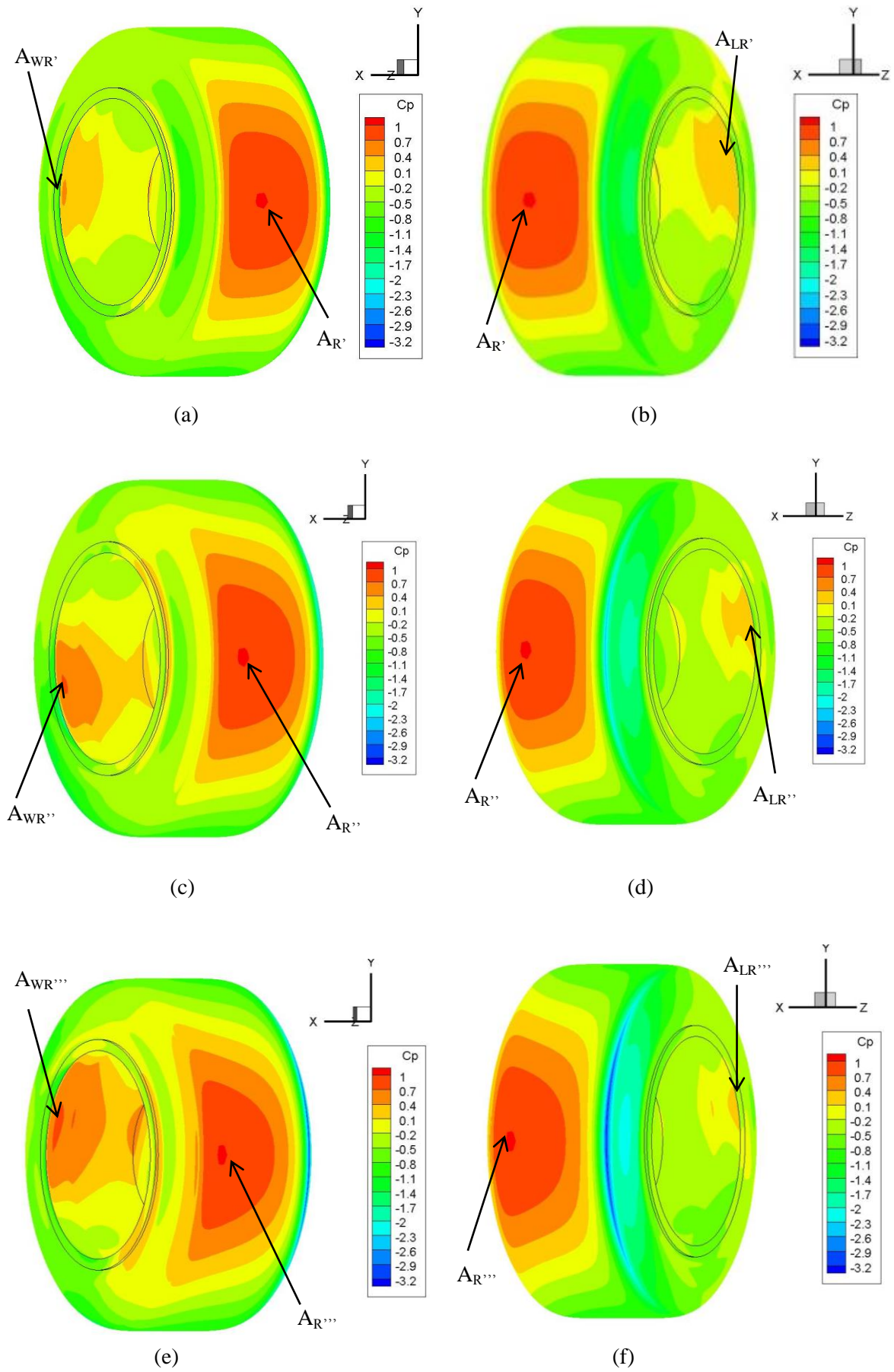


Figure 114 – Rotating wheel centreline mean surface pressure coefficient with added yaw angle

observed in Figure 92. Further downstream the front central region, the three cases comprising of different yaw angles show good correlation to one another until  $\theta = 71.5^\circ$ , as the flow approached the lower surface of the wheel. Subsequent to this region, the flow is accelerated around the bottom surface of the wheel to velocity magnitudes up to 56m/s for all yaw cases, before pressure recovery begins, as the flow travels around the lower rear surface of the wheel. Flow separation, similar to the previous cases, is defined where pressure recovery ceases and where large scale pressure fluctuations no longer occur [22, 30], and are observed on the upper surface at  $\theta = 263^\circ$ ,  $\theta = 255^\circ$  and  $\theta = 247^\circ$  at  $5^\circ$ ,  $10^\circ$  and  $15^\circ$  yawed configuration respectively, as can be identified by the centreline pressure graph shown in Figure 114. Comparing these positions to the stationary separation locations for the yawed cases (Figure 92), separation occurs further upstream on the rotating wheel, showing good agreement with previous literature comparing stationary and rotating cases. However, a decrease in separation angle is observed from these results showing that separation occurs further downstream towards the rear surface of the wheel with increasing yaw angle. In addition, Figure 114 indicates a decrease in average base pressure as the yaw angle is increased.

Contour plots of mean surface pressure on the rotating wheel surface and at  $y/d = 0.5$ , for all three yawed configurations are shown in Figure 115 and Figure 116 respectively, clearly illustrating the previously identified transverse shift in front stagnation position towards the windward side of the wheels. The horizontal displacement of this region from the centreline of the wheel was  $\Delta x/d = 0.04$  ( $A_{R'}$ ),  $\Delta x/d = 0.08$  ( $A_{R''}$ ),  $\Delta x/d = 0.11$  ( $A_{R'''}$ ) for  $5^\circ$ ,  $10^\circ$ ,  $15^\circ$  yaw respectively. Around either sides of this stagnation region, the flow travels around the sides of the wheel and illustrates an increase in maximum velocity on the leeside with increasing yaw angle showing 61.1m/s with  $C_p = -1.37$  ( $B_{R1}$ ), 70m/s with  $C_p = -2.3$  ( $B_{R3}$ ), 77m/s with  $C_p = -2.81$  ( $B_{R5}$ ). The increase in velocity on the leeside acts in unison with a decrease in maximum velocity on the windward side indicating 53.5m/s with  $C_p = -0.92$  ( $B_{R2}$ ), 50.8m/s with  $C_p = -0.61$  ( $B_{R4}$ ), 46.3m/s with  $C_p = -0.33$  ( $B_{R6}$ ). The increase in flow velocity on the leeside edge is expected due to the respective side being angled at a position in which the free-stream flow can travel streamwise upon stagnation, however a reduction in flow velocity on the windward side occurs due to the stagnated flow having to travel around the edge of the wheel which is located further upstream towards the inlet than the leeside edge. The contour plots obtained at wheel mid-height (Figure 116) also shows the region of flow impingement on the rear surface of each hub.

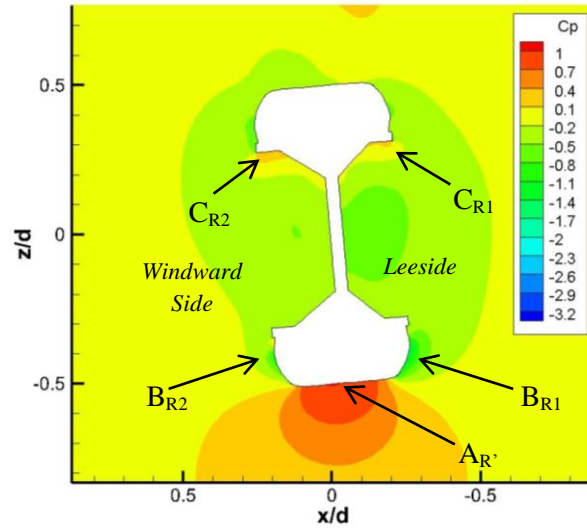


**Figure 115 – Contours of mean  $C_p$  on rotating wheel surface when looking downstream: (a) 5° left, (b) 5° right, (c) 10° left, (d) 10° right, (e) 15° left, (f) 15° right**

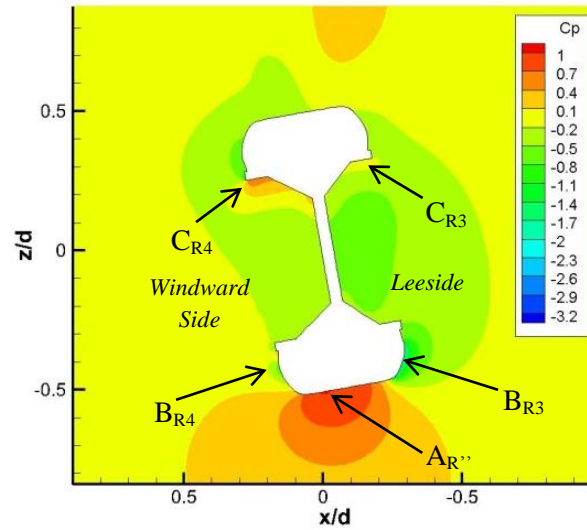
As has been observed previously, from the non-rotating yawed cases,  $C_p$  decreases on the leeside due to the obstruction of the flow, caused by the front of the wheel providing pressure coefficients of:  $C_p = 0.29$  ( $C_{R1}$ ),  $C_p = 0.164$  ( $C_{R3}$ ) and  $C_p = -0.17$  ( $C_{R5}$ ) for  $5^\circ$ ,  $10^\circ$  and  $15^\circ$  yaw respectively.

In addition,  $C_p$  on the windward side rear hub surface increases as it is exposed further with increasing yaw angle, providing pressure coefficients of:  $C_p = 0.41$  ( $C_{R2}$ ),  $C_p = 0.52$  ( $C_{R4}$ ) and  $C_p = 0.69$  ( $C_{R6}$ ) for  $5^\circ$ ,  $10^\circ$  and  $15^\circ$  yaw respectively. However, although stagnation pressure regions are observed on the rear surface of the hub, direct hub impingement was found to occur on either sides of the wheel mid-height location, as was found earlier to have an influence on the wake region and vortices formed.

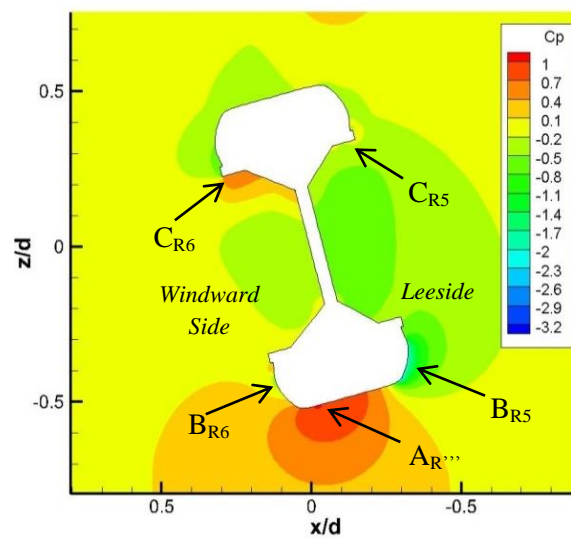




(a)



(b)



(c)

Figure 116 – Contours of mean  $C_p$  on rotating wheel at cross-sectional plane at  $y/d=0.5$ : (a)  $5^\circ$ , (b)  $10^\circ$ , (c)  $15^\circ$

## 5.4.2 Wake Physics

The wheel with combined yaw and rotation continues to possess a dominant two vortex wake. With the application of  $5^\circ$  yaw on the wheel, the two vortices have rotated clockwise towards the windward side, as illustrated in Figure 117. Comparing vortex positions to the non-yawed rotating case (Figure 110),  $\Delta x/d = 0.08$ ,  $\Delta y/d = -0.03$  for  $V_{1R'}$  relative to  $V_{1R}$ , and  $\Delta x/d = 0.01$ ,  $\Delta y/d = -0.33$  for  $V_{2R'}$  relative to  $V_{2R}$ . As a result of the applied yaw angle on the rotating wheel, the up-wash ( $E_R'$ ) is also skewed towards the windward side of the wheel and together with the rotation on the wheel and the flow separating off the upper edge of the wheel, the upper vortex ( $V_{1R'}$ ) is translated in the  $+x$  direction. The majority of the flow was found to leave the hub on the lower half (Figure 118), as this side represents the wheel rotation and free stream flow travelling in the same direction, therefore the flow travelling

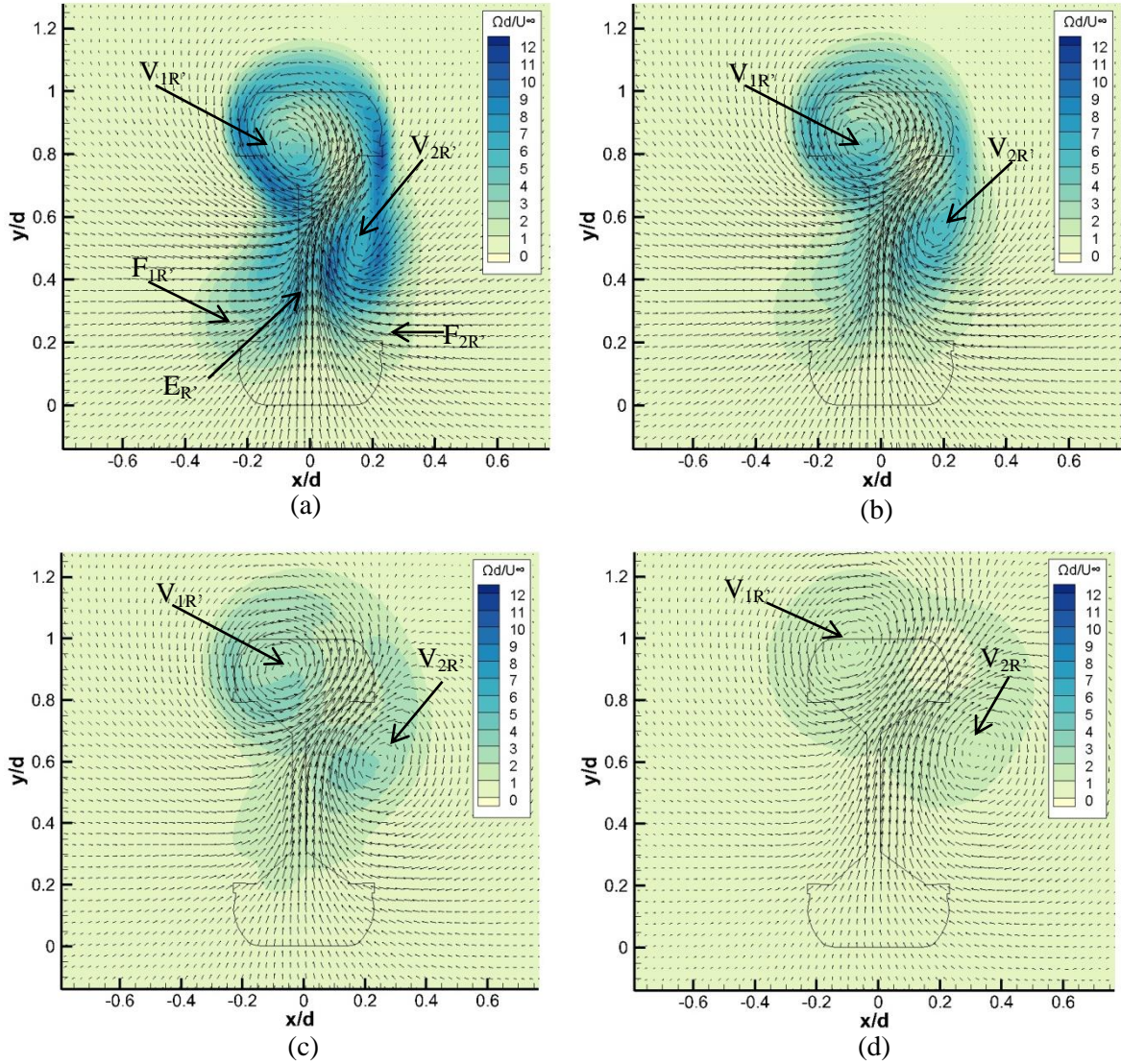
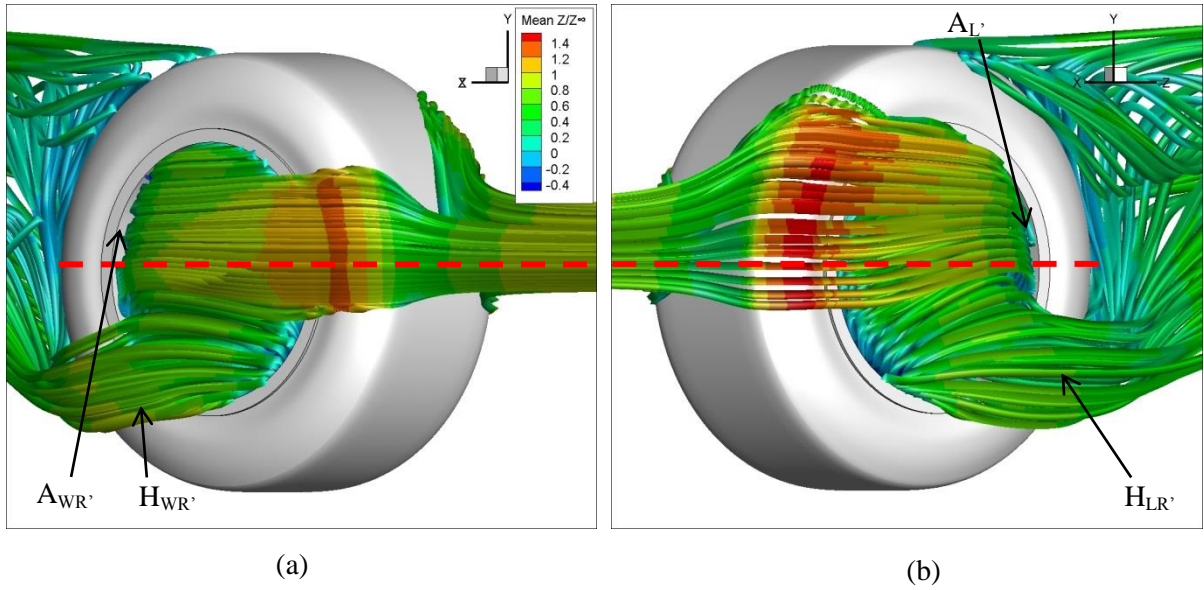


Figure 117 – Non-dimensional vorticity plots for  $5^\circ$  yaw + rotation; (a)  $z/d=0.75$ , (b)  $z/d=1$ , (c)  $z/d=1.5$ , (d)  $z/d=2.5$



**Figure 118 - Streamlines (coloured by mean streamwise velocity) showing hub flow on the 5° yaw rotating wheel, (a) windward side (b) leeward side, when looking in the streamwise direction**

alongside the hub entrains the hub flow towards the back of the wheel. The low velocity flow on the leeward side of the wheel is entrained by the skewed up-wash behind the wheel and contributes primarily to the upper vortex  $V_{1R'}$ , whilst the skewness also entrains some of the flow into  $V_{2R'}$ . On the other hand, the lower vortex  $V_{2R'}$  is formed due to the recirculation caused by the attached flow on the wheel edge once it interacts with the skewed up-wash. As most of the flow from the leeward side contributes to the upper vortex  $V_{1R'}$ , the magnitude is reduced although the size of the vortex is larger than  $V_{2R'}$ . This was also observed in [30] and in the previous results analysed where the low velocity hub flow contributing to a vortex will represent a lower magnitude for the corresponding vortex. Comparing vorticity magnitude and visual size between  $V_{1R'}$  and  $V_{2R'}$ , the lower vortex ( $V_{2R'}$ ) is smaller but stronger by up to 50%, ( $V_{1R'}$ :  $\Omega d/U_\infty = 4.32$ ,  $V_{2R'}$ :  $\Omega d/U_\infty = 6.61$  at  $z/d = 0.75$ ) respectively. However, the difference in vorticity magnitude between the two vortices reduces to approximately below 5% further downstream  $z/d \geq 1.5$ . As has been discussed previously, internal hub impingement location was found to be a key factor when determining the direction of circulation inside the hub, subsequently affecting how the flow leaves the hub and enters the wake. These regions were found to occur in this case at  $\theta = 184^\circ$ ,  $C_p = 0.42$  and  $\theta = 202^\circ$ ,  $C_p = 0.39$  for the windward ( $A_{WR'}$ ) and leeward ( $A_{LR'}$ ) respectively. Due to both of these regions being located above wheel mid-height ( $\theta = 180^\circ$ ), the flow is directed into the hub and circulated downwards before leaving on the lower half of the hub ( $H_{WR'}$ ,  $H_{LR'}$ ), causing a low vorticity region on the lower half of the wheel (as observed in Figure 117(a) –  $F_{1R'}$ ,  $F_{2R'}$ ),



similar to that observed on the windward hub on the non-yawed rotating case, Figure 110(a). Considering vortex core position with downstream propagation for this  $5^\circ$  case from  $z/d = 0.75$  to  $z/d = 2.5$ ,  $V_{1R'}$  has a 26% greater vertical displacement upwards than  $V_{2R'}$ , ( $V_{1R'}$ :  $\Delta y/d = 0.147$ ,  $V_{2R'}$ :  $\Delta y/d = 0.117$ ). However,  $V_{2R'}$  propagates downstream with a higher transverse displacement of  $\Delta x/d = 0.156$  compared to  $V_{1R'}$ :  $\Delta x/d = -0.027$ . From Figure 117, this is suggested to be caused by the up-wash ( $E_{R'}$ ), essentially pushing  $V_{1R'}$  upwards and  $V_{2R'}$  in the  $+x$ -direction due to the skewness.

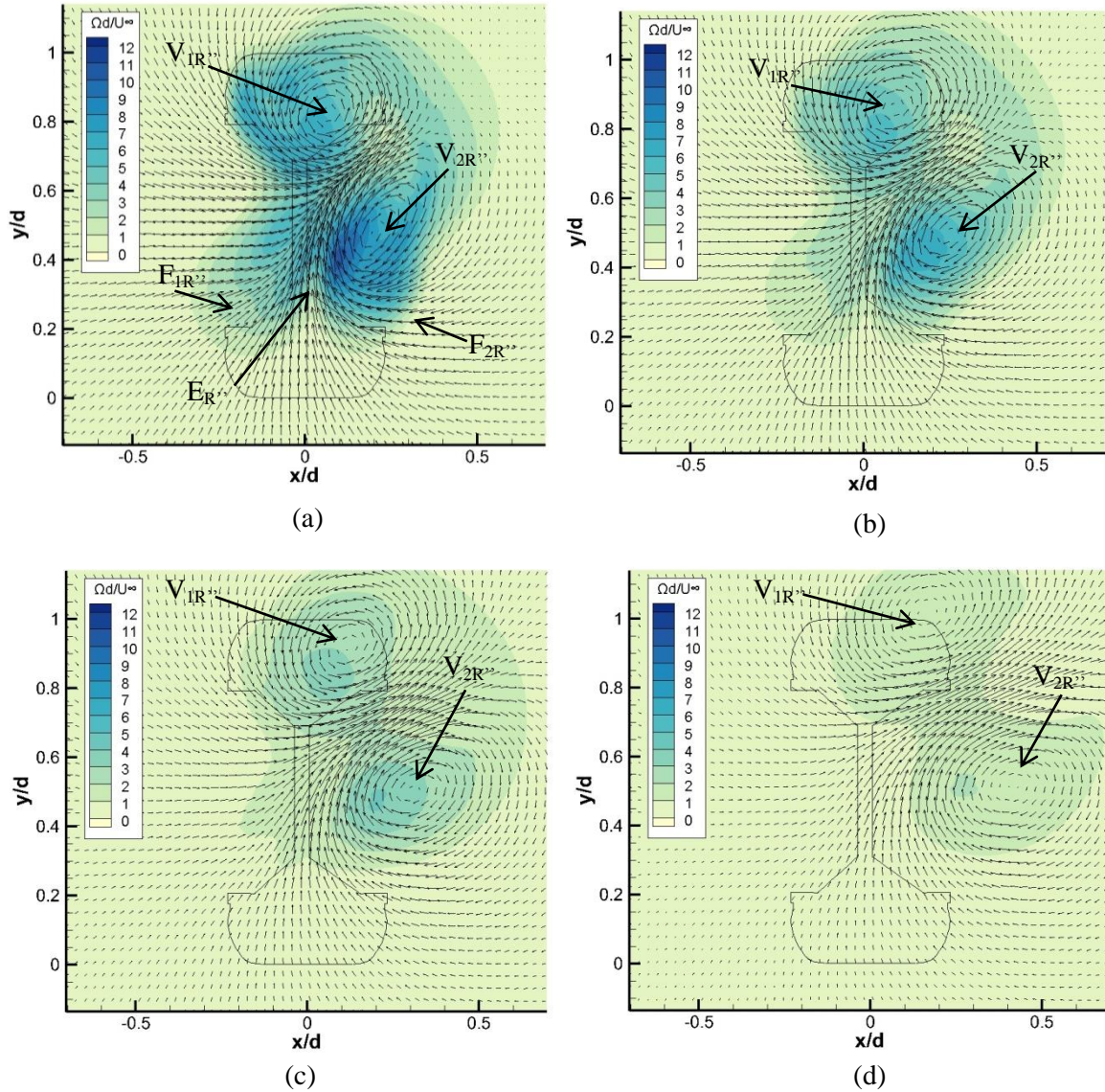


Figure 119 – Non-dimensional vorticity plots for  $10^\circ$  yaw + rotation; (a)  $z/d=0.75$ , (b)  $z/d=1$ , (c)  $z/d=1.5$ , (d)  $z/d=2.5$

From initial observation of the vorticity magnitude contours in the rear wake of the rotating wheel with the application of  $10^\circ$  yaw, a further shift in vortex position is shown (Figure 119). As established from the rotating wheel with  $5^\circ$  yaw, the two vortices appear to have rotated further towards the windward side. Considering the data plane at  $z/d = 0.75$ , Figure 119(a), the up-wash ( $E_{R''}$ ) caused by the rotation of the wheel on the flow, travelling from the bottom of the wheel is skewed further to the windward side than observed for the previous case ( $E_{R''}$  relative to  $E_{R'}$ ). Similarly, the two low vorticity regions ( $F_{1R''}$ ,  $F_{2R''}$ ) are created as a result of the flow exiting the hub cavities and being entrained upwards by the rotation of the wheel. At  $5^\circ$  yaw, the upper vortex ( $V_{1R'}$ ) was positioned in the negative  $x/d$  side of the wheel

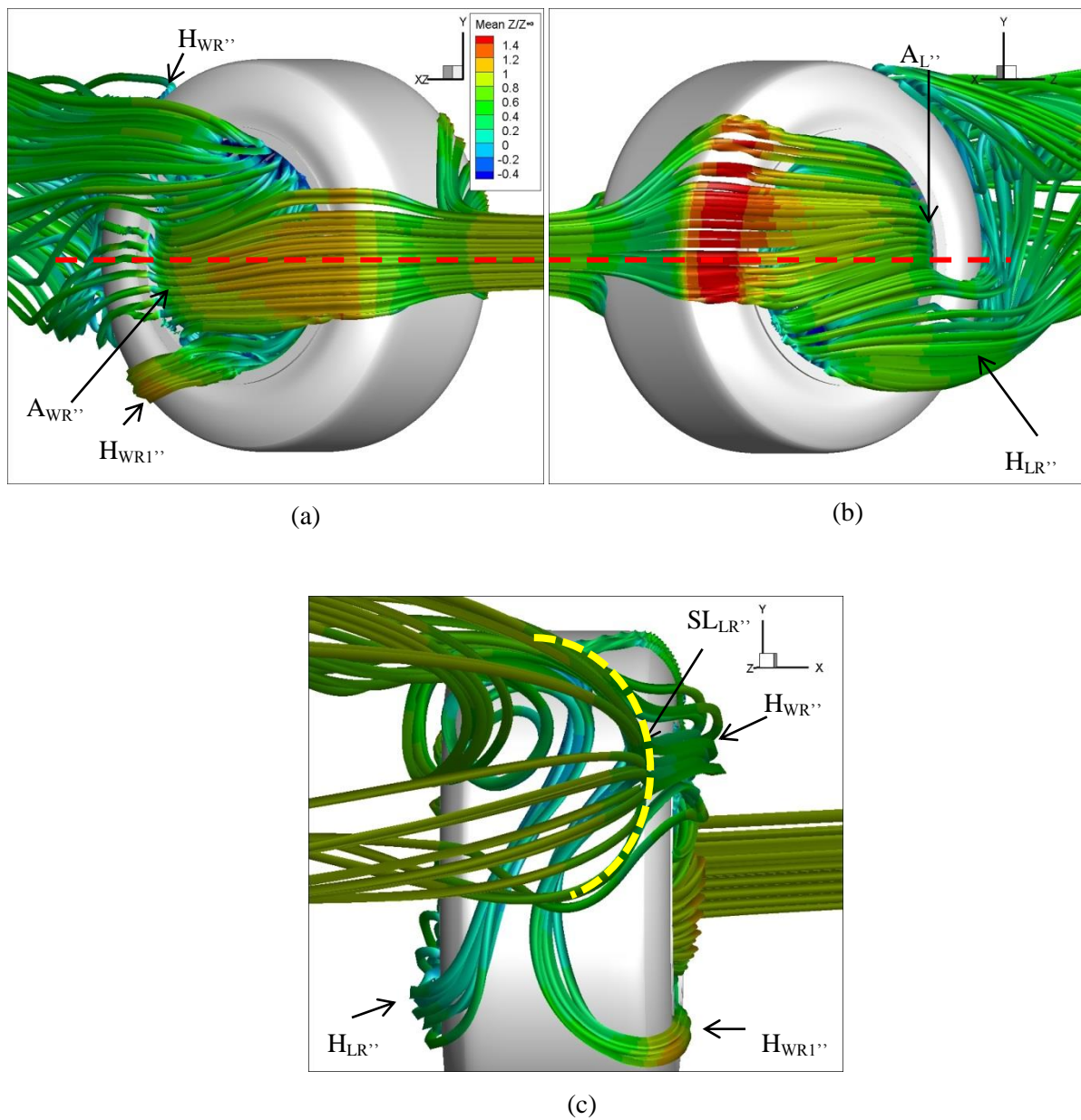


Figure 120 - Streamlines (coloured by mean streamwise velocity) showing hub flow on the  $10^\circ$  yaw rotating wheel, (a) windward side (b) leeward side, when looking in the streamwise direction & (c) rear view

(leeside) but with a further application of an extra  $5^\circ$  yaw, both vortices appear to be on the positive  $x/d$  side (windward side). The upper vortex ( $V_{1R''}$ ) is now positioned at  $x/d = 0.066$  and  $y/d = 0.824$  whilst the lower vortex  $V_{2R''}$  is positioned at  $x/d = 0.196$  and  $y/d = 0.477$  at  $z/d = 0.75$ , representing vortex core position displacements relative to the vortices on the  $5^\circ$  yaw case of  $V_{1R''}$ :  $\Delta x/d = 0.121$ ,  $\Delta y/d = 0.002$  and  $V_{2R''}$ :  $\Delta x/d = 0.027$ ,  $\Delta y/d = -0.041$ . A change in internal hub impingement on the windward side of the wheel, located below mid-height at  $\theta = 167.2^\circ$  indicates the flow being forced to circulate upwards into the hub, Figure 120(a) –  $A_{WR''}$ . The circulated flow exits on the upper half of the hub ( $H_{WR''}$ ) and separates off the edge due to the wheel rotating in the opposing direction, creating an arch-shaped shear layer (as shown in Figure 120(c) -  $S_{LR''}$ , with yellow dashed line). The flow on the lower half of the hub ( $H_{WR1''}$ ) is entrained into the rear wake by the free stream flow and is forced into the upper half of the wheel by the up-wash behind the wheel forming the stronger lower vortex  $V_{2R''}$  after interacting with the arch-shaped shear layer. The flow on the leeside of the wheel impinges on the rear hub surface at  $\theta = 193.6^\circ$  ( $A_{L''}$ ), above wheel mid-height as experienced on the previous case, resulting in the flow exiting the hub on the lower side of the wheel ( $H_{LR''}$ ), therefore, forced upwards by the up-wash until recirculation occurs after interacting with the shear layer forming  $V_{1R''}$ . Vortex core vorticity magnitude indicated  $\Omega d/U_\infty = 5.60$  for  $V_{1R''}$  and  $\Omega d/U_\infty = 7.57$  for  $V_{2R''}$  respectively, at  $z/d = 0.75$ ; indicating the lower vortex being stronger by up to 35%, which can be expected due to the combination of the stream-wise flow and rotation of the wheel in that region creating an increased velocity in flow entering the rear wake from the lower windward side of the wheel. Further downstream to  $z/d = 2.5$ , the difference in central core vorticity magnitude reduces to 9% and the two vortices translate in the positive  $x$  &  $y$  direction.

With the maximum yaw angle ( $\Psi = 15^\circ$ ) being applied on the rotating wheel, immediate differences in wake size, vortex core magnitude and vortex positions can be observed from Figure 121. Similar flow characteristics previously observed at lower yaw angles are still present in this case such as the presence of two dominant vortical structures and the up-wash ( $E_{R''}$ ) which is skewed further towards the windward side of the wheel. The downwash ( $D_{R''}$ ) that appears on the upper half of the wheel is a result of the flow which is entrained by the rotated shear layer formed on the upper rear surface of the wheel. This shear layer is directed in the streamwise flow direction and as the upper vortex ( $V_{1R''}$ ) is rotating anti-clockwise, the downwash is also pulled in the direction of rotation of the vortex; also visible in the previously discussed  $10^\circ$  yaw rotating case. Additionally, the symmetry between the



upper and lower halves intensifies with increasing yaw angle, resulting in improved symmetry between the two vortices. Comparing the vortices formed behind this 15° yaw wheel (Figure 121(a) -  $V_{1R''''}$  and  $V_{2R''''}$ ) relative to the vortices observed on the 10° yaw wheel ( $V_{1R''}$  and  $V_{2R''}$ ) at  $z/d=0.5$ , Figure 119(a), the vortex core displacement for the upper vortex ( $V_{1R''''}$ ) is  $\Delta x/d = 0.12$ ,  $\Delta y/d = -0.07$  and for the lower vortex  $V_{2R''''}$   $\Delta x/d = -0.585$ ,  $\Delta y/d = -0.09$ . The increased skewness of the up-wash ( $E_{R''''}$ ) towards the windward side, combined with the more prominent downwash ( $D_{R''''}$ ) observed on the 15° yaw case, reduces the vertical displacement of the two vortices, whilst also increasing the transverse displacement. The application of 15° of yaw allows the air to travel directly on to the rear surface of the windward hub cavity as has been described earlier in the pressure contour plots in Figure

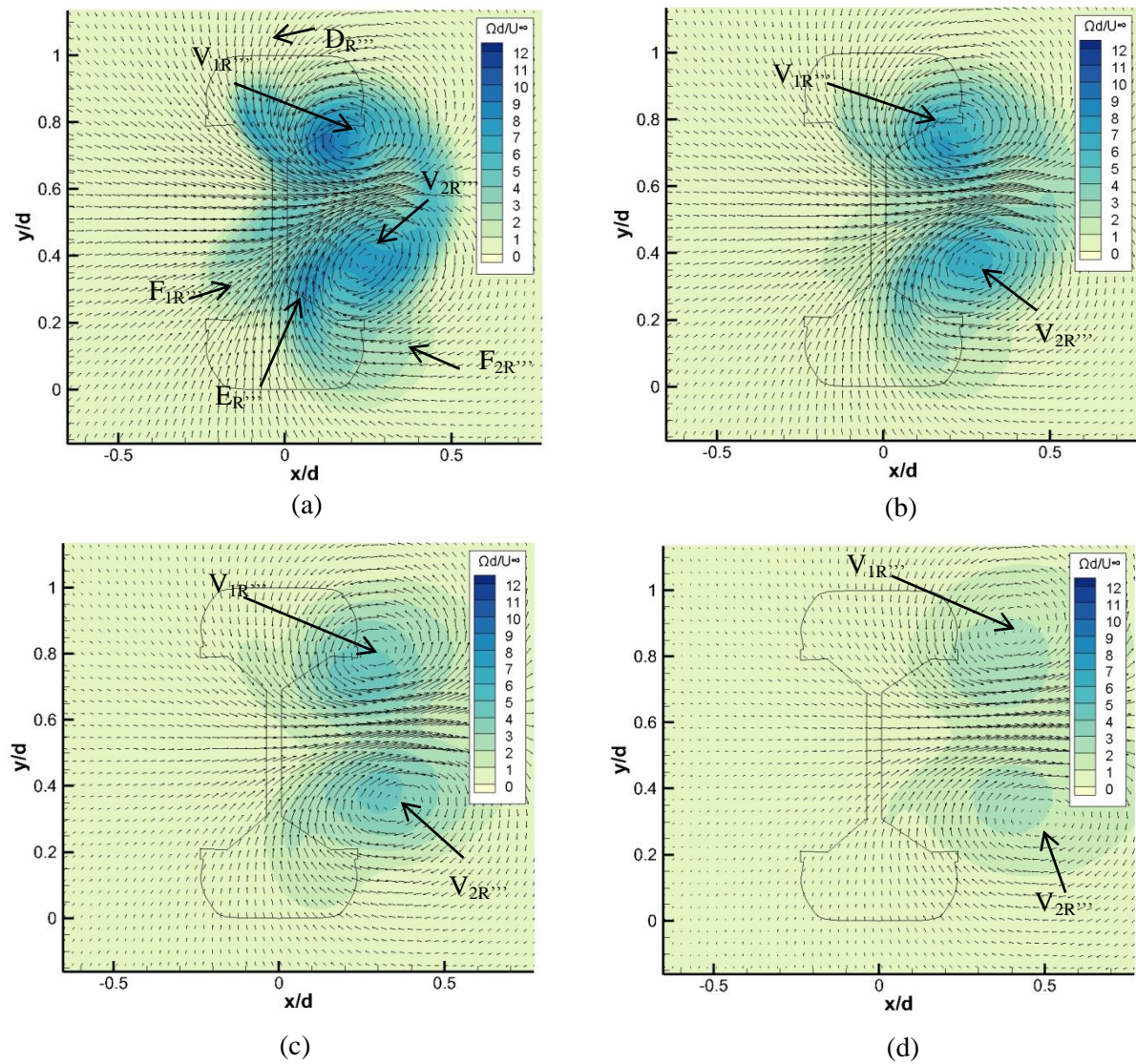


Figure 121 – Non-dimensional vorticity plots for 15° yaw + rotation; (a)  $z/d=0.75$ , (b)  $z/d=1$ , (c)  $z/d=1.5$ , (d)  $z/d=2.5$

115(e) and Figure 116(c). This impingement location is above wheel mid-height at  $\theta = 194.5^\circ$  ( $A_{WR}'''$ ) indicating the direction of hub flow circulation inwards and downwards as shown in Figure 122(a). As the flow reaches the lower edge of the hub, due to the hub and the free-stream flow moving in the same streamwise direction, the flow is drawn out of the hub ( $H_{WR}'''$ ). In the near rear wake region, the flow is entrained by the up-wash, subsequently contributing to the lower vortex ( $V_{2R}'''$ ). Therefore, the outflow from the lower half of the hub on the windward side is greater in size ( $F_{2R}'''$ ) than previously observed at lower yaw angles, as shown in Figure 121. The same reasoning of the wheel and streamwise flow travelling in the same direction is valid for the flow exiting the hub on the lower leeside. However, the lower velocity flow leaving the evacuated leeside rear wheel edge ( $H_{LR}'''$ ) is

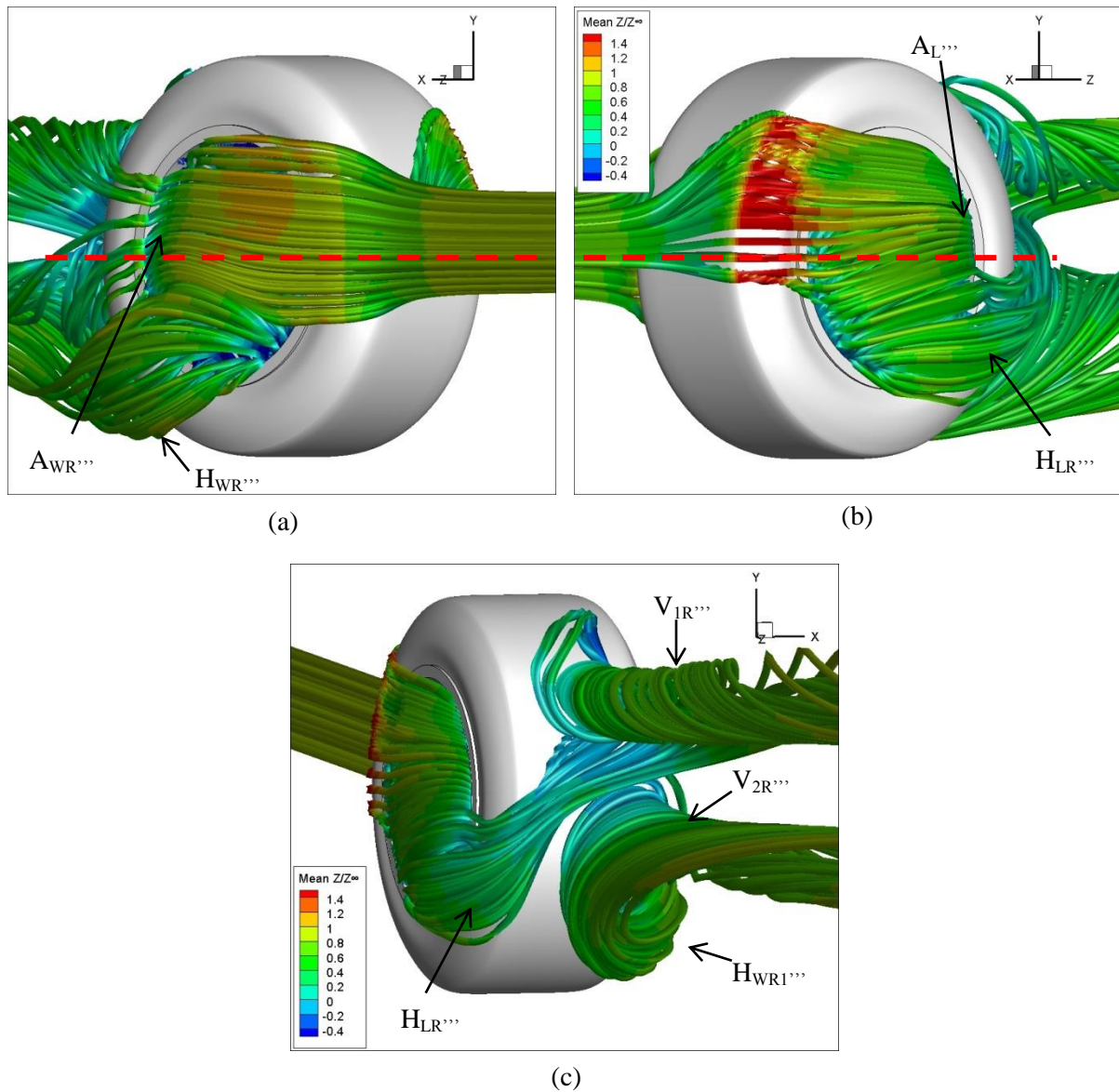


Figure 122 - Streamlines (coloured by mean streamwise velocity) showing hub flow on the  $15^\circ$  yaw rotating wheel, (a) left side (b) right side, when looking in the streamwise direction & (c) rear view



entrained up into  $V_{IR'''}$  by the skewed up-wash. Considering both vortex core vorticity magnitudes,  $V_{IR'''}$  has a larger vortex core magnitude by 9.3% at  $z/d = 0.75$ . However, further downstream ( $z/d > 0.75$ ) the difference between the two reduces significantly to 3%.

### 5.4.3 Aerodynamic Forces

Force coefficients on the rotating wheel cases with applied yaw angle are shown in Table 4. The drag force on the rotating wheel continues to increase with applied yaw angle up to 16% from  $0^\circ$  to  $15^\circ$  yaw. However, the most significant and noticeable difference between the force coefficients is the lift. The lift force is observed to increase with increasing yaw angle towards zero. The negative lift force on a rotating wheel with zero yaw is expected, as described in Section 5.3.3, and is due to the direction of rotation on the bottom of the wheel being equivalent to the free-stream flow direction, thereby inducing the velocity and decreasing the pressure in that region. A reduction in velocity also occurs on the top of the rotating wheel due to the earlier separation region at  $\theta = 264^\circ$ , creating a pressure differential between the upper and lower surfaces of the wheel. However, with increasing yaw angle, the flow was observed to separate further downstream from the top of the wheel as shown in Figure 114. Therefore a lower pressure persists on the top of the wheel, until separation occurs further downstream towards the rear of the wheel, resulting in a reduction in the pressure differential as the yaw angle is increased. The side force remained to mimic what has already been shown and discussed in the results on the stationary wheel with applied yaw, with very similar results for  $C_X$ .

Wheel Yaw Angle	Force Coefficient		
	$C_D$	$C_L$	$C_X$
$0^\circ$	0.44	-0.25	0.01
$5^\circ$	0.43	-0.24	-0.14
$10^\circ$	0.46	-0.21	-0.31
$15^\circ$	0.51	-0.11	-0.54

Table 4 – Rotating wheel force coefficients

#### 5.4.4 The combined effect of both Yaw & Rotation

The application of combined yaw and rotation continued to produce the two vortices in the rear wake, as observed on the rotating case. Frontal stagnation position on the rotating wheel with no applied yaw, occurred on the central front surface of the wheel  $x/d = 0$ ,  $y/d = 0$ ,  $z/d = 0$ , Figure 109-A<sub>R</sub>. However, with applied yaw, the shift in the vertical direction is negligible but experiences a transverse displacement away from the wheel centreline towards the windward side as shown in Figure 115 & Figure 116. The horizontal displacement of this region is  $x/d = 0.04$ ,  $x/d = 0.08$ ,  $x/d = 0.11$  for  $5^\circ$ ,  $10^\circ$ ,  $15^\circ$  yaw respectively, relative to the wheel centreline. Figure 123 shows a clear linear relationship in horizontal displacement with  $\Delta x/d \approx 0.04$ , with  $5^\circ$  increments of yaw. This was identical to that observed on the stationary wheel with applied yaw, revealing that, although yaw has an effect on this region, the application of rotation does not influence the front stagnation position in ‘free-air’.

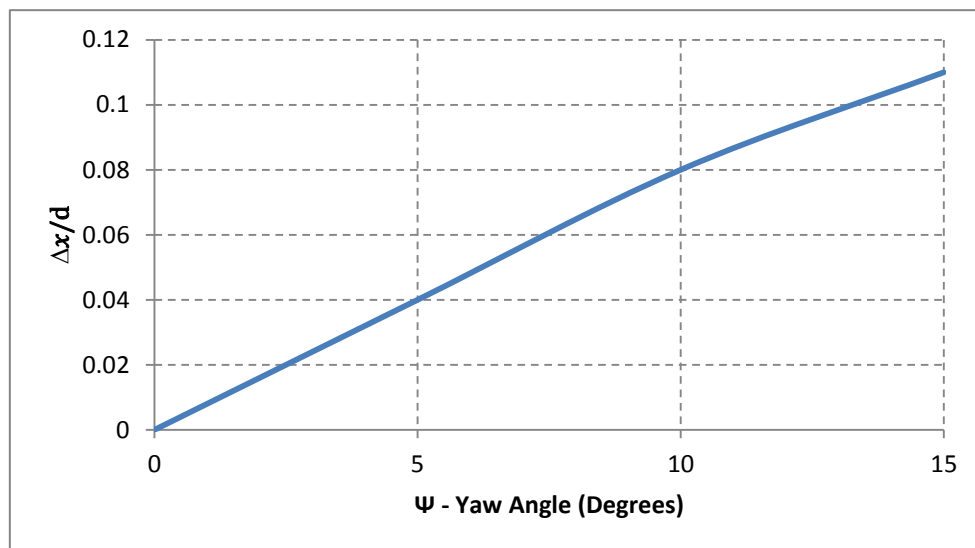


Figure 123 - Change in transverse displacement of stagnation region from rotating wheel centreline with increasing yaw angle

Subsequent to flow stagnation on the frontal surface of the wheel, the flow travels in the longitudinal and lateral directions around the wheel. The rotating wheel with zero yaw, experiences almost symmetrical flow behaviour on either sides of the stagnation region with maximum velocity magnitude of 57m/s around the sides of the wheel. However, the application of yaw showed an increase in maximum flow velocity to 61.1m/s, 70m/s and 77m/s at  $5^\circ$ ,  $10^\circ$ , and  $15^\circ$  yaw respectively on the front leeward edge, whilst a reduction in velocity takes place on the front windward edge of the wheel with maximum flow velocity of

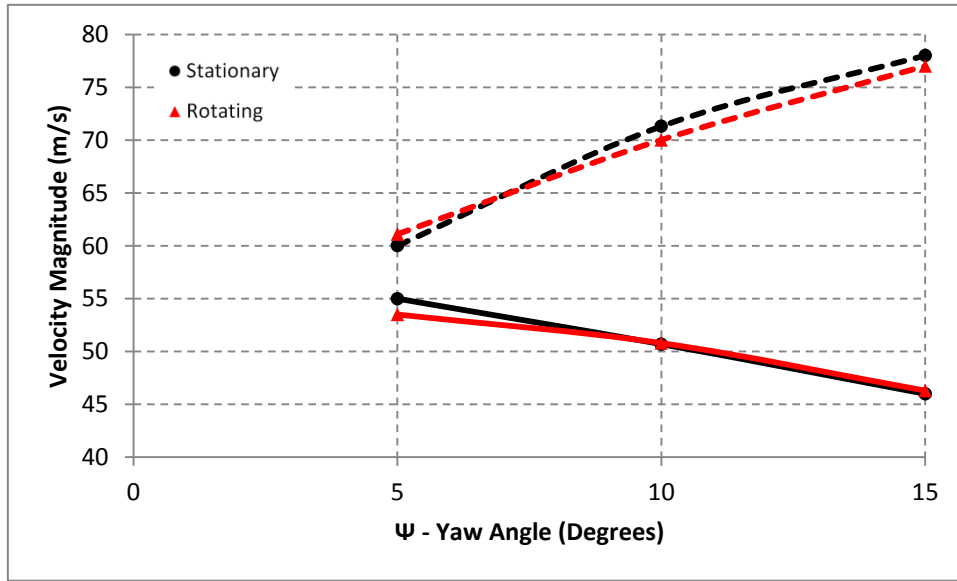


Figure 124 - Velocity magnitude around sides of the wheel at  $y/d = 0.5$ , Solid line: Windward side & Dashed line: Leeward side

53.5, 50.8 and 46.3 m/s for 5°, 10°, and 15° yaw respectively, which is also illustrated in Figure 124. Comparing the velocities in these regions for both the stationary and rotating case with increasing yaw angle, both sides on both configurations experience a linear increase on the leeward side, and a linear reduction on the windward side, with marginal differences between the rotating and stationary cases.

Upon passing the front sides of the wheel, the flow enters the hub cavities and impinges on the rear hub surface and circulates within the hub cavity before exiting either from the upper or lower half of the hub. For most of the cases combining rotation, internal hub impingement is located above wheel mid-height indicating flow circulation into and out of hub from the lower side. However, the 10° yaw case with combined rotation experienced impingement at  $\theta = 167.2^\circ$ , indicating circulation into and upwards inside the hub, whilst leaving the hub on the upper half, although some flow does escape from the lower half due to the entrainment of the streamwise flow travelling in the same direction as the rotation of the wheel.

On the zero yaw rotating wheel case, separation is predicted at  $\theta = 264^\circ$ ; 6° downstream from the top of the wheel. However, with increasing yaw angle, the separation position moves further downstream towards the back of the wheel to  $\theta = 263^\circ$ ,  $\theta = 255^\circ$  and  $\theta = 247^\circ$  at 5°, 10° and 15° yaw respectively. Comparing these positions to those from the stationary yaw cases, the separation positions on the rotating wheel occurs further upstream, as also observed in literature comparing stationary and rotating wheels [22, 29, 10]. Separation from the lower

surface is also observed at  $\theta \approx 142^\circ$  for all configurations, however, at this centreline location, separation is caused by the flow interaction on the lower central region of the wheel, as the flow wraps itself around the sides of the wheel after being entrained by the up-wash. At lower yaw angles, this can be visualised as the point where the up-wash from the low vorticity circulation regions on either sides of wheel meet (denoted  $F_{1R}$  &  $F_{2R}$  in the vorticity plots). After flow separation, shear layers are formed off the top of the wheel which entrains the flow, which is re-circulated upon interacting with the up-wash, forming two vortices in the wake region. The two vortices created in the zero yaw rotating case, are nearly symmetrical both in magnitude and position about the  $x/d=0$  centreline. However, with the addition of yaw at  $5^\circ$  increments up to  $15^\circ$  yaw, the vortex pair positions appear to rotate clockwise up to approximately  $80^\circ$  at the largest yaw angle, when comparing the vorticity plots for each case at  $z/d = 0.75$ . Time-averaged central vortex core vorticity magnitude show the vortex pair at  $0^\circ$  yaw to be near identical, with  $V_{2R}$  marginally larger by up to 12% relative to  $V_{1R}$ . Yet, as  $5^\circ$  increments of yaw is applied on the wheel, the lower vortex  $V_{2R}$  and  $V_{2R''}$  at  $5^\circ$  and  $10^\circ$  yaw respectively, possess a larger vorticity magnitude over their paired upper vortex  $V_{1R}$  and  $V_{1R''}$  respectively, as illustrated in Figure 125. This is suggested to be due to the contributing flow from the leeside hub, being entrained by the up-wash into the upper vortex reducing the intensity. Results from [30] also found that the hub flow contributing to any of the vortices in the rear wake would reduce the vortex intensity. The  $15^\circ$

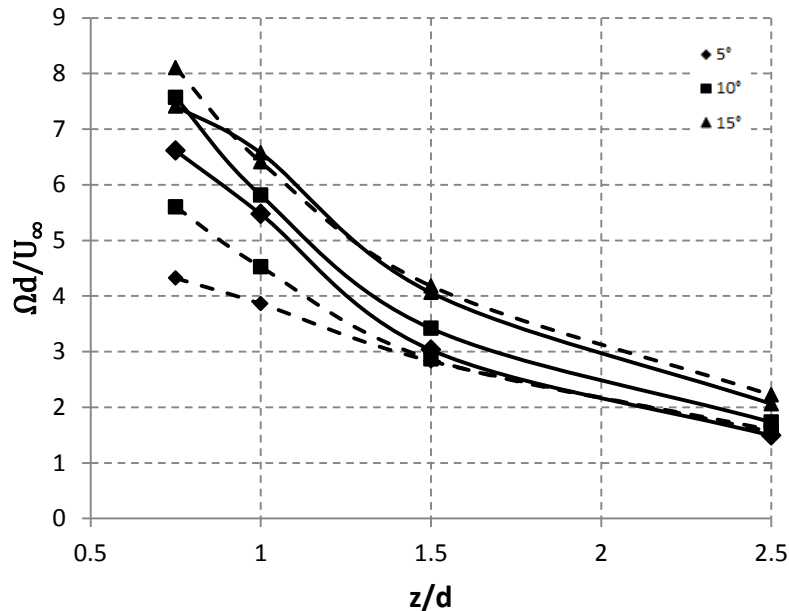


Figure 125 - Vortex core vorticity magnitude (on yawed rotating wheel) with downstream propagation into the rear wake; Upper vortex -  $V_{1R}$  (dashed), Lower vortex -  $V_{2R}$  (solid)

yaw case shows the difference in magnitude of the two vortices to be almost negligible at  $z/d = 0.75$ . At the furthest downstream plane ( $z/d = 2.5$ ), the difference in vorticity magnitude between the vortices for each case reduces to  $\approx 9\%$  on the three rotating yaw cases.

Based on the un-yawed rotating case, it is evident from Figure 110 that  $V_{1R}$  &  $V_{2R}$  possess a negative and positive transverse displacement respectively. Figure 126 displays the calculated relative displacement of the two dominant vortex structures ( $V_{1R}$ ,  $V_{2R}$ ), with downstream propagation referenced to  $z/d = 0.75$  ( $\Delta x/d = 0$ ,  $\Delta y/d = 0$ ). Considering the lateral relative displacement ( $\Delta x/d$ ), the results show that as the yaw angle increases, the lateral displacement towards the windward side of the wheel increases. Nonetheless, the upper vortex at  $5^\circ$  yaw ( $V_{1R}$ ) indicates a small displacement of  $\Delta x/d = -0.03$  at the furthest downstream plane  $z/d = 2.5$ . This difference in negative displacement, indicates that the shift towards the leeside of the wheel is due to the upwash not being able to fully entrain the flow towards the windward side. At  $\Psi \geq 10^\circ$ , the shear layer is rotated towards the upper windward side of the wheel causing regions of recirculation to be entrained within this region. Vortex core displacement on the rotating wheel with no yaw, Figure 110 & Figure 113(a), shows  $V_{1R}$  propagating downstream on the leeside of the wheel ( $-x$  direction relative to the wheel centreline). Therefore due to the smaller angle of  $5^\circ$  yaw applied, the upper vortex  $V_{1R}$  remains to propagate on the leeside of the rotating wheel, although, the transverse displacement for both vortices in all configurations, remains to have a constant linear displacement downstream with increasing yaw angle. Likewise, Figure 126(b) shows the vortex core displacement in the vertical direction for increasing yaw angles. Changes in vertical position are relatively

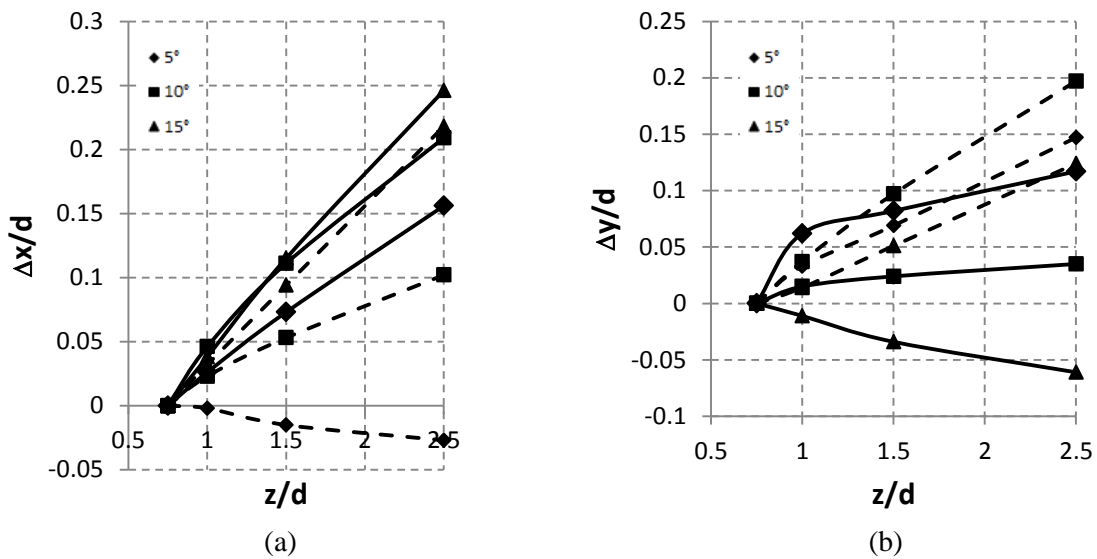
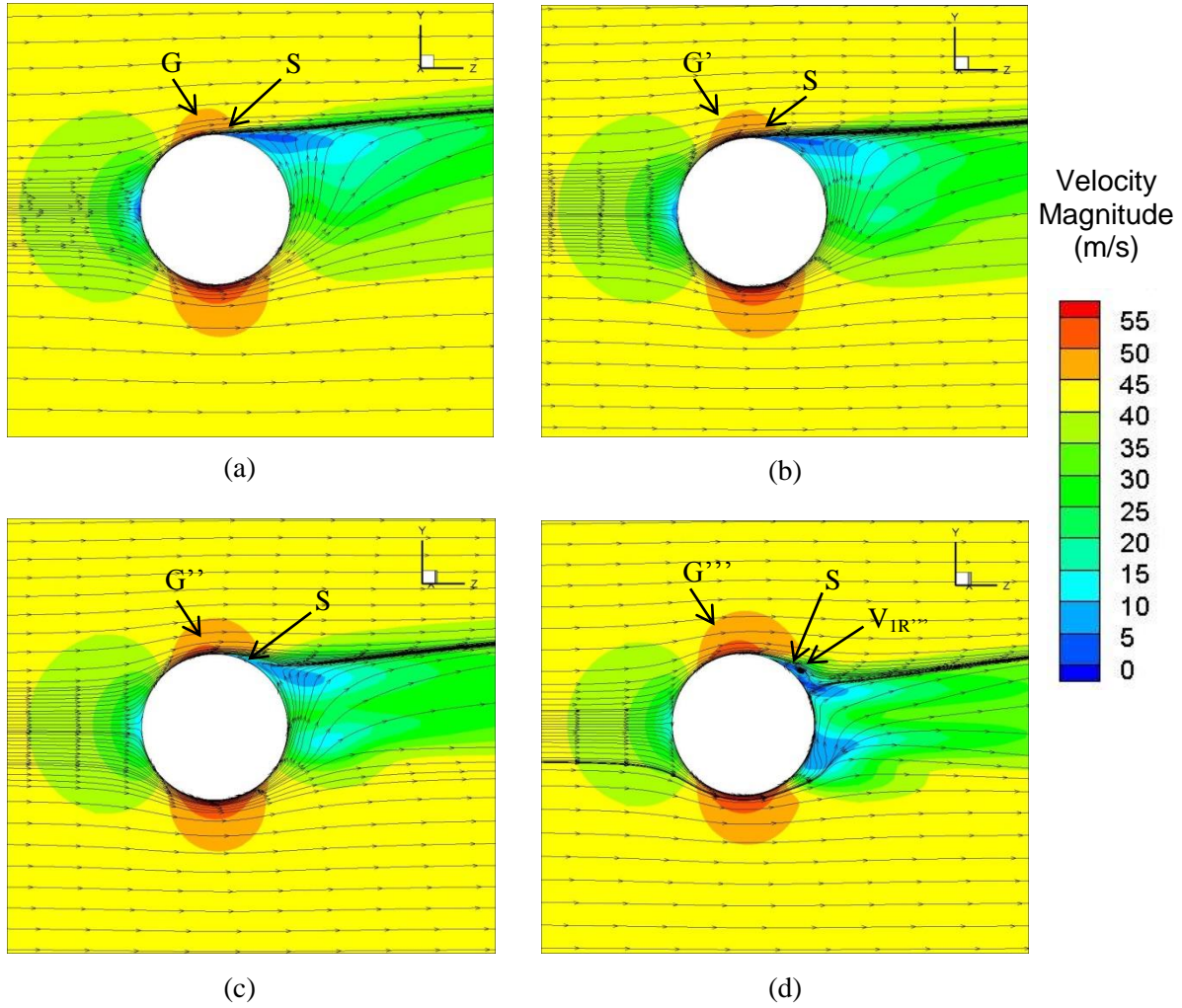


Figure 126 – Vortex core displacements (on yawed rotating wheel) relative to  $z/d = 0.75$  with downstream propagation;  $V_{1R}$  (dashed),  $V_{2R}$  (solid)

small compared to the transverse differences. Linear downstream propagation is also evident with increasing yaw angles, except for the lower vortex ( $V_{2R'}$ ) on the  $5^\circ$  yaw configuration. Yet, the non-linear trend only occurs until the  $z/d = 1$  position downstream, therefore this may be due to the unsteady nature of the flow in the near wake region. Application of the largest yaw angle ( $\Psi = 15^\circ$ ) results in the two vortices being near symmetrical about the horizontal centreline of the wheel ( $\Delta y/d = 0$ ) regardless of the applied rotation on the wheel. Although, through comparison of vortex core displacement, the displacement of the lower vortex ( $V_{2R''}$ ) on the rotating wheel is very similar to the same vortex observed on the stationary configuration. The displacement at the furthest downstream plane ( $z/d = 2.5$ ) indicates a reduced  $\Delta y/d$ , and is a result of the rotation on the wheel (travelling upwards at the rear of the wheel) displacing the wake at an up-wash angle, which is a known flow field characteristic on a rotating wheel [34].

Contour plots of centreline cross-sectional non-dimensional velocity magnitude at  $0^\circ$ ,  $5^\circ$ ,  $10^\circ$  and  $15^\circ$  yaw (Figure 127), show the wake displaced at an up-wash angle on the rotating wheel. General flow topology around the wheel mimics what has been described earlier; stagnation on the frontal region, flow acceleration around the upper and lower surfaces with an increased mean velocity magnitude on the latter as a result of the rotatory motion of the wheel inducing the flow on the bottom surface of the wheel. Separation (S) can be seen on top of the wheel, with a slight delay in separation position towards the rear of the wheel as yaw angle increases. The up-wash caused by the rotation of the wheel is also evident and directs the flow upwards on the rear surface and into the upper shear layer where the flow circulates. The formation of the upper vortex  $V_{1R''}$  on the  $15^\circ$  yaw case, is also visible showing the flow recirculation, as already illustrated in Figure 122(c). Vortices for lower angles of yaw ( $\Psi < 15^\circ$ ) are not detectable in Figure 127 as they do not reside on the wheel centreline plane. Considering the size of the rear wake, it is clearly evident that the  $15^\circ$  yaw configuration exhibits a larger region of low velocity, covering almost the entire rear surface due to the vortical structures behind the wheel. Although these vortical structures are still present at lower yaw angles, a reduction in their size and magnitude results in a smaller wake. As has been mentioned in the discussion for the stationary cases, a larger wake region is expected to induce a larger drag force due to the earlier separation forming the two shear layers which entrain the flow in the wake region [12], and the obtained results for these rotating cases are in agreement. Figure 128 shows the coefficients for drag, lift and side force on the rotating wheel with applied yaw angle. A 16% increase in drag, is experienced as the



**Figure 127 – Contour plots of velocity magnitude on rotating wheel centreline cross-sectional plane; (a) 0° yaw, (b) 5° yaw, (c) 10° yaw & (d) 15° yaw, with velocity streamlines**

yaw angle is increased from 0° to 15° yaw due to the increasing wake region behind the wheel. In addition, similar to the non-rotating yawed cases, the larger spread of lateral velocity vectors in the rear wake of the yawed wheels were suggested to contribute to the drag as described in [30]. A negative linear decrease was observed for the side force, representing the force acting towards the leeside of the wheel. The increased exposure of the windward side hub cavity to the free-stream flow, at larger yaw angles, is thought to be the cause of this, as the force applied on the windward side hub would increase with increasing yaw angle, subsequently increasing the side force acting towards the leeside. An increase in lift is also evident and was found to be one of the main findings from the influence of both yaw and rotation. Primarily, a negative lift force (acting downwards) is experienced on the non-yawed rotating wheel, coinciding directly with the Magnus effect [20] due to the pressure differential between the upper and lower surfaces of the wheel. Consequently, with



the application of yaw, the lift increases from  $C_L = -0.25$  at  $0^\circ$  yaw to  $C_L = -0.11$  at  $15^\circ$  yaw. The pressure differential comprising a low pressure on the lower surface of the rotating wheel ( $C_P = -1$ ) caused by the streamwise flow travelling in the same direction as the wheel, acting in unison with the higher negative pressure of  $C_P = -0.33$  on top of the wheel, is initially what causes the negative lift experienced on the wheel. Though, with increasing yaw angle, the pressure on top of the wheel decreases to  $C_P = -0.39$ ,  $C_P = -0.60$  and  $C_P = -0.76$  at  $5^\circ$ ,  $10^\circ$  and  $15^\circ$  yaw respectively. Furthermore, as has been discussed previously, the increase in yaw angle indicates separation to occur further downstream the wheel, moving further behind the top of the wheel from the initial position of  $\theta = 264^\circ$  at  $0^\circ$  yaw, located  $6^\circ$  after the top of the wheel. Due to this later separation position, an increase in size of the maximum velocity region (up to  $53\text{m/s}$  at  $15^\circ$  yaw) persists further along the top surface until separation occurs, as shown Figure 127 ( $G$ ,  $G'$ ,  $G''$ ,  $G'''$  for increasing yaw angle respectively). This decrease in pressure representing an increase in velocity subsequently reduces the pressure differential between the top and bottom surface, ultimately resulting in an increase in lift towards zero.

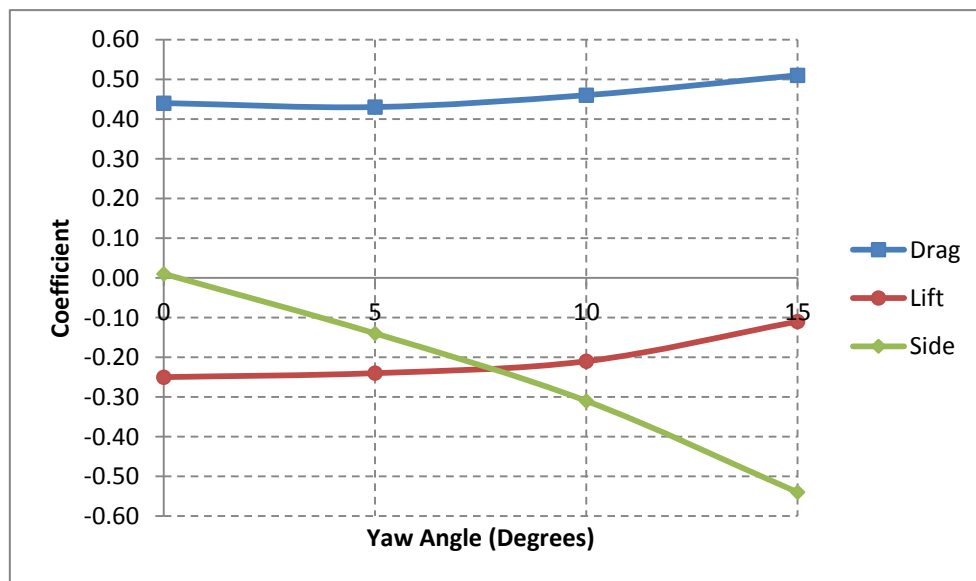


Figure 128 - Force coefficients on the rotating wheel with increasing yaw angle

## 6 Conclusion

An exploratory investigation was completed on single isolated wheel, subsequently implementing yaw and rotation to understand the flow-field characteristics around a wheel during the take-off and landing phase of an aircraft. The ‘A2’ wheel geometry, initially introduced by Fackrell [22] was computationally modelled and simulated using the Unsteady Reynolds-Averaged Navier-Stokes (URANS) method. The wheel was initially modelled in a ‘free-air’ configuration with a free-stream velocity of 40m/s so the computational method could be validated to the literature. Due to the unsteady nature of the flow-field, time averaged results were obtained for aerodynamic force coefficients, surface pressure data, velocities and vorticity, identifying central vortex core vorticity magnitudes and displacement downstream into the rear wake. Both existing and new flow characteristics were identified with comparisons made to the available literature where possible, although a significant gap is present regarding ‘free air’ wheel aerodynamics.

### 6.1 Effect of stationary wheel in free air

The initial case of the stationary wheel in free air showed an asymmetric wake containing four distinct vortical structures, with vortices ( $V_2$ ,  $V_3$ ) being up to 34% stronger in magnitude than the other two ( $V_1$ ,  $V_4$ ) as they are entrained into the central region of the rear wake by the intense up-wash and downwash observed travelling from the lower and upper surfaces respectively.

Internal hub impingement was found to influence the direction of circulation inside the hub cavity, which had a resultant effect on the location the flow exits the hub and joins the rear wake due to the entrainment of the flow travelling around the sides of the wheel. Flow separation was observed at  $\theta = 140^\circ$  and  $\theta = 220^\circ$ , showing good agreement with available experimental results which predicted separation at  $\theta = 150^\circ$  &  $\theta = 220^\circ$  in [32],  $\theta = 148^\circ$  &  $\theta = 226^\circ$  in [7] and  $\theta = 140^\circ$  &  $\theta = 230^\circ$  in [47].

A drag coefficient of 0.35 was obtained for this baseline case, predicting a larger force compared to the experimentally obtained coefficient of  $C_D = 0.19$ . However, Fackrell [22] found that the ‘A2’ wheel hub contributed approximately  $C_D = 0.08$  to the total drag force. Therefore, considering that the experimental investigation [32] used a wheel geometry with a hub detail consisting of a ‘boss’ geometry (as explained in the literature review-Section

2.2.1), the hub can be considered as very nearly faired. Consequently, subtracting the overall predicted drag contribution by the hub [22] from the present drag result, a resultant drag force of  $C_D = 0.27$  would be obtained, providing good agreement with the experimental results and with the results obtained from the computationally modelled geometry of Zhang et al [32]. Coefficients for both lift and side force remained negligible as the flow field around the top and bottom, and around both sides were observed to be near symmetrical. Overall, the present results for this case, showed good agreement to the literature when comparing surface pressure distribution and separation positions, and showing agreement with the rear wake flow physics.

## 6.2 Effect of Yaw

The principal effects of yaw showed a dominant two vortex wake being translated clockwise towards the windward side with increasing yaw angle, eventually being near-symmetrically positioned about the horizontal centreline of the wheel ( $y/d = 0.5$ ) at the largest yaw angle ( $\Psi = 15^\circ$ ).

The influence of yaw demonstrated a linear increase in front stagnation position towards the windward side by approximately  $x/d = 0.04$  with each  $5^\circ$  incremental increase in yaw angle. Subsequent to flow stagnation, the increase in yaw angle demonstrated a linear increase in velocity magnitude by up to 30% on the leeside of the wheel, together with a 20% decrease on the windward side.

Separation positions on the upper surface remained fairly constant at  $\theta = 230^\circ$ , although the lower separation position was displaced further towards the bottom of the wheel, indicating a maximum angular displacement of  $10^\circ$  at  $15^\circ$  yaw, relative to the un-yawed case.

Internal hub impingement was also found to influence the rear wake due to the direction of circulation within the hub, followed by the location of flow departure out of the hub, subsequently contributing to the rear vortices.

A linear transverse and longitudinal displacement of the vortices are present. Both vortices for each case appear to have a transverse shift at a constant rate and distance, although at  $5^\circ$  yaw the lower vortex ( $V_{4'}$ ) has a larger transverse displacement relative to  $V_{2'}$  by  $x/d = 0.145$  (at  $z/d = 2.5$ ), and is suggested to be due to the downwash not being able to fully entrain the flow towards the windward side. The vortices appear to propagate both in the transverse and

longitudinal direction at a similar rate to one another as the yaw angle increases, with central core vorticity magnitude rapidly decreasing to approximately  $\Omega d/U_\infty = 2$ .

Aerodynamic drag force showed an increase, as expected, due to the reduction in base pressure with increasing yaw angle with the combination of the increasing lateral spread of the flow behind the wheel forming a larger wake. Side force also increased with increasing yaw angle, directing the force towards the leeside of the wheel, due to the amplified exposure of the windward side of the wheel.

### **6.3 Effect of Rotation**

The effect of rotation essentially mimicked what had already been discovered in the literature, particularly when focussing on the upper half of the wheel when comparing to ground effect investigations. Two dominant vortices are formed on the upper rear wake due to the intense up-wash interacting with the separated shear layer on top of the wheel. Separation was also found to occur further upstream towards the top of the wheel, agreeing with the literature comparing rotating and stationary cases.

Force coefficients obtained for this case showed that the rotating wheel generates more drag than the stationary case. Although the majority of the literature states the opposite trend, those investigations were conducted with a wheel in contact with the ground. Moreover, Cogotti [36] had also observed the trend found in this study, at small ground clearances. Side force remained negligible due to the flow on either side of the wheel being near symmetrical. Furthermore a negative lift was present on the rotating wheel due to the streamwise flow and wheel rotation, moving in the same direction creating a pressure differential between the upper and lower halves of the wheel, directing the lift force towards the ground.

### **6.4 Effect of Yaw & Rotation**

The general flow field around a rotating wheel with applied yaw, showed a combination of flow features that were identified, on the individual yaw and rotating cases. The shift in front stagnation observed on the stationary yawed cases, appear to be identical to that observed on the yawed rotating wheels, signifying that although the effect of yaw influences the position of this region, it is insensitive to the application of rotation. Similarly, an almost linear trend was also observed in velocity magnitude around the sides of the wheel subsequent to the

stagnation region, revealing that the effect of rotation has minimal influence on the flow velocity around the sides of the wheel.

The arch-shaped shear layer formed in the rear wake of the rotating wheel was found to, essentially, rotate clockwise (when looking from behind), with increasing yaw angle. Flow separation on top of the rotating wheel, which was initially observed on the upper surface of the un-yawed wheel, was found to occur further downstream towards the back of the wheel with increasing yaw angle. This finding was suggested to be the reason for the identified increase in lift towards zero, as the delayed separation region would allow the flow to travel further around the top of the wheel, maintaining the suction velocity, subsequently reducing the pressure differential. Side force on the wheel showed to be insensitive to the application of rotation as similar forces were observed on the stationary yawed wheel. The drag force measured, continued to increase with increasing yaw angle, as experienced on the stationary case, although found to be higher than the values obtained on the stationary wheel. Table 5 (as has been discussed already), shows the net influence the applied variables of yaw and rotation, and both combined have on the aerodynamic force coefficients, relative to the stationary un-yawed configuration. Note that the signs in Table 5 are respective of the co-ordinate axis used to define the direction of the forces in this study.

	$C_D$	$C_L$	$C_X$
<b>Rotating</b>	↑	↓	—
<b>Stationary + Yaw</b>	↑	—	↓
<b>Rotating + Yaw</b>	↑	↑	↓

**Table 5 - Variation in aerodynamic force coefficients with applied variables relative to the stationary un-yawed case**  
(‘—’ representing a negligible force)

Overall, the aims and objectives of this study have been achieved. The non-rotating, un-yawed single isolated wheel case was modelled and validated with the experimental investigation [32] showing good agreement in surface pressure distributions and wake dynamics.

The principal influences of the effect of yaw and rotation were characterised, subsequently determining central vortex core vorticity magnitudes and vortex core displacement with downstream propagation.

Aerodynamic forces were also obtained for all cases showing identifiable trends with increasing yaw angle, on both the stationary and rotating wheel.

## 7 Recommendations for future work

Due to imposed constraints during this study with regard to time and computational resources because of the number and nature of the test cases that needed to be simulated, the investigation was limited to only fulfilling the earlier described aims and objectives. However, throughout the course of this exploratory study, additional ideas arose that would further strengthen the knowledge and understanding of the flow field around aircraft wheels. These are described below as recommendations for future work:

- To computationally model the wheel with faired hubs to negate the influence of hub flow enabling direct comparisons to be made to the literature.
- Conducting an experimental investigation on a wheel in free-air corresponding to the configurations used in this study with the applied variables of yaw and rotation and both combined. This would provide insight into the flow field so direct comparisons can be made to this computational study.
- To model the wheel in contact with the ground with subsequent application of yaw and rotation to identify key flow characteristics with comparisons made to the literature; which mostly consists of ‘in-contact with the ground’ studies.
- Using different turbulence models and a LES model would be beneficial in comparing the key flow characteristics, particularly due to the higher accuracy expected from an LES model. However, computational time constraints would be major factors due to the mesh size required to model a configuration with complex rim and hub detail.
- As this study is mainly focused on identifying the flow field characteristics around a wheel during the approach and landing phase of an aircraft, it would be interesting to model the influence of ground proximity. Modelling this scenario will provide an understanding into how and when these key flow features observed in a free-air configuration changes as a ground plane is approached. By comparing the literature to the present study, it was learnt that the aerodynamic force coefficients were higher on a stationary wheel in contact with the ground, as opposed to the rotating wheel coefficients being larger in this free-air configuration with additional validation from Cogotti [36]. Therefore, it will be interesting to find out at what particular height of the ground this phenomenon, (acting somewhat like a ‘point of inflection’), occurs and the height that the ground plane starts to show an effect on the flow field.



- As this was an exploratory investigation, the modelled configuration was simplified to an isolated wheel. Although this provides insight into the flow characteristics around a single wheel; for application purposes, this has to be applied to a landing gear configuration. Therefore, it may be of interest to model a landing gear configuration. Still, this would be a challenging and tedious task to complete, due to the small landing gear components having to be modelled with a sufficient grid resolution and accuracy. Consequently, it could be more practical in taking smaller steps by modelling a two-wheel configuration, followed by a four-wheel configuration and making comparisons before subsequently modelling an entire landing gear configuration.
- Furthermore, understanding the aeroacoustic aspect of the single and multiple wheel configurations would be useful, as one of the main objectives associated with landing gear in the aerospace industry is to reduce the overall noise signature.

## Bibliography

- [1] W. Dobrzynski, "Almost 40 Years of Airframe Noise Research: What did we achieve?," *Journal of Aircraft*, vol. 47, no. 2, pp. 353-367, 2010.
- [2] H. P. Van Essen, B. H. Boon, S. Mitchell, D. Yates, D. Greenwood and N. Porter, "Sound Noise Limits: Options for a Uniform Noise Limiting Scheme for EU Airports," CE, Solution for Environment, Economy and Technology, 2005.
- [3] D. Casalino, F. Diozzi, R. Sannino and A. Paonessa, "Aircraft Noise Reduction Technologies: A Bibliographic Review," *Aerospace Science and Technology*, vol. 12, pp. 1-17, 2008.
- [4] J. Moss, "The Design of Low-Noise Vehicles for Air, Road and Rail Transportation," *Noise/News International*, vol. 18, pp. 13-15, 2010.
- [5] Y. P. Guo, K. J. Yamamoto and R. W. Stoker, "Experimental Study on Aircraft Landing Gear Noise," *Journal of Aircraft*, vol. 43, no. 2, pp. 306-317, 2006.
- [6] H. H. Heller and W. M. Dobrzynski, "Unsteady Surface Pressure Characteristics on Aircraft Components and Farfield Radiated Airframe Noise," *AIAA*, 1977.
- [7] B. S. Lazos, "Mean Flow Features Around the Inline Wheels of Four-Wheel Landing Gear," *AIAA*, vol. 40, no. 2, pp. 193-198, 2002.
- [8] B. S. Lazos, "Surface Topology on the Wheels of a Generic Four-Wheel Landing Gear," *AIAA*, vol. 40, no. 12, pp. 2402-2411, 2002.
- [9] L. S. Hedges, A. K. Travin and P. R. Spalart, "Detached-Eddy Simulations Over a Simplified Landing Gear," *Journal of Fluids Engineering*, vol. 124, pp. 413-423, 2002.
- [10] A. J. Saddington, R. D. Knowles and K. Knowles, "Laser Doppler Anemometry Measurements in the Near-Wake of an Isolated Formula One Wheel," *Experiments in Fluids*, vol. 42, pp. 671-681, 2007.

- [11] C. J. Doolan, "Computational Bluff Body Aerodynamic Noise Prediction using a Statistical Approach," *Applied Acoustics*, 2010.
- [12] N. H. MacCarthy, An Experimental Study of the Aerodynamics of Exposed Wheels, PhD Thesis, UK: Department of Aeronautics, Imperial College, 2010.
- [13] H. K. Versteeg and W. Malalasekera, An Introduction to Computational Fluid Dynamics - The Finite Volume Method Second Edition, Pearson Education Limited, 2007.
- [14] M. Morkovin, "Flow Around Circular Cylinder - A Kaleidoscope of Challenging Fluid Phenomena," *Symposium of Fully Separated Flows - ASME*, 1969.
- [15] S. F. Hoerner, Fluid-Dynamic Drag: Theoretical, Experimental and Statistical Information, Hoerner Fluid Dynamics, Bakersfield, CA, 1965.
- [16] R. Merrick and G. Bitsuamlak, "Control of Flow around a Circular Cylinder by the use of Surface Roughness: A Computational and Experimental Approach," *Journal of Fluid Mechanics*, vol. 123, pp. 363-378, 1982.
- [17] J. L. Heseltine, Flow Around a Circular Cylinder with a Free End, Masters Thesis, University of Saskatchewan, Canada, 2003.
- [18] A. C. Benim, E. Pasqualotto and S. H. Suh, "Modelling Turbulent Flow past a Circular Cylinder by RANS, URANS, LES and DES," *Progress in Computational Fluid Dynamics*, vol. 8, no. 5, pp. 299-307, 2008.
- [19] W. S. Chiu and J. H. Lienhard, "On Real Fluid Flow over Yawed Circular Cylinders," *ASME*, no. 67, 1967.
- [20] M. M. Zdravkovich, Flow Around Circular Cylinders, Oxford University Press, 2003.
- [21] M. M. Zdravkovich, A. J. Flaherty, M. G. Pahle and I. A. Skelthorne, "Some Aerodynamic Aspect of Coin - Like Cylinders," *Journal of Fluid Mechanics*, vol. 360, pp. 73-84, 1998.
- [22] J. E. Fackrell, The Aerodynamics of an Isolated Wheel Rotating in Contact with the Ground, London, UK: University of London, 1974.

- [23] J. Seifert, "A Review of the Magnus Effect in Aeronautics," *Progress in Aerospace Sciences*, 2012.
- [24] N. Thouault, C. Breitsamter, J. Seifert, C. Badalamenti, N. A. Adams and S. A. Prince, "Numerical Analysis of a Rotating Cylinder with Spanwise Discs," in *27th International Congress of the Aeronautical Sciences*, Nice, France, 2010.
- [25] W. R. Sears, "The Boundary Layer of Yawed Cylinders," *Journal of the Aeronautical Sciences (Institute of the Aeronautical Sciences)*, vol. 15, no. 1, pp. 49-52, 1948.
- [26] R. A. Smith, W. T. Moon and T. W. Kao, "Experiments on Flow about a Yawed Circular Cylinder," *Journal of Basic Engineering*, pp. 771-776, 1972.
- [27] T. Hayashi, F. Yoshino, R. Waka, S. Tanabe and T. Kawamura, "Turbulent Structure in a Vortex Wake shed from an Inclined Circular Cylinder," *Trans. JSME*, vol. 58, pp. 297-304, 1992.
- [28] P. W. Bearman and M. M. Zdravkovich, "Flow around a Circular Cylinder near a Plane Boundary," *Journal of Fluid Mechanics*, vol. 89, pp. 33-47, 1978.
- [29] J. McManus and X. Zhang, "A Computational Study of the Flow Around an Isolated Wheel in Contact with the Ground," *Journal of Fluids Engineering*, vol. 128, pp. 520-530, 2006.
- [30] J. Axerio-Cilies and G. Iaccarino, "An Aerodynamic Investigation of an Isolated Rotating Formula 1 Wheel Assembly," *Journal of Fluids Engineering, Transaction of the ASME*, vol. 134, pp. 121101-1-16, 2012.
- [31] R. D. Knowles, Monoposto Racecar Wheel Aerodynamics: Investigation of Near-Wake Structure & Support-Sting Interference, PhD Thesis, Cranfield University, 2005.
- [32] X. Zhang, Z. Ma, S. Smith and M. Sanderson, "Aerodynamic and Acoustic Measurements of a Single Landing Gear Wheel," in *19th AIAA/CEAS Aeroacoustics Conference*, Berlin, Germany, 2013.

- [33] A. Morelli, "Aerodynamic Effects on an Automobile Wheel," *MIRA. ATA*, vol. 22, pp. 281-288, 1969.
- [34] W. R. Stapleford and G. W. Carr, "Aerodynamic Characteristics of Exposed Rotating Wheels," The Motor Industry Research Association, Report No: 1970/2, 1969.
- [35] J. E. Fackrell and J. K. Harvey, "The Aerodynamics of an Isolated Road Wheel," in *Proceeding of the Second AIAA Symposium of Aerodynamics of Sports and Competition Automobiles*, Los Angeles, California, USA, 1975.
- [36] A. Cogotti, "Aerodynamic Characteristics of Car Wheels," *International Journal of Vehicle Design, Technological Advances in Vehicle Design Series*, Vols. SP3, Impact of Aerodynamics on Vehicle Design, pp. 173-196, 1983.
- [37] A. Waschle, S. Cyr, T. Kuthada and J. Wiedemann, "Flow Around an Isolated Wheel - Experimental and Numerical Comparison of Two CFD Codes," *SAE International*, 2004.
- [38] L. Axon, K. Garry and J. Howell, "An Evaluation of CFD for Modelling the Flow around Stationary and Rotating Isolated Wheels," *SAE Technical Paper Series*, 1998.
- [39] A. P. Mears, R. G. Dominy and D. B. Sims-Williams, "The Air Flow about an Exposed Racing Wheel," *SAE International*, 2002.
- [40] A. P. Mears, S. C. Crossland and R. G. Dominy, "An Investigation into the Flow-Field about an Exposed Racing Wheel," *SAE International*, 2004.
- [41] A. P. Mears and R. G. Dominy, "Racing Car Wheel Aerodynamics - Comparisons between Experimental and CFD derived Flow-Field Data," *SAE International*, 2004.
- [42] D. Ramachandran and G. C. Doig, "Unsteady Flow around an Exposed Rotating Wheel," School of Mechanical and Manufacturing Engineering, University of New South Wales, Sydney, Australia, 2012.
- [43] R. D. Knowles, A. J. Saddington and K. Knowles, "On the Near Wake of a Formula One Front Wheel," *Journal of Automobile Engineering*, 2013.

- [44] M. A. Van den berg, Aerodynamic Interaction of an Inverted Wing with a Rotating Wheel, PhD Thesis, UK: University of Southampton, 2007.
- [45] M. Hinson, Measurement of the Lift Produced by an Isolated, Rotating Formula one wheel using a new Pressure Measurement System, MSc Thesis, UK: Cranfield University, 1999.
- [46] P. W. Bearman, "Near Wake Flows behind Two and Three Dimensional Bluff Bodies," *Journal of Wind Engineering*, Vols. 69-71, pp. 33-54, 1997.
- [47] F. Li, M. R. Khorrami and M. R. Malik, "Unsteady Simulation of a Landing-Gear Flowfield," *AIAA*, pp. 1-12, 2002.
- [48] L. Venkatakrishnan and N. Karthikeyan, "Experimental Studies on a Rudimentary Four wheel Landing Gear," *AIAA*, 2011.
- [49] S. Krajnovic, R. Larusson and B. Basara, "Superiority of PANS compared to LES in predicting Rudimentary Landing Gear flow with affordable meshes," *International Journal of Heat and Fluid Flow*, vol. 37, pp. 109-122, 2012.
- [50] W. Dobrzynski, M. Pott-Pollenske, D. Foot and M. Goodwin, "Landing Gears Aerodynamic Interaction Noise," *European Congress on Computational Methods in Applied Sciences and Engineering*, 2004.
- [51] B. Khanal, K. Knowles, A. J. Saddington and S. Obayashi, "Computational Aeroacoustic Study of a Landing Gear," in *5th International Conference on Flow Dynamics*, Sendai, 2008.
- [52] J. Chawner, "Quality and Control - Two Reasons why Structured Grids aren't going away," *The Connector, Pointwise*, 2013.
- [53] "Ansys Fluent User's Guide, Release 13.0," 2010.
- [54] "Pointwise User Manual," 2013.
- [55] "Ansys Fluent Theory Guide, Release 13.0," 2010.

- [56] P. R. Spalart and S. R. Allmaras, "A One-Equation Turbulence Model for Aerodynamic Flows," *AIAA*, 1992.
- [57] T. H. Shih, W. W. Liou, A. Shabbir, Z. Yang and J. Zhu, "A new k-e Eddy Viscosity Model for High Reynolds Number Turbulent Flows," *Computational Fluids*, vol. 24, pp. 227-238, 1995.
- [58] S. Mahon and X. Zhang, "Computational Analysis of Pressure and Wake Characteristics of an Aerofoil in Ground Effect," *ASME*, vol. 127, pp. 290-298, 2005.
- [59] A. P. Mears, The Aerodynamic Characteristics of an Exposed Racing Car Wheel. PhD Thesis, University of Durham, 2004.
- [60] A. C. Benim, A. Nahavandi and K. J. Syed, "URANS and LES analysis of Turbulent Swirling Flows," *Progress in Computational Fluid Dynamics*, vol. 5, no. 8, pp. 444-454, 2005.
- [61] B. S. Lazos, "Mean Flow Features Around the Inline Wheels of Four-Wheel Landing Gear," *AIAA*, vol. 40, no. 2, pp. 193-198, 2002.